Theory and Experimental Evaluation of Electrodynamic Tether Systems and Related Technologies

by

Keith R. P. Fuhrhop

A dissertation submitted in partial fulfillment
of the requirements for the degree of
Doctor of Philosophy
(Electrical Engineering)
In The University of Michigan
2007

Doctoral Committee:

Professor Brian E. Gilchrist, Chair
Professor Mahta Moghaddam
Associate Professor John E. Foster
Dr. Robert Hoyt, Tethers Unlimited Inc.

To my whole family for their incredible support and motivation
Ronald, Barbara and Suzanne Fuhrhop

Especially to my lovely wife Kristin
for putting up with and inspiring me all along the way.

ACKNOWLEDGEMENTS

In addition, NASA Marshall Space Flight Center (MSFC) has provided experience in dealing with an actual mission. I am grateful to all the members of the ProSEDS team for their invaluable knowledge of spacecraft missions. I would also like to acknowledge the continual support of Tethers Unlimited for their experience and knowledge of electrodynamic tethers and the space industry. Special thanks to Nestor Voronka, and again to Robert Hoyt.

Numerous staff members have not only made my experience at the University of Michigan administratively possible, but much more plesant. I would like to thank Jan Beltran, Karen Kirchener, Mary Eyler, Beth Stalnaker, Karen Liska, Michelle Chapman, Beth Olsen, Melissa Lee, and Karla Johnson.

My family has given me loving encouragement and assistance throughout my life in graduate school, which I am most grateful for. In addition, as an added bonus I am grateful for the support of my wife's family for over the past 2 years as well. After all the years of their waiting and wondering I am very proud to finally be able to complete this work.

Last but not least is my wonderful wife Kristin. She has offered her continual loving support over the most strenuous times of compiling this thesis. Continual discussion of the jargon filled intracacies of my thesis pervaded much of our time together. Not only has she tolerated this, but she has contributed significantly, allowing me to think and approach problems from different points of view. I am looking forward to making up for the countless late nights I had to spend in the lab.

<div align="right">
Keith Ronald Pearson Fuhrhop

January 23, 2007
</div>

TABLE OF CONTENTS

LIST OF FIGURES

LIST OF TABLES

LIST OF APPENDICES

LIST OF ACRONYMS

ASI   Italian Space Agency

CHARGE   Cooperative High Altitude Rocket Gun Experiment

EDT   Electrodynamic Tether

EGA   Electron Gun Assembly

EMF   ElectroMotive Force

FEA   Field Emitter Array

FRDT   Facilities Requirements Definition Team

GLAST   Gamma ray Large Area Space Telescope

GTO   Geostationary Transfer Orbit

GTOSS   Generalized Tethered Object Simulation System

HC   Hollow Cathode

HCA   Hollow Cathode Assembly

HCPC   Hollow Cathode Plasma Contactor

HVPS   High Voltage Power Supply

MSIS   Mass Spectrometer Incoherent Scatter

IGRF   International Geomagnetic Reference Field

IRI   International Reference Ionosphere

ISS   International Space Station

JPL   Jet Propulsion Laboratory

KCL	Kirchoff's Current Law
KVL	Kirchoff's Voltage Law
LEO	Low Earth Orbit
MKS	Meters Kilograms Seconds
MT	Metric Ton
MXER	Momentum eXchange Electrodynamic Reboost
NASA	National Aeronautics and Space Administration
NEXIS	Nuclear Electric Xenon Ion System
NOAA	National Oceanic and Atmospheric Administration
OML	Orbital Motion Limited
PM	Parker Murphy
PMG	Plasma Motor Generator
ProSEDS	Propulsive Small Expendable Deployer System
SAA	South Atlantic Anomaly
SAIC	Science Applications International Corporation
SEC	Space Environments Center
SCL	Space Charge Limited
STS	Shuttle Transportation System
STV	Space Transfer Vehicle
SWO	Space Weather Operations
TATS	Tether Assisted Transportation System
TC	Thermionic Cathode
TSS	Tethered Satellite System

GLOSSARY

A = Cross sectional surface area [m^2]

A_R = Richardson constant [A/cm^2]

A_e = Surface area of an electron emitter [m^2]

A_{FN} = Fowler Nordheim constant [A/V^2]

alt_{sys} = Altitude of the system with respect to the center of Earth [m]

B = Magnetic field [T]

B_{FN} = Fowler Nordheim constant [V/m]

B_{mag} = Magnitude of the magnetic field [T]

B_{North} = Magnetic flux density component in the north-south direction [T]

C_d = Coefficient of drag [ ]

$C_{passive}$ = Capacitance across the plasma sheath [F]

D = Distance across the plasma sheath [m]

d_k = Diameter of the circular gap of the HC keeper [m]

E_{FN} = Electric field across the gate to tip gap in an FEA. [V/m]

di/dt = Change in inclination with respect to time [°/s]

dL = Differential section of tether [m]

dF = Differential component of force [N]

F_{out} = Out-of-plane force [N]

E_{ion} = Ion beam energy (also equals V_{emit}) [eV]

E_{num} = Number of electron emitters in the system [ ]

E_{solve} = Potential at which I_{ram} begins to deviate. The boundary between 'Region A' and 'Region C' of Figure 2-11 [V]

E_{thresh} = Potential at which Eq. 2-9 begins to deviate. The boundary between 'Region B' and 'Region C' of Figure 2-11, also equals E_{ion} [V]

f   = Escape fraction of electrons moving beyond the keeper. This is based on the geometry of the keeper. [ ]

F_d = Atmospheric drag force [N]

F_{gg} = Gravitational gradient force [N]

F_{mag} = Magnitude of the Lorentz force produced by the EDT system [N]

F_{out} = Out of plane force exerted by an EDT system [N]

G   = Universal gravitational constant [N·m^2/kg^2]

H_u = Intermediate step for calculating the sheath size. (Eq. 2-6)

I   = Current [A]

I_{anode} = The current collected by the endbody collector end of the tether [A]

I_{avg} = Average current across the tether [A]

I_C = Current at cathode end of the tether [A]

I_{CL} = Current collected due to the 1D Child Langmuir law [A]

$I_{collecta}$ = Current collected in 'Region A' of Figure 2-11 [A]

$I_{collectb}$ = Current collected in 'Region B' of Figure 2-11 [A]

$I_{collectc}$ = Current collected in 'Region C' of Figure 2-11 [A]

$I_{element}$ = Current collected along a particular element of tether [A]

$I_{emitter}$ = Current emitted by the electron emitter on the cathode end of the tether [A]

I_{epc} = Total current to (or from) the plasma contactor [A]

I_i = Hollow cathode emitted ion current [A]

I_{local} = Current collection along a unit of tether [A]

I_{match} = Current collection at the E_{thresh} potential [A]

I_o = Electron thermal current at plasma potential [A]

$I_{passive}$ = Passive current collected from electrons and ion naturally impacting [A]

I_{ram} = Ram current [A]

I_{return} = Current that returns to the spacecraft as the result of SCLs or an opposing potential drawing the electrons back [A]

I_{solve} = Current collected at the E_{solve} potential [V]

I_t = Current through a particular point in the tether system [A]

I_{tether} = Current through a particular point in the tether system [A]

$I_{tetherend}$ = The electron current at the cathode end of the tether [A]

I_{the} = Electron thermal current [A]

I_{thi} = Ion thermal current [A]

J_{the} = Electron thermal current density [A/m^2]

J_{thi} = Ion thermal current density [A/m^2]

L = Length of the tether [m]

lat_{sys} = Latitude of an orbiting system about the Earth [°]

l_{ck} = Gap between the orifice and the keeper of the HC [m]

m_{body} = Mass of an orbiting body [kg]

m_e = Electron mass [kg]

M_{Earth} = Mass of the Earth [kg]

m_i = Ion mass [kg]

N = The nth numbed element in the system (= L/dl) [ ]

n_e = Electron density of the ambient plasma [m^{-3}]

n_i = Ion density of the ambient plasma [m^{-3}]

n_o = Density of the ambient plasma [m^{-3}]

n_{or} = Electron plasma density at the orifice of the HC [m^{-3}]

P_{hvps} = Power of the high voltage power supply [W]

q = Charge of an electron [C]

r_b = Radius of the emitter [m]

R = Larger of the two semi-axes radius of an elliptical electron emission device [m]

R_{load} = Resistance of the load resistor [Ω]

r_o = Radius of the system's center of gravity from the center of the Earth [m]

r_{or} = Radius of the orifice of the plasma contactor [m]

r_{sh} = Distance across the plasma sheath [m]

r_s = Radius of the surface [m]

R_t = Resistance along the tether [Ω/m]

SA = Total Surface area [m^2]

SA2d = 2D Surface area [m^2]

T_e = Electron temperature [eV]

T_{epc} = Temperature of the electrons emitted at the HC orifice [eV]

T_i = Ion temperature [eV]

t_k = Thickness of the HC keeper [m]

t_u = Intermediate step for calculating the sheath size. (Eq. 2-5) [m]

V_{anode} = Potential of the anode, or electron collecting end of the tether [V]

$V_{cathode}$ = Potential of the cathode, or electron emitting end of the tether [V]

V_{Corot} = Velocity the Earth rotates in an Earth-centered inertial frame [m/s]

$V_{element}$ = Potential of the tether with respect to the plasma at a particular element along its length [V]

V_{emf} = Motional electro-motive force potential [V]

$V_{emitter}$ = Potential of the electron emitter [V]

V_{hvps} = Potential of the high voltage power supply [V]

V_{load} = Potential of load inserted at the end of the tether before the cathode [V]

V_{local} = Potential of a section of tether with respect to the plasma [V]

v_{orb} = Orbital velocity in an Earth-centered inertial frame [m/s]

v_{orbt} = Orbital velocity minus the Earth's rotation in an Earth-centered inertial frame [m/s]

V_p = Potential of the collecting body with respect to the plasma [V]

V_{sat} = Potential of the satellite with respect to the plasma [V]

V_{sh} = Potential across the plasma sheath [V]

$V_t - V_p$ = Potential of the tether with respect to the plasma [V]

V_{to} = Potential difference between the tether to orbiter across the break of the TSS-1R mission [V]

V_{tether} = Total resistive potential loss across the entire EDT [V]

W = Smaller of the two semi-axes diameters of an elliptical electron emission device. [m]

α = Experimental correction factor for Parker Murphy calculation

α_{in} = In-plane angle of the tether length along the x-z plane with respect to the z-axis (Figure 3-1) [°]

α_{out} = Out-of-plane angle of the tether length from the α_{in} to the tether (Figure 3-1) [°]

β = Experimental correction factor for Parker Murphy calculation [ ]

β_{cf} = Ballistic coefficient [kg/m^2]

ΔV_A = Potential of the anode, or electron collecting end of the tether [V]

ΔV_C = Potential of the cathode, or electron emitting end of the tether [V]

ΔV_{tc} = Potential across the anode to cathode gap in an electron gun [V]

ε_o = Permitivity off free space [F/m]

η = Emission efficiency factor of the TC / electron gun pair [ ]

θ_t = Intermediate value used to calculate the escape fraction of the HC [°]

λ_{De} = Debye length [m]

λ_{in} = Angle of the velocity in the x-z plane [°]

λ_{out} = Angle of the velocity in the y-z plane [°]

ϕ_o = Intermediate potential for Parker Murphy calculation [V]

ρ = The perveance associated with a particular electron gun [pervs]

ρ_a = Neutral atmospheric density [km/m^3]

ρ_o = Material resistivity [$\Omega \cdot$m]

ρ_{res} = Actual resistivity of a material after considering temperature affects [$\Omega \cdot$m]

ω_{ce} = Electron cyclotron (Gyro-) frequency [Hz]

ω_{ci} = Ion cyclotron (Gyro-) frequency [Hz]

ω_o = Orbital angular velocity of the center of gravity [s^{-1}]

ABSTRACT

THEORY AND EXPERIMENTAL EVALUATION OF ELECTRODYNAMIC TETHER SYSTEMS AND RELATED TECHNOLOGIES

by

Keith R. P. Fuhrhop

Chair: Brian E. Gilchrist

The unique work presented in this thesis will first focus on integration of the latest theoretical and experimental electrodynamic aspects of an electrodynamic tether (EDT) into a time-independent simulation tool. Numerous elements have then be compared on a system level, including passive electron collection (or active ion emission) technologies, active electron emission technologies, bare versus insulated tether scenarios, boosting and de-boosting conditions, and various system element configurations. These results indicate that in many cases bare tether anodes are the optimal electron collection mechanism. In addition, it was shown that while hollow cathodes may be the best active electron emission technique, field emitter arrays result in less than 1% difference in system thrusting and use no consumables. This is based on the assumption that several-amp field emitter arrays can be built eventually.

Issues that have troubled previous systems are the efficiency at which the tether collects current, the total surface area, and the bare tether geometry. Experimental work was

conducted to compare the effects of porous flat-tape tether geometries to those of slotted and solid geometries. The experiment investigated these different tether configurations to better understand the physics involved and how to apply the different tether geometries to an EDT system. This work has resulted in evidence showing that, regardless of the orientation of the probe with respect to the flowing plasma, equivalent mass holed tapes outperform that of slotted tapes. These slotted tapes, in turn, outperform solid tapes on an equivalent mass basis.

Modeling of hollow cathodes and other ion emission technologies has been a key concern to EDT technology and will have great implications to EDT systems. As tether systems venture outside of the ionosphere, there will likely need to be an alternate method for collecting electrons. An initial investigation using a hollow cathode as an electron collection source in the momentum exchange electrodynamic reboost (MXER) system was conducted. Results indicated that although this technology may produce a slight enhancement in thrust over a bare tether in altitudes over 1000 km, however, it requires too much consumable mass to be feasable. Other ion emission techniques may solve this issue to an extent, however, much experimentation work needs to be done to accurately prove the effectiveness of such technology.

CHAPTER 1

INTRODUCTION, BACKGROUND, AND PREVIOUS RESEARCH

1.1 Research Motivation and Definition of the Problem

1.1.1 Purpose

Conductive Electrodynamic Tether (EDT) technology has made significant progress through simulations and experimentation during several space missions. In addition, the need for tethers has been discussed in numerous publications. One example includes reboosting the International Space Station (ISS), which could save ~$100 million dollars per year by using this technology [10]. Other applications could drastically reduce the increasing space debris orbiting the Earth [11]. Additionally, the fuel requirements for getting from low Earth orbit (LEO) to geostationary transfer orbit (GTO) could be nearly eliminated [12] [13].

Furthermore, there are other more exciting long term projects that would directly compliment NASA's current space initiative [14]. One example would be an enhancement in the Momentum eXchange Electrodynamic Re-boost (MXER) concept, which would allow for orbital transfer to the Moon [15] or even Mars[16]. There is even a proposed mission that would take an object in LEO, and, without the use of any consumables, completely transport that object to the Moon <u>and</u> set it down at a specified location [17]. Such projects have been designed and published in the relevant literature. The core theory on how EDTs work is known, but this technology needs to be expanded upon. Verifiable simulation codes exist for basic tether systems, as there is an

understanding of the fundamental physics involved in designing these systems. The issue now is how to optimize and improve upon certain aspects of these previous simulations. New technologies for electron and ion emission, as well as electron collection, have emerged and are currently being developed. Also, the understanding of electron collection to bare tethers and porous bodies are still being investigated. These emerging tether technologies need to be studied from an integrated system standpoint to understand their potential impact.

A model that can integrate this understanding and optimize the resulting forces would not only increase the system efficiency and safety, but will also decrease the financial burden of all future missions involving EDTs. Enhanced current collection and emission due to these new technologies would allow for smaller power and mass requirements. In addition, it would allow for the investigation into new types of missions and areas that were not even conceived as a possibility until such a model became available.

1.1.2 Uses for ED Tethers

Over the years, numerous applications for electrodynamic tethers have been identified for potential use in industry, government, and scientific exploration. Table 1-1 is a summary of some of the potential applications proposed thus far. Some of these applications are general concepts, while others are well-defined systems. Many of these concepts overlap into other areas; however, they are simply placed under the most appropriate heading for the purposes of this table. All of the applications mentioned in the table are elaborated upon in the Tethers Handbook [18]. Three fundamental concepts that tethers possess, that will be discussed within this thesis are gravity gradients, momentum exchange, and electrodynamics.

ELECTRODYNAMICS	
Electrodynamic Power Generation	Electrodynamic Thrust Generation
ULF/ELF/VLF Communication Antenna	Radiation Belt Remediation
SPACE STATION	
Microgravity Laboratory	Shuttle De-orbit from Space Station
Tethered Space Transfer Vehicle (STV) Launch	Variable/Low Gravity Laboratory
Attitude Stabilization and Control	ISS Reboost
TRANSPORTATION	
Generalized Momentum Scavenging from Spent Stages	Internal Forces for Orbital Modification
Satellite Boost from Orbiter	Tether Assisted Transportation System (TATS)
Tether Re-boosting of Decaying Satellites	Upper Stage Boost from Orbiter

Table 1-1: Possible Tether Applications

1.1.2.1 Gravity Gradient

A non-rotating tether system has a stable orientation that is aligned along the local vertical of the Earth. This can be inderstood by inspection of Figure 1-1 where two spacecraft at two different altitudes have been connected by a tether. Normally, each spacecraft would have a balance of gravitational (e.g. F_{g1}) and centrifugal (e.g. F_{c1}), but when tied together by a tether these values begin to change with respect to one another. This phenomenon occurs because, without the tether, the higher altitude mass would travel slower than the lower mass. The system must move at a single speed, so the tether must therefore slow down the lower mass and speed up the upper one. The centrifugal force of the tethered upper body is increased while that of the lower altitude body is reduced. This results in the centrifugal force of the upper body and the gravitational force of the lower body being dominant. This difference in forces naturally aligns the system along the local vertical, as seen in Figure 1-1 [18].
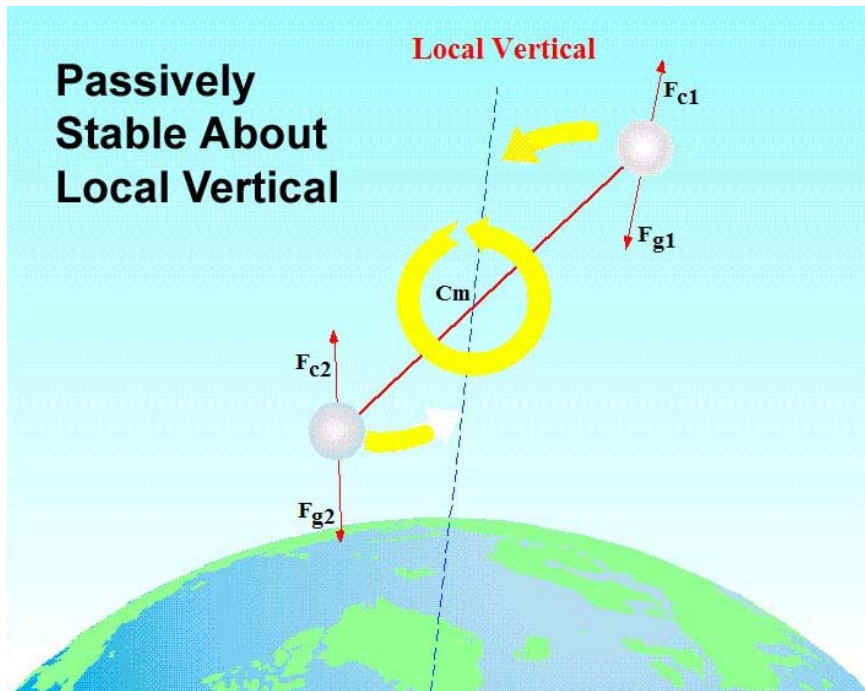
Figure 1-1: Description of the forces contributing towards maintaining a gravity gradient alignment in the EDT system.

1.1.2.2 Momentum Exchange

Due to the centrifugal acceleration, the act of spinning a long tether will create a controlled force on the end-masses of the system. If the tether system is spun at a particular angular frequency then the objects on either end of the EDT system will experience continous acceleration. This controlled gravity is manipulated by control of the angular frequency. From this, momentum exchange can occur if an endbody is released during the controlled rotation. The transfer in momentum to the released object will cause the system to lose orbital energy, and thus lose altitude. However, using electrodynamic tether thrusting it is possible to re-boost itself again without the expenditure of consumables, which will be explained in the upcoming section.

1.1.2.3 Electrodynamics

Finally, the particular concept that will be focused on for this thesis research is the electrodynamics of an EDT system. Understanding the physical behaviors underlying the electromagnetic interactions between a conducting tether and its environment is the core of EDT research. Electrical power generation and propellant-less thrust generation are a few of the concepts relating to electrodynamics that will be thoroughly discussed in this thesis [18].

1.1.3 Electrodynamic Tether Fundamentals

A motional Electromotive Force (EMF) is generated across a tether element, given by Eq. 1-1, as it moves relative to a magnetic field.

$$V_{emf} = \int_0^L \left(\overline{v}_{orb} \times \overline{B} \right) \cdot d\overline{L} \qquad \text{Eq. 1-1}$$

Without loss of generality, it is assumed the tether system is in Earth orbit and it moves relative to Earth's magnetic field. Similarly, if current flows in the tether element, a force can be generated as described in Eq. 1-2. In self-powered mode (de-orbit mode), this EMF can be used by the tether system to drive the current through the tether and other electrical loads (e.g. resistors, batteries), emit electrons at the emitting end, or collect electrons at the opposite. In boost mode, on-board power supplies must overcome this motional EMF to drive current in the opposite direction, thus creating a force in the opposite direction, as seen in Figure 1-2, and boosting the system.

B-Field Lines

Magnetic South

Boost

e⁻ HVPS

Anode

e⁻

→ I

V$_{orbt}$

Insulation

Earth

e⁻

Anode

e⁻

← I

V$_{orbt}$

De-boost

Magnetic North

The tether to Earth sizes are not to scale

From Eq. 1-1: Higher alt. = higher EMF Potential

From Eq. 1-2: Thrust is in v$_{orb}$ direction for 'Boost' and opposite in 'De-boost'
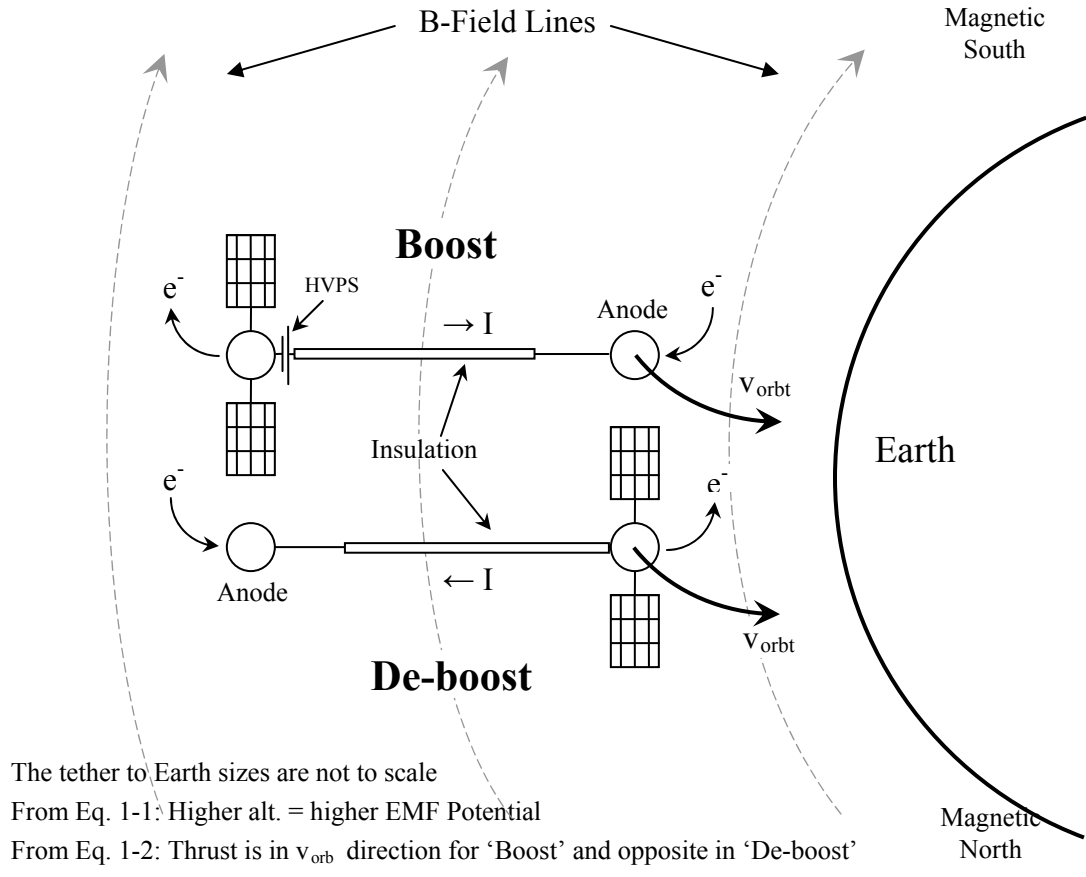
Figure 1-2: Illustration of the EDT concept.

$$\overline{F} = \int_{0}^{L} I(L) \cdot d\overline{L} \times \overline{B}$$ **Eq. 1-2**

Take, for example, the NASA Propulsive Small Expendable Deployer System (ProSEDS) mission as seen in Figure 1-2 [19] [20] [21] [22] [23]. At 300-km altitude, the Earth's magnetic field, in the north-south direction, is approximately $0.18 - 0.32$ Gauss up to ~40º inclination, and the orbital velocity with respect to the local plasma is about 7500 m/s. This results in a V$_{emf}$ range of $35 - 250$ V/km along the 5-km length of tether. This EMF dictates the potential difference across the bare tether which controls where electrons are collected and / or repelled. Here, the ProSEDS de-boost tether system is configured to enable electron collection to the positively biased higher altitude section of the bare tether, and returned to the ionosphere at the lower altitude end. This flow of electrons through the length of the tether in the presence of the Earth's magnetic

6

field creates a force that produces a drag thrust that helps de-orbit the system, as given by the Eq. 1-2.

The boost mode is similar to the de-orbit mode, except for the fact that a High Voltage Power Supply (HVPS) is also inserted in series with the tether system between the tether and the higher positive potential end. The power supply voltage must be greater than the EMF and the polar opposite. This drives the current in the opposite direction, which in turn causes the higher altitude end to be negatively charged,[1] while the lower altitude end is positively charged.

To further emphasize the de-boosting phenomenon, a schematic sketch of a bare tether system with no insulation (all bare) can be seen in Figure 1-3.
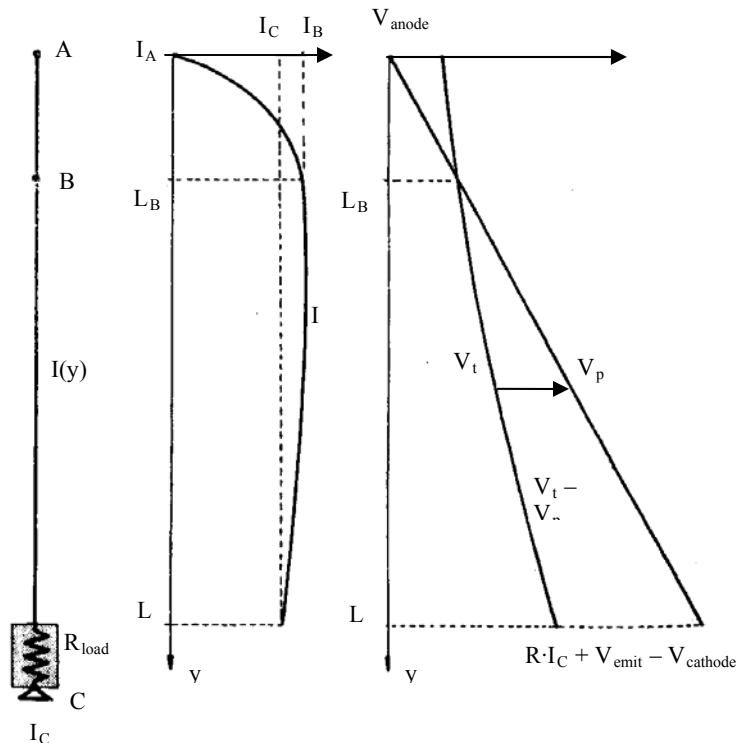
Figure 1-3: Current and Voltage plots vs. distance of a bare tether operating in generator (de-boost) mode [1].

The top of the diagram, point 'A', represents the electron collection end. The bottom of the tether, point 'C', is the electron emission end. Similarly, V_{anode} and $V_{cathode}$ represent the potential difference from their respective tether ends to the plasma, and V - V_p is the potential anywhere along the tether with respect to the plasma. Finally, point 'B'

---

[1] Assuming a standard east to west orbit around Earth.

is the point at which the potential of the tether is equal to the plasma. The location of point 'B' will vary depending on the equilibrium state of the tether, which is determined by the solution of Kirchoff's Voltage Law (KVL) and Kirchoff's Current Law (KCL)[2] along the tether, presented in Eq. 1-3 and Eq. 1-4, respectively. I_{AB}, I_{BC}, and I_C describe the current gain from point A to B, the current lost from point B to C, and the current lost at point C, respectively.

$$V_{anode} + \int_A^C I(y) \cdot dR_t + R_{load} \cdot I_C + V_{emit} + V_{cathode} = V_{emf} \qquad \textbf{Eq. 1-3}$$

$$I_{AB} = I_{BC} + I_C \qquad \textbf{Eq. 1-4}$$

Since the current is continuously changing along the bare length of the tether, the potential loss due to the resistive nature of the wire is represented as $\int_A^C I(y) \cdot dR_t$. Along an infinitesimal section of tether, the resistance 'dR$_t$' multiplied by the current traveling across that section 'I(y)' calculates the resistive potential loss.

After evaluating Eq. 1-3 and Eq. 1-4 for the system, the results will yield a current and potential profile along the tether, as seen in Figure 1-3. This diagram shows that, from point A of the tether down to point B, there is a positive potential bias, which increases the collected current. Below that point, the V - V_p becomes negative and the collection of ion current begins. Since it takes a much greater potential difference to collect an equivalent amount of ion current (for a given area), the total current in the tether is reduced by a smaller amount. Then, at point C, the remaining current in the system is drawn through the resistive load (R_{load}), and emitted from an electron emissive device (V_{emit}), and finally across the plasma sheath ($V_{cathode}$). The KVL voltage loop is then closed in the ionosphere where the potential difference is effectively zero[3].

Due to the nature of the bare EDTs, it is often not optional to have the entire tether bare. In order to maximize the thrusting capability of the system a significant portion of the bare tether should be insulated. This insulation amount depends on a number of effects, some of which are plasma density, the tether length and width, the

---

[2] KVL and KCL will be discussed further in Section 3.1.1.
[3] The current closure process is discussed further in Section 3.1.1.

orbiting velocity, and the Earth's magnetic flux density. This will be discussed more thoroughly in Chapter 3.

1.2   History of ED Tethers - Past and Present Missions

A number of missions have flown where the purpose was to verify tether physics and related technology. For the purpose of this thesis, the missions involving verification of tether electrodynamics will be discussed as well as their contribution to EDT knowledge [18].

1.2.1   TSS-1

One of the first missions, Tethered Satellite System (TSS), was proposed by NASA and the Italian Space Agency (ASI) in the early 1970's by Mario Grossi, of the Smithsonian Astrophysical Observatory, and Giuseppe Colombo, of Padua University. In 1979, the Facilities Requirements Definition Team (FRDT) met to discuss the potential scientific applications for tethered systems and whether they were justified in designing them. In 1980, the FRDT report strongly endorsed a shuttle based tether system. Finally, in 1984 a formal memorandum was drafted in which NASA and ASI agreed to work together in completing this project [18].

The purpose of the TSS mission was to verify the tether concept of gravity gradient stabilization, as well as to provide a research facility for investigating space physics and plasma electrodynamics. The mission was launched on July 31, 1992 on the Shuttle Transportation System (STS) -46. The mission only deployed 268 m of the 20 km proposed amount due to mechanical problems. Despite this issue, the results conclusively proved that the basic concept of long gravity-gradient stabilized tethers was sound. It also settled several short deployment dynamics issues, reduced safety concerns, and clearly demonstrated the feasibility of deploying the satellite to long distances. This allowed the TSS-1R mission to focus on scientific objectives [18].

1.2.2 TSS-1R

The TSS-1R mission objective was to deploy the tether 20.7 km above the space station and remain there collecting data. Scientific objectives for the TSS-1R mission were to conduct exploratory experiments in space plasma physics. Projections indicated that the motion of the long conducting tether through the Earth's magnetic field would produce a motional EMF that would drive a current through the tether system. TSS-1R was launched on February 22, 1996 on STS-75.

TSS-1R was deployed to 19.7 km, but this was still long enough to verify numerous scientific speculations. These findings included the measurements of the motional EMF [24], the satellite potential [25], the orbiter potential [26], the current in the tether [27], the changing resistance in the tether [28], the charged particle distributions around a highly charged spherical satellite [29], and the ambient electric field [24]. In addition, a particularly significant finding used in this thesis concerns the current collection at different potentials on a spherical endmass. As seen in Figure 1-4, measured currents on the tether far exceeded predictions of previous numerical models [30] by up to a factor of three. A more descriptive explanation of these results can be found in Thompson et al. [31].
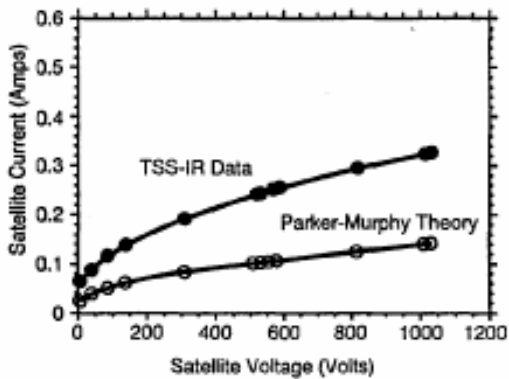
Figure 1-4: Measured TSS-1R and theoretically predicted I-V characteristics [18].

Other scientific advancements have resulted from this mission. Improvements have been made in modeling the electron charging of the shuttle and how it effects current collection [27]. In addition, much was learned concerning the interaction of bodies with surrounding plasma, as well as the production of electrical power [32].

1.2.3   CHARGE 2

The Cooperative High Altitude Rocket Gun Experiment (CHARGE) 2 was jointly developed by Japan and NASA, to observe the current collection along with many other phenomena. The major objective was to measure the payload charging and return currents during periods of electron emission. Secondary objectives were related to plasma processes associated with direct current and pulsed firings of a low-power electron beam source. On December 14, 1985, the CHARGE mission was launched at White Sands Missile Range, New Mexico [33]. The results indicated that it is, in fact, possible to enhance the electron current collection capability of positively charged vehicles by means of deliberate neutral gas releases into an undisturbed space plasma.

In addition, it was observed that the release of neutral gas or argon gas into the undisturbed plasma region surrounding a positively biased platform has been found to cause enhancements to electron current collection. This was due to the fact that a fraction of the gas was ionized, which increased the local plasma density, and therefore the level of return current [25].

1.2.4   PMG

The objectives of the Plasma Motor Generator (PMG) mission were to test the ability of a Hollow Cathode Assembly (HCA) to provide a low impedance bipolar electrical current between a spacecraft and the ionosphere. In addition, other expectations were to show that the mission configuration could function as an orbit-boosting motor as well as a generator, by converting orbital energy into electricity. The mission was launched on June 26, 1993, as the secondary payload on a Delta II rocket [18].

The total experiment lasted approximately seven hours. In that time, the results demonstrated that current is fully reversible, and therefore was capable of operating in power generator and orbit boosting modes. The hollow cathode was able to provide a

low power way of connecting the electrons to and from the ambient plasma. This means that the HC demonstrated its electron collection and emission capabilities.

1.2.5 ProSEDS

The use of a bare section of a space-borne electrodynamic tether for an electron-collection device has been suggested [1] as a promising alternative to end-body electron collectors for certain applications, provided that electrons are collected in a quasi-orbital-motion-limited regime.[4] For a given V - V_p, plasma probe theory predicts that the collected electron current per unit area (not total current) is maximized in the orbital-motion-limited regime, which is only valid with sufficiently thin wires (explained in Section 2.1.1) [34, 66]. NASA's Propulsive Small Expendable Deployer System (ProSEDS) would deploy 5-km of tether to collect up to $1 - 2$ A of current from the ionosphere. The current interacting with the Earth's magnetic field would produce an electrodynamic drag thrust and reduce the de-orbit time by more than 5-km / day compared to the atmospheric drag.

The bare tether concept was to be tested first during this ProSEDS mission [20]. While the mission was canceled [23] after NASA's space shuttle Columbia accident, the concept could potentially be undertaken in the future. Present bare tether designs, such as the one developed for the ProSEDS mission, use a small, closely packed cross-section of wires or even a single wire as the anode. In future designs, concerns for survivability to collisions with micro-meteoroids and space debris will need to be considered. This will require the use of distributed or sparse tether cross-section geometries, which could span tens of Debye lengths depending on plasma density and temperature [35]. One such technology that has been developed is the Hoytether [36].

1.3 Dissertation Overview

The tether community has experienced numerous tether technology development successes (as previously mentioned); however, it has yet to incorporate these results into

---

[4] The orbit motion limited regime is discussed in Chapter 2.

a simulation that can effectively compare the array of possible variables for a viable system. That, combined with the lack of knowledge for the most efficient system setup for a given scenario, can result in the reduction of boosting capabilities when trying to simulate EDTs. As missions become more elaborate, factors such as the power efficiency and thrust to mass ratios can mean the difference between a safe profitable result and a complete failure.

The work presented in this thesis will focus on each element of the EDT system individually and then integrate them through simulation. Several elements will be compared on a system level, including: the electron collection (ion emission) technologies for the anode end; electron emission (ion collection) technologies for the cathode end; bare versus insulated tether scenarios; boosting and de-boosting conditions; and various system configurations.

Selected case studies will be conducted on various new tether geometry concepts. Particular tether system aspects, such as the efficiency at which the tether collects current, the total surface area, and the bare tether length, will be explored. In addition, the goals of the experiment will be to investigate different tether configurations in order to understand the physics involved so as to apply it to an EDT system.

The modeling of hollow cathode technologies has been a key concern to EDT technology and will have significant effects to EDT systems. As tether systems venture outside of the ionosphere, there will need to be an alternate method for collecting electrons. HCs may solve this issue to an extent; however, significant experimentation work is needed in order to describe accurately the effectiveness of this technology.

There have been a number of models created that detail the electrodynamic aspects of EDTs and their various resulting affects through orbit. At least four major simulation codes have been developed that incorporate system electrodynamics, orbital dynamics, and the major models of Earth: the Mass Spectrometer Incoherent Scatter (MSIS) atmospheric model, the International Reference Ionosphere (IRI) model, and the International Geomagnetic Reference Field (IGRF) model. These models are detailed in Table 1-2.

Code Name	Designer
GTOSS (Generalized Tethered Object Simulation System)	NASA –Marshall Space Flight Center [37]
TEMPEST	University of Michigan [19, 38]
TetherSim	Tethers Unlimited Inc. [39]
MASTER20	Smithsonian Astrophysical Observatory [23]

Table 1-2: Complete EDT simulation modeling programs.

In addition, many generic studies and future plans for EDT systems have been performed by a number of groups in the tether community [40] [18] [41] [4] [42] [43]. Individual contributions have also advanced tether technology, as seen in Table 1-3. The groups involved in advancing theory in EDT systems did so with either their own simulation codes, mentioned in Table 1-2, or with their own independent simulation tools focusing on their particular area of tether technology.

Institutes Contribution	EDT Simulation Work
Istituto di Fisica Spazio Interplanetario and Universita di Roma, Rome, Italy	De-orbiting General Analysis [44] De-orbiting Tether Collection Comparison [45, 46] Current Enhancement for De-orbiting [47] Electron Collection in Ionosphere by Satellite [48]
Universidad Polit´ecnica de Madrid - Madrid, Spain	De-orbiting Physics and Tradeoffs [49] Bare Tethers as Atmosphere Probe [50] Bare Wire Physics [1] Close Parallel Tether Current Collection [22]
University of Michigan – Ann Arbor, MI	Transient Plasma Sheath Model [51] EMF Measurements and Circuit Analysis [52] Transmission Line Analysis and Current Enhancement [53] Electron Collection in Flowing Plasmas [54] RF Enhancement to Current Collection [55] Tether Current Collection [38] Current Collection Varying Tether Geometries [56]
Smithsonian Astrophysical Observatory, Cambridge, MA	Transient Equivalent Circuit Model [57] Bare Tether Performance [58, 59] Tether Electromagnetic Interactions [60]
NASA - Marshall Space Flight Center, Huntsville, AL	Tether Material Performance [61]
Tethers Unlimited Inc. Bothell, WA	Bare Tether Collection w/o Contactors [62]
Massachusetts Institute of Technology, Cambridge, MA	Tether Electron Collection in Magnetized Plasma [63] Magnetic Field Effects on Bare Tether Current Collection [64]

Table 1-3: Contributions from various groups on EDT performance and understanding.

The ultimate goal of this thesis work will be to increase the understanding of EDT systems. Work will be presented on many relevant configurations and scenarios, with results stressing the tradeoffs and efficiencies of present state of the art technologies. Ideally, this thesis work will be applied toward a simulation which will incorporate all dynamical and electromagnetic aspects, such as the ones listed in Table 1-2. Some of this work has already been directly applied to the TetherSim code, as part of funded NASA research. All future ED tether missions should directly benefit from this investigation. Once the mission scenario is known, the design process can be accomplished. The efficiencies for all technology types can then be investigated and compared.

Summary of Unique Contributions:

- Integration of the latest theoretical and experimental electrodynamic aspects of an EDT into a time independent simulation tool. These include active electron emitters and passive electron and ion collection.

- In-depth evaluation of the effects many key variables have on the overall system, such as tether length, tether geometry, the high voltage power supply (HVPS), and the ambient electron density.

- Assessment of tradeoffs to optimize the amount of bare tether necessary for many EDT scenarios

- Experimental analysis comparing the effects of holed tether geometries to those of slotted and solid, on a current collecting tape

- Experimental verification of optimal tether geometries for particular scenarios

- EDT analysis method for determining the best system design for various mission objectives

- Analysis of hollow cathode use in EDT systems for high current applications, particularly for possible use in the momentum exchange electrofynamic reboost (MXER) system.

CHAPTER 2

CURRENT COLLECTION AND ELECTRON EMISSION FOR AN EDT SYSTEM: THEORY AND TECHNOLOGY

Understanding electron and ion current collection to and from the surrounding ambient plasma is critical for most EDT systems. Any exposed conducting section of the EDT system can passively[5] collect electron or ion current, depending on the electric potential of the spacecraft body with respect to the ambient plasma. In addition, the geometry of the conducting body plays an important role in the size of the sheath and thus the total collection capability. As a result, there are a number of theories for the varying collection techniques. The first part of this chapter will discuss this passive collection theory.

The primary passive processes that control the electron and ion collection on an EDT system are thermal current collection, ion ram collection affects, electron photoemission, and possibly secondary electron and ion emission. In addition, the collection along a thin bare tether is described using orbital motion limited (OML) theory as well as theoretical derivations from this model depending on the physical size with respect to the plasma Debye length. These processes take place all along the exposed conducting material of the entire system. Environmental and orbital parameters can significantly influence the amount collected current. Some important parameters include plasma density, electron and ion temperature, ion molecular weight, magnetic field strength and orbital velocity relative to the surrounding plasma.

---

[5] 'passive' and 'active' emission refers to the use of pre-stored energy in order to achieve the desired affect

This chapter will then discuss the active collection and emission techniques involved in an EDT system. This occurs through devices such as a hollow cathode plasma contactors, thermionic cathodes, and field emitter arrays. The physical design of each of these structures as well as the current emission capabilities are thoroughly discussed. Each active emission device will be employed into the EDT simulation in future chapters.

2.1   Bare conductive tethers

The concept of current collection to a bare conducting tether was first formalized by Sanmartin and Martinez-Sanchez [1]. They note that the most area efficient current collecting cylindrical surface is one that has an effective radius less than ~1 Debye length where current collection physics is known as orbital motion limited (OML) in a collisionless plasma. As the effective radius of the the bare conductivr tether increases past this point then there are predictable reductions in collection efficiency compared to OML theory. In addition to this theory (which has been derived for a non-flowing plasma), current collection in space occurs in a flowing plasma, which introduces another collection affect. These issues are explored in greater detail below.

2.1.1   Orbital Motion Limited (OML) Theory

The electron Debye length [65] is defined as the characteristic shielding distance in a plasma, and is described in Eq. 2-1.

$$\lambda_{De} \cong \sqrt{\frac{\varepsilon_0 \cdot T_e}{q \cdot n_0}} \qquad\qquad \textbf{Eq. 2-1}$$

This distance, where all electic fields in the plasma resulting from the conductive body have fallen off by 1/e, can be calculated. OML theory [34] is defined with the assumption that the electron Debye length is equal to or larger than the size of the object and the plasma is not flowing. The OML regime occurs when the sheath becomes sufficiently thick such that orbital effects become important in particle collection. This

theory accounts for and conserves particle energy and angular momentum. As a result, not all particles that are incident onto the surface of the thick sheath are collected. The voltage of the collecting structure with respect to the ambient plasma, as well as the ambient plasma density and temperature, determines the size of the sheath. This accelerating (or decelerating) voltage combined with the energy and momentum of the incoming particles determines the amount of current collected across the plasma sheath.

The orbital-motion-limit regime is attained when the cylinder radius is small enough such that that all incoming particle trajectories that are collected are terminated on the cylinder's surface are connected to the background plasma, regardless of their initial angular momentum (i.e., none are connected to another location on the probe's surface). Since, in a quasi-neutral collisionless plasma, the distribution function is conserved along particle orbits, having all "directions of arrival" populated corresponds to an upper limit on the collected current per unit area (not total current) [66].

In an EDT system, the best performance for a given tether mass is for a tether diameter chosen to be smaller than an electron Debye length for typical ionospheric ambient conditions[6], so it is therefore within the OML regime. Tether geometries outside this dimension will be addressed in section 2.1.2. OML collection will be used as a baseline when comparing the current collection results for various sample tether geometries and sizes. OML current collection by a thin cylinder is given by Eq. 2-2, where $erfc(x) = (2/\sqrt{\pi}) \cdot \int_x^\infty e^{-t^2} dt$ [34] [66].

$$I_{omle,omli} = \underbrace{A_p \cdot n_{e,i} \cdot q \sqrt{\frac{qT_{e,i}}{2\pi \cdot m_{e,i}}}}_{I_{the,thi}} \left\{ \frac{2}{\sqrt{\pi}} \sqrt{\frac{(+,-)(V-V_p)}{T_{e,i}}} + \exp\left(\frac{(+,-)(V-V_p)}{T_{e,i}}\right) erfc\left(\sqrt{\frac{(+,-)(V-V_p)}{T_{e,i}}}\right) \right\} \quad (a)$$

$$I_{omle,omli} = I_{the,thi} \exp\left(\frac{(+,-)(V-V_p)}{T_{e,i}}\right) \quad (b)$$

$$I_{oml} = I_{omli} - I_{omle} \quad (c)$$

Eq. 2-2

In this equation there are two distinct regions of OML collection defined as I_{omle} and I_{omli}. When the potential of the collecting body with respect to the plasma potential, $V - V_p$, is negative, ions are collected according to Eq. 2-2a (I_{omli}) and electrons are collected

---

[6] Typical ionospheric conditions in the from 200 to 2000 km altitude range , have a T_e ranging from 0.1 eV to 0.35 eV, and n_e ranging from 10^{10} m^{-3} to 10^{12} m^{-3} .

according to the retardation regime equation of Eq. 2-2b (I_{omle}). The converse is true when $V - V_p$ is positive. The total OML current collection, I_{oml}, is then the difference of the two phenomena in each potential region, seen in Eq. 2-2c. A_p is the cylinder area and q is the electron charge magnitude.[7] $I_{the,thi}$ is the electron and ion thermal current, and represents the quantity of electrons or ions that randomly cross a given area per unit time.

For simplifications in simulation, approximations can be made to Eq. 2-2. When $V - V_p > 2T_e$, an approximation can be made to Eq. 2-2b resulting in Eq. 2-3a [67].

$$I_{omle,omli} = I_{the,thi} \frac{2}{\sqrt{\pi}} \sqrt{1 + \frac{^{(+,-)}V_p}{T_{e,i}}} \; for \; V_p > 0 \qquad (a)$$

Eq. 2-3

$$I_{rtd} = I_{the} \exp\left(\frac{V_p}{T_e}\right) for \; V_p < 0 \qquad (b)$$

Also, when $V - V_p$ is positive, the contribution of the retarding potential I_{omli}, in Eq. 2-2a, is negligible compared to I_{omle} in Eq. 2-3a, and as a result is dropped. The resulting two equation approximations shown in Eq. 2-3 are plotted and shown in Figure 2-1.
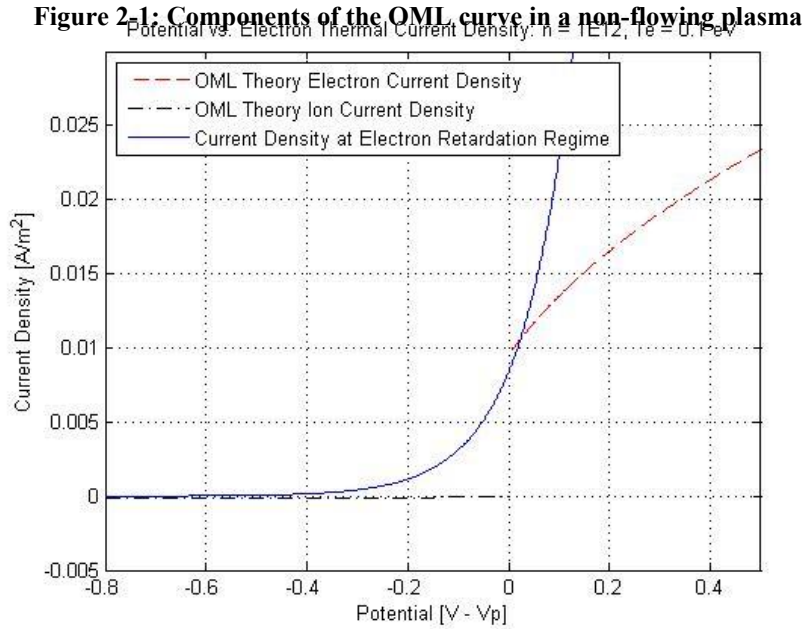
Figure 2-1: Components of the OML curve in a non-flowing plasma

Potential vs. Electron Thermal Current Density: n = 1E12, Te = 0.1eV

20

When $V - V_p$ is biased negative the ion collection is summed with the electron collection in the retardation regime. Using the assumptions in Eq. 2-3, when $V - V_p$ is positive, then the lesser of the I_{omle} or I_{rtd} is applied. The final result can be seen in Figure 2-2, along with the un-approximated Eq. 2-2. A slight discrepancy can be observed at $V - V_p$ values between 0 V and 0.2 V. This is the result of the condition where the assumption for the approximation in Eq. 2-3a did not hold. Since the majority of the EDT is normally far outside this region, the discrepancy is considered insignificant.
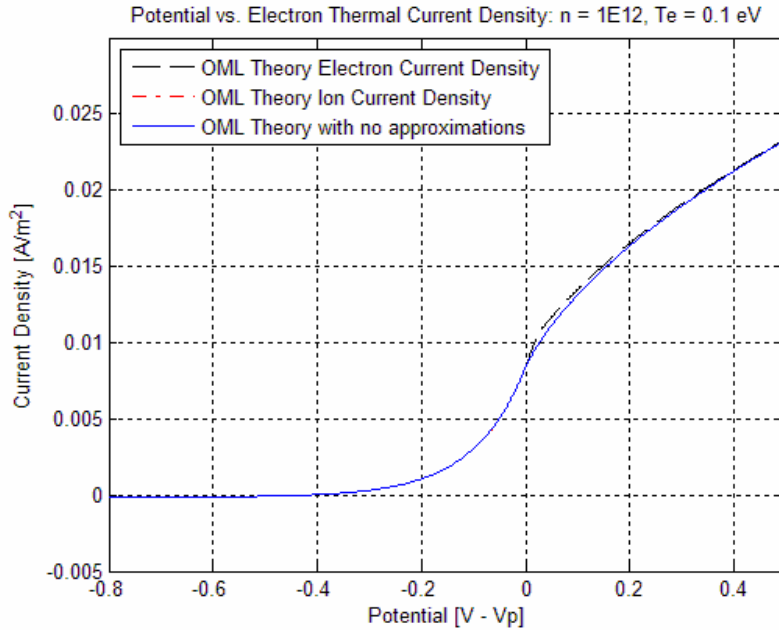
Figure 2-2: Raw OML theory and piecewise approximation

2.1.2 Deviations from OML Theory in a Non-Flowing Plasma

For a variety of practical reasons, current collection to a bare EDT does not always satisfy the assumption of OML collection theory. Understanding how the predicted performance deviates from theory is important for these conditions. Two commonly proposed geometries for an EDT involve the use of a cylindrical wire and a flat tape. As long as the cylindrical tether is less than one Debye length in radius, it will collect according to the OML theory in Eq. 2-3. However, once the width exceeds this distance, then the collection increasingly deviates from this theory. If the tether geometry

is a flat tape, then an approximation can be used to convert the normalized tape width to an equivalent cylinder radius. This was first done by Sanmartin and Estes [2] and more recently using the 2-Dimentional Kinetic Plasma Solver (KiPS 2-D) by Choiniere et al. [66]. These approximations are shown in Figure 2-3, which assumes a normalized potential[8] of $\phi_0 = 300$, and solves for an equivalent surface charge. This approximation is used in Chapter 6 to simulate flat tape geometry tethers.

As the width of the tether increases in a non-flowing plasma for a normalized potential, the amount of deviation from OML can be predicted. This simulation data was taken using KiPS 1-D & KiPS 2-D [66], as well as another approximation by Estes and Sanmartin [2], and can be seen in Figure 2-4. This deviation is then applied along the entire length of the tether. Since the Debye length is continuously changing along an orbit due to the changing electron density and tempeature, the collection efficiency is as well. The normalized potential of the tether during this measurement is 300. As the normalized potential increases, the collection efficiency with respect to OML is only altered by only a fraction of a percent[9] [66].
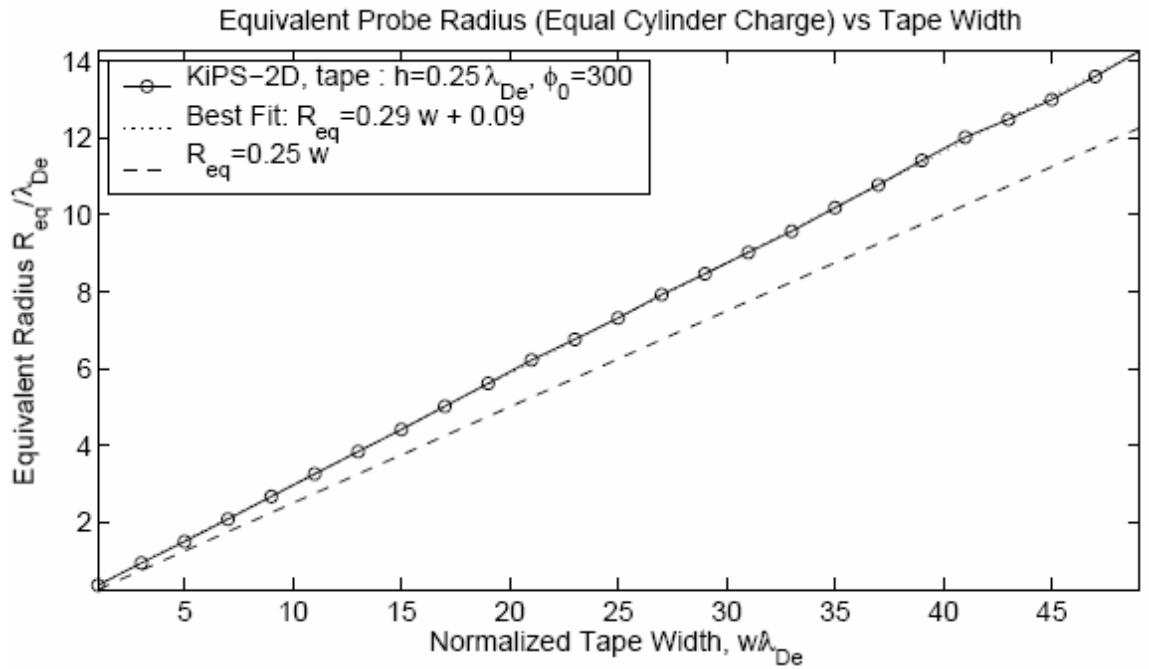
Figure 2-3: Equivalent circular probe radius as a function of width for a solid tape electron collector biased at $\phi_0 = 300$. The equivalent probe radius R_{eq} is computed based on equal surface charge.

---

[8] The normalized potential is the potential of the tether with respect to the plasma potential divided by the electron temperature: $\phi_0 = (V - V_p)/T_e$

[9] The normalized potential was tested up to $\phi_0 = 3000$.

Results are compared against the theoretical predictions made by Sanmartin and Estes [2] (R_{eq} = w/4).
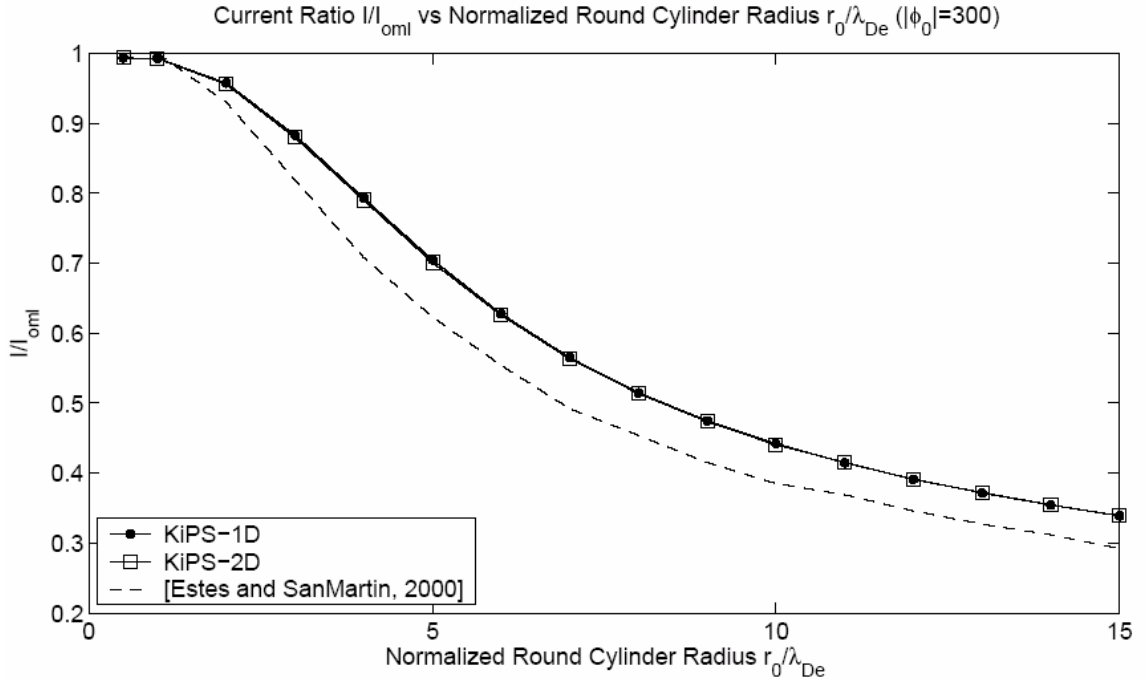
Figure 2-4: Current ratio I / I_{oml} as a function of the radius of a round conductive cylinder immersed in a stationary plasma. Results obtained using the KiPS-1D and KiPS-2D solvers are shown for a bias potential values of $|\phi_0|$ = 300. A comparison is shown with calculations published by *Sanmartın and Estes* [2] for $T_i = T_e$.

Another important current collection factor is how the collection varies depending on the proximity of parallel bare tethers. This particular case is important because tether geometries are being explored that involve having multiple strands next to one another (see Chapter 4) to dramatically improve tether life in an environment where micrometeoroids and debris can sever all or a portion of the tether. Figure 2-5 displays the current collection with respect to OML of two tethers as the separation distance is varied in a non-flowing plasma. These simulations were derived using KiPS 2-D [66]. The current ratio initially drops as the cylinder spacing is increased due to the increasing empty ion orbits, or ambient current collection being physically blocked by the adjacent. Eventually, as the cylinder spacing grows the wires have their own separate sheaths and the empty ion orbits begin to increase [66]. The point at which the separation distance again allows OML current collection efficiency on both tethers is beyond the center-to-center spacing recorded in the plot. The figure only goes up to 200 Debye lengths, and there is still only ~0.9 times the collection of OML theory. It is therefore implied that it

will likely be several hundred Debye lengths before the two tethers achieve the same collection efficiency of two completely isolated tethers.
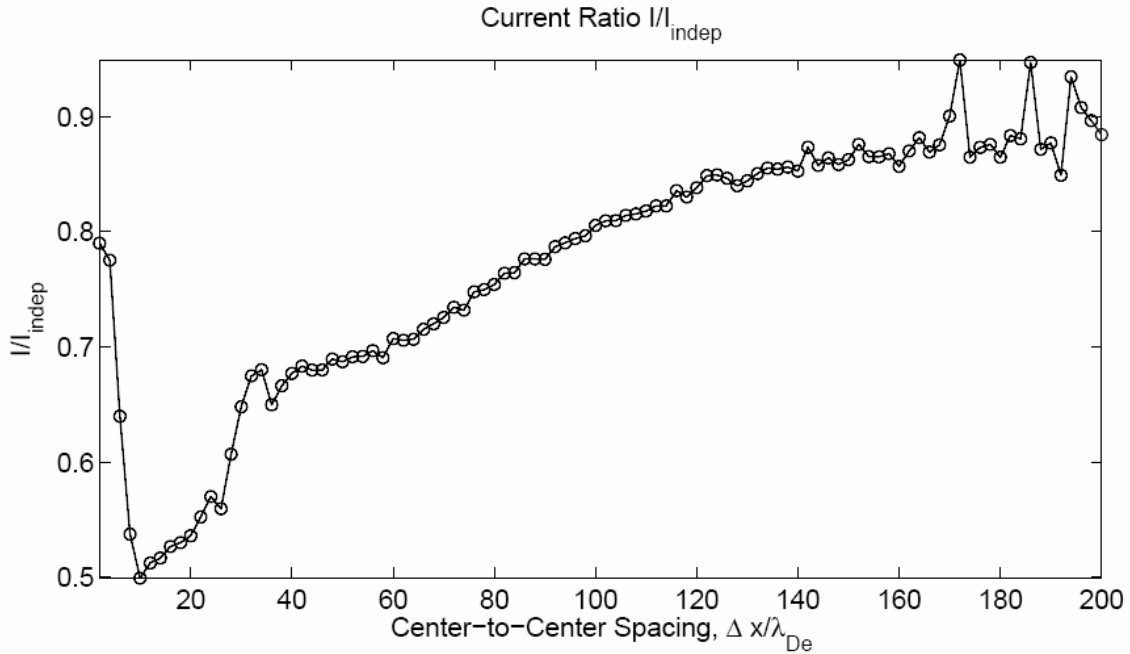
Figure 2-5: Current ratio as a function of center-to-center spacing for the two-cylinder configuration. The current ratio is defined as the ratio of the total collection current to the current that would be collected by two independent cylinders. The ϕ = -320.

2.1.3 Flowing Plasma Effect

The bare tether current collection theory presented thus far has been for an assumed non-flowing plasma. There is at present, no closed-form solution to account for the effects of plasma flow relative to the bare tether. Numerical simulation has been recently developed by Choiniere et al. using KiPS-2D which can simulate flowing cases for simple geometries at high bias potentials [68].   Two conducting tethers in a flowing plasma have been plotted as the distance between them grows, similar to Figure 2-5. This analysis has broken down the collection regimes into perpendicular and parallel oriented with respect to the flowing direction, which can be seen in Figure 2-6a. These regimes have been further broken down into collection from the ram side (facing the oncoming flow) and the wake side, and are shown in Figure 2-6b and c.

(a)

(b)

25
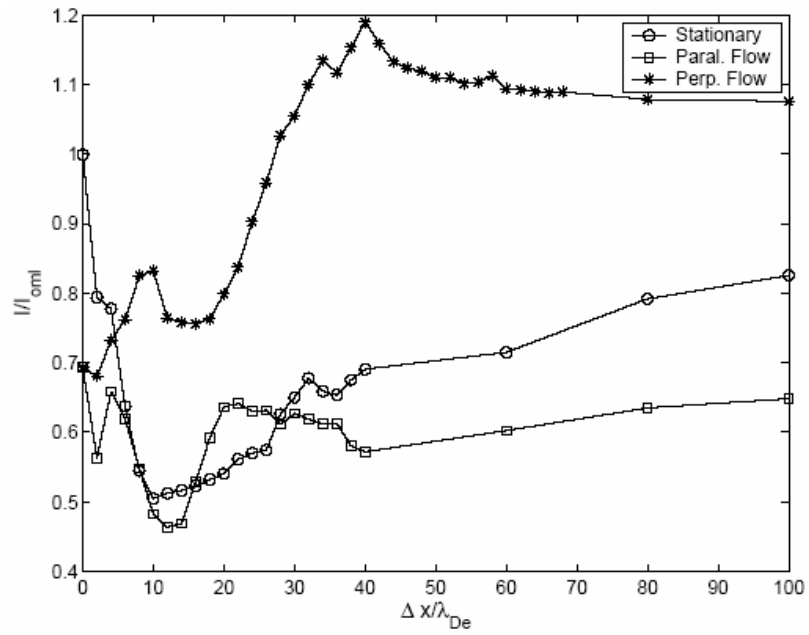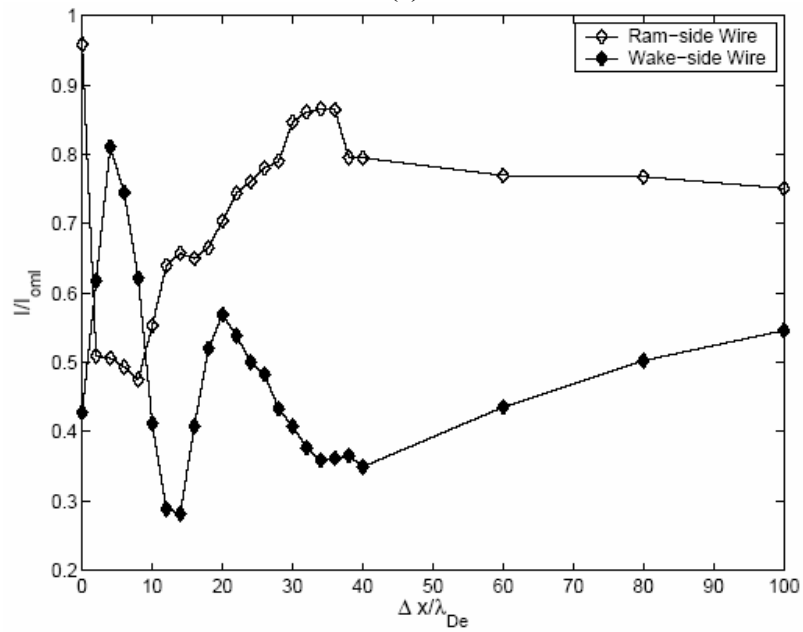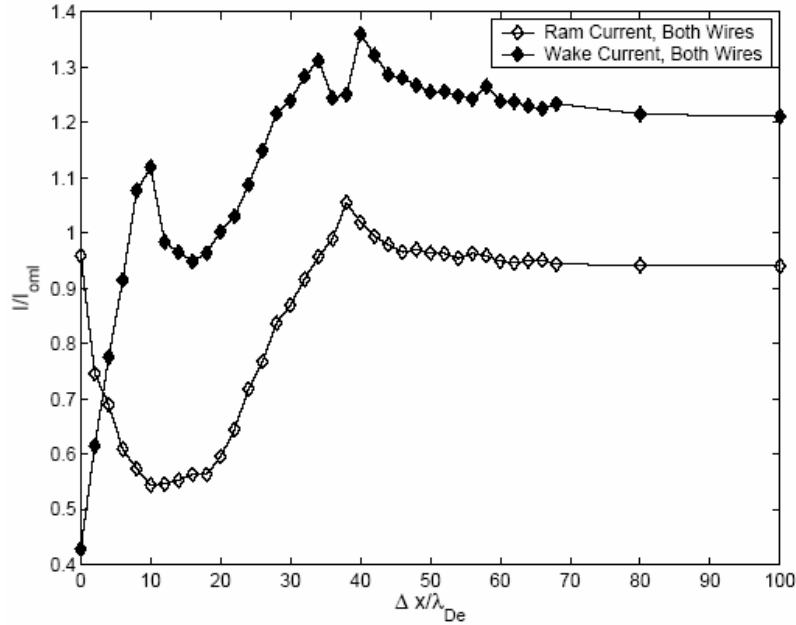
(c)

Figure 2-6: Collected ion current as a function of the center-to-center spacing of the wires. Ion current is normalized with respect to the orbital-motion-limit value, I_{oml}. (a) Total collected current in the stationary and flowing cases with results for both the parallel anf perpendicular orientations of the set of wires with respect to the plasma flow. (b) Current collected on the ram-side and wake-side wires, for the parallel orientation. (c) Total current collected on the ram and wake sides of both wires, for the perpendicular orientation.

It can be seen that perpendicular orientation collects more than OML theory for a stationary plasma at distances more than ~30 Debye lengths. Samples oriented parallel to the flow usually collect less than stationary plasma. The breakdown of the wake and ram affect shows that depending on the orientation the ram or wake side is the dominant collector. Further discussion of the simulated work as well as the experimental verification of the flowing plasma effects can be seen in Section 4.4. It has been experimentally shown in this section that flowing plasmas causes enhanced current collection compared to that of what OML theory predicts. This phenomenon is presently being investigated through recent work, and is not fully understood. As a result, for the purposes of simulation of tether current collection in this thesis, the non-flowing plasma theory will be applied.

26

2.2 Endbody Collection

This section discusses the plasma physics theory that explains passive current collection to a large conductive body which will be applied at the end of an ED tether. When the size of the sheath is much smaller than the radius of the collecting body then depending on the polarity of $(V - V_p)$, it is assumed that all of the incoming electrons or ions that enter the plasma sheath are collected by the conductive body [66] [65]. This 'thin sheath' theory involving non-flowing plasmas is discussed, and then the modifications to this theory for flowing plasma is presented. Other current collection mechanisms will then be discussed. All of the theory presented is used towards developing a current collection model to account for all conditions encountered during an EDT mission.

2.2.1 Passive Collection Theory

In a non-flowing quasi-neutral plasma with no magnetic field, it can be assumed that a spherical conducting object will collect equally in all directions. The electron and ion collection at the end-body is governed by the thermal collection process, which is given by I_{the} and I_{thi}. The spherical sheath calculation for a non-flowing plasma was conducted using a method developed by Parker, and given in Eq. 2-4[10] through Eq. 2-7 [69].

$$J_{thi,the} = 1.53 \cdot \frac{1}{4} \cdot n \cdot q \cdot \sqrt{\frac{8 \cdot q \cdot T_{i,e}}{\pi \cdot m_{i,e}}}$$

Eq. 2-4

$$t_u = \frac{2}{3}\sqrt{\left(\frac{2 \cdot q}{m_{i,e}}\right)^{1/2}\left(\frac{\varepsilon_o \cdot V_{sh}^{3/2}}{J_{thi,the}}\right)}$$

Eq. 2-5

$$H_u = 0 \; If \cdot \left(\left(\frac{t_u}{r_s} - 0.2\right) < 0\right), \; else \; H_u = 1$$

Eq. 2-6

---

[10] The J_{the} does not include the 1.53 factor labeled in Eq. 2-4.

$$r_{sh} = r_s \cdot \left(0.5 + \sqrt{0.25 + \frac{t_u}{r_s} + 0.052 \cdot \frac{t_u}{r_s} \cdot H_u} \right) - r_s \qquad \textbf{Eq. 2-7}$$

H_u and t_u are intermediate steps for calculating sheath size. There is also a factor termed the Bohm sheath criterion (value of ~1.53) which is multiplied to the calculation of the ion thermal current when the probe is sufficiently negative that only ions are collected [70] [71]. The Bohm sheath criterion is an approximation that states what velocity ions must have in order for a stable sheath to exist [65]. V_{sh} is the potential across the sheath in Volts, r_s is the radius of the conducting sphere, and $m_{i,e}$ is the ion or electron mass. The assumptions used for this model are:

1)   The model is applicable when the sheath is small with respect to the body dimensions

2)   The conductor (the emission end-mass) is a sphere

3)   Angular momentum is not accounted for

2.2.2   Flowing Plasma Electron Collection Model

The next step in developing a more realistic model for current collection is to include the magnetic field effects and plasma flow effects. Assuming a collisionless plasma, electrons and ions gyrate around magnetic field lines as they travel between the poles around the Earth due to magnetic mirroring forces and gradient-curvature drift [72]. They gyrate at a particular radius and frequency dependance upon their mass, the magnetic field strength, and energy. These factors must be considered in current collection models.

Electron current collection by a biased conducting sphere, in a non-flowing plasma, is illustrated by the Parker-Murphy Equation [30]. For a flowing plasma, different effects occur when $V - V_p$ is biased positive and negative. The ion collection in a flowing plasma will be explained in Section 2.2.3. The corrected version of the Parker-Murphy Equation for electron collection is based on mission data from the TSS-1R

mission [31]. These electron collection equations are used in the simulations of this thesis and shown in Eq. 2-8 and Eq. 2-9.

$$\phi_o = \frac{m_e \cdot \omega_{ce}^2 r_s^2}{8 \cdot q}$$ **Eq. 2-8**

$$I_e = \alpha \cdot I_o \cdot \left[1 + \left(\frac{V_p}{\phi_o} \right)^\beta \right]$$ **Eq. 2-9**

ϕ_o is an intermediate potential used for the Parker Murphy Equation. I_o is the product of the electron thermal current and the 2-d surface area projection of the front and back of the collecting sphere, $2 \cdot \pi \cdot r_s^2$. The electron gyro-frequency[11] is ω_{ce}, and α and β are the corrections based on experimental data from of Thompson et al. [31]. The assumptions for the Parker-Murphy collection theory are:

1)   The cyclotron radius is small with respect to the collector
2)   The electron current being collected does not deplete
3)   Object is a spherical conducting body
4)   Angular momentum of attracted particles are conserved
5)   Collisionless plasma
6)   No cross-field transport
7)   Absence of an electric field

Based on the TSS-1R results it is estimated that there is an overall enhancement to the original Parker Murphy collection by a factor of ~2.5, shown in Figure 2-7. When accounting for plasma flow effects for a positively biased conducting body, many interesting phenomena can be seen. For the TSS-1R mission when the satellite body exceeded the ram kinetic energy of the ambient plasma[12], a non-uniform distribution of 'suprathermal' electron appears on the surface [29]. In addition, there were magnetic perturbations detected which show indications of anisotropic current collections due to

---

[11] The electron and ion gyro-frequencies are defined as $\omega_{ce,ci} = \frac{q \cdot B}{m_{e,i}}$.

[12] Or when $\frac{1}{2} m v_{orb}^2 > T_e$

'local cross field transport [73]. It has been initially predicted using TSS-1R data [74] and then experimentally verified that one of the causes of the increased current collection over that of Parker-Murphy is due to the ExB drift into the collecting sheath [75]. Other possible reasons have been shown in Particle-In-Cell (PIC) simulations, which predict electron heating and acceleration due to instabilities generated by ion reflection from the sheath potential barrier [76]. Work still remains concerning the understanding of the comprehensive interactions involving all the reasons presented, as well as further experimental verification of them. Figure 2-8 describes many of the processes involved in this mesosonic electron collection in a flowing plasma [32].
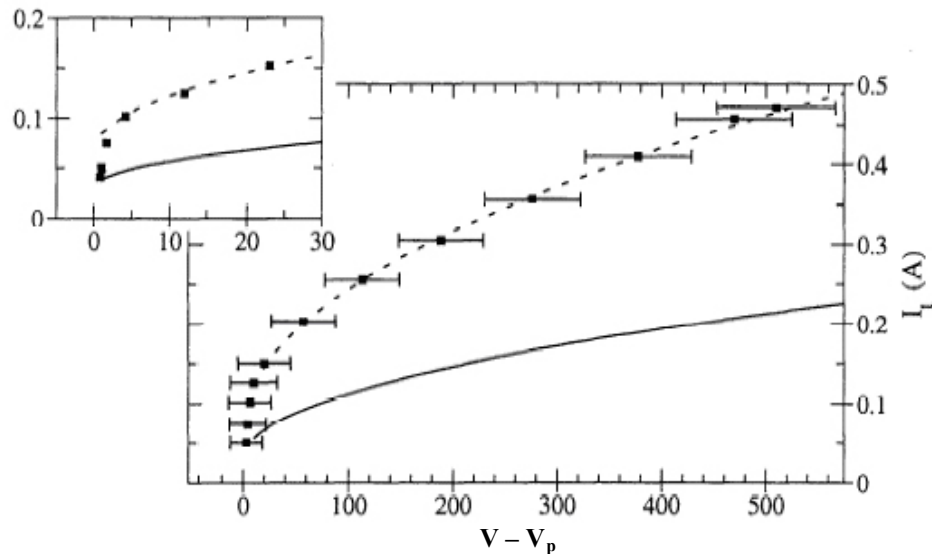
Figure 2-7: I-V response for a typical sweep on the TSS-1R mission. The data is plotted as squares with error bars representing uncertainties in the calculated satellite potential. Parker-Murphy model values are shown for this case (solid line), and multiplied by a factor of 2.17 (dotted line). The inset expands the low voltage region.
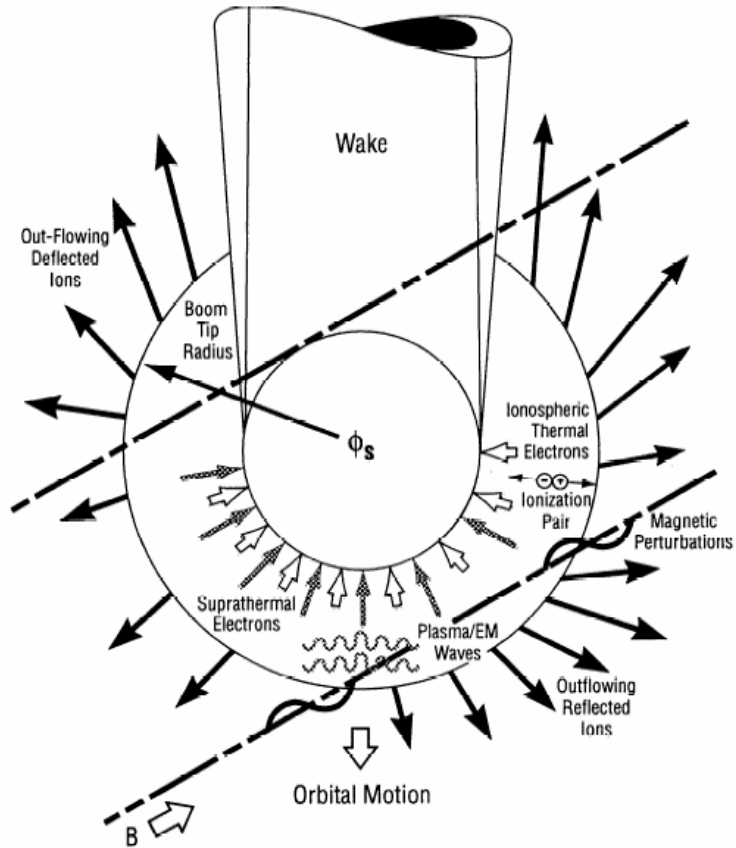
Figure 2-8: A composite schematic of the complex array of physical effects and characteristics observed in the near environment of the TSS satellite [3].

2.2.3 Flowing Plasma Ion Collection Model

When the conducting body is negatively biased with respect to the plasma and traveling above the ion thermal velocity, there are additional collection mechanisms at work. For typical Low Earth Orbits (LEOs), between 200 km and 2000 km [77], the velocities in an inertial reference frame range from 7.8 km/s to 6.9 km/s for a circular orbit and the atmospheric molecular weights range from 25.0 amu (O^+, O_2^+, & NO^+) to 1.2 amu (mostly H^+), respectively [78] [79] [80]. Assuming that the electron and ion temperatures range from ~0.1 eV to 0.35 eV, the resulting ion velocity ranges from 875 m/s to 4.0 km/s from 200 km to 2000 km altitude, respectively. The electrons are traveling at approximately 188 km/s throughout LEO. This means that the orbiting body is traveling faster than the ions and slower than the electrons, or at a mesosonic speed. This results in a unique phenomenon whereby the orbiting body 'rams' through the

surrounding ions in the plasma creating a beam like effect in the reference frame of the orbiting body.

Assuming cold ions, the ram current is the total number of ions that impact the ram surface, which can be seen in Eq. 2-10.

$$I_{ram} = SA2d \cdot n_i \cdot v_{orb} \cdot q$$

<div align="right">**Eq. 2-10**</div>

This is effectively thermal current collection across a virtual 2-D surface area that grows according to the sheath size. As the ion thermal motion approaches the orbital velocity it should be noted that it is more appropriate to consider the ion motion as a 'drifting maxwellian'. It is also important to note that this is a thin sheath regime, as explained earlier in this section, where all the current that enters the sheath is collected [81]. This implies that the ion thermal collection still occurs across the sheath along the side but not on the wake side. These effects can be seen in Figure 2-9. A cylinder is used to show the added thermal collection affects that are not due to the ram collection[13].
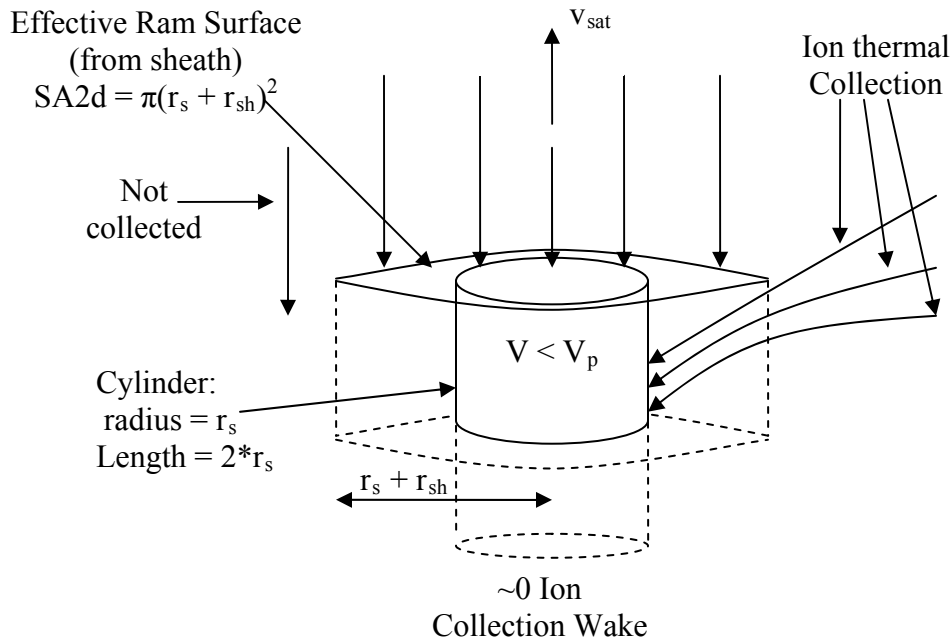
Figure 2-9: Schematic of the ion collection process

---

[13] As opposed to a sphere which would be all ram current collection.

2.2.4 Theoretical Collection Within Potential Transition Regions for a Conducting Sphere

Models have been developed for the current collection of potentials positive and negative with respect to the plasma potential in a flowing plasma for a sphere. There remains the question of how to transition between the two for simulation purposes. This is especially a problem because the defining equations are not continuous functions at $V - V_p = 0$ V, as seen in Figure 2-10. There is a jump from the ion collection, the solid line, to the electron collection, the dashed line. For simulation purposes a continuous transition is required. To resolve this issue three regions are defined here: Region A, passive ion collection equations; Region B, the transition region; and Region C, the TSS-1R corrected Parker Murphy electron collection model valid region.
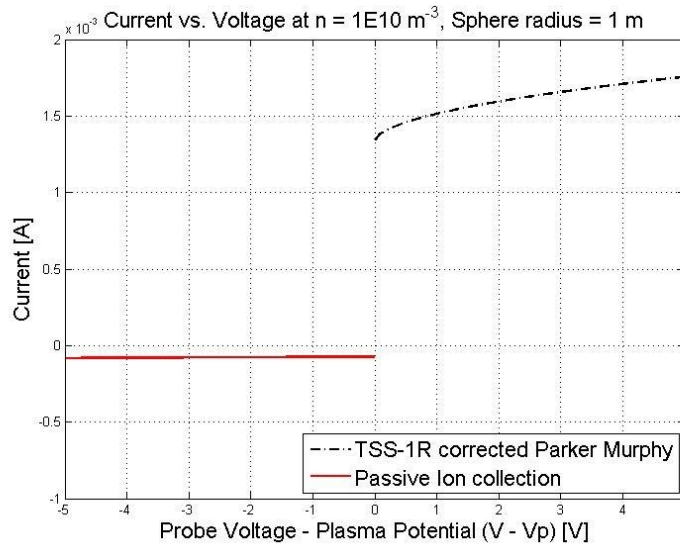
Figure 2-10: Transition region of the current collection models at and around the plasma potential

The experimental data seen in Figure 2-7 from the TSS-1R mission allows for an approximation to be made. When the spacecraft is at the plasma potential, $V - V_p$, the collected current is approximately the thermal electron current, I_o, as expected. This current rises linearly as the potential is increased. Then, when $q \cdot (V - V_p)$ equals approximately the threshold ion beam energy at the orbital altitude, $V_{anode} \approx V_{thresh}$, the electron collection current transitions to Eq. 2-9. For simulation purposes, this threshold

voltage was set at 0.8 times the ion beam energy because it is the approximate value according to the experimental data shown in Figure 2-7 [31]. This approximation can change if new information about this process becomes available. The characteristic was reported by Thompson et al. [31], although a particular function to model the behavior at less than this threshold ion beam voltage was not specified. From I_o, a straight line fit is assumed between $0 < V_{anode} < V_{thresh}$, as seen in Figure 2-11. This is shown by the dashed straight line.
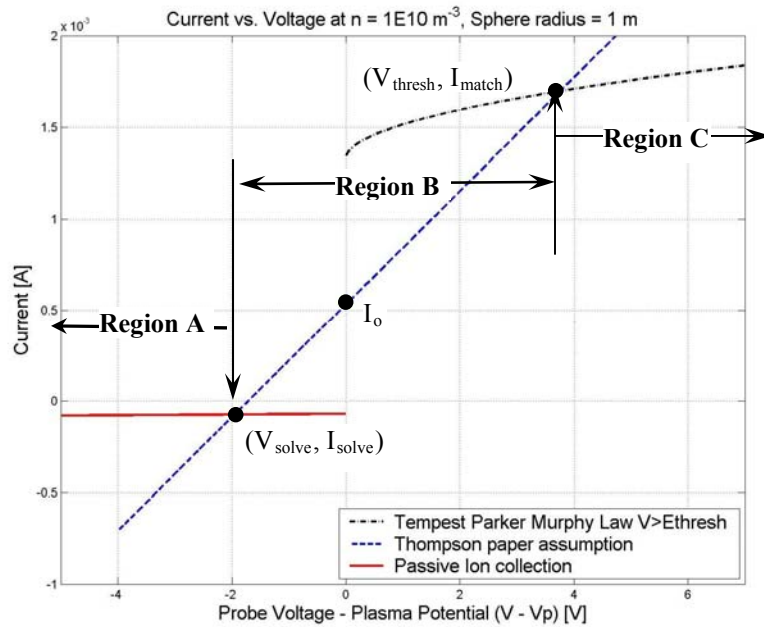
Figure 2-11: Plot of transition region between the TSS-1R corrected PM collection and the passive ion collection using the TSS-1R experimental results

The second point that must be determined is the transition between Regions A and B, as it is just an extension of the line created from (V_{thresh}, I_{match}) to $(0, I_o)$. The equations are known for the lines in these two regions. They also always have positive slopes. As a result a simple check can be done. Input the V_{anode} into $I_{collecta}$ and $I_{collectb}$ (defined in Table 2-1, and the greater of the two equations will yield the current solution. Finding V_{sokve} is not necessary, but it is worth labeling for definition purposes, and can be seen in Figure 2-11. Using Table 2-1, all the values for each of the points and regions previously described can be obtained.

I_{match} (Transition between Region B & C)	$I_o + \left[I_o \cdot \alpha \cdot \left(1 + \left(\dfrac{V_{thresh}}{\phi_0} \right)^{\beta} \right) - I_o \right]$	PM, TSS-1R Electron Collection [A]
$I_{collecta}$ ($V_{anode} < V_{solve}$)	$-\left(I_{photo} + I_{ram} \right)$	Total collected current [A]
$I_{collectb}$ ($V_{solve} < V_{anode} < V_{thresh}$)	$I_o + \left(\dfrac{V_{anode}}{V_{thresh}} \right) \left[I_o \cdot \alpha \cdot \left(1 + \left(\dfrac{V_{thresh}}{\phi_0} \right)^{\beta} \right) - I_o \right]$	Linear Approximation of current between 0 and E_{thresh} [A]
$I_{collectc}$ ($V_{anode} > V_{thresh}$)	$\alpha \cdot I_o \cdot \left[1 + \left(\dfrac{V_{anode}}{\phi_0} \right)^{\beta} \right]$	PM (TSS -1R corrected) electron Collection [A]
Vsolve	Input V_{anode} into $I_{collecta}$ & $I_{collectb}$	Transition between Region A & B
I_{solve}	$I_o + \left(\dfrac{V_{solve}}{V_{thresh}} \right) \left[I_o \cdot \alpha \cdot \left(1 + \left(\dfrac{V_{thresh}}{\phi_0} \right)^{\beta} \right) - I_o \right]$	Current at Esolve

Table 2-1: The particular equations to use when calculating the total current collection from a positively charged body

2.2.5 Porous Endbodies

Porous endbodies have been proposed as a way to reduce the drag of a collecting endbody while ideally maintaining a similar current collection. They are often modeled as solid endbodies, except they are a small percentage of the solid spheres surface area. This is, however, an extreme over simplification of the concept. Much has to be learned about the interactions between the sheath structure, the geometry of the mesh, the size of the endbody, and its relation to current collection. This technology also has the potential to resolve a number of issues concerning EDTs. Diminishing returns with collection current and drag area have set a limit that porous tethers might be able to overcome. Work has been accomplished on current collection using porous spheres, by Stone et. al. [82] [83] and Khazanov et al. [84].

It has been shown that the maximum current collected by a grid sphere compared to the mass and drag reduction can be estimated. The drag per unit of collected current for a grid sphere with a transparency of 80 to 90% is approximately 1.2 – 1.4 times

smaller than that of a solid sphere of the same radius. The reduction in mass per unit volume, for this same comparison, is 2.4 – 2.8 times [84].

2.2.6 Other Current Collection methods

In addition to the electron thermal collection, other processes that could influence the current collection in an EDT system are photoemission, secondary electron emission, and secondary ion emission. These effects pertain to all conducting surfaces on an EDT system, not just the end-body.

In photoemission, incoming photons cause bound electrons within a particular material to be ejected from their atomic orbits if they are of sufficient energy. The ejection energy is equal to the difference between the incident photon energy and the ionization energy of the particular atom [80]. A typical value for current emission density due to photoemission in a low Earth orbit (LEO) is 2.4×10^{-5} A/m^2 assuming a stainless steel collecting body [8]. This value is only valid for the surfaces of the collecting body that face the Sun. It varies according to orbital configuration and time of day. More photoemissive values for various materials can be seen in Table 2-2. Photoemission would only affect the net current on an EDT system when $V – V_p$ is negative. Emitted photoelectrons would be attracted back to the surface when $V – V_p$ is positive. For this negative bias scenario, the ram current would be the dominant means of passive ion collection, as defined in Section 2.2.3. The ram collection current for the typical plasma density of the TSS-1 mission at 300 km (4×10^{11} m^{-3}) [81], is 4.6×10^{-4} A/m^2. This indicates that in the worst case scenario, when there is relatively no ion collecting plasma sheath (-10 V < ($V – V_p$) < 0 V), that the electrons emitted through photoemission can be up to 10% of the total ion current collected. However, in a typical EDT system, the amount of conducting tether where the plasma sheath is small enough for photoemission to make its most significant impact is only a few meters. Similarly, the end-body on the EDT system anode end is rarely at a potential low enough for photoemission to reduce the total electron current collected by even a small percentage.

Material	Photoelectron Current (A/m^2)
Aluminum	4.8 x 10^{-5}
Gold	2.9 x 10^{-5}
Stainless Steel	2.4 x 10^{-5}
Vitreous Carbon	2.1 x 10^{-5}
Graphite	7.2 x 10^{-6}
Indium Oxide	3.2 x 10^{-5}

Table 2-2: Integrated photoelectric current under solar irradiation [8]

When incoming electrons or ions impact a surface they can be reflected or absorbed into the material. If this particle is absorbed, it may collide with atoms in the material and eventually reverse direction and backscatter out. The particles that do not backscatter lose their energy into the material. Some of this energy is used to excite electrons which can escape the material if they surpass the atoms work function. This process is called secondary electron emission.

Similar to photoemission, when electrons are accelerated across an electron collecting sheath $(V - V_p > 0)$, the energy at which secondary electrons are emitted at is less than their initial 0.1 eV. This results in all secondary electron emission being collected back into the EDT system. Also, when the $V - V_p$ is negative there are negligable electron impacts, and thus negligable secondary ionization due to electrons. The regime where the maximum secondary electron emission can occur is in the electron retardation regime, seen in Figure 2-1. For this small potential region (-0.4 V < x < 0 V) the secondary electron emission can yield up to 5% that of the incoming electron current [85].

Secondary electron emission due to ion impact has a negligable contribution when the $V - V_p$ is positive, because there are almost no impacts. For incident energies of negative a few hundered volts the electron emission yields can be up to 10%. In addition, the electron yields can reach unity at ion energies above 10 keV [8]. For EDT systems no exposed conductive material of the system should reach potentials greater than negative a few hundred volts, as will be seen in Chapter 5. In addition, the ion collection due to these low potentials is usually < 1% that of the average electron current in the tether. An additional 10%, or even 100% will not affect the EDT system performance significantly.

As a result, the voltages of a properly designed EDT system rarely approach values that could produce more than negligable secondary electron emission due to ion impact.

Secondary ion emission has shown to contribute < 0.1% for both oxidized copper and aluminum surfaces under 2 kV Ar^+ ion bombardment [86]. From this information and the following assumptions, a prediction can be made:

- The dominant species in the ionosphere has an atomic mass ranging from 16 amu at 300 km to ~1.3 amu above 2000 km

- Oxidized materials have greater ion emission percentages [87-89]

Smaller particles result in a reduced collision frequency. This implies the secondary ion emission in the ionosphere has a further reduction than was quoted.

There are also other less significant methods of passive current collection or emission. Methods such as: secondary ion emission due to electron impact; thermionic emission; field emission; impact ionization; and impact vaporization; are possible ways to collect current [8]. The low ion and electron energies that are encountered in the ionosphere result in a negligable effects from these methods.

2.3   Space Charge Limits Across Plasma Sheaths

In any application where electrons are emitted across a vacuum gap, there is a maximum allowable current for a given bias due to the self repulsion of the electron beam[14]. This classical 1-D space charge limit (SCL) is derived for charged particles of zero initial energy, and is termed the Child-Langmuir Law [90-92] and can be seen in Eq. 2-11a.

---

[14] The description in this section is for the SCL of an electron beam. The SCL description for an ion beam is identical, except the opposite charge particles are involved having a different mass.

$$I_{CL} = \frac{4\varepsilon_o}{9}\sqrt{\frac{2q}{m_{ei}}}\,\frac{V_{sh}^{3/2}}{D^2}^{\,3} A_e \qquad (a)$$

$$I_{CL}(1) = \frac{4\varepsilon_o}{9q}\sqrt{\frac{2}{m_e}}\,\frac{V_{emit}^{3/2}}{D^2}\left[1+\sqrt{1+\frac{V_{sh}}{V_{emit}}}\right]^3 A_e \qquad (b)$$

Eq. 2-11

For applications where the charged particled have an initial velocity, the 1-D Child-Langmuir law has been expanded, and shown in Eq. 2-11b [93]. The space charge limit depends on current density, gap width, D, gap potentials, V_{sh}, geometry, and the kinetic energy of a current beam, V_{emit}. Eq. 2-11b assumes that:

1)   The electrons are non-relativistic
2)   The motion is 1 dimensional
3)   The self magnetic field is negligible

Using the 1-d Child Langmuir equation, a derivation has been accomplished to describe the 2-d affects of the SCL [94, 95]. This can be seen in Eq. 2-12, where W is the width of the emitting surface and D is the gap distance, both in meters.

$$\frac{J_{CL}(2)}{J_{CL}(1)} \cong \frac{0.3145}{W\!/\!D} - \frac{0.0004}{\left(W\!/\!D\right)^2} \qquad \textbf{Eq. 2-12}$$

A 3-d SCL model was then derived by Lau which describes emission flow coming from an ellipse as seen in Eq. 2-13 [94].

$$\frac{J_{CL}(3)}{J_{CL}(1)} \cong 1 + \frac{D}{\pi W} + \left(\frac{1}{4}-\frac{1}{2\pi}\right)\cdot\frac{D}{R} \cong 1 + 0.32\frac{D}{W} + 0.091\frac{D}{R} \qquad \textbf{Eq. 2-13}$$

The assumptions for this are:

1)   The ellipse has semi-axes R and W / 2 and with the restriction R > W / 2
2)   The equation approached the 2-d derived condition when W and R approach zero

A second 3-d SCL model has been derived by Humphries for an expanding 'pencil-beam' (circular emitter), and seen in Eq. 2-14, using Eq. 2-11 to simplify it [96, 97].

$$\frac{J_{CL}(3)}{J_{CL}(1)} = \frac{\left[r_b^2 + (D/2)^2\right]}{r_b^2} = \left[1 + \left(\frac{D}{2r_b}\right)^2\right]$$

Eq. 2-14

A description of this emission can be seen in Figure 2-12. This model assumes that:

1)   There is beam spreading
2)   The gap size is greater than the radius of the emitter, $r_{sh} > r_b$
3)   It is a flat circular emitter
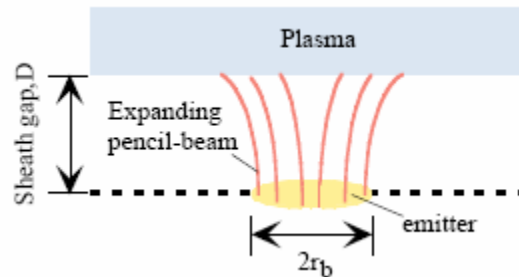
Figure 2-12: Description of a 3-d expanding pencil beam emitter [4]

Both the Humphries and Lau models are used in the simulations developed for this thesis when calculating the SCL capabilities for field emitter arrays and thermionic cathodes at small sheath distances. These 3-d equations produce equivalent results at sheath voltages near zero. As the sheath voltage increases, the allowable current gradually becomes greater in the Humphries model. This is because the Humphries method accounts for beam spreading, which becomes significant beyond a sheath size of a few cm. For the Lau method, the beam remains collimated, but the vacant expanse surrounding the beam, as opposed to the continuous charge of the one-dimensional approximation, improves the space charge limit. The Lau equation also assumes that the charge density varies only with emission direction, and not laterally [97]. As a result, Eq. 2-14 is predominantly used for the EDT simulations presented in this thesis. An

important note is that if more than one emitter is used for a simulation, the assumption is that the emitters are spaced far enough apart such that they do not affect the SCL of each other.

For the applications in an EDT system, the "gap" is an ion-rich[15] plasma sheath transitioning from the background plasma to the spacecraft surface. The presence of ions in the gap (sheath) improves space charge constraints because the ions act to neutralize electron charge. In addition to the transmission of the electron beam across an ion-rich sheath, its penetration into and accommodation by the plasma must be considered. The larger the density of the electron beam relative to the background plasma density, the stronger the space charge effects will be in the plasma. Thus SCLs will likely be most acute for ED tether applications where the emitted current density is high and background plasma densities are lower [98].

2.4   Electron Emitters

There are three active electron emission technologies usually considered for EDT applications: hollow cathode plasma contactors (HCPCs), thermionic cathodes (TCs), and field emitter arrays (FEAs). System level configurations will be presented for each device, as well as the relative costs, benefits, and validation.

2.4.1 Thermionic Cathode (TC)

Thermionic emission is the flow of electrons from a heated charged metal or metal oxide surface, caused by thermal vibrational energy overcoming the work function (electrostatic forces holding electrons to the surface). The thermionic emission current density, *J,* rises rapidly with increasing temperature, releasing a significant number of electrons into the vacuum near the surface. The quantitative relation is given in Eq. 2-15,

---

[15] The 'ion rich' term is used to describe that within the sheath the ions greatly outnumber the electrons. It should be noted that the ion density within the sheath is still much less than the ambient quasi-neutral plasma.

and is called the Richardson−Dushman, or Richardson equation (ϕ is approximately 4.54 eV and A_R ~120 A/cm^2 for tungsten) [99].

$$J_{the} = A_R T^2 e^{-\left(\phi/kT\right)}$$ **Eq. 2-15**

Once the electrons are thermionically emitted from the TC surface they require an acceleration potential to cross a gap, or in this case, the plasma sheath. Electrons can attain this necessary energy to escape the SCL of the plasma sheath if an accelerated grid, or electron gun, is used. Eq. 2-16 shows what potential is needed across the grid in order to emit a certain current entering the device [100, 101].

$$\Delta V_{tc} = \left[\frac{\eta \cdot I_t}{\rho}\right]^{2/3}$$ **Eq. 2-16**

Here, η is the electron gun assembly (EGA) efficiency (~0.97 in TSS-1), ρ is the perveance of the EGA (7.2 micropervs in TSS-1), ΔV_{tc} is the voltage across the accelerating grid of the EGA, and I_t is the emitted current [100]. The perveance defines the space charge limited current that can be emitted from a device. Figure 2-13 displays commercial examples of thermionic emitters and electron guns produced at Heatwave Labs Inc.

<div align="center">(a)   (b)</div>
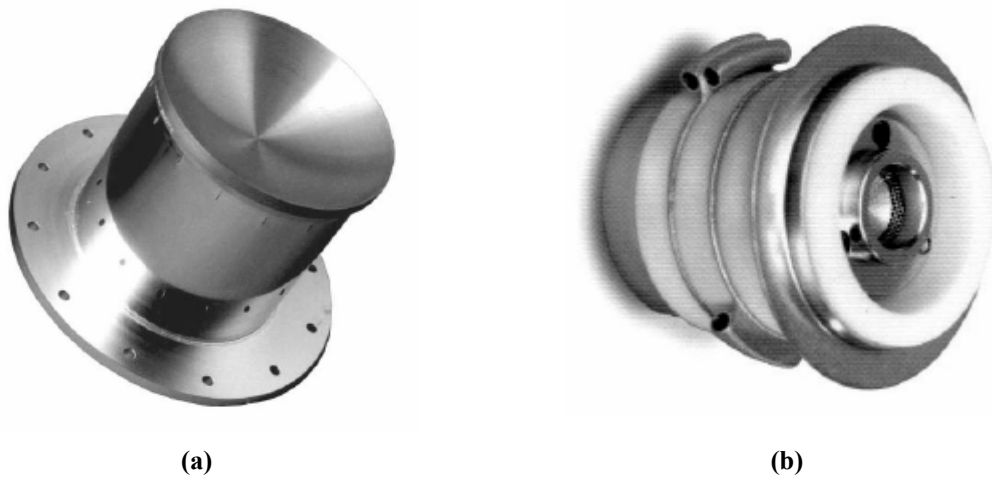
Figure 2-13: Example of an electron emitting a) Thermionic Emitter and an electron accelerating b) Electron Gun Assembly [5]

TC electron emission will occur in one of two different regimes: temperature or space charge limited current flow. For temperature limited flow every electron that obtains enough energy to escape from the cathode surface is emitted, assumimg the acceleration potential of the electron gun is large enough. In this case, the emission current is regulated by the thermionic emission process, given by Eq. 2-15. In SCL electron current flow there are so many electrons emitted from the cathode that not all of them are accelerated enough by the electron gun to escape the space charge. In this case, the electron gun acceleration potential limits the emission current. Figure 2-14 displays the temperature limiting currents and SCL effects. As the beam energy of the electrons is increased, the total escaping electrons can be seen to increase. The curves that become horizontal are temperature limited cases.
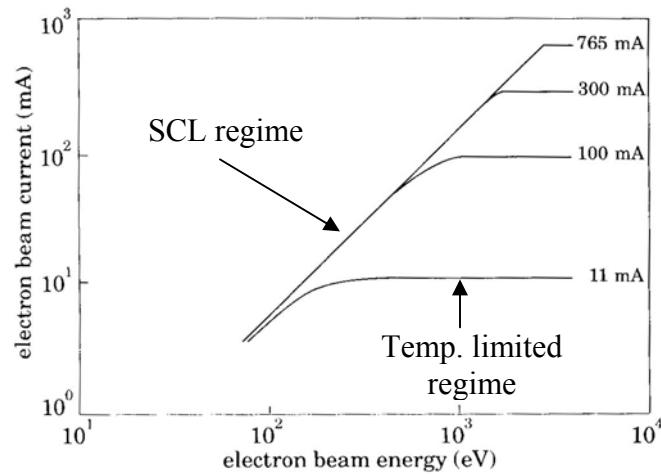
Figure 2-14: Typical Electron Generator Assembly (EGA) current voltage characteristics as measured in a vacuum chamber.

2.4.1.1 Validation

The thermionic cathode was chosen and verified from the TSS-1 experiment (experiment describd in Section 1.2.1) [100]. The emission on this device was controlled by the thermionic emission of the insert, following Eq. 2-15. There were known preset temperature limited currents, which could be verified using Figure 2-15a. Once the specifications used in the electron gun part of the thermionic cathode system were experimentally acquired, shown in Table 2-3, the SCL curve of Figure 2-15a could be

accurately verified, and seen in Figure 2-15b. For the purposes of the simulations conducted in the following chapters, this same electron gun was used, and the user determined the amount of current generated by the thermionic emission process, rather than the temperature.   There was no maximum potential found for the electron gun, although it was experimentally tested up to 4000 V.

Thermionic Cathode Electron Gun

Perveance	7.2×10^{-6} pervs
Area of Emission	3.33×10^{-4} m^2
Emitter Efficiency	0.97

Table 2-3: Specifications of the Electron Gun part of the Thermionic Emitter

(a)   (b)
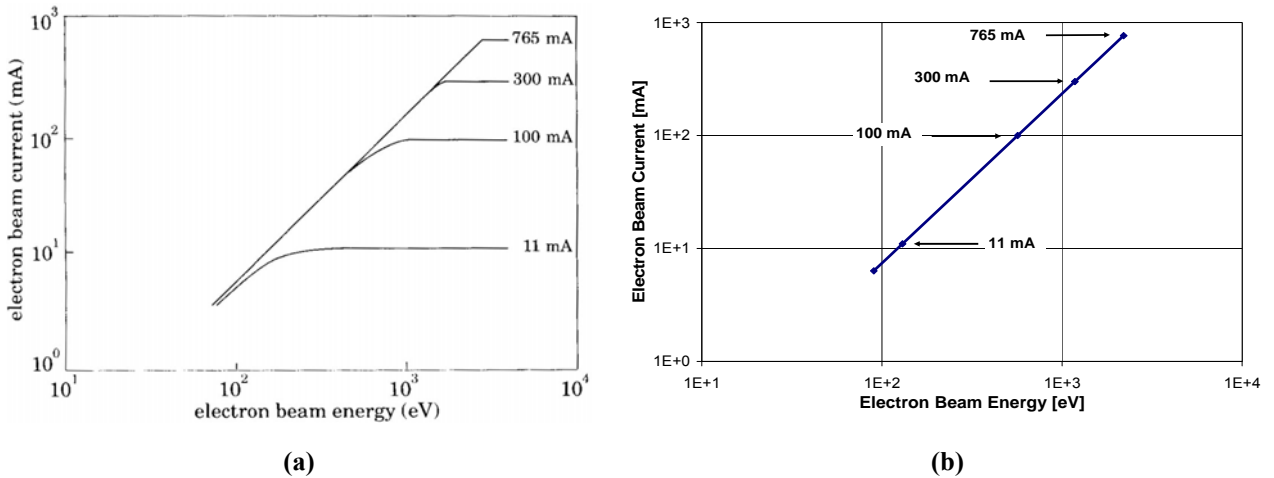
Figure 2-15 Error! Reference source not found.**: a) Figure 2-14 is shown again for visual comparison purposes against b) the theoretical plot using the electron gun values acquired from the TSS-1 experimental data**

2.4.2 Electron Field Emitter Arrays (FEAs)

In field emission, electrons tunnel through a potential barrier, rather than escaping over it as in thermionic emission or photoemission [102]. For a metal at low temperature, the process can be understood in terms of Figure 2-16. The metal can be considered a potential box, filled with electrons to the Fermi level (which lies below the vacuum level by several electron volts). The vacuum level represents the potential energy of an electron at rest outside the metal in the absence of an external field. In the presence of a strong electric field, the potential outside the metal will be deformed along the line *AB,* so that a triangular barrier is formed, through which electrons can tunnel. Electrons are extracted

from the conduction band with a current density given by the Fowler−Nordheim equation in Eq. 2-17.

$$J_{the} = A_{FN} \cdot E_{FN}{}^2 \cdot e^{-B_{FN}/E_{FN}}$$ **Eq. 2-17**
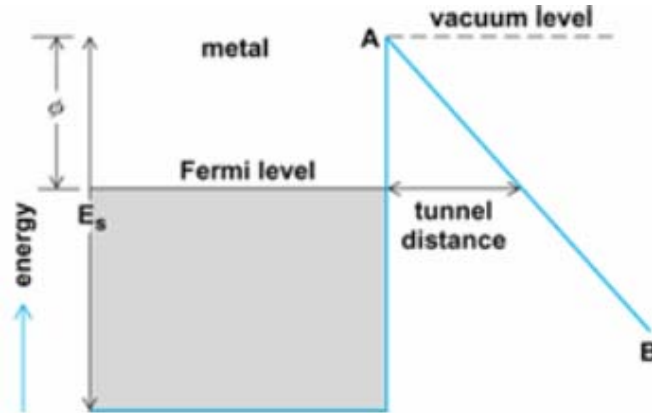
Figure 2-16: Energy level scheme for field emission from a metal at absolute zero temperature [102].

A_{FN} and B_{FN} are the constants determined by measurements of the FEA with units of A/V^2 and V/m, respectively. E_{FN} is the electric field that exists between the electron emissive tip and the positively biased structure drawing the electrons out. Typical constants for Spindt type cathodes include: $A_{FN} = 3.14$ x 10^{-8} A/V^2 and $B_{FN} = 771$ V/m. (Stanford Research Institute data sheet). An accelerating structure is typically placed in close proximity with the emitting material as in Figure 2-17 [97]. Close (micron scale) proximity between the emitter and gate, combined with natural or artificial focusing structures, efficiently provide the high field strengths required for emission with relatively low applied voltage and power. Figure 2-18 displays close up visual images of a Spindt emitter [103].
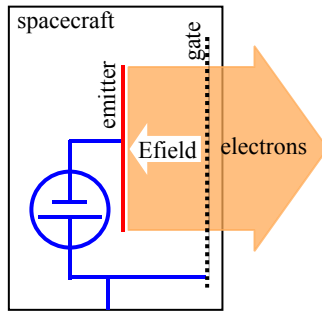
**Figure 2-17: Electrical diagram of
the basic field emission concept.**
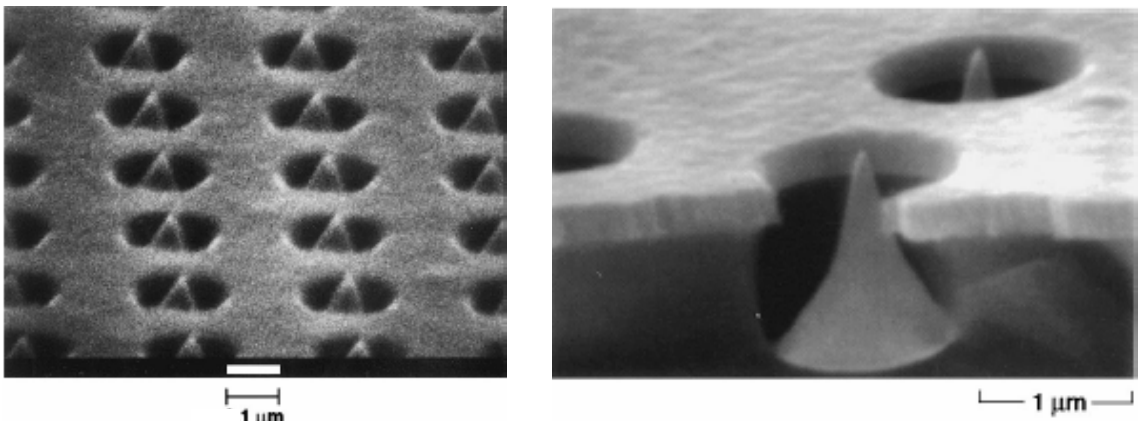
Figure 2-18: Magnified pictures of a field emitter array[16]

A variety of materials have been developed for field emitter arrays, ranging from silicon to semiconductor fabricated molybdenum tips with integrated gates to a plate of randomly distributed carbon nanotubes with a separate gate structure suspended above [97]. The advantages of field emission technologies over alternative electron emission methods are:

1)   No requirement for a consumable (gas) and no resulting safety considerations for handling a pressurized vessel

2)   A low-power capability

3)   Having moderate power impacts due to space-charge limits in the emission of the electrons in to the surrounding plasma.

---

[16] SEM photograph of an SRI Ring Cathode developed for the ARPA/NRL/NASA Vacuum Microelectronics Initiative by Capp Spindt

One major issue to consider for field emitters is the effect of contamination. In order to achieve electron emission at low voltages, field emitter array tips are built on a micron-level scale sizes. Their performance depends on the precise construction of these small structures. They are also dependent on being constructed with a material possessing a low work-function. These factors can render the device extremely sensitive to contamination, especially from hydrocarbons and other large, easily polymerized molecules [97]. Techniques for avoiding, eliminating, or operating in the presence of contaminations in ground testing and ionospheric (e.g. spacecraft outgassing) environments are critical. Research at the University of Michigan and elsewhere has focused on this outgassing issue. Protective enclosures, electron cleaning, robust coatings, and other design features are being developed as potential solutions [97]. FEAs used for space applications still require the demonstration of long term stability, repeatability, and reliability of operation at gate potentials appropriate to the space applications [98].

2.4.2.1   Validation

The field emitter array is a relatively new technology and the experimental results in appropriate settings for in-space applications are limited. Figure 2-19a details the experimental results from a Spindt emitter for a 0.0625 mm^2 surface area [104]. The Fowler-Nordheim constants A_{FN} and B_{FN} were derived using this data and then the plotted using Eq. 2-17 and shown in Figure 2-19b. Table 2-4 details the experimental and theoretical results of the Spindt emitter model developed by Jensen [105]. When comparing the theory and experimental figures it can be seen that at the higher gate-to-tip voltages the Spindt emitter emits slightly less than the Fowler-Nordheim prediction.

(a) **(b)**
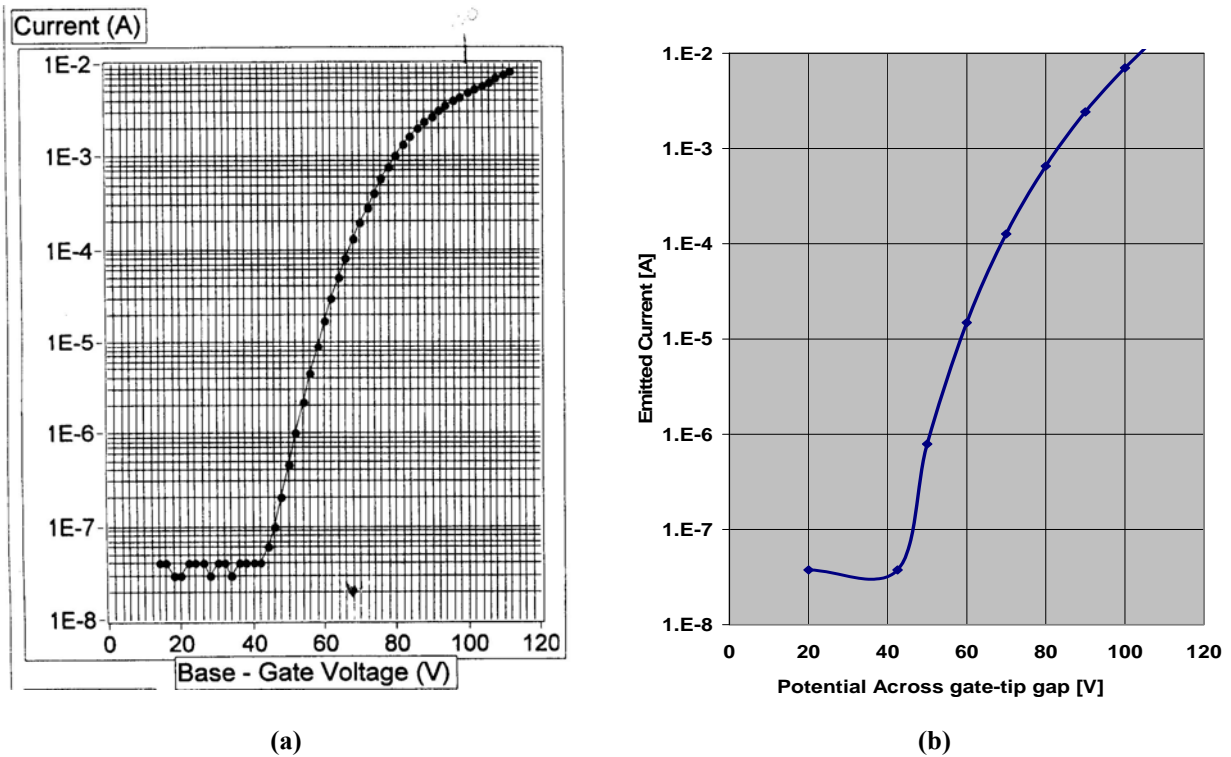
Figure 2-19: a) Stanford Research Institute measured profile of a 52M Spindt (Field) Emitter Array [104] and b) Theoretical plot using the Fowler-Nordheim constants acquired from the experimental data.

Based on the space charge limits of the gate to tip geometry and the assumption that field emitters emit uniformly across the entire structure, larger FEAs current can be predicted. Using the FEA model by Jensen [106], a 10 A FEA was predicted. These parameter specifications are shown in Table 2-4. It can be seen that the variables of this device are much greater than anything that has been produced thus far, and hopefully will be within reason for a mission many years in the future. Although the emitter devised by Jensen has not been built and tested yet it was necessary to use it for the simulations since it is theoretically capable of emitting currents that may be encountered in a variety of EDT missions.

	# of Tips	Surface Area [cm^2]	Max Potential [V]	A_{FN} [A/V^2]	B_{FN} [V]
Spindt Emitter	5×10^4	1	112	1.57×10^{-3}	771
10 A Jensen Theory	2×10^7	650	59	3.73×10^4	962.5

Table 2-4: Experimental and Theoretical Field Emitter Specifications for the Spindt emitter [104] and a predicted 10 A FEA [106]

The FEA technology exhibits the greatest outlook for the propellantless propulsion capabilities of the EDT concept. The power requirements for this device are

very low, theoretically requiring only ~60 V to emit up to 10 A of electron current, as seen in Figure 2-20. FEAs have been fabricated and experimentally tested in a laboratory setting and shown to work at areas from 10 μm to 12.5 cm in diameter with packing densities up to 10 tips/cm^2 [103].

10A Max ED Tether Predicted Optimum
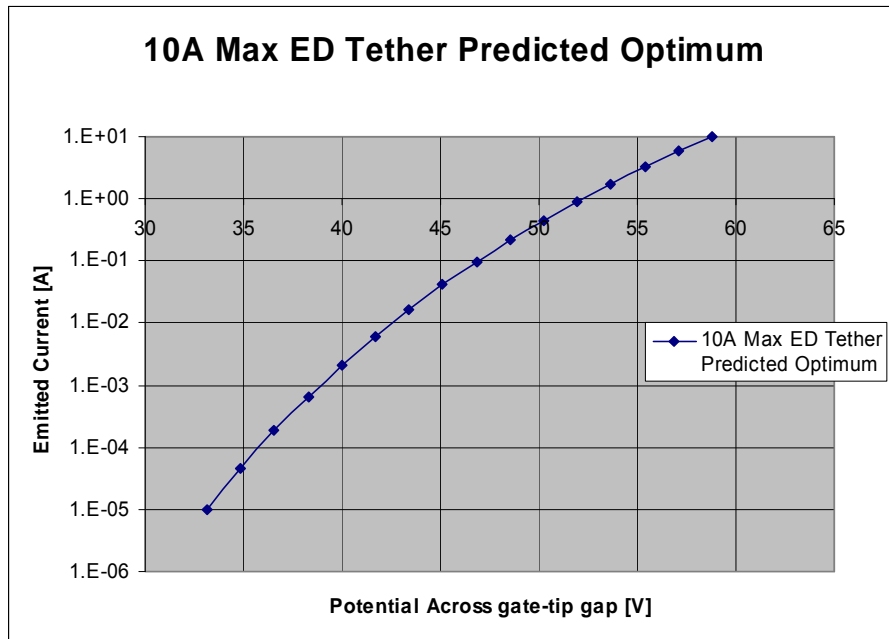
Figure 2-20: 10 A FEA predicted by Jensen [106]

2.4.3 Hollow Cathodes

Hollow cathodes emits a dense cloud of plasma by first ionizing a gas. This creates a high density plasma plume which makes contact with the surrounding plasma. The region between the high density plume and the surrounding plasma is termed a double sheath or double layer. This double layer is essentially two adjacent layers of charge. The first layer is a positive layer at the edge of the high potential plasma (the contactor plasma cloud). The second layer is a negative layer at the edge of the low potential plasma (the ambient plasma). Further investigation of the double layer phenomenon has been conducted by several people [107-110]. One type of hollow cathode consists of a metal tube lined with a sintered barium oxide impregnated tungsten insert, capped at one end by a plate with a small orifice, as shown in Figure 2-21 [111]. Electrons are emitted from the barium oxide impregnated insert by thermionic emission.

A noble gas flows into the insert region of the HC and is partially ionized by the emitted electrons that are accelerated by an electric field near the orifice[17]. Many of the ionized xenon atoms are accelerated into the walls where their energy maintains the thermionic emission temperature. The ionized xenon also exits out of the orifice. Electrons are accelerated from the insert region, through the orifice to the keeper, which is always at a more positive bias.
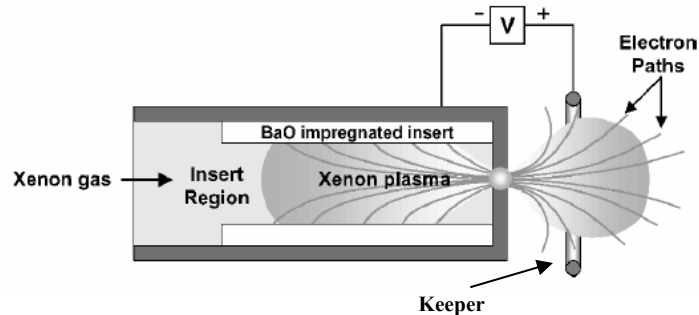
Figure 2-21: Schematic of a Hollow Cathode System [111]

In electron emission mode, the ambient plasma is positively biased with respect to the keeper. In the contactor plasma, the electron density is approximately equal to the ion density. The higher energy electrons stream through the slowly expanding ion cloud, while the lower energy electrons are trapped within the cloud by the keeper potential [112]. The high electron velocities lead to electron currents much greater than xenon ion currents. Below the electron emission saturation limit the contactor acts as a bipolar emissive probe. Each outgoing ion generated by an electron allows a number of electrons to be emitted. This number is approximately equal to the square root of the ratio of the ion mass to the electron mass.

It can be seen in Figure 2-22 what a typical I-V curve looks like for a hollow cathode in electron emission mode. Given a certain keeper geometry (the ring in Figure 2-21 that the electrons exit through), ion flow rate, and V_p, the I-V profile can be determined [111-113].

---

[17] Xenon is a common gas used for HCs as it has a low specific ionization energy (ionization potential per unit mass). For EDT purposes, a lower mass would be more beneficial because the total system mass would be less. This gas is just used for charge exchange and not propulsion.
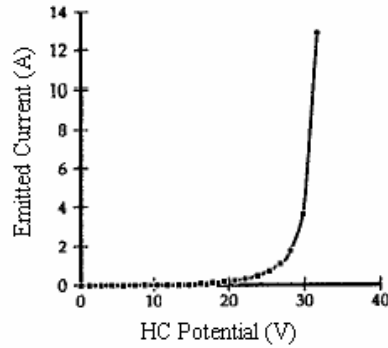
**Figure 2-22: Typical I-V Characteristic
curve for a Hollow Cathode [113]**

The operation of the HC in the electron collection mode is called the plasma contacting (or ignited) operating mode. The "ignited mode" is so termed because it indicates that multi-ampere current levels can be achieved by using the voltage drop at the plasma contactor. This accelerates space plasma electrons which ionize neutral expellant flow from the contactor. If electron collection currents are high and/or ambient electron densities are low, the sheath at which electron current collection is sustained simply expands or shrinks until the required current is collected.

In addition, the geometry affects the emission of the plasma from the HC as seen in Figure 2-23. Here it can be seen that, depending on the diameter and thickness of the keeper and the distance of it with respect to the orifice, the total emission percentage can be affected [114].
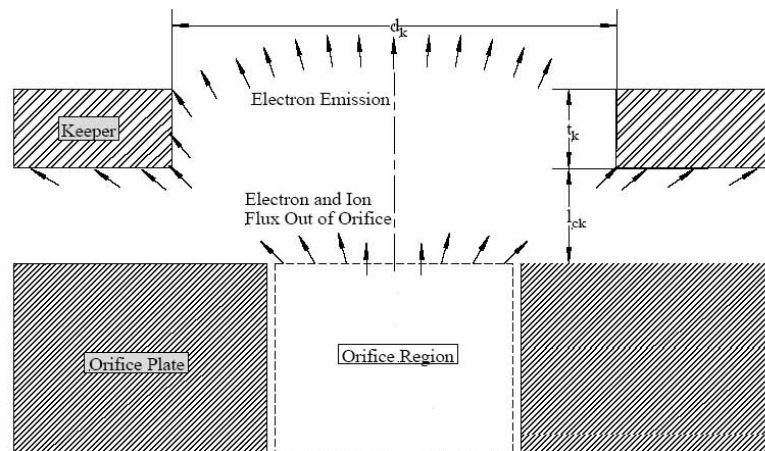
Figure 2-23: Schematic detailing the HC emission geometry [114]

51

All of these concepts must be quantified in order to apply them towards a useful simulation. For a non-ideal HC the equation that describes the current emission is seen in Eq. 2-18.

$$I_{emitter} = \left(I_{epc} - I_i\right) \cdot E_{num}$$

Eq. 2-18

Here, he total current of the emitter, $I_{emitter}$ is calculated by knowing the emitted electron current of plasma contactor, I_{epc}, the emitted ion current, I_i, and the number of HCs, E_{num}. The ion current emitted by the orifice of the HC is detailed in Eq. 2-19.

$$I_i = \left[n_{or} \cdot q \cdot \sqrt{\frac{q \cdot T_{epc}}{2\pi \cdot m_i}} \right] \cdot \pi \cdot r_{or}^2$$

Eq. 2-19

Here, the temperature of the plasma contactor, the plasma density at the HC orifice and the radius of the HC orifice are defines as T_{epc}, n_{or}, and r_{or}, respectively. The electron current of the electron plasma contactor (I_{epc}) is determined by Eq. 2-20.

$$I_{epc} = I_i \cdot f \cdot \sqrt{\frac{m_i}{2\pi \cdot m_e}} \cdot \exp\left[\frac{-\left(V_{emitter} + V_{element}(N)\right)}{T_{epc}} \right]$$

Eq. 2-20

In this equation, if the potential from the orifice to the keeper ($V_{emitter}$) plus the potential at the end of the tether (with respect to the plasma potential, $V_{element}(N)$) is greater than zero then it follows, Eq. 2-20, otherwise it follows the same equation without the exponential term [115]. The geometry effects the emission of the plasma from the HC as seen in Figure 2-23. Here it can be seen that depending on the diameter and thickness of the keeper and the distance of it with respect to the orifice, the total emission percentage can be affected as dictated by 'f', in Eq. 2-21 [114].

$$f = \sin^2\left(\frac{\pi}{2} - \theta_t\right) \quad \text{where} \quad \theta_t = \arctan\left(\frac{l_{ck} + t_k}{d_k/2}\right)$$

Eq. 2-21

Additional, research has been conducted which details the limits of high current emission hollow cathodes and the limiting factors associated with them and can be seen in the Appendix A.

2.4.3.1   Validation

For the purposes of simulation, code was obtained from Science Applications International Corporation called Environment Workbench. This code is an integrated analysis tool for the study of the environment surrounding spacecraft and interaction of spacecraft within their environment. Within the Environment Workbench is the code for simulating an HC. This HC model is based off of the results from the experiments done by P. J. Wilbur and colleagues at Colorado State University and M. J. Patterson and colleagues at NASA/LeRC. Eq. 2-18 through Eq. 2-21 are obtained from this code [115].

The hollow cathode experimentation data was obtained from work accomplished by John Williams and Paul Wilbur at Colorado State University in 1989 [116, 117]. In this work by Williams et al., a particular HC was tested to determine its performance. The experimental values of the HC determined in the research by Williams et al. can be seen in Table 2-5. All the values are obtained directly from Williams et al. [116, 117], except for the approximations of the B-field and the electron temperature. According to Williams, the estimation of the B-Field for the experiment ranged from 0 to 1.6×10^{-5} T. A value in that range was estimated in order to make the plot fit accurately. This magnetic field value affects the ignition voltage point (where the curve begins collecting electrons). The electron temperature of the HC used in this experiment was determined to yield a value of ~1.5 to 3 eV [118].

Electron Temp Emitted from Orifice	3 eV
Supply Fuel Flow	Xenon: 4.1 sccm
Potential from Orifice to Keeper	18 V
Potential from Keeper to Plasma	See Figure 2-24
Keeper Current and Power	0.3 A, 5.4 W
Electron Emission Current	See Figure 2-24
Orifice Emitted Ion Current	0.021 A
Double layer potential drop	4 V
Geometry – see Figure 2-24	$d_k = 5$ mm, $t_k = 0.25$ mm, $l_{ck} = 2$ mm
Ambient Electron Temperature and Density	6 eV, 8×10^{13} m^{-3}
Magnetic Field	2×10^{-9} T

Table 2-5: Parameters determined from the Williams et al. experiment [116, 117] and inserted into the SAIC HC model [115]. The starred indicate values from a personal correspondence.

The values in Table 2-5 were then inserted into and compared against the theoretical SAIC model [115]. These comparison plots can be seen in Figure 2-24. With these values it can be seen that the experimental and theoretical plots are +- 5% off of one another.

(a)   (b)
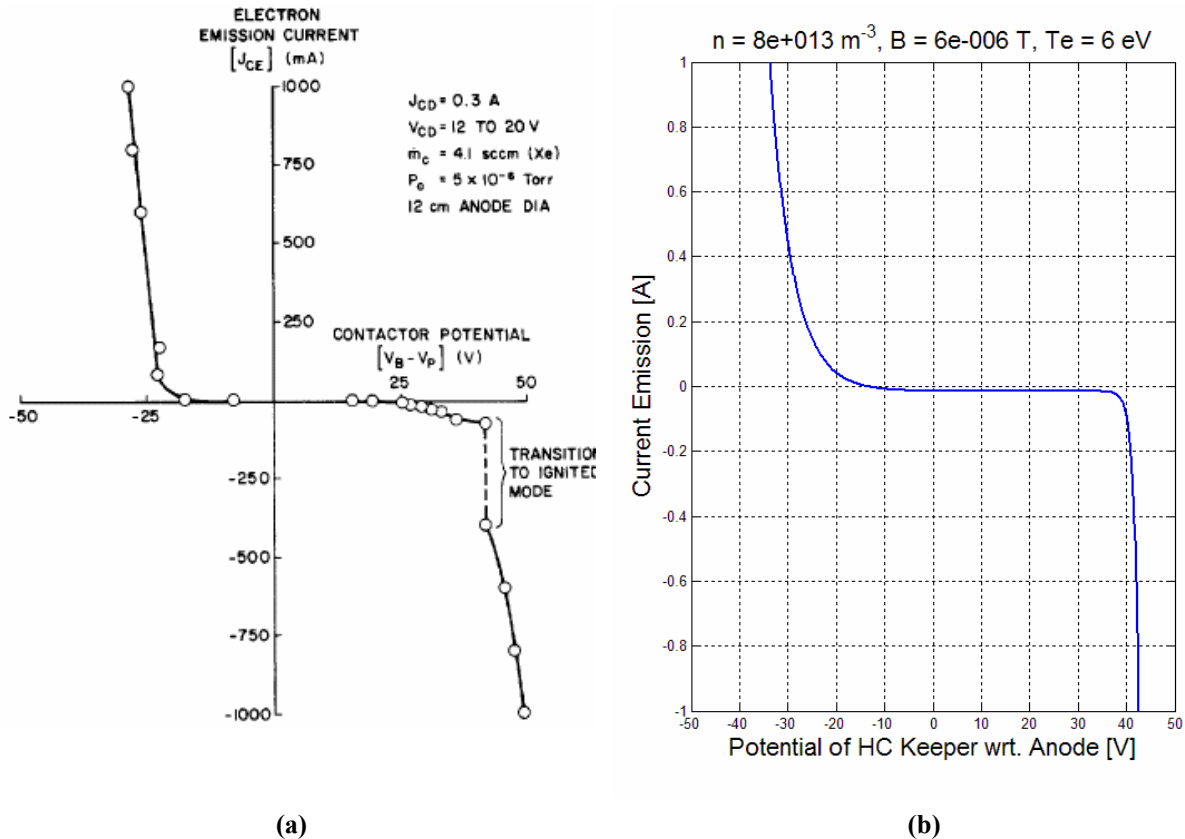
Figure 2-24: Experimental plot of an a) HC where the contactor potential is the keeper with respect to the surrounding plasma, and b) the SAIC Model of a HC under the same conditions

Once the theoretical HC model was verified a particular hollow cathode was chosen where very accurate measurements were performed inside and outside along the central axis [119]. In addition, this HC was relatively low power (53 W) and capable of relatively high emission currents (25 A) [119]. This particular HC may not presently be the best choice for plasma contactor purposes as there have been many newer HCs developed. It was primarily chosen for use in the simulations of this thesis because of the very precise measurements taken on it by Goebel et al. and his unique method. The values of this HC can be seen in Table 2-6. This particular HC information was used in the EDT simulations of this thesis.

Electron Temp Emitted from Orifice	3.9 eV
Supply Fuel Flow	Xenon: 5.5 sccm
Potential from Orifice to Keeper	26.5 V
Potential from Keeper to Plasma	See Figure 2-24
Keeper Current and Power	0.3 A, 5.4 W
Electron Emission Current	See
Orifice Emitted Ion Current	0.13 A
Double layer potential drop	4 V
Geometry – see Figure 2-24	$d_k = 4.7$ mm, $t_k = 0.24$ mm, $l_{ck} = 0.24$ mm

Table 2-6: HC parameters determined by Goebel et al. [119] and used in the simulations here.

Plasma Collection and Emission Summary

All of the electron emission and collection techniques can be summarized in Table 2-7. For each method listed there is a description as to whether the electrons or ions in the system increased or decreased based on the potential of the spacecraft with respect to the plasma. e-$\uparrow\downarrow$ and ions$^+$ $\uparrow\downarrow$ indicates that electrons or ions are being increased or reduced, respectively. Also, for each method some special conditions apply. See the respective section within this chapter for further clarification of when and where it applies.

Passive e- & ion Emission / Collection	$V - V_p < 0$	$V - V_p > 0$
Bare Tether: OML	Eq. 2-2, ions$^+$ $\uparrow$	Eq. 2-2, e- $\uparrow$
Ram Collection	Eq. 2-10, ions$^+$ $\uparrow$	0
Thermal Collection	Eq. 2-4, ions$^+$ $\uparrow$	Eq. 2-4, e- $\uparrow$
Photoemission	Table 2-2, e- $\downarrow$	e- $\downarrow$, ~0
Secondary Electron Emission	e- $\downarrow$	e- $\downarrow$
Secondary Ion Emission	ions$^+$ $\downarrow$, ~0	0
Retardation Regime	Eq. 2-2, e- $\uparrow$	Eq. 2-2, ions$^+$ $\uparrow$, ~0
Active e- & ion Emission	**Potential does not matter**	
Thermionic Emission	Eq. 2-15, Eq. 2-16, e- $\downarrow$	
Field Emitter Arrays	Eq. 2-17, e- $\downarrow$	
Hollow Cathodes	e- $\downarrow$ Eq. 2-18 - Eq. 2-21	e- $\uparrow$ Eq. 2-18 - Eq. 2-21

Table 2-7: Summary of the passive and active electron and ion collection and emission techniques.

For use in EDT system modeling, each of the passive electron collection and emission theory models has been verified by reproducing previously published equations and results. These plots include: orbital motion limited theory [66], Ram collection, and thermal collection [81], photoemission [8], secondary electron emission [85], and secondary ion emission [86, 87].

CHAPTER 3

ELECTRODYNAMIC TETHER FUNDAMENTALS

In order to integrate all the most recent electron emitters, collectors, and theory into a single model, the EDT system must first be defined and derived. Once this is accomplished it will be possible to apply this theory toward determining optimizations of system attributes.

There are a number of derivations that solve for the potentials and currents involved in an EDT system numerically [48, 57, 120, 121]. The derivation and numerical methodology of a full EDT system that includes a bare tether section, insulating conducting tether, electron (and ion) endbody emitters, and passive electron collection is described. This is followed by the simplified, all insulated tether model. Special EDT phenomena and verification of the EDT system model using experimental mission data will then be discussed.

3.1 Bare Tether System Derivation

An important note concerning an EDT derivation pertains to the celestial body which the tether system orbits. For practicality, Earth will be used as the body that is orbited; however, this theory applies to any celestial body with an ionosphere and a magnetic field.

The coordinates are the first thing that must be identified. For the purposes of this derivation, the x- and y-axis are defined as the east-west, and north-south directions with

respect to the Earth's surface, respectively. The z-axis is defined as up-down from the Earth's center, as seen in Figure 3-1. The parameters - magnetic field 'B', tether length 'L', and the orbital velocity 'v_{orb}' - are now defined in terms of this coordinate system, and can be seen in Eq. 3-1, Eq. 3-2, and Eq. 3-3.

$$\overline{B} = B_x\,\hat{x} + B_y\,\hat{y} + B_z\,\hat{z}$$ **Eq. 3-1**

$$\overline{L} = L\cos\alpha_{out}\,\sin\alpha_{in}\,\hat{x} + L\sin\alpha_{out}\,\hat{y} + L\cos\alpha_{out}\,\cos\alpha_{in}\,\hat{z}$$ **Eq. 3-2**

$$\overline{v}_{orb} = v_{orb}\cos\lambda_{out}\,\sin\lambda_{in}\,\hat{x} + v_{orb}\sin\lambda_{out}\,\hat{y} + v_{orb}\cos\lambda_{out}\,\cos\lambda_{in}\,\hat{z}$$ **Eq. 3-3**

The components of the magnetic field can be obtained directly from the International Geomagnetic Reference Field (IGRF) model. This model is compiled from a collaborative effort between magnetic field modelers and the institutes involved in collecting and disseminating magnetic field data from satellites and from observatories and surveys around the world. For this derivation, it is assumed that the magnetic field lines are all the same angle throughout the length of the tether, and that the tether is rigid.
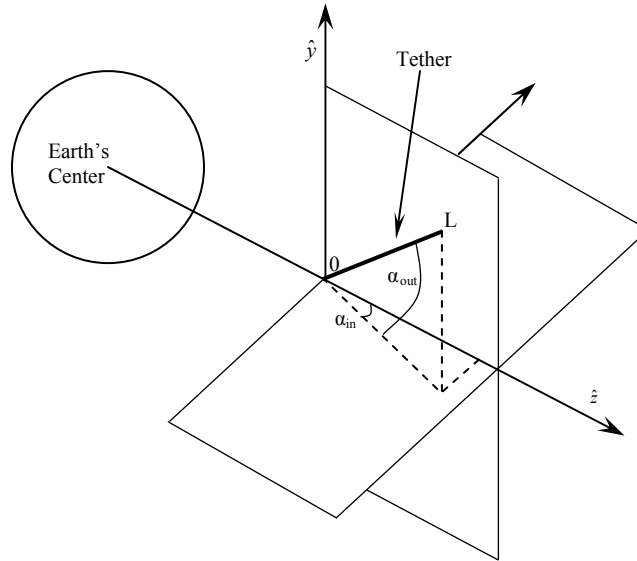
Figure 3-1: Orientation of a tether system in orbit.

Realistically, the transverse electrodynamic forces cause the tether to bow and to swing away from the local vertical. Gravity gradient forces then produce a restoring force that pulls the tether back towards the local vertical; however, this results in a pendulum-

like motion[18]. The $\bar{B}$ direction changes as the tether orbits the Earth, and thus the direction and magnitude of the ED forces also change. This pendulum motion can develop into complex librations in both the in-plane and out-of-plane directions. Then, due to coupling between the in-plane motion and longitudinal elastic oscillations, as well as coupling between in-plane and out-of-plane motions, an electrodynamic tether operated at a constant current can continually add energy to the libration motions. This effect then has a chance to cause the libration amplitudes to grow and eventually cause wild oscillations, including one such as the 'skip-rope effect' [122], but that is beyond the scope of this derivation. In a non-rotating EDT system,[19] the tether is predominantly in the z-direction due to the natural gravity gradient alignment with the Earth.

The orbital velocity of the spacecraft with respect to the Earth's magnetic field also needs to be obtained. By using the assumption that the magnetic field co-rotates with the Earth, and knowing the altitude and latitude of the orbiting body, the relative velocity can be determined. Figure 3-2 describes how to calculate the components of orbital velocity. The tether velocity components are seen in Eq. 3-3 and used to calculate the v_{orb} components from Figure 3-1.
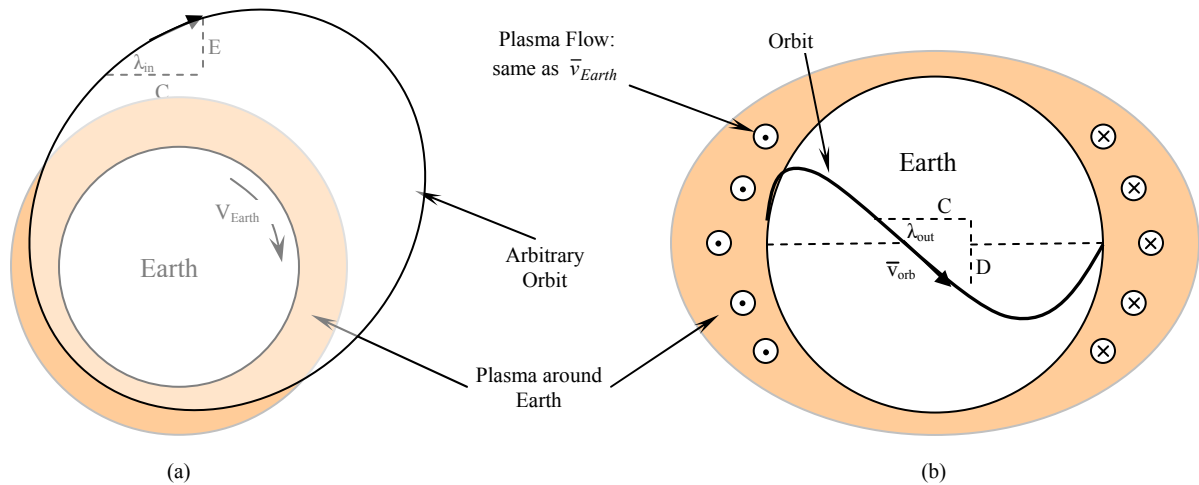
Figure 3-2: Orbital Velocity Calculation: a) bottom view, b) side view.

---

[18] Gravity gradient forces also result in pendulus motions without ED forces.
[19] A rotating system, called Momentum Exchange Electrodynamic Reboost [MXER], is presented in section 6.4.

Using geometry, the velocity of Earth's rotation, which is also the relative velocity of the magnetic field lines, is calculated and shown in Eq. 3-4.

$$v_{Corot} = \frac{2\pi \cdot (6378100 + alt_{sys}) \cdot \cos(lat_{sys})}{86400} \hat{x} \quad [m/s]$$

Eq. 3-4

There, alt_{sys} and lat_{sys} are the system center of mass altitude in meters and latitude in degrees, respectively. Finally, Eq. 3-5 details the entire orbital velocity equation, where $v_{orbx,y,z}$ are the components given in Eq. 3-3.

$$\bar{v}_{orbt} = (v_{orbx} - v_{Corot})\hat{x} + v_{orby}\,\hat{y} + v_{orbz}\,\hat{z}$$

Eq. 3-5

Physical behaviors of the components can be determined before any of the derivation begins. For non-rotating EDT systems, the z-component of the tether length, L, should naturally be the dominant component. This is because the tether physically aligns itself with the center of the Earth as a result of the gravity gradient force, as mentioned earlier. A particular study performed by Hoyt [122] has shown that, using feedback, an in-plane and out-of-plane libration amplitude can be held at approximately ±8° and ±20°, respectively[20]. This suggests tether libration and active libration managementmust be carefully considered. In addition, systems such as the MXER will be continuously rotating and the L_x, L_y, and L_z components will change drastically.

 The x-component of the B-field is commonly small compared to the y and z components, but can be up to 8% of the total B-field magnitude, as seen in Table 3-1. In addition, the y-component of the B-field should be large when the tether is around the equator and small when at high latitude orbits. The opposite effect holds true with the z-component [78, 79]. In addition, if the system has a circular orbit, v_{orbz} will be negligible. These velocity comparisons can be seen in Table 3-2. The v_{orbz} value solely depends on the elipticity of the orbit, being zero at a circular orbit and increasing from there [123].

---

[20] This study was used on the GLAST mission (see Section 6.2 for description of mission) as it was de-orbiting.

270° Longitude	Alt. [km]	B_{mag} [nT]	B_x [nT]	B_y [nT]	B_z [nT]
0° Lat	300	27113	2124	25300	9512
80° Lat	300	50156	-1251	453	50139

Table 3-1: Magnetic field values at high and low latitudes.

Circular Orbits	Alt. [km]	V_{orb} [m/s]	V_{orbx} [m/s]	V_{orby} [m/s]	V_{orbz} [m/s]	V_{Earth}
0° Lat (80° Inc.)	300	7730	1340	7610	0	486
80° Lat (80° Inc.)	300	7730	7730	0	0	85
0° Lat (0° Inc.)	300	7730	7730	0	0	486

Table 3-2: Orbital velocity values encountered at particular inclination orbits in an Earth-centered inertial frame.

3.1.1   Derivations

The following derivation will describe the exact solution to the system accounting for all vector quantities involved, and then a second solution with the nominal condition where the magnetic field, the orbital velocity, and the tether orientation are all perpendicular to one another. The final solution of the nominal case is solved for in terms of just the electron density, n_e, the tether resistance per unit length, R_t, and the power of the high voltage power supply, P_{hvps}.

Figure 3-3 describes a typical EDT system in a series bias grounded gate configuration[21] with a blow-up of an infinitesimal section of bare tether. This figure is symmetrically set up so either end can be used as the anode. This tether system is symmetrical because rotating tether systems will need to use both ends as anodes and cathodes at some point in its rotation. The V_{hvps} will only be used in the cathode end of the EDT syetem, and is turned off otherwise.

---

[21] A further description of the various types of configurations analyzed is presented in Section 3.4.
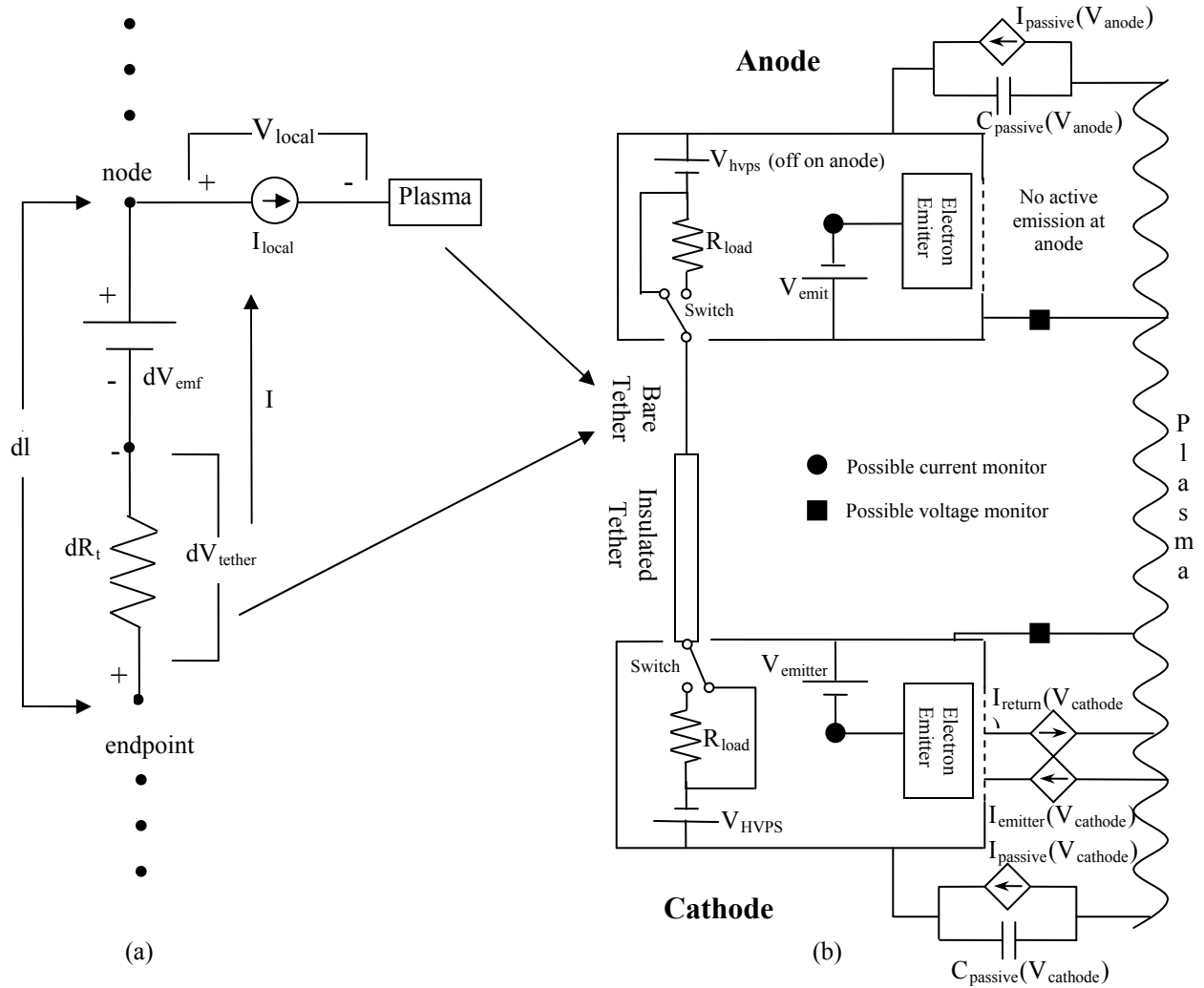
Figure 3-3: (a) A circuit diagram of a bare tether segment with (b) an equivalent EDT system circuit model showing the series bias grounded gate configuration.

The two equations that are used to acquire the solution to EDT systems are Kirchoff's current law (KCL) and Kirchoff's voltage law (KVL). In order for the voltage law to be valid, there must be a circuit loop. It can be seen in Figure 3-3 that the circuit loop for KVL begins and ends in the plasma. After the current is emitted, it induces a cross-field plasma current which excites a Whistler wave. This induced cross-field current eventually connects to the other B-field-alligned current from the other end of the tether. Experimentation has been conducted to confirm this particular current closure phenomenon as a possible explanation [124-126]. A key assumption is that the impedance between the electron emission and collection ends of the EDT system can be considered negligable traveling through the plasma. Previous work has been conducted

which has calculated that the impedance of this radiation through the ionosphere is ~13 Ω [127].

From the plasma, the circuit continues into the EDT system across the plasma sheath of the electron collection end (V_{anode}) and into the tether. This process breaks up the tether into 'N' number of sections in series and evaluates the circuit in Figure 3-3a at each section. The summation of these sections determines the potential drop from the resistive losses within the tether (V_{tether}) and the EMF potential (V_{emf}) dictated by Eq. 1-1. An important note concerning the tether segment is that for an insulated segment there would be no electron collection or emission. In this case, the current collecting portion of the circuit in Figure 3-3a would not be there. The next element in the circuit is the option of going through a resistive load (V_{load}) or a short circuit. After that is the potential across the High Voltage Power Supply (HVPS) (V_{hvps}) followed by the potential of the electron emitter ($V_{emitter}$). The last element in the circuit loop before returning to the plasma is the potential of the sheath surrounding the electron emitter ($V_{cathode}$). This potential can collect more electrons or ions depending on the potential with respect to the plasma, described in section 2.2 of this thesis.

In order to apply KCL, a particular node must be selected. The point where electrons are emitted back into the plasma was found to be a useful site. At this node, electron current is 1) emitted from the electron emitter ($I_{emitter}$), 2) supplied by the tether ($I_{tetherend}$), 3) passively collected or emitted (depending on the potential of the spacecraft at that point and whether it is conductive and electrically connected to the circuit) ($I_{passive}$), and 4) returned to the spacecraft by space charge limits or attracted back to the spacecraft as a result of electron emission into a plasma with a more negative potential than the emitter (in the cases of Field Emitter Arrays - FEAs, and Thermionic Cathodes - TCs) (I_{return}). Eq. 3-8 displays how all of the current entering the emitter must equal the current that is exiting.

From Figure 3-3, Eq. 3-6, Eq. 3-7, Eq. 3-8, and Eq. 3-9 can be obtained.

$$V_{anode} + \Sigma dV_{emf} + \Sigma dR_t \cdot dl \cdot I(z) + V_{load} + V_{emit} + V_{cathode} = V_{hvps} \qquad \textbf{Eq. 3-6}$$

$$V_{anode} + \Sigma dR_t \cdot dl \cdot I(z) + V_{load} + V_{emit} + V_{cathode} = \Sigma dV_{emf} \qquad \textbf{Eq. 3-7}$$

$$I_{tetherend} = I_{emitter} - I_{passive} - I_{return} \qquad \textbf{Eq. 3-8}$$

$$I(z) = \Sigma I_{local} \qquad \textbf{Eq. 3-9}$$

The EMF potential and the resistance potential are differential, because throughout the iterative process each step must calculate these values. In the KVL of the de-boost condition, Eq. 3-7, the major difference, other than the lack of an HVPS, is the direction of the current flow in the circuit, and thus the sign of the EMF potential. Eq. 3-6 and Eq. 3-7 represent the KVL for the boosting and de-boosting cases, respectively. Also, Eq. 3-9 describes the total current collected at any point along the tether.

The unknown variable in this system that must be solved for is the potential of the anode with respect to the ambient plasma, V_{anode}. In the case of bare tethers, this can be accomplished through iteration; in the case of insulated tethers, it can be accomplished through the solution of roots. These solutions will be discussed later in this section. The electron current collection of the anode is dependant on the ambient conditions in space as well as the potential, with respect to the plasma. This relationship is described in Eq. 3-10, and is an experimental modification of the Parker-Murphy electron current collection theory from the TSS-1R mission, which is mentioned in Chapter 1 [30, 31].

$$I_{anode} = \alpha \cdot I_o \cdot \left[1 + \left(\frac{V_{anode}}{\phi_o} \right)^{\beta} \right]$$

Eq. 3-10

The electromotive force potential, V_{emf}, shown in Eq. 1-1, can be expanded, as shown in Eq. 3-11, and then broken up into components, as detailed in Table 3-3. Each of the individual scalar elements of the table come from Eq. 3-1, Eq. 3-2, and Eq. 3-5.

$$V_{emf} = \int_0^{Lx} \left(\bar{v}_{orbt} \times \bar{B} \right) \cdot \hat{x} dL_x + \int_0^{Ly} \left(\bar{v}_{orbt} \times \bar{B} \right) \cdot \hat{y} dL_y + \int_0^{Lz} \left(\bar{v}_{orbt} \times \bar{B} \right) \cdot \hat{z} dL_z$$

Eq. 3-11

x-components	y-components	z-components
(A) $\left(v_{orbty} B_z \right) L_x \, \hat{x}$	(C) $\left(v_{orbtx} B_z \right) L_y \, \hat{y}$	(E) $\left(v_{orbtx} B_y \right) L_z \, \hat{z}$
(B) $-\left(B_y v_{orbtz} \right) L_x \, \hat{x}$	(D) $-\left(B_x v_{orbtz} \right) L_y \, \hat{y}$	(F) $-\left(B_x v_{orbty} \right) L_z \, \hat{z}$

Table 3-3: Chart of V_{emf} components.

Using the physical observations made in Table 3-1 and Table 3-2, it can be determined from Table 3-3 that component (E) is the dominant value during low-inclination, circular, or rotating orbits. It can, however, become small in high inclination scenarios. It can also be observed that components (D) and (F) are almost always less

than 10% of the other components because of the B_x terms. Components (A) through (C) are usually only a few percent of component (E), but can become significant under librations or a rotating tether system. The total EMF potential across the tether is then the magnitude of the components in Table 3-3, and shown in Figure 3-3. For iteration purposes, V_{emf} can be written as Eq. 3-12, where the initial case is $V_{emf}(0) = 0$.

$$V_{emf}(n) = V_{emf}(n-1) + V_{emf}(per\ element)$$

Eq. 3-12

The next variable to be calculated is the total potential resulting from the resistive losses across the tether, and can be seen in Eq. 3-13.

$$V_{tether}(total) = \sum_{I}^{N} \left[I_{tether}(n) \cdot R_t \cdot dL \right]$$

Eq. 3-13

'N' represents the last element in the tether (L/dL). V_{tether} depends upon the system constraints defined by the user, and the simultaneous equations Eq. 3-12 through Eq. 3-13.

$$I_{element}(n) = \pm SA \cdot J_{the,thi} \cdot \frac{2}{\sqrt{\pi}} \sqrt{1 + \frac{V_{element}(n-1)}{T_{e,i}}}$$

Eq. 3-14

$$V_{element}(n) = V_{element}(n-1) - \left[R_t \cdot I_{tether}(n) \cdot dL \right] - V_{emf}(n)$$

Eq. 3-15

$$I_{tether}(n) = I_{tether}(n-1) + I_{element}(n)$$

Eq. 3-16

Eq. 3-14 is the OML theory for electron and ion collection, respectively. This equation is only applied for the bare sections of tether. Further description of this equation along with the transition region from negative to positive potentials is explained in Chapter 2. For an insulated section of tether the current collection always equals zero, $I_{element}(n) = 0$. Within Eq. 3-14 is the potential of each element, defined in Eq. 3-15, and within that equation is the current of the tether, which is defined in Eq. 3-16. For Eq. 3-15 and Eq. 3-16, $V_{element}(0) = 0$ and $I_{tether}(0) = I_{anode}$, respectively.

The potential across a load resistor (V_{load}) inserted in series with a tether system, located immediately after the tether, is defined in Eq. 3-17.

$$V_{load} = -R_{load} \cdot I_{tether}(N)$$

Eq. 3-17

This potential can be used as a load resistor for creating an effective open-circuit to stop most current from flowing across the tether. Another possible application for the load resistor would be for it to represent a battery that is charged by the naturally induced current (in the de-boost mode). There will still, however, be electrodynamic effects such as the phantom current, discussed later in this section. Overall, the load potential hinders the altitude boosting or de-boosting effects of an EDT.

Following the load resistor is the HVPS, which has two different operational modes. These modes are constant voltage and constant power mode. If the device is in constant voltage mode then whatever the user inputs as the potential is the value used in the KVL equation. The physical drawbacks to this method are that, in certain cases when the system draws a few amps across the tether, the HVPS may exceed its design power limitation. In these cases it would cap the total current being transferred through the system and be a limiting factor. The alternate, constant power mode, would result in the value defined in Eq. 3-18.

$$V_{hvps} = \frac{P_{hvps}}{I_{tether}(N)}$$

Eq. 3-18

The physical limitation for this mode would be similar to the constant voltage mode in that the HVPS would be capped at a maximum potential. In the case of very small currents, the potential required to maintain a constant power could exceed that maximum. In that instance the power of the HVPS would be forced to reduce until the point is reached where the maximum potential equates.

The emitter potential is the next item in the KVL circuit path. This value depends on the type of emitter being used. The emitters being considered in this thesis are thermionic cathodes, field emitter arrays, and the hollow cathodes, which are discussed in Chapter 2. For the purposes of this derivation, the hollow cathode will be analyzed. In this particular case, the non-ideal HC can have a variety of discharge potentials that dictate how much power is required for the system. A common HC that can emit up to 25 A was found to have a $V_{emitter} = 26.5$ V [119]; however, this can change depending on the system applications and objectives.

The last item in the KVL circuit for this particular tether system configuration is the potential across the plasma sheath from the electron emitter to the ambient plasma. This value is physically the potential difference with respect to the plasma that is left over after traveling through all the system components. The value is defined in Eq. 3-19.

$$V_{cathode} = V_{element}(N) - V_{emitter}$$
<div align="right">**Eq. 3-19**</div>

This cathode sheath potential is very important with respect to the electron emission. The larger this value, the greater the space charge limits that must be overcome for the emitter. This effect will be explained later, in section 3.2.

The cathode end is a particular point of interest, where KCL will help solve the tether system of equations. For this particular derivation it will be assumed that the emitter is not at a space charge limiting potential and that the return current equals zero (which is commonly the case using an HC). Under these assumptions, the current at the end of the tether must equal the electron current emitted by the emitter, according to Eq. 3-8. The electron emission current is defined using Eq. 2-17 for FEAs, Eq. 2-15 and Eq. 2-16 for TCs and Eq. 2-18 for HCs.

Once a solution is obtained that solves KVL and KCL for the system, it is possible to calculate the resulting forces. Eq. 3-20 displays the integral calculation of force.

$$\overline{F}_{mag} = \int_0^{\overline{L}} \left(I_{tether}\ d\overline{L} \right) \times \overline{B}$$
<div align="right">**Eq. 3-20**</div>

Here, 'I_{tether}' represents the total current at each infinitesimal length of tether, dL, as defined in the above derivation. As a result, it is impossible to calculate this value by an integral because it is imbedded in a series of simultaneous non-linear equations. The only way to calculate this is through numerical iterations, which are shown in Eq. 3-21.

$$\overline{F}_{mag}(total) = \sum_1^n I_{tether}(n)\ d\overline{L} \times \overline{B}$$
<div align="right">**Eq. 3-21**</div>

From this point, the components of Eq. 3-20 can be determined. They are shown in Table 3-4. A physical observation made on these components shows that, unless the tether has significant librations, the only major dominant component is (H). With no

librations, the tether naturally aligns itself up with the gravity gradient, or the previously defined z-axis of the Earth, and thus causes L_x and L_y to be negligible. Component (J) is only a few percent of (H) because of the B_x factor in it, and component (L) is a few percent of that, due to the L_y factor. Components (I) and (K) could result in small forces depending on the inclination of the orbit and the alignment of the tether with respect to the gravity gradient. Component (G) directly opposes the dominant in-plane component (H) force; however, this is insignificant unless the tether system is at a high latitude and / or librating significantly.

x-components	y-components	z-components
(G) $\left(I_{tether}\, L_y\right) B_z\, \hat{x}$	(I) $\left(I_{tether}\, L_x\right) B_z\, \hat{y}$	(K) $\left(I_{tether}\, L_x\right) B_y\, \hat{z}$
(H) $-B_y \left(I_{tether}\, L_z\right) \hat{x}$	(J) $-B_x \left(I_{tether}\, L_z\right) \hat{y}$	(L) $-B_x \left(I_{tether}\, L_y\right) \hat{z}$

Table 3-4: Components of the force equation.

In-plane and out-of-plane direction is determined by the orbital velocity vector of the system. An in-plane force is in the direction of travel. It will add or remove energy to the orbit, thereby increasing the altitude by changing the orbit into an elliptical one. An out-of-plane force is in the direction perpendicular to the plane of travel, which causes a change in inclination. This will be explained in the following section.

To calculate the in-plane and out-of-plane directions, the components of the velocity and magnetic field vectors must be obtained and the force values calculated (as in Table 3-4). The component of the force in the direction of travel will serve to enhance the orbit raising capabilities, while the out-of-plane component of thrust will alter the inclination. In Figure 3-4, the magnetic field vector is solely in the north (or y-axis) direction, and the resulting forces on an orbit, with some inclination, can be seen. An orbit with no inclination would have all the thrust in the in-plane direction [128].
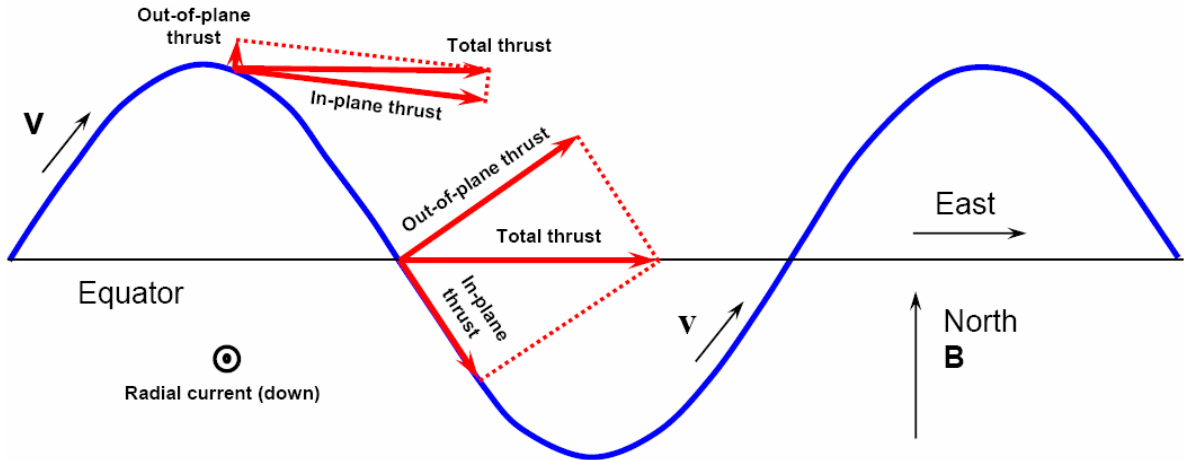
Figure 3-4: Description of an in-plane and out-of-plane force [195].

There has been work conducted to stabilize the librations of the tether system to prevent misalignment of the tether with the gravity gradient. Figure 3-5 displays the drag effects an EDT system will encounter for a typical orbit. The in-plane angle, α_{ip}, and out-of-plane angle, α_{op}, can be reduced by increasing the endmass of the system described in Eq. 6-2, or by employing feedback technology [122]. Any deviations in the gravity alignment must be understood, and accounted for in the system design.
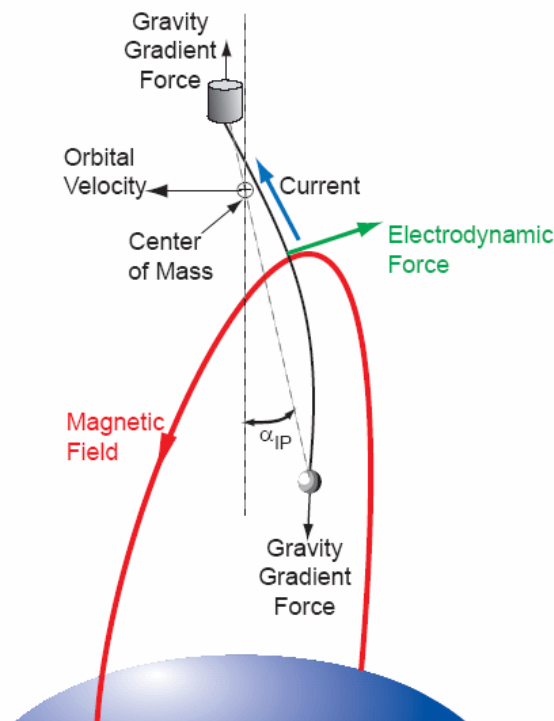
Figure 3-5: Drag effects on an Electrodynamic Tether system [195].

3.1.2 Assumptions for Simulation Work

The simulation work conducted in this thesis makes two important assumptions. The first assumption is that the tether system is always considered to be alligned with the gravity gradient. This assumption is made because as mentioned earlier in this section, the system naturally orients itself in this configuration. This simplifies the EMF and force equations of Table 3-3 and Table 3-4 by removing the components that contain an L_x or L_y term.

The second assumption is that only the y-component of the magnetic field is considered in the calculations. This assumption should only be applied to systems of low inclination. For the V_{emf} calculation, only equations (E) and (F) in Table 3-3 are used. The remaining force components, equations (H) and (J) in Table 3-4, are in the x- and y-axis, respectively. The particular forces that are of importance for the simulations of this thesis are the altitude raising and lowering forces. This in-plane force, as described in the previous section, is the force in the direction of motion. For example, in a 0º inclination orbit, it would not matter what the y-axis force is, using (J), because the direction of motion is solely in the x-axis, which is determined by (H). Since (H) is determined by only B_y, this is the reason for the second assumption. Unless otherwise stated, all the simulations of the thesis will be 0º inclination.

For the cases where there is an inclination, as in the case study in Section 6.2, which uses a 28.5º inclination for the GLAST case study and 51.6 for the International Space Station case, the error of just using B_y can be calculated. Every minute over the course of an entire orbit a data point can be taken that details the velocity and magnetic field vector components. For example, at the maximum inclination of 28.5º, which occurs as the spacecraft is crossing the equator as seen in Figure 3-4, the velocity component is 0.88x ± 0.48y at this point[22]. Using this metric and (H) and (J), the actual in-plane force can be calculated (using only the assumption of a gravitational gradient alligned system). Comparing this force to the force using only B_y yields ~+3.8% difference. This percent error grows as the inclination increases and/or the altitude

---

[22] It is + for an ascending node, and – for a decensding node.

70

decreases. A similar calculation can be accomplished for the 51.6º inclination at 350 km and 450 km altitude. The results yield a ~+18.3% and a ~+15.4% difference for the 350 km and 450 km altitudes, respectively. This value is accounted for in the simulation results for the GLAST and ISS systems in sections 6.2 and 6.3.

3.2   Insulated Tether Derivation

The derivation of an insulated EDT system follows the same method as the bare tether EDT system, except for the iterative process required when calculating the tether potential value. Since there will be no collection along the length of the tether, the current that is collected at the anode will be the current that is entering the emitter. The entire iterative process can be replaced by a single step.

To begin, every element in $I_{element}(n)$ (Eq. 3-14) is always equal to zero under the assumption of insulation. This means that Eq. 3-16 equals Eq. 3-10, as well as the $I_{emitter}$ of a non-ideal HC, and is represented in Eq. 3-22. From here, the tether (Eq. 3-13), the load (Eq. 3-17), and the HVPS (Eq. 3-18) potentials can be recalculated after substituting Eq. 3-22 into them. The results are that Eq. 3-13 becomes Eq. 3-23, Eq. 3-17 becomes Eq. 3-24, and Eq. 3-18 becomes Eq. 3-25.

$$I_{tether}(n) = I_{anode} = I_{emitter} \qquad\qquad \textbf{Eq. 3-22}$$

$$V_{tether}(total) = I_{anode} \cdot R_t \cdot L \qquad\qquad \textbf{Eq. 3-23}$$

$$V_{load} = -R_{load} \cdot I_{anode} \qquad\qquad \textbf{Eq. 3-24}$$

$$V_{hvps} = \frac{P_{hvps}}{I_{anode}} \qquad\qquad \textbf{Eq. 3-25}$$

In Eq. 3-23, since the same value is summed as many times as there are 'dl' elements, the original value is just multiplied by the total element number, N. The V_{emf} and $V_{cathode}$ potential values still remain the same. Again, since the non-ideal HC is being used, the $V_{emitter}$ equals 26.5 V.

Now, assuming an HC electron emitter, using Eq. 2-18, and substituting in Eq. 3-22, the element potential can be solved for. This value is seen in Eq. 3-26.

$$V_{element} = T_{epc} \cdot \ln \left[\frac{\left(I_{anode} \big/ E_{num} \right) + I_i}{I_i \cdot f \cdot \sqrt{\left(m_i \big/ 2 \cdot \pi \cdot m_e \right)} \cdot \exp\left(-V_{emitter} \big/ T_{epc} \right)} \right]$$ **Eq. 3-26**

At this point, every potential in the KVL loop, Eq. 3-6, is defined in terms of: V_{anode}, v_{orbt}, B, L, R_t, T_e, n_e, m_i, R_{load}, P_{hvps}, E_{num}, and the HC geometry. The only variable that cannot be measured or obtained from atmospheric models is V_{anode}. As a result, after applying the appropriate potential equations to the KVL equation, Eq. 3-6, and solving for the roots, the anode potential can be determined. Then the total force on the system is found using Eq. 3-20. The de-boost condition solution to this problem is solved in the same way as the bare tether, by using Eq. 3-7 as the KVL loop.

3.3   EDT System Phenomenon

3.3.1   Phantom Current

Even when the end collectors / emitters are isolated from a bare tether, creating what might be considered an open-circuit in the KVL loop in Eq. 3-6, it is possible to have current flow within the bare tether system. The open-circuit effectively removes the V_{anode}, V_{load}, V_{hvps}, and $V_{emitter}$ values from the KVL equation. All of the current is collected and emitted passively only through the tether. The induced V_{emf} drives the system to have a positive potential with respect to the plasma near the higher altitude end of the bare tether,[23] and a negative potential at the lower altitude end. The potential differences yield electron and ion collection at their respective ends.   In addition, according to KCL, all the passive electron current collected must equal the passive ion current collected. However, due to the difference in mobility between the electrons and ions, the electron collection only occurs along the first few percent of the bare section length of the highest altitude portion of the tether. It then takes the remaining lower portion of the bare tether for the ion thermal current collection to equal the electrons

---

[23] In a typical west to east orbit around Earth.

collected in the upper part. The resulting current in the tether, moving across a B-field, produces an $I \cdot dL \times B$ force, which de-orbits the EDT system.

This phenomenon was applied to the proposed ProSEDS mission as an example.[24] In this system, a 4860 m single strand 0.6 mm radius aluminum bare tether with a resistance of 0.015 Ω/m was used. The altitude started at approximately 285 km and the simulation date was February 3, 2004. TEMPEST simulations predict an EMF potential drop of 10–40 V across the bare section of the tether, shown in Figure 3-6a. This V_{emf} results in a "phantom current" of ~5–60 mA, as shown in Figure 3-6b. The added altitude reduction due to this 'phantom' drag force is shown in Figure 3-6c. This illustrates how the potential drop and current flow produces approximately a 0.2-km-per-day altitude reduction to the ProSEDS mission.

(a)

(b)

(c)
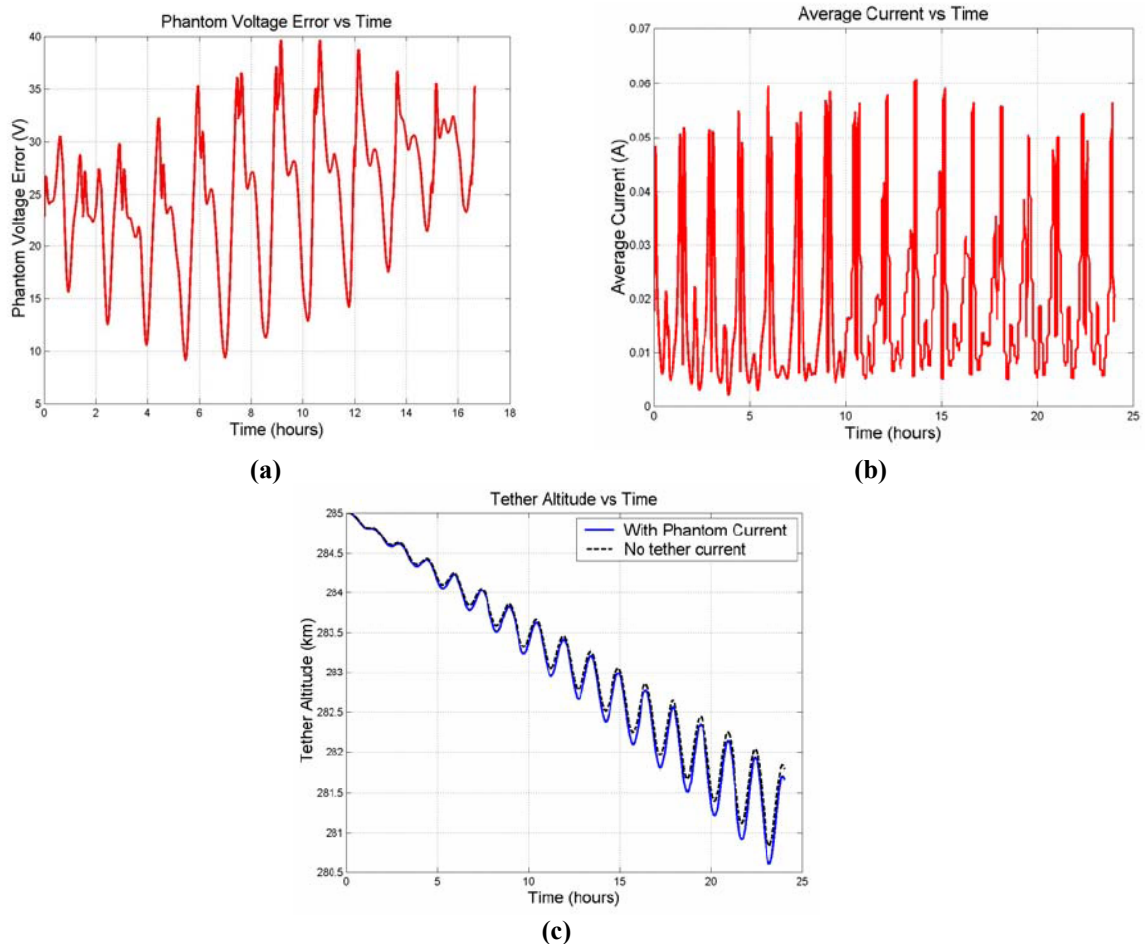
Figure 3-6: A 24-hour TEMPEST run for ProSEDS in open circuit mode for (a) average current, (b) potential drop, and (c) altitude drop.

---

[24] A description of this mission is in section 1.2.5.

3.3.2   Inclination Change

It can be seen in Figure 3-4 that the maximum out-of-plane force occurs at the equatorial crossing, while the minimum point occurs at the maximum latitude of the orbit. This out-of-plane force causes the system to change inclination, i, as given by Eq. 3-27. Here, m_{body} represents the mass of the orbiting body.

$$\frac{di}{dt} = \frac{F_{out}}{m_{body} v_{orbt}} \cos(lat_{sys})$$

Eq. 3-27

The result of the changing inclination can be seen in Figure 3-7, where (a) combines Figure 3-4 and Eq. 3-27 to demonstrate the magnitudes and directions of the out-of-plane force as spacecraft orbits Earth. In order for inclination change to take place, boosting must occur during the crossing of one node, and deboosting across the other. Figure 3-7b shows the resulting change in inclination. Another interesting note is that the change of inclination using an EDT ideally should not consume any energy. All of the out-of-plane forces are perpendicular to the in-plane forces, and thus do not impact the altitude of the orbit. In actuality, the electrical resistance in the conductive material, the energy storage losses, and the potential drops across the plasma sheaths result in minor expenditures of energy [128].

(a)   (b)
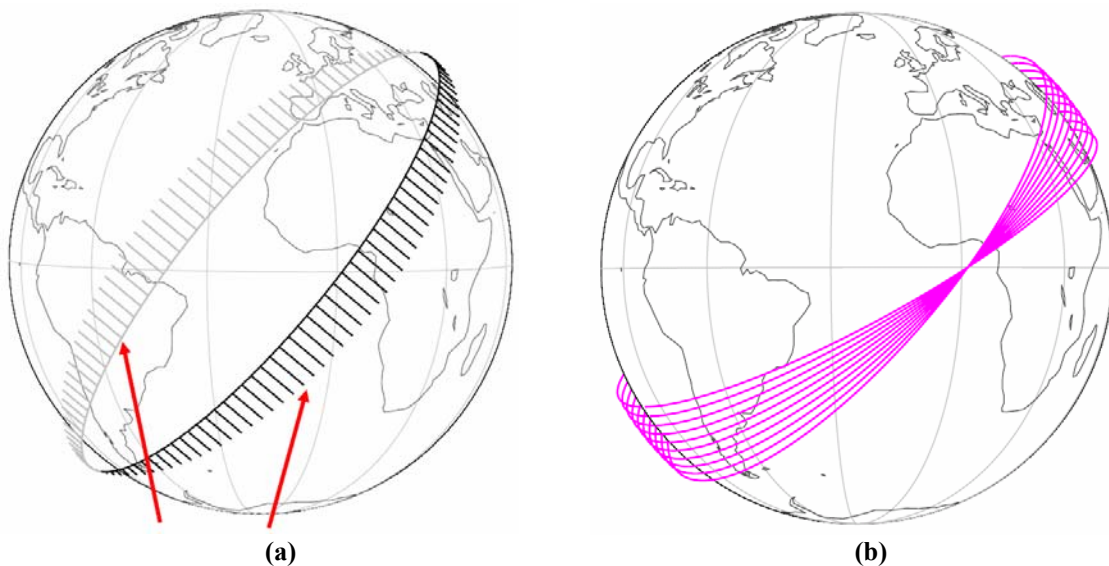
Figure 3-7: Demonstrates (a) the magnitudes of the out of plane force as an EDT system would orbit the Earth and (b) the resulting change in inclination [195].

3.4   Configurations and Modes

There are three configurations considered for connecting the electron emitter to the tether circuit, as shown in Figure 3-8. They are identified as: (a) Grounded tip/emitter, (b) grounded gate, and (c) grounded gate, isolated tether.   The grounded emitter configuration effectively isolates the tether and high-voltage power supply (HVPS) circuit from the electron emitter. The electron emitter bias is exclusively set by the 'emitter bias' supply. The gate, however, is at a positive potential with respect to the surrounding space plasma that can attract electrons from the plasma drawing current through the power supply [97, 129]. Electron emitters can be set up in any of the three configurations, however due to the design of the HC, the only way to model it is using the grounded emitter configuration. Here, the spacecraft body is forced negative by the positively charged xenon released from the hollow cathode.

A grounded gate configuration is shown in both Figure 3-8b and Figure 3-8c. The grounded gate configuration allows all external structures, including the field emission gate itself, to be held at the floating potential of the spacecraft. This should minimize the V_0 - V_p when the electron emitter is providing all of the tethers current. The Figure 3-8b configuration has the draw back that if the electron emitter can not provide all of the tether current, then the spacecraft potential will be pulled negative, and possibly substantially negative, through the electron 'emitter bias' supply if the system is left to float. However, if a set power supply is used as the emitter bias, then this supply would lock the gate-to-emitter bias and protect the emitter. The drawback to this is the expenditure of much more power, as opposed to zero power if letting the emitter float. The initial assessment, therefore, is that the series bias - grounded gate configuration in Figure 3-8c will be the most robust option. The drawback to this configuration is that the emitter bias supply is not part of the KVL loop, now must supply its own power [130].
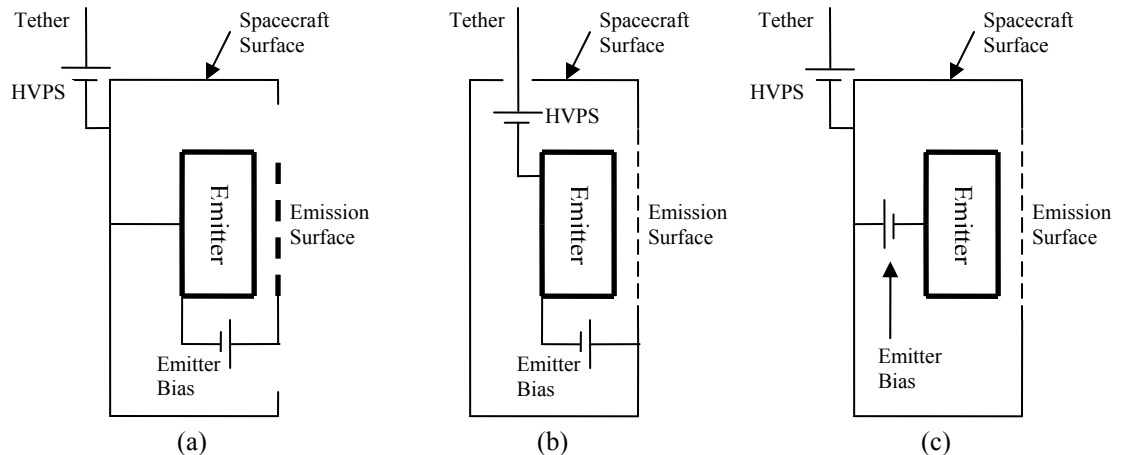
Figure 3-8: Possible electrical configurations of the electron emitter with the tether and high voltage power supply (HVPS): Grounded tip/emitter (a), grounded gate (b) and grounded gate, isolated tether (c) configurations.

Emission velocity depends upon the field strength required to pull electrons from the emitter material at sufficient current densities. For the TC, the voltage required by the electron gun is high enough such that the beam escapes into the plasma freely. For the FEAs, this extraction energy can be low enough such that the beam immediately beyond the emitter will be forbidden to escape due to SCLs. The electrons will then be reflected back to the spacecraft. This effect can be countered by increasing emission voltage or adding an additional accelerating grid, but costs additional power. Other solutions exist such as adding a secondary gate outside the emitter to defocus the departing beam, or pulsing the emitting beam at certain frequencies to avoid space charge limitations [130, 131].

When FEAs and TCs are used, they have to emit the electrons as close to floating potential as possible in order to be the most efficient [131]. The grounded gate configurations allow this to occur. The spacecraft surface is at the floating potential in these cases, provided all the current from the tether is being released through the emitter without any returning from space charge limits.

3.5   Simulation Tools

Two software tools were developed for this research: a spreadsheet style tool using *Microsoft Excel*^{TM} 2003 (11.8107.8117, Service Pack 2) titled '*EDT-Trades*' and a

Matlab^{TM} code (version 7.2.0.232, R2006a) titled '*EDT-Survey*'. An important reason for the implementation of two computer codes was for redundancy and verification. Each code used a unique iterative method for arriving at a solution to the system. This also resulted in two unique perspectives on the EDT system simulation. *EDT-Trades* was also useful for solving many different types of system configurations such as that seen in Figure 3-8, as well as employing the various electron emission technologies. The *EDT-Survey* code can be seen in Appendix B.

The equations discussed in Sections 3.1 and 3.2 are utilized to complete the system of equations necessary to solve an EDT system. The user must first enter the atmospheric, ionospheric, and magnetic values associated with the particular point in space and time the system is at. The user must then identify a number of system setup settings before the simulation can begin:[25]

- Boosting or De-boosting system

- Anode - Spherical conducting endmass, bare tether, or HC (then associated information such as radius or HC parameters)

- Tether - Length, radius, impedance (assuming a cylinder), number of segments it will be divided into for analysis, and insulated vs. bare length amount

- HVPS - Constant voltage or constant power mode (and the respective voltage or power value)

- Load Resistor - what value (0, if no load)

- Emitter Type - TC, FEA, or HC and the respective information associated with each device

- Emitter configuration – see Figure 3-8

- For the grounded gate configuration: Forced to a particular potential, or allowed to float (using the potential of the system to drive it)

- Cathode – radius (assuming a conducting sphere)

---

[25] All values entered into and received from the simulation tools are of double precision.

3.4.1 *Excel^{TM}* Simulations: *EDT-Trades*

The *Excel^{TM} 'EDT-Trades'* spreadsheet tool developed was a more visual method for simulating an EDT system. It was apparent what equations were used in the system step-by-step in the iterative process. In addition, the currents and potentials at each point along the tether were readily observable. The manipulation of any value causes the entire spreadsheet to immediately update according to the new information. This allows the user to see instantly the implications of any altered component.

Once the system values described above were entered into the system the 'Solver' function was employed. As described in Chapter 3, the KCL of the system at the emitter was solved by changing the V_{anode} of the system. The current was solved to a precision of 1×10^{-5}. The *Microsoft Excel^{TM}* Solver tool uses the Generalized Reduced Gradient (GRG2) nonlinear optimization code developed by Leon Lasdon, University of Texas at Austin, and Allan Waren, Cleveland State University.

The major drawback was that the analysis could not be conducted over a period of time due to the coding limitations. Only a particular instant could be solved for at one time before the user had to enter the next position and re-solve.

3.4.2 *Matlab^{TM}* Simulations: *EDT-Survey*

The *Matlab^{TM} EDT-Survey* simulation tool was developed for simulating elaborate system setups. This high-level scripting language is capable of accomplishing the same simulations as the *Excel^{TM}* software, except that it can more easily repeat the simulation for multiple scenarios in a single run.

An additional function that was added so the *EDT-Survey* simulation performed was to allow for the effects of a solid flat tape tether geometry. For this particular case, if the tether specified was above a certain width, the current collection would not behave according to OML theory, as with all previous simulations. Another added effect to the simulation code was to calculate the impedance of the tether based on the temperature and geometry. A more in-depth description of these added features can be seen in section 6.1.1.

The major enhancement of the *EDT-Survey* simulation tool was its ability to effectively incorporate various parameters across an orbit. In order to accomplish this the IGRF, IRI, and MSIS models were employed. Using these models, TEMPEST output the values of user defined orbits during user specified times. As a result, the values of an actual orbit were used in some of the simulations. Using a similar method, system variables were manipulated across these orbits in a single run, as seen in section 5.1. These system variables are bare tether lengths, total tether lengths, varying endbody collectors, varying emitters, electron densities, HVPSs, and tether resistances.

3.4.3   Simulation Limitations and Physical Explanations

The following cases result in extreme circumstances that ended in failures in the simulation. This section presents these cases and the explanation of what is physically occurring. All of the following cases refer to the boosting and de-boosting cases unless otherwise specified.

HC emitter scenarios:

In the HVPS constant power mode there is an issue if the input electron density is too low, or if the power is chosen to be too large (values depend on each particular case). In the low e-density case, the tether can only collect a fraction of the electron current due to the lack of available electrons, as seen in Figure 5-3. As a result, the potential across the HVPS becomes many kilovolts in order to retain a constant power. The V_{anode} then becomes an equivalently large voltage so it can collect enough current in attempts to drive the V_{hvps} down (to solve KVL), as seen in Figure 5-11.

A way to avoid this issue is to lower the power supply value. If this is done, the boosting force will drop as well because the collected current will be less.[26] Physically, unless the power supply can handle high voltages, the HVPS would be voltage limited and operate at a lower current, thus reducing the boosting capabilities anyway ($P = VI$, so if $I \downarrow$ then $V \uparrow$ in order to compensate).

---

[26] To allow the code to solve this system, greater bounds will need to be chosen. They are currently set to 10,000 V.

FEA emitter scenarios:

Boosting Only: If the tether resistance, R_t, becomes so large such that ($I_{ave} \cdot R_t \cdot L$) > V_{emf}, then the tether will cease to boost and fail. In this case, the resistive loss along the tether will be too great for the potential, V_{emf}, and there will not be enough energy to drive the electrons down the tether.

If the field emitter array potential, V_{FEA}, is set too large for the user defined grounded gate – isolated tether configuration (seen in Figure 3-8c) and there is not enough electron collection at the endbody collector (because the ionosphere density is too small, or there is not enough bare tether, or the endbody collector is too small), then the system will fail. Physically, the cathode will be attempting to emit more than the system can collect. This will result in much of that emitted current returning back into the system at the cathode because of SCLs.

TC emitter scenarios:

The user determined grounded gate configuration (seen in Figure 3-8b) does not work when the user sets too high a potential. In certain cases, in order to emit this current, the TC requires more potential than is available in the system. In order for KVL to hold, the V_{anode} is driven down (negative); however, there is no solution to the system that allows the collected current to be emitted at the desired electron gum potential (no solution to KVL and KCL). Physically, the emitter would just emit less electron current, overriding the set potential, until it reached a stable solution.

In the grounded gate – isolated tether configuration (seen in Figure 3-8c), there is no issue because the potential used in this emitter is not part of the KVL loop (V_{eg}'s are usually on the order of 2000 V).

3.5 Validation of EDT Systems

3.5.1   TSS-1R Verification

The TSS-1R mission has been shown to be a good mission to use for verifying the total EDT code written. A description of this mission can be found in section 1.2.2. The data taken from TSS-1R provides readings on all of the variables necessary for a test run.

On February 27th (day 57), 1996 at 1:29.16 GMT the tether broke [117]. Table 3-5 details the parameters of the system before and after this event. The approximate coordinates were found to be 1.3° latitude, 262.9° longitude, 28.5° inclination, and 297 km altitude. B was experimentally shown to be less than 100 nT different than the IGRF model by Williams [117]. The IGRF model said that the B-field was 2.79×10^{-5} T [78, 79]. Also, using various ionospheric models, the predicted electron density at that particular location and time varied from 6×10^{11} m^{-3}, to 1.3×10^{12} m^{-3}. As a result, a value of 8×10^{11} m^{-3} was used as it was within the range of the models [132]. The r_{anode} and β values were taken from Thompson et al. [31]. All the remaining values in Table 3-5, except for the calculated ones, were taken from Gilchrist et al. [133].

**- these values were calculated

Values	Name	Shorted to Orbiter	Tether Separated
V_{emf} [V]	Induced EMF Potential	3482	
V_{to} [V]	Tether to Orbiter Potential	82	
$V_{cathode}$ [V]	Potential of Orbiter or sheath (after separation)	-596 ± 75	-122.6**
V_{sat} [V]	Satellite Potential	1222**	1560.8**
I_{end} [A]	Tether Current at end	0.97	1.1
R_t [Ω/m]	Tether Resistance	0.083 (1800 Ω)	0.083 (1635 Ω)
B [T]	Earth's Mag. Field	2.79×10^{-5}	
D_{alt} [km]	Altitude of device	297	
v_{orb} [m/s]	Calculated Orb. Vel. (East)	6335**	
r_{anode} [m]	Radius of Anode	0.8	
β	Corrected Parker Murphy	0.55	
α	Calculated Cor. P.M.	2.482**	
r_o [mm]	Radius of tether	0.6	
n_e [m^{-3}]	Electron Density	8×10^{11}	
T_i, T_e [eV]	Ion / Electron Temperature	0.1	
L_{tether} [m]	Tether Length	20700	19700

Table 3-5: Numbers obtained from the TSS-1R system, used to verify the developed EDT code.

The orbital velocity in the x-axis (east to west) was solved to be 6335 m/s using the equation $V_{emf} = v_{orb} \times B_N \cdot dL$. All the variables in this equation were known except for the orbital velocity. For the excel code, the velocity needed to be entered; however, this was not necessary to solve the two KVL equations before and after the break.

The code that was written for this thesis relies on a tether resistivity estimate to be able to do the calculations throughout the system. In order to simulate the system, only 19700 m of tether was actually used to create the emf. The rest was still wound up in the tether deployer. From Gilchrist et al. [133], however, it was estimated that the total resistance along the total tether, including the wound up part, was 1800 Ω. As a result, a new equivalent R_t value had to be calculated to use in the simulation. Even though the electrical path was 20700 m long at 0.083 Ω /m the total is the same (1800 Ω) using the new 0.09137 Ω/m for the 19700 m. (1800 Ω / 19700 m = 0.09137 Ω/m).

To obtain the satellite potential with respect to the plasma, KVL had to be utilized, as seen in Eq. 3-28.

$$V_{emf} = V_{sat} + I_t \cdot R_t \cdot L + V_{to} - V_{cathode}$$

Eq. 3-28

The V_{to} is the potential from the tether to the orbiter, and V_o is the potential of the orbiter, shown in Figure 3-9 [133]. Every value has been measured except for the potential of the satellite, V_{sat}, and as a result this can be determined. Now, using the P-M TSS-1R corrected equation (Eq. 2-9) and the assumption that β is 0.55, α can be calculated, and equals 2.482.
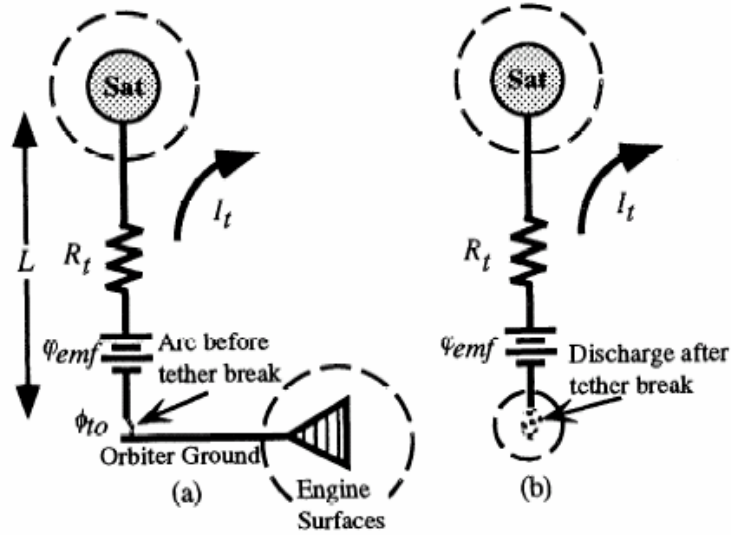
Figure 3-9: Simplifies drawing of an electrodynamic tether (a) just prior to and (b) after the tether break. Electrical contact with the space plasma is made at each end of the long tether through effective sheath impedances (Dotted lines).

To verify the case before the tether break, all of the values from Table 3-5, except for the potential of the orbiter, $V_{cathode}$ (and the tether length and tether resistance per meter as mentioned in the previous paragraph), were inserted into the *EDT-Trades* simulation. The 82 V from the measured potential from the tether to the orbiter was simulated by inserting that value as the HVPS value. The orbiter potential result was confirmed to be -596 V, as was the collected electron current, which was exactly 0.97 A. Since there was no active electron emission device before the tether break, all the current was emitted from passive ion collection on the orbiter. The total surface area in the flowing plasma was such that at -596 V all 0.97 A could be emitted.

For the case after the tether break, the same KVL equation as before was used (Eq. 3-28). This time there was no tether to orbiter potential since the connection was severed. The cathode potential was simply a sheath from the end of the tether to the plasma. Using the solved α and β from the case before the tether break, and the known tether current after the tether break, 1.1 A, the satellite potential was calculated to be 1560.8 V. Every value of the KVL equation is now known except for the potential of the cathode, which was solved to be -122.6 V.

To verify the condition after the break, a similar process was conducted. All the values of the Table 3-5, except for the orbiter potential, were inserted, including the

newly calculated α value. The result at the end of the tether was exactly a current of 1.1 A and a cathode potential of -122.6 V, similar to what was predicted.

An assumption made by Gilchrist et al. was that the exposed surface area was negligible and the current exchange from that section was determined by the sheath or plume generated by the released air that was trapped inside the insulation and the ablating insulation [133]. The neutral gas would create a 'poor man's hollow cathode' by having the emitted electrons ionize part of the neutral cloud as they escaped.

It is clear that ion collection due to the exposed wire is not the current collection mechanism, since there was relatively no exposed conductive surface. In addition, other effects of electron emission are ruled out (thermionic emission, secondary emission due to high potential ions, and field emission) because the currents observed were many orders of magnitude greater than what could be produced by these other effects.

The calculations made for the $V_{cathode}$ and V_{sat} were slightly different than previous calculations made by Gilchrist et al. The previous calculations were $V_o = 100$ V and $V_{sat} = 1585$ V. This was likely due to the fact that there was a small discrepancy in the α value. In addition, the n_e used in the initial calculations was not defined exactly.

The β value was assumed to be similar to the most recent recorded value. Gilchrist et al. predicts β = 0.55, in order for the α to be between the range of 2.2 to 2.9, as specified by Thompson et al. Using the assumption of 0.55 for β, α results in a value of 2.482. The tolerance the Thompson paper gives for β is 0.52 ± 0.03.

3.5.2   Thermionic Cathodes on the TSS-1R Validation

A TC on the TSS-1R mission was used to emit the electron current that flowed through the tether [31]. This TC was the same one chosen for the simulations of this thesis, and described in section 2.4.2. The TC emitter was physically set up in a grounded gate configuration as seen in Figure 3-8b. The TSS-1R mission ran an I-V sweep varying the temperature limited current across the TC, which is shown in Figure 3-10. Beginning at exactly 57 / 1:19.23 GMT, the values of the system, labeled in Table 3-6, were obtained. This resulted in the emission current being temperature limited up until a certain point, where the emf potential of the system could not drive any more

current out of the emitters even though the thermionic emission process could allow more. The system became space charge limited at that point.
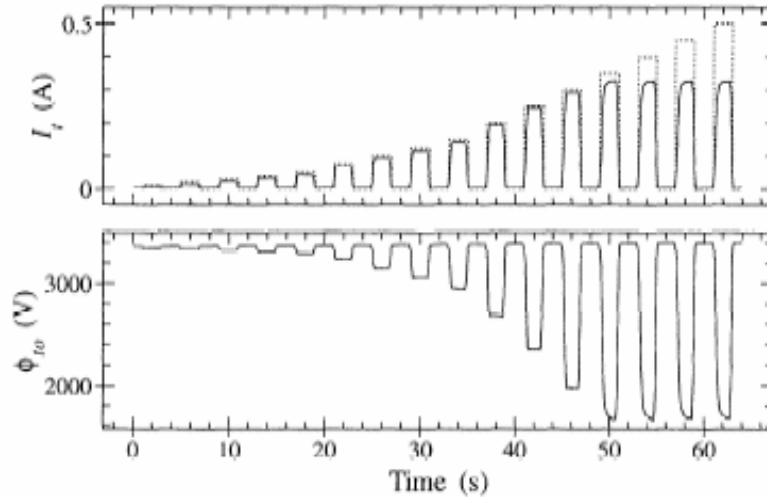
Figure 3-10: Commanded (dotted line) and measured (solid line) tether currents (upper panel); and measured potentials applied to the EGA during a typical I-V sweep (lower panel).

Mission Time	2006, 57 / 1:18:19
Electron Density	2.7×10^{11} m^{-3}
Tether Deployed	18700 m [**]
Magnetic Field	3.255×10^{-5} T
Orbit Velocity	5586 m/s [**]
Resistance	0.094 Ω/m
alpha	2.7
beta	0.54
Electron Temperature	0.142 eV
EMF Potential	3400 V [**]

Table 3-6: System values used to calculate and verify the thermionic cathode used in the TSS-1R system and then in the simulation.

All of the values were given by Thompson et al. [Thompson], except for those labeled with [**], in which case Williams defined them [24, 117]. The orbital velocity is calculated using the simplified $V_{emf} = v_{orb} \times B \cdot dL$ equation. The orbital velocity is calculated to make the emf potential equal the value given (3400 V). It can be seen in Figure 3-11 that the results of the simulation are nearly identical to that of the TSS-1R mission. Table 3-7 shows all of the system potentials at each point in time in the I-V sweep, according to Eq. 3-28.
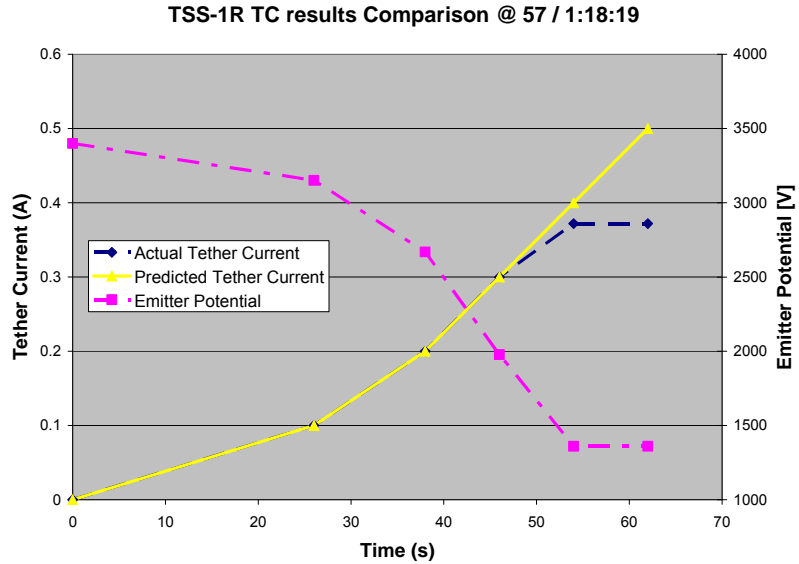
Figure 3-11: Validation between the collected currents from the tether of the TSS-1R mission using the EGA and the simulation code.

MET [s]	0	26	38	46	54	62
Predicted Current [A]	0	0.1	0.2	0.3	0.4	0.5
Actual Current [A]	0	0.1	0.2	0.3	0.372	0.372
V_{sat} [V]	0	74	380	897	1389	1389
V_{to} [V]	3400	3151	2669	1978	1360	1360
V_{emf} [V]	3400	3400	3400	3400	3400	3400
V_{tether} [V]	0	175	350	525	651	651
$V_{cathode}$ [V]	0	0	0	0	0	0

Table 3-7: Simulated system potential values and emission currents corresponding to the EGA I-V sweep on the TSS-1R mission.

The particular case simulated has a mission value of 0.328 A, as opposed to the 0.372 A calculated. This discrepancy can be due the fact that the tether length and emf seen in Table 3-6 were estimated from a plot, rather than an exact number from a data sheet. In addition, the magnetic field that was given in the Thompson et al. paper [31] was different to the value given by the IGRF model, although the number given by Thompson et al. was used. Finally, small changes in the alpha and beta calculated could have altered the results, as these calculated values have a range of potential values associated with them. The α and β used were those of the initial time the I-V sweep began. These could have changed slightly throughout the sweep. Also, Thompson et al. states many uncertainties such as 10 V of the orbiter potential, 100 Ω of the tether resistance, $\pm(10 + 100 \cdot I_t)$ V uncertainty for the satellite potential, and 20% uncertainty in

both the electron density and the electron temperature measurements made by the Langmuir probe. These uncertainties are large enough to explain the current collection discrepancy.

CHAPTER 4

MEASUREMENT OF ELECTRON COLLECTION TO POROUS TAPE PROBES IN A HIGH-SPEED FLOWING PLASMA

This chapter presents the analysis of measurements of electron current collection to porous tape probes in a mesosonic flowing plasma, and a comparison to similar measurements with round cylinder, solid, and slotted tape samples previously reported[27] [134]. In these experiments, a Hall thruster was used to create a high-speed (~8 km/s) flowing unmagnetized plasma in a large 6 m × 9 m vacuum chamber. Experimental results of solid tape samples with widths spanning from 7.2 to 20.4 Debye lengths, and slotted tapes with center to-center line spacings spanning from 2.1 to 6.0 Debye lengths (gap widths from 1.3 to 3.6), were compared to measurements of holed tapes with hole diameters spanning from 1.4 to 9.4 Debye lengths. Several conclusions can be drawn from the analysis of the results in the regime tested: 1) Beyond a threshold bias probably close to the beam energy, holed tapes collect more current when oriented transverse (perpendicular) to the flow, as do solid and slotted tapes; 2) Holed tapes are more efficient electron collectors than both solid and slotted tapes in terms of collected electron current per unit area when oriented perpendicular to plasma flow. However, when oriented parallel to plasma flow, slotted tapes are more efficient than holed or solid tapes. And 3) When the tapes were oriented parallel to the flow, the electron current collected on holed tapes per unit area decreases with increasing hole size until a minimum is attained, beyond which it starts increasing again. The opposite effect occurred when the

---

[27] 'Porous' tapes will be referred to as 'holed' tapes for the remainder of this chapter.

holed probes were oriented transverse to the flow, and a maximum efficiency was observed. We conclude that the holed tethers, which have better structural stability, have an electron collection efficiency similar to that of slotted tethers.

An elaborate description for this particular experiment of the background, design and assembly, and vacuum chamber setup was originally written by Choiniere et al. [136]. For the purposes of being complete and to minimize using the same reference repeatedly, many paragraphs in these respective sections are reworded, yet still similar to the original work.

4.1 Background

The use of a bare section of a space-borne electrodynamic tether as an electron-collection device has been suggested [1] to be a propitious alternative to end-body electron collectors for certain applications, assuming that electrons are collected in a quasi-orbital-motion-limited regime [34]. For a given bias potential, plasma probe theory predicts that the collected electron current per unit area (not total current) is maximized in the orbital-motion-limited regime, which is only valid with adequately thin wires (explained in Section 2.1.1) [66].

The bare tether concept was to be first tested during NASA's Propulsive Small Expendable Deployer System (ProSEDS) mission [135]. Although the mission was canceled [23], the concept is still being considered for future missions. The ProSEDS bare tether design used a small, closely packed cross-section of smaller wires. In future designs, addressing concerns of survivability to collisions with micro-meteoroids and space debris will require the use of distributed or sparse tether cross-section geometries. These geometries could span tens of Debye lengths, depending on plasma density and temperature [35].

Collected current per unit area is maximized in the orbital-motion-limited regime of single thin cylinders [34, 66]. This experiment sought to further understand how distributed or sparse geometries perform in terms of electron current collection, as compared to thin cylinders, all in a high-speed plasma. In addition, the effect of the high-speed flow on the electron collection to these alternative geometries, as well as to thin

cylinders, has yet to be fully understood [136] [137]. Ultimately, designers will need to know how to configure a tether for adequate lifetime, minimum mass, and maximized current collection, for example. Work from this chapter is intended to contribute toward this goal.

As in Choinière et al. [136], the orbital-motion limit (OML) will be used as a baseline when comparing the current collection results for various sample geometries and sizes. Recall that the theoretical expression for the OML electron current collected by a thin cylinder is [34, 138]: $I = A_p n_e e \sqrt{\dfrac{eT_e}{2\pi m_e}} \dfrac{2}{\sqrt{\pi}} \sqrt{1 + \dfrac{V_0 - V_p}{T_e}}$. The electron density, mass, and temperature are defined as n_e, m_e, and T_e. In addition, the potential with respect to the plasma is labeled V_0-V_p, and the probe surface area A_p. This normalization allows one to directly compare our experimental results, which involve various tether geometries in a flowing plasma, against OML theory.

Previous experimental data [137, 139] indicated that a tape width of 6.9 Debye lengths would collect about 85%–90% of the electron current collected by an equal-area round cylinder, and that the perpendicular tape orientation, with respect to plasma flow, would consistently outperform the parallel orientation in terms of collected current by varying percentages up to ~9%.

In this chapter, previously unreported data from a serious of plasma chamber experiments [136] are analyzed and reported pertaining to the "holed tape" geometry with various hole sizes and spacings. The issue of end effects was addressed by adding guards to the tether samples, which are described in Table 4-1, and was discussed in Choiniere et al. [140].
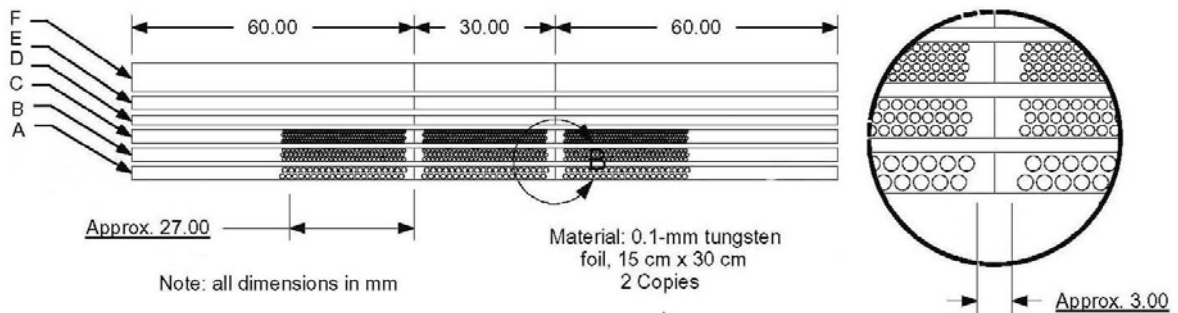
Sample	Description	Width	Hole Description

90

		(mm)	
A	50% porosity, largest holes, offset matrix	2.89	Holes: Ø1.10 mm, spacing: 1.33 mm staggered
B	50% porosity, medium holes, offset matrix	2.89	Holes: Ø0.74 mm, spacing: 0.91 mm staggered
C	50% porosity, smallest holes, offset matrix	2.89	Holes: Ø0.56 mm, spacing: 0.69 mm staggered
E	Solid Tape	2.89	N/A
F	Slotted Tape	2.89	N/A

Table 4-1: Drawing a Description of the Guarded Tether Samples Shown Before Assembly, the Lengths Indicated in the Drawing are in mm (30 mm Probe, 60 mm Guards).

4.2 Design and Assembly of Guarded Tape Tether Samples

The tether samples tested here, in addition to a thin cylindrical reference sample, included a solid tape sample, a slotted tape sample, and a holed tape sample with 3 separate hole diameters and spacings. The slotted sample and all three holed tape samples had approximately 50% porosity. Each of these samples had a length of about 3 cm and was mounted with two 6 cm guards as seen in Figure 4-1. Details of the guard assemblies are given in [136]. Each tape sample was tested in two different orientations: parallel and perpendicular to the plasma flow. All of the samples, including the reference sample, were tested at three different distances from the hall thruster plasma source. Tungsten metal was used for all samples to ensure that they would endure the expected high temperatures that are caused by the collection of high-energy electrons at the samples' surfaces.
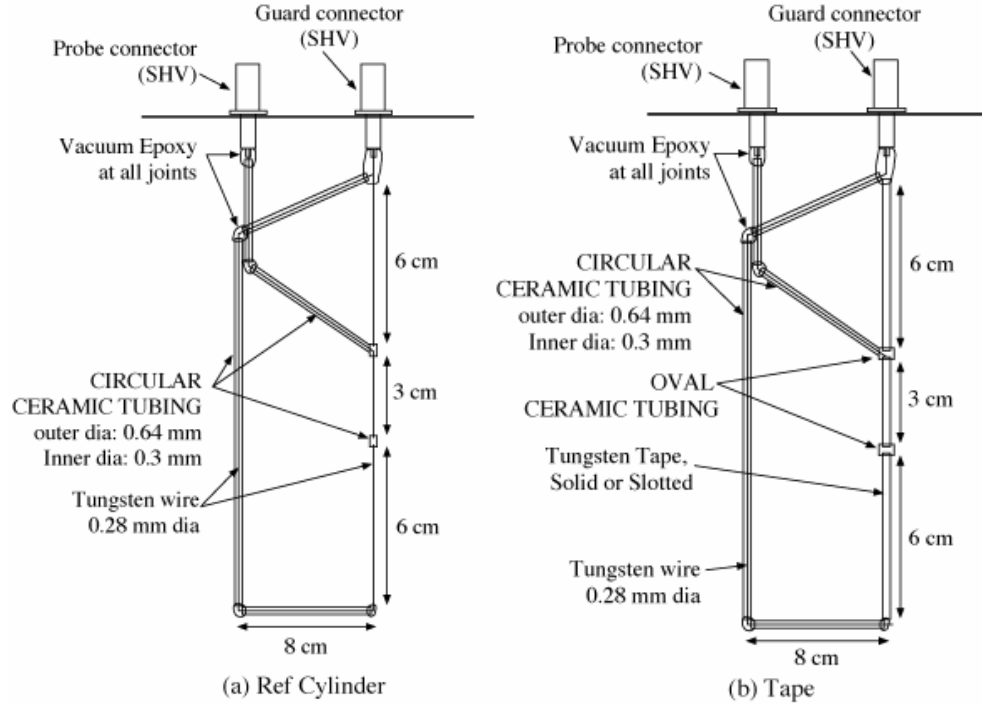
Figure 4-1: Assemblies of the (a) reference cylinder and (b) tape guarded tether samples.

The reference cylinder diameter and end widths of the three solid tape samples are given in Table 4-2 in terms of the Langmuir- probe-determined local Debye length at the three chamber test positions. In addition, the holed probe dimensions are given in Table 4-3. The reference cylinder's diameter, spanning from 0.7 to 2.0 Debye lengths depending on position, was sufficiently thin to collect electron current under conditions close to that of the OML regime in a stationary plasma. The solid tape widths spanned from 4.9 to 41.9 Debye lengths, extending the range of previously tested widths, which spanned from 6 to 19 Debye lengths [137].

The three holed samples were designed with the same overall widths. This strategy allowed a direction comparison of hole size for all three equivalent-porosity holed samples. In addition, the width of the holed tapes is equal to the width of the solid and slotted tapes, and their porosity is approximately the same as that of the slotted tape.

The primary goal for this experiment was to apply the results to very long electrodynamic tethers. As a result, a technique was sought to mitigate any probe end-effects. Guards were included in all of our tether sample assemblies. Each guard is essentially identical to the center section and is biased at the same potential. The effect

of the guards is to extend the cylindrical sheath to the full length of the sample. This extension is five times the length of the center probe on which current is measured.

The guarded tether sample schematics of the full assemblies are shown in Figure 4-1. Due to the very small thickness of the tungsten samples under consideration here (0.1 mm thick), it was not possible to feed the center probe using a wire that would have been inserted in one of the guards, as is typically done on some larger tri-axial Langmuir probes. Instead, the center feed wire runs through an oblique ceramic tube and connects to the center probe at one of its ends. On all samples, the feed wires to both the guards and the probe were soldered to the center conductor of a bulk-head SHV (safe high voltage) connector. The connector-sample interfaces were then covered with vacuum epoxy. The aluminum support structure for the SHV connectors provided a localized ground.

Position	Ref. Cyl.	Solid Tape	Slotted Tape
75 cm	2.0	20.4	6.0
160 cm	1.1	11.0	3.2
300 cm	0.7	7.2	2.1

Table 4-2: Diameter of the Reference Cylinder, Width of the Solid Tape, and Center-To-Center Line Spacing of the Slotted Tape, Expressed in Terms of the Local Debye Length.

Position	Hole size (diameter)			Hole Spacing (center to center)		
	Small	Medium	Large	Small	Medium	Large
75 cm	4.0	5.2	7.8	4.9	6.4	9.4
160 cm	2.1	2.8	4.2	2.6	3.5	5.1
300 cm	1.4	1.9	2.8	1.7	2.3	3.3

Table 4-3: Size and Center-to-Center Spacing of Holed Tapes at all Three Locations, Expressed in Terms of Local Debye Length.

The probe and guards also had to be mechanically attached but electrically insulated from each other. Ceramic joints were used to this effect, an example of which is shown in Figure 4-2, and were attached to the tungsten probes and guards using very small stainless-steel machine screws that were then carefully sanded down into a flat surface to minimize discontinuity effects. The portion of the surface area of the ceramic joint covering the tungsten probe and not covered by the screw head was accounted for in the calculation of the total area of each probe.
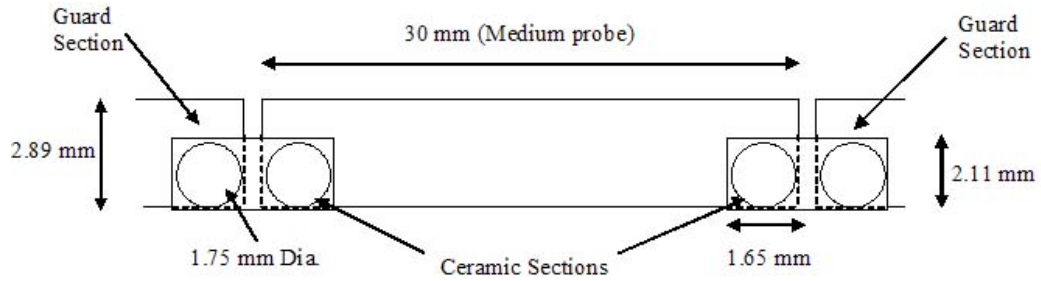
Figure 4-2: Example of the ceramic attachment used on all solid and slotted tape samples to attach the probe and guards while preserving electrical isolation. Dimensions shown here correspond to the medium slotted probe (sample B in Table I).

Figure 4-3 shows pictures of three of our tether sample assemblies: the reference cylinder, the wide solid tape, and the wide holed tape. The solid and holed samples are shown with both SHV connectors installed, while the reference cylinder sample is shown prior to the installation of the connectors.
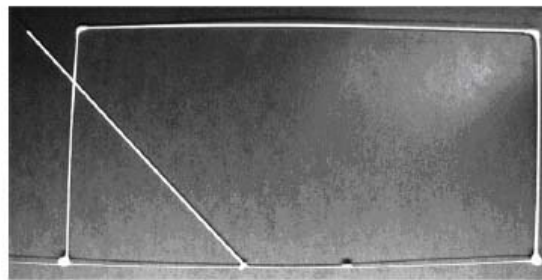
Figure 4-3: Pictures of three typical tether samples: (a) 0.28 mm diameter reference cylinder; (b) 2.89 mm-wide solid tape; (c) 2.89 mm-wide holed tape.

4.3   Vacuum Chamber Setup and Plasma Source Characteristics

The vacuum chamber tests were performed using the Large Vacuum Test Facility (LVTF) from the Plasmadynamics and Electric Propulsion Laboratory (PEPL) at the University of Michigan, Ann Arbor. This chamber is a 9 m by 6 m cylindrical stainless-steel-clad tank. For this experiment, four of the seven available cryopumps were used to reach a high vacuum with a maximum pressure of 9.1 μtorr.

Figure 4-4 shows a diagram of the experimental setup within the LVTF. Two positioning tables were used to change the separation distance between the thruster and sample plane and to locate the sample under test directly along the thruster's centerline. The Hall thruster was mounted on a table (the x-y table) that could move axially over a 1.0 m range and over a sufficient radial range to cover all samples. The thruster emitted its high-speed plasma in the +y-direction. The samples were mounted on an aluminum frame that was connected to the other table (the *axial* table) that could span a 1.5 m axial range. Combined table movement allowed thruster–sample separation distance to change from 0.75 to 3 m; measurements were taken at 0.75 m, 1.60 m, and 3.00 m separation distance from the thruster. Changing separation distance was the primary mechanism for changing the plasma density seen at the sample plane.
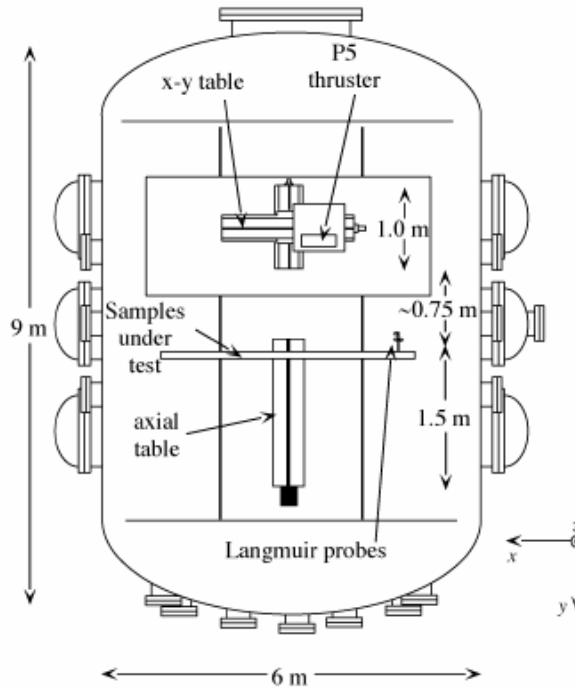
Figure 4-4: Experimental setup in the LVTF at the PEPL.

Figure 4-5 shows an overall picture of the aluminum structure supporting our tether samples and Langmuir probes, together with the Hall thruster used as a plasma source. The latter is a 5 kW-class Hall thruster named "P5," which was developed by the PEPL and the Air Force Research Laboratory; more detail is given by Haas et al. [141]. For these tests, the thruster was set at off-nominal conditions in order to lower the plasma velocity and density seen along the thruster's axial direction. Its operating conditions are given in Table 4-4. The primary changes in those settings from the ones used in the two data sets presented by Gilchrist et al. [137] are the discharge current, which was raised from 4–5.3 A to 12.5 A, and the anode flow rate, which had to be raised from 45–60 sccm to 112.1 sccm to support the increased discharge current.

Support Structure with Sample
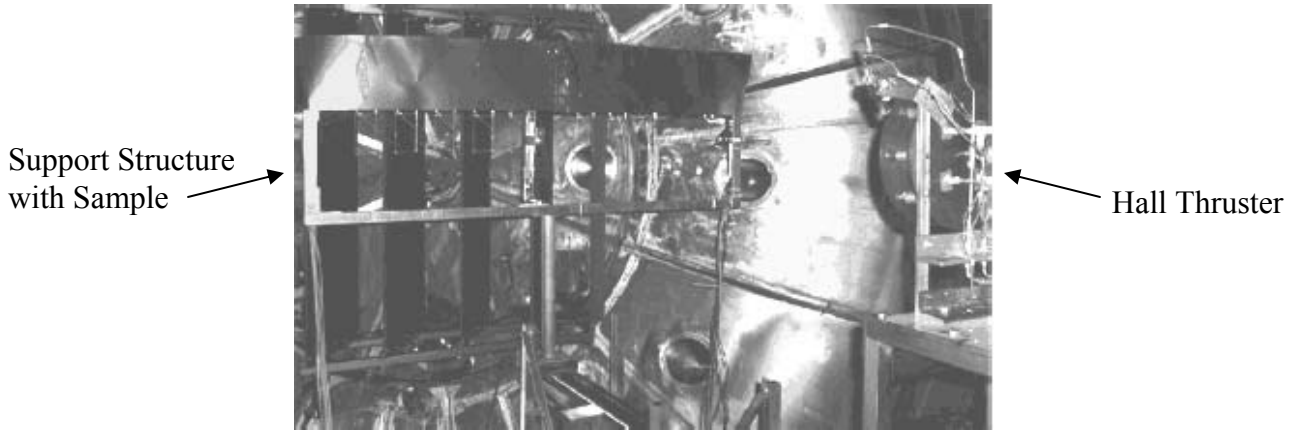
Hall Thruster

Figure 4-5: (left) Picture of the guarded sample support structure and (right) P5 Hall thruster used as a high-speed plasma source.

Maximum Chamber Pressure	9.1μtorr
Discharge Voltage, V_d	100 V
Discharge Current, I_d	12.5 A
Inner Magnet Current, I_{im}	3.0 A
Outer Magnet Current, I_{om}	2.0 A
Cathode Voltage, V_c	[-17, -18] V
Heater Voltage, V_{htr}	8.3 V
Anode Flow rate, $\dot{m}_a$	112.1 sccm
Cathode Flow rate, $\dot{m}_c$	6.0 sccm

Table 4-4: Operating Parameters of the Plasma Source (P5 Hall Thruster).

The emitted beam energy assessment was performed using two different techniques. Laser-induced fluorescence (LIF) measurements using the off-axis multiplex technique have provided an estimate of 43 eV [142], whereas Langmuir probe (LP) measurements in the ion saturation regime have yielded a value of 25 eV. More detail regarding the off-axis multiplex LIF measurement technique is given by Gilchrist et al. [137] and Williams et al. [142]. It should be noted that the LP value of 25 eV is close to, if not within, the bounds of the error in the LIF-determined beam energy value, which is about 38%, given that the relative error in the velocity determined using the multiplex technique was about 19%. This relative error[28] is obtained from the ratio of the absolute error in velocity, which was about 1.5 km/s [143], to the value of the measured velocity, 7.95 km/s. Here we note that this particularly large relative error is due to the operation of the P5 Hall thruster at off-nominal conditions, with an unusually low discharge voltage. At higher beam velocities, the absolute error of 1.5 km/s results in a much lower

---

[28] Note: $(m_i (7950 \text{ m/s})^2 / 2e) \approx 43$ eV with $m_i = 2.18 \times 10^{-25}$ kg for Xe^+ .

relative error. Also, recent improvements of the LIF measurement technique, using an "axial injection" procedure [143], have allowed significant improvements in the accuracy of the beam velocity measurements and will be used in future experiments.

Both measurements given by the LIF and LP were measured 75 cm away from the thruster on its centerline axis. According to the LIF measurement, the ions have an offset Maxwellian distribution, with a directed energy as given above, and a temperature of about 0.4 eV at 75 cm. The electron temperature, as determined by the LP measurements, varied as a function of position between 1.47 eV and 1.80 eV (see Table 4-5).

Figure 4-6 details a schematic of the current–voltage measurement system. A Universal Voltronics BRC 20,000 high voltage (HV) power supply is connected to the tether samples through a high-voltage relay box inside the chamber. The HV power supply was controlled via RS-232 by the computer controller running a custom virtual instrument (VI) under LabVIEW. The computer commanded the HV power supply to a specified voltage and then quickly back to zero (within 50 to 100 ms), followed by several seconds of cool-down to minimize sample heating. Current measurement on the sample probes was achieved using an American Aerospace Controls 835-2-10 current sensor; increased current sensitivity was obtained by looping the HV supply line ten times through the sensor. The current to the sample guards was measured separately using a F.W. Bell ma-2000 current sensor. An HP 34970 data acquisition unit was used to measure the voltage signals generated by both current sensors. The data were recorded as triplets containing the applied voltage, the probe current, and the guard current.
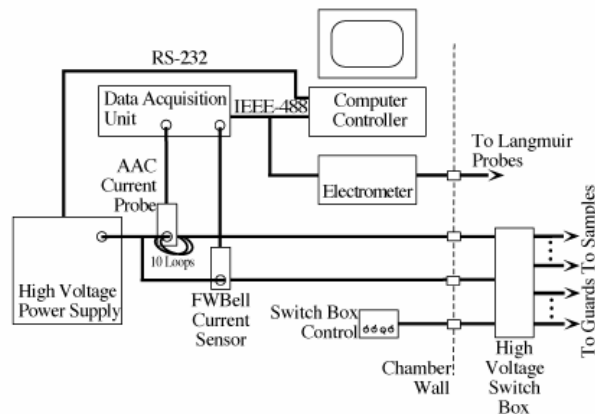
Figure 4-6: Schematic of the computer-controlled high-voltage test equipment setup.

Plasma density, temperature, flow speed, and the fraction of beam ions to background ions were determined using a 4 cm long, vertically oriented (i.e., perpendicular to the flow) LP with a diameter of 0.28 mm (the same diameter as our reference cylinder sample). All LP sweeps were performed using a Keithley 2410 source electrometer controlled via a custom LabVIEW script running on a personal computer.

The plasma parameters, shown in Table 4-5, were extracted from the ion saturation (OML regime) and electron retardation regions of the *I–V* characteristics using a LP oriented transverse to the direction of the flow. In the OML regime, there are several advantages to selecting the ion saturation as opposed to the electron saturation region for parameter extraction. An ion-attracting cylindrical probe oriented transverse to the flow in a high-speed plasma is known to be virtually free of end effects [9]. In addition, a simple but fairly accurate ion collection model is available that accounts for the velocity of the flow in the ion saturation regime [144]. By contrast, at the time of this experiment there were no accurate models for the electron collection to an electron-attracting probe that could account for the plasma flow. Recent work by Choiniere, however has resulted in a simulation tool that can model this affect called KiPS [68]. In the mesosonic regime, where the plasma flow is much faster than the thermal ion velocity, yet much slower than the electron thermal velocity, important sheath asymmetries and elongations exist in the electron-attracting mode that get stronger with the applied bias, which makes the prediction of collected current a complex problem. One of the aims of the experimental work presented here is, in fact, to improve the understanding of the macroscopic effect of plasma flow on electron collection. An accurate model of electron collection in flowing plasmas is also currently being developed [54, 66, 140].

Position	n_e (m^{-3})	T_e (eV)	λ_{De} (mm)	μ_b
75 cm	4.95×10^{15}	1.8	0.14	95%
160 cm	1.37×10^{15}	1.72	0.26	53%
300 cm	0.51×10^{15}	1.47	0.40	32%

Table 4-5: Variation of the measured plasma parameters as a function of distance from the Hall thruster measurements were performed using the ion saturation and electron retardation data from a transverse LP. The beam energy value determined using the LP is 25 eV. The "beam fraction", μ_b,, indicates the fraction of all ions that are believed to be beam (high-speed) ions. Density,

4.4　　　　Experimental Results and Analysis

Following a discussion of the error analysis, we describe and analyze results pertaining to the reference cylinder, the holed tapes, and then perform a comparison of the results obtained for solid, slotted, and holed tapes. All results are presented in the normalized form I_n vs. ϕ_o, where $I_n \equiv (I/I_{the})$ and $\phi_o \equiv ((V_0 - V_p)T_e)$, consistent with the notation employed by Choinière et al.[136]. The values used for the electron temperature T_e and the electron thermal current I_{the} are based on the Langmuir probe-measured electron temperature and plasma density. This normalization provides a means of evaluating the performance of various probes by comparing them to OML theory, as well as by comparing their current characteristics in terms of collected current per unit area. Note that the extent of the axis of the normalized voltage ϕ_o varies from one test position to another due to differences in the electron temperatures (used in the normalization) measured at the three positions, and from variations in the applied voltage range.

4.4.1　　　　Error Analysis

Before discussing experimental results, a brief error estimate is provided. Experimental errors resulted primarily from the repeatability of the experiment. Noise and sporadic phenomena such as arcing and current limiting effects were associated with many runs, which is why numerous runs were taken per probe. Additional errors associated with specified device tolerances and determination of probe area were also taken into consideration.

Multiple runs were conducted for which results differed slightly. The variations among these results were used to determine a measure of the "repeatability" error in measurements. The device tolerances and area calculation errors were added to this repeatability error.

Overall, the total experimental errors remained under ±1% in most cases. The error increased up to ±10% in some cases when ϕ_o was less than 15, but then settled to

slightly less than ±1%. Particular cases such as the perpendicular and parallel medium holed sample at 160 cm had up to ±3%. These errors are indicative of a sample that had runs that arced frequently, or did not have any runs with repeatable data.

4.4.2   Reference Cylinder – Analysis of Results

Figure 4-7 includes the normalized results for the reference cylinder at the three test distances from the plasma source. As pointed out in Choinière et al. [136], the reference cylinder at 75 cm is seen to collect much more current than that predicted by OML theory, by as much as 40% at a bias of 100 T_e. This enhancement is seen to decrease as we move away from the thruster to 160 cm and 300 cm. In fact, there appears to be no enhancement at 300 cm. This is argued to be due to the fact that the fraction of beam versus thermal ions was also estimated to fall off with distance and to be mostly thermal by 300 cm (see Table 4-5) [136].

Through simulations by Choiniere [68], current collection by a Langmuir probe in a high-speed flowing plasma has been accurately described. It has been shown that in a flowing plasma, the wake side of a collecting cylinder possesses a deficiency of electrons compared to that of the ambient density, while there is a surplus on the ram side. As a result, the sum of the electron current collected by the ram side and the wake side results in enhanced collection over that of OML collection in a non-flowing plasma [66, 140, 145].

4.4.3   Holed Tapes – Observations and Analysis of Results

Figure 4-7 presents results for all three holed tape samples at all three distances from the plasma source (75 cm, 160 cm, and 300 cm). The overall tape width, shown in terms of the Debye length, spans from 7.2 to 20.4 electron Debye lengths, while the radius of the holes on each tape ranges from 1.4 to 7.8, as shown in Table 4-2 and Table 4-3. It should be emphasized that the overall widths of the holed tapes are the same as the medium solid tape width (2.89 mm) reported in[136]. We note that the quantitative comparisons among samples made in the remainder of this chapter are all made at the

highest recorded normalized potential points of the experiment. Three major observations are noted from these results.

Normalized Current Characteristics of Holed Samples at 75 cm

(a)

Normalized Current Characteristics of Holed Samples at 160 cm

(b)

Normalized Current Characteristics of Holed Samples at 300 cm

Legend:
- Reference Cylinder, dia=0.28mm=0.7λde
- Paral. Holed Tape, hole width=0.56mm=1.4λde
- Perp. Holed Tape, hole width=0.56mm=1.4λde
- Paral. Holed Tape, hole width=0.74mm=1.9λde
- Perp. Holed Tape, hole width=0.74mm=1.9λde
- Paral. Holed Tape, hole width=1.1mm=2.8λde
- Perp. Holed Tape, hole width=1.1mm=2.8λde
- Theory: Retardation and OML
- Electron Thermal Current

$n_e = 5.1 \times 10^{14}$ m^{-3}, $T_e = 1.5$ eV, $\mu_b \approx 32$ %

y-axis: $I / (A_p\, J_{the})$

x-axis: $\phi_0 = (V_0 - V_p) / T_e$

(c)

Figure 4-7: Plot the average run along with its associated tolerance for the (a) 75 cm, (b) 160 cm, and (c) 300 cm cases. The tolerances include device error as well as average run error.

1) At all three distances, all the holed tape samples collected more current when oriented perpendicular (transverse) rather than parallel to the flow. According to Figure 4-7, the most efficient perpendicular and parallel configuration per unit area are the medium hole and large holed configuration. The ratio of the most efficient perpendicular case to the best parallel case is 18.5%, 20.0% and 6.5% for the 75 cm, 160 cm and 300 cm distances, respectively.

2) For the perpendicular orientation at 75 cm, the medium- and small- holed tapes collect the most current per unit area. At 160 cm and 300 cm, however, where the density and high-speed fraction are lower, the medium-holed sample collected the most current per unit area. Collection to the most efficient hole size tape compared with the least efficient (always the large-holed case) is by 7.3%, 14.7% and 7.7% for the 75 cm, 160 cm and 300 cm, respectively. This may suggest the existence of an optimum hole size which maximizes current collection.

103

3)   In the parallel orientation, an opposite observation can be made, i.e. a hole size that minimizes current collection. At 75 cm, the parallel medium-holed tape collects the least current on a per-area basis, followed by the small- and large-holed parallel tapes. At distances further from the source, the medium-holed tape became increasingly less efficient as compared to the most efficient large-holed sample, by 3.7%, 6.6% and 10.7% at 75 cm, 160 cm and 300 cm, respectively. This is another indication of the existence of a hole size that minimizes current collection.

The observations concerning the comparative magnitudes of the collection orientations made above are similar to previous simulations and experimental results for slotted tapes [66]. Similar to the reference probe, it has been argued that this is likely due to the plasma sheath elongation on the wake side of flow which also results in a region of reduced density to that of the ambient [54, 140]. In addition, as described by Choiniere, the parallel orientation for slotted probes has much of the tape being shadowed, implying that many of the possible electron collection trajectories are empty because they are being blocked by the neighboring structure. The perpendicularly oriented samples, on the other hand, are not in the wake region. It can be inferred that this is the primary cause for the enhanced perpendicular oriented collection over that of parallel oriented samples [68]. Holed tethers have more complex sheath structures due to the geometry differences; however, both cases are 50% porous and the slotted spacing is approximately equal to the diameter of the small holes on the holed samples. Since the holed tape is structurally comparable, it is assumed that the same concepts of shadowing and wake affect can be applied for the holed case.

As explained by Gilchrist et al., a "knee" appears in the current characteristics obtained with the parallel-oriented tapes beyond which the data points follow a $V^{0.5}$ slope [137]. This effect is very prominent in Figure 4-7a around a net bias $(V_0-V_p) \cong 30T_e$, which is on the order of the ion beam energy [136].

Also, the existence of a minimum current collection point as a function of hole diameter in the parallel configuration is similar to previous experimental effects for slotted geometries [136]. The maximum collection point as a function of hole diameter

in the perpendicular orientation, however, appears to be unique to the holed tape cases. Both the maximum and minimum collection trends are discussed below.

4.4.3.1 Parallel Oriented Minimum Case

This phenomenon is likely due to probe shadowing effects, wake effects, and plasma focusing effects as was described for two independent collecting cylinders and quantatively descrived in Figure 2-6b. For example, it has been shown that in a non-flowing plasma, there exists a minimum current collection point between two parallel conducting wires as the gap between them increases [66, 145].

Simulations have been conducted for the parallel oriented slotted configuration in a flowing plasma, which details the OML current collection as the distance between the two cylinders increase [68]. It can be seen in Figure 2-6b that the shadowing effect is observed for the wires of this flowing case because some of each others' thermal collection paths are being blocked. On the wire in the wake of the first, a focusing effect can be observed. The ram side wire deflects the incoming plasma toward the wake side wire, thereby enhancing its current collection. The overall result implies that there exist a couple of minimum points as the gap spacing increases. Again, since the holed cases are physically similar to the slotted cases, the same overall trends are likely to occur.

4.4.3.2 Perpendicular Oriented Maximum Case

Possible causes for the perpendicular case current collection maximum at a particular hole size are also likely a combination of shadowing affects as well as focusing affects, as suggested in Figure 2-6c. As shown through these simulations, the wake side of the perpendicularly oriented slotted tape in a flowing plasma also behaves similarly to the shadowing encountered in the non-flowing case [68]. In addition, the wake side of this orientation is enhanced due to focusing. The incoming plasma is being deflected by the holed tape into a trajectory that results in the collection on the wake side. This collection enhancement exceeds that of the wake side collection as seen in Figure 2-6c. The overall result produces a few maximum collection points due to presently unexplained oscillations in the wake collection [68].

As the porosity of the collecting tape becomes much larger than 50%, the difficulty in maintaining a uniform pattern and a constant porosity becomes increasingly complicated. As a result, the distances between the holes will begin to impact the results, since they will not be uniform in all directions. Predicting the complex sheath interactions within such geometry will require additional experimentation and simulation.

In order to further validate the predicted effects of the perpendicular and parallel orientations, experiments must be conducted that maintain the porosity of the tether at other hole sizes. For example, the small and large slotted samples were 28% and 75% porous, respectively. A possible test would be to design a uniform holed pattern that could maintain this porosity for various hole sizes, as this experiment has done.

4.4.4   Comparison of the Holed, Slotted, and Solid Tapes

Figure 4-8, Figure 4-9, and Figure 4-10 display the same sets of results shown in Figure 4-7, but with the holed, solid, and slotted tapes plotted on common graphs to facilitate their comparison. An important note is that the solid and slotted tape samples compared were the same width (2.89 mm) as the holed tape samples. The following is observed:

1)   Despite the holed samples being more efficient per unit area, the absolute amount of current collected by the solid tape samples was higher than that collected by the holed tape samples. This can be seen by comparing the holed and slotted tapes in Figure 4-11. This trend is expected, since the total surface area of the solid tape was about twice that of holed and slotted tapes.

2)   The slotted and holed tape samples were more efficient current collectors on a per-area basis than their solid counterparts in both perpendicular and parallel configurations, as seen in the figures. In addition, for all three hole sizes, the holed samples were more efficient than the slotted samples in the perpendicular orientation. However, at all three distances, the slotted samples were more efficient than the holed counterparts in the parallel orientations. This might suggest that the sheath interactions,

due to flow-induced sheath elongation, are greater with the holed probes at parallel configurations and for slotted probes at perpendicular configurations. The relationships between the slotted, solid, and holed tape probes, along with the associated error for each probe, are detailed in Table 4-6. A complete of these sheath interations is beyond the scope of this thesis.

(a)

(b)
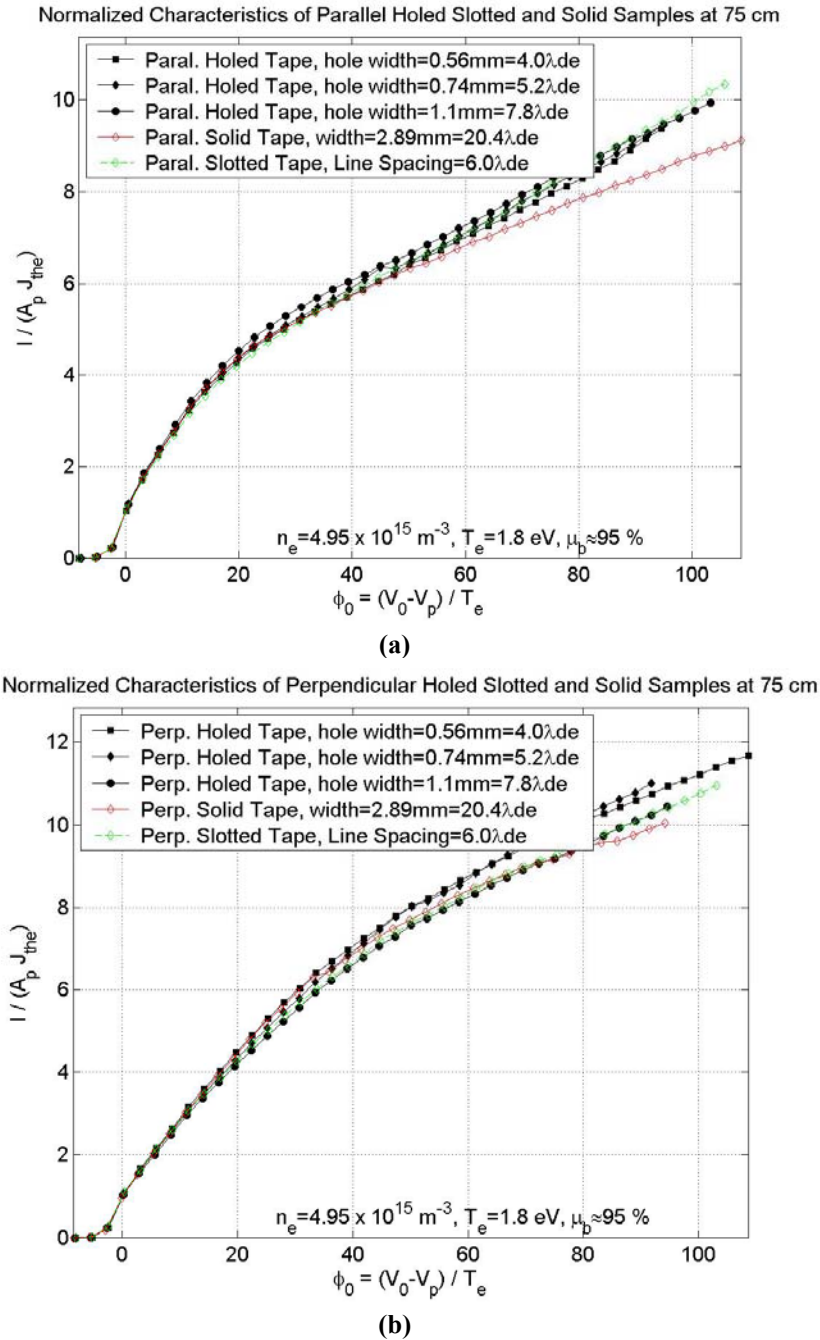
Figure 4-8: Comparison of the *I–V* characteristics of holed, solid, and slotted tapes at 75 cm. Upper and lower graphs are applicable to parallel and perpendicular tape orientations, respectively.

107

Figure 4-9: Comparison of the *I–V* characteristics of holed, solid, and slotted tapes at 160 cm. Upper and lower graphs are applicable to parallel and perpendicular tape orientations, respectively.

108

Normalized Characteristics of Parallel Holed Slotted and Solid Samples at 300 cm

(a)
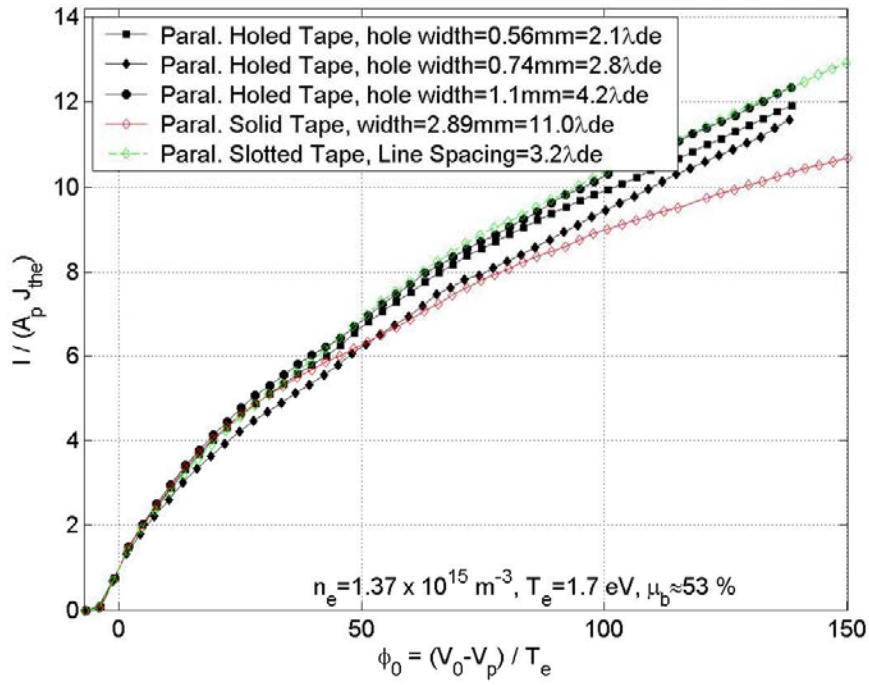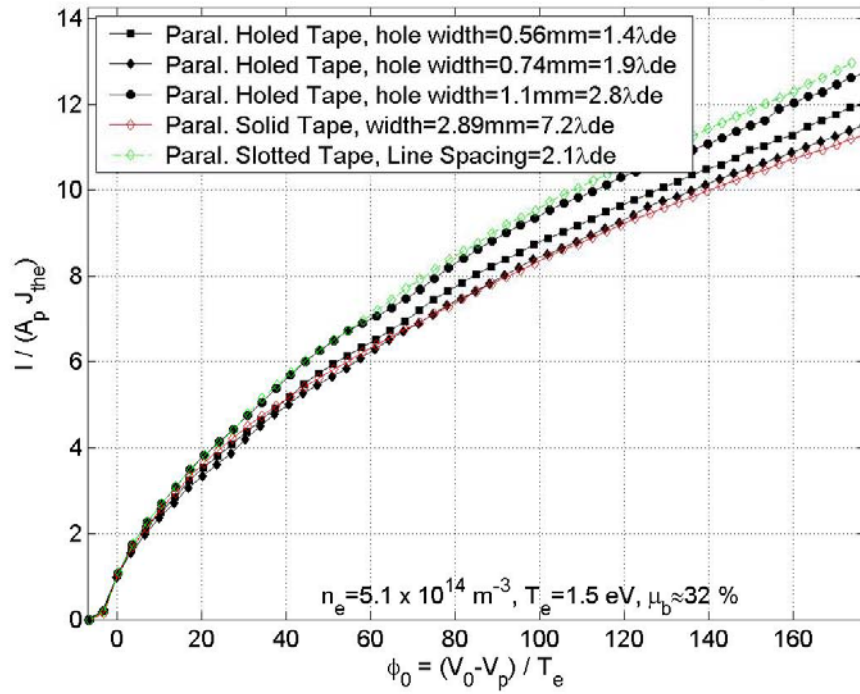
Normalized Characteristics of Perpendicular Holed Slotted and Solid Samples at 300 cm
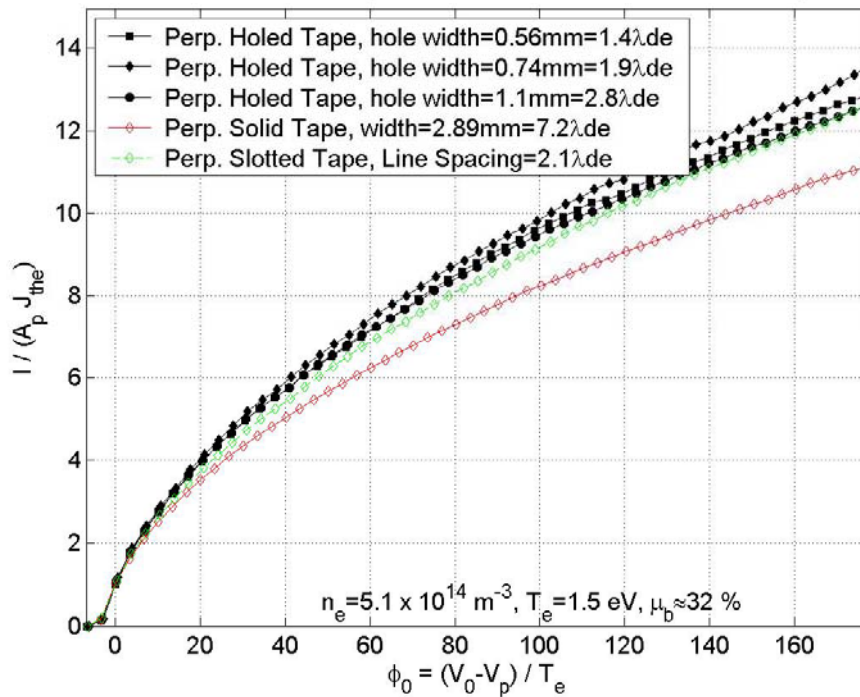
(b)

Figure 4-10: Comparison of the *I–V* characteristics of holed, solid, and slotted tapes at 300 cm. Upper and lower graphs are applicable to parallel and perpendicular tape orientations, respectively.

109

% Difference	75 cm Perp.	75 cm Par.	160 cm Perp.	160 cm Par.	300 cm Perp.	300 cm Par.
Best Hole to Slot	7.0	-0.8, in Noise	14.1	-0.1, in Noise	7.7	-2.7
Best Hole to Solid	11.1	10.8	16.5	19.4	21.8	11.7
% Error ±	1.4	1.3	1.2	1.5	1.5	1.4

Table 4-6: Comparison of the percentage difference between the most efficient electron collection (per unit area) holed probe to a slotted or solid probe along with the percent error associated with that probe.

3)   In both orientations, the large-holed tape samples were very similar to the slotted tape samples at all three distances. Two cases had less than 1% difference, which is within experimental error according to Table 4-6, except possibly for the parallel oriented case at 300 cm (which had ~2.7% difference). The major difference between the large holed and slotted cases was that the large holed tape was often more efficient per unit area at lower bias potential values, and then eventually became equivalent starting above $(V_o - V_p) = 40\text{-}60 \; T_e$. Provided that the porosity remains the same, it appears that the more the hole size increases in the holed samples, the closer the electron current collection would mimic the slotted samples. This holed sample structure physically resembles, and thus collects similar to, the slotted sample because of the many thin lines for collection. More experimental investigation must be conducted to ascertain the cause of this phenomenon.

4.5   Resulting System Implications

Other implications of holed tether technology would be to reduce greatly the total mass of a solid tether while maintaining the electron collection. If the holes are very small with respect to the thickness of the tether, the physical path through the collecting tape would resemble a long cylindrical tube and it would be very difficult for an electron entering a hole to avoid being collected. Thus it may be appropriate to predicted that it would collect similarly to a solid tape. But, the total mass of the tether compared to the solid tape would be reduced by the fraction of the porosity.

This trend seems to be strongly suggested in Figure 4-11 for the 75 cm case. The total electron current collection grows and becomes closer to the solid current collection as the holes get smaller. For the 160 cm and 300 cm cases the large holes still collect the least amount of current; however, the small and medium holes are equivalent to each other within the error of the experiment, which may indicate a limit is being approached. In these cases, the complex sheath interactions, explained earlier, make it difficult to determine the exact physical mechanism causing this similarity.

In order for the path through the tape to be a long cylindrical tube as mentioned earlier in this section, the hole sizes would have to be many times smaller than a Debye length. The results presented in this experiment are not sufficient to prove this phenomenon, but indicate a possible trend.

(a)

Normalized Characteristics of Perpendicular Holed and Solid Samples at 160 cm

Legend:
- Perp. Holed Tape, hole width=0.56mm=2.1λde
- Perp. Holed Tape, hole width=0.74mm=2.8λde
- Perp. Holed Tape, hole width=1.1mm=4.2λde
- Perp. Solid Tape, width=2.89mm=11.0λde
- Perp. Slotted Tape, Line Spacing=3.2λde

$n_e = 1.37 \times 10^{15}$ m^{-3}, $T_e = 1.7$ eV, $\mu_b \approx 53$ %

$\phi_0 = (V_0 - V_p) / T_e$

(b)

Normalized Characteristics of Perpendicular Holed and Solid Samples at 300 cm

Legend:
- Perp. Holed Tape, hole width=0.56mm=1.4λde
- Perp. Holed Tape, hole width=0.74mm=1.9λde
- Perp. Holed Tape, hole width=1.1mm=2.8λde
- Perp. Solid Tape, width=2.89mm=7.2λde
- Perp. Slotted Tape, Line Spacing=2.1λde

$n_e = 5.1 \times 10^{14}$ m^{-3}, $T_e = 1.5$ eV, $\mu_b \approx 32$ %

$\phi_0 = (V_0 - V_p) / T_e$

(c)

Figure 4-11: Absolute current collected from small, medium, and large size holes compared to the equivalent width solid tape at a) 75 cm, b) 160 cm, and c) 300 cm distance.

4.5.1   Electron Current Collection and Drag Maximization

For the same reason that more current will be collected from smaller holes, there will also be an increase in atmospheric drag to the point where it equals that of the solid tape. This fact negates the original motivation for the porous tape, which was to maximize current collection and minimize drag. The reason atmospheric drag approaches that of a solid tape is because the tether twists. Since atmospheric drag depends on a 2-dimensional projection, if a very small hole twists then it takes only a small angle before the path through the hole is effectively blocked, and thus becomes similar to the drag of a solid tape.

For space system design purposes, it is important to compare technologies on an equal mass perspective. To account for an equal mass system, the current collection for the slotted and holed tape should be doubled. Further investigation can deduce that a maximum point in the ratio of force generated by the current collection, F_i, over the force generated by drag, F_d, must exist. F_i and F_d are defined in Eq. 4-1[29] and Eq. 4-2.

$$F_i = \left| I \cdot \int_0^L d\overline{L} \times \overline{B} \right| \qquad\qquad \textbf{Eq. 4-1}$$

$$F_D = \frac{C_D \cdot \rho \cdot A \cdot v^2}{2} \qquad\qquad \textbf{Eq. 4-2}$$

The only variables that impact Eq. 4-1 and Eq. 4-2, and are determined by tether geometry, are the 2-d surface area and the electron current collection. These values, I and A, both impact their respective equations in a linear way.

Another important factor to be aware of is that for tape geometries, the 2-d surface area changes as the tape rotates from its thickness to its width relative to the direction of plasma flow, as seen in Figure 4-12 (i.e. from parallel to perpendicular orientation). If a solid tape tether has more than one full 360º twist in it throughout its length, then the total 2-d surface area, '2dSA', will follow Eq. 4-3 [6], where 'w' and 't' represent the tape width and thickness.

---

[29] F_i is the magnitude of the electrodynamic force because it must be compared to the drag force, which is always in the exact opposite direction.

$$SA2d = \frac{1000 \cdot 2 \cdot (w+t)}{\pi} \quad [m^2 / km] \qquad \textbf{Eq. 4-3}$$

A similar technique can be applied to determine the total drag surface area of a holed tether. Here, the thickness and hole size determines the angle that the holed tether becomes effectively a solid tether surface as it twists. The thicker the tape, the smaller the twist angle it takes before there is no clear path through the holes in the tape.
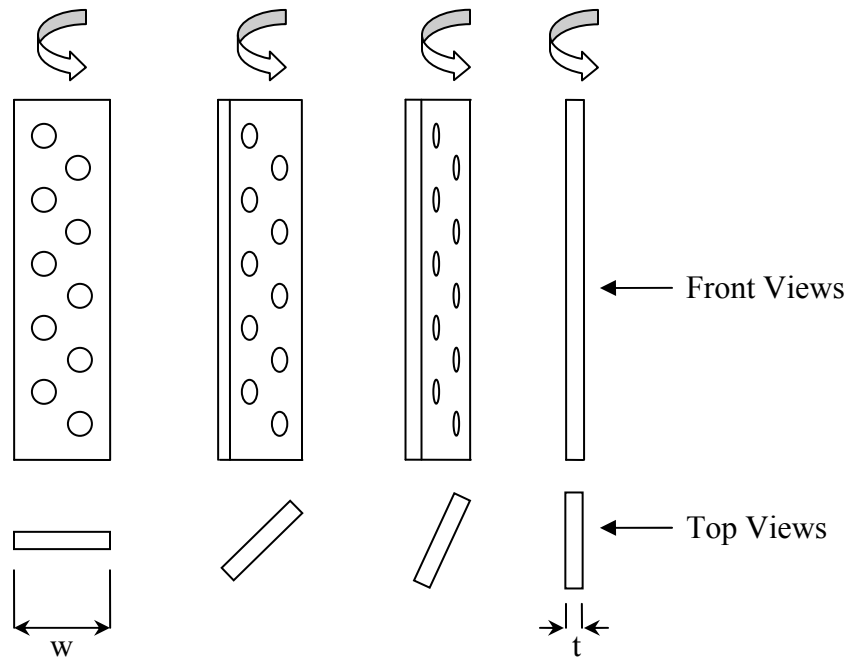
Figure 4-12: 2-d surface area as a holed tape tether rotates.

In addition, more plots were created similar to Figure 4-11 except for the parallel orientation, and are shown in Figure 4-13. These plots also describe the total collected current with respect to the normalized potential. The holed and slotted tapes in each plot are 50% porous and thus 50% the total mass of the solid tape. In order to compare the current collection of the slotted and holed tapes on an equal mass basis to that of the solid tape, their total collected current should be doubled. From this fact, and after reviewing all the samples from the parallel and perpendicular orientations (Figure 4-11 and Figure 4-13), it can be deduced that the small holed tether samples collect the most electron current in all cases for a given tape width and thickness. This indicates that a maximum value can be obtained for the F_i / F_d ratio. This will be the optimum tape design for any given system when maximizing electron current collection and minimizing drag is a

114

concern for a 50% porous tether with its respective dimensions. Further testing on the current collection properties of smaller holed tapes must be conducted to attain this current collection value for this particular tether width and porosity.

Characteristics of Parallel Holed and Solid Samples at 75 cm

(a)

Normalized Characteristics of Parallel Holed and Solid Samples at 160 cm

(b)

115
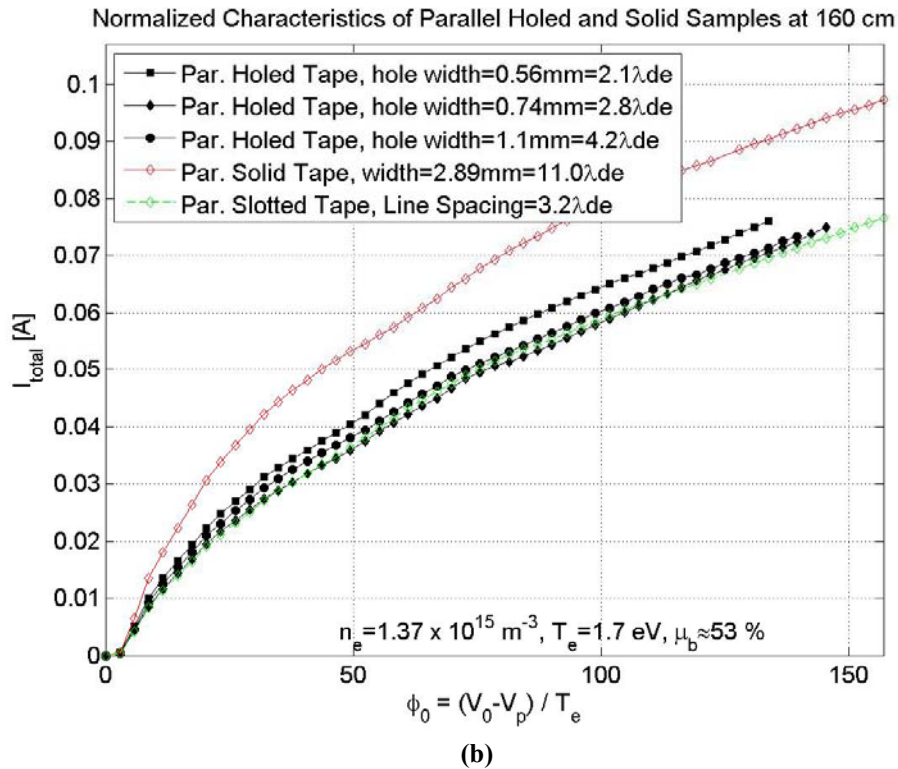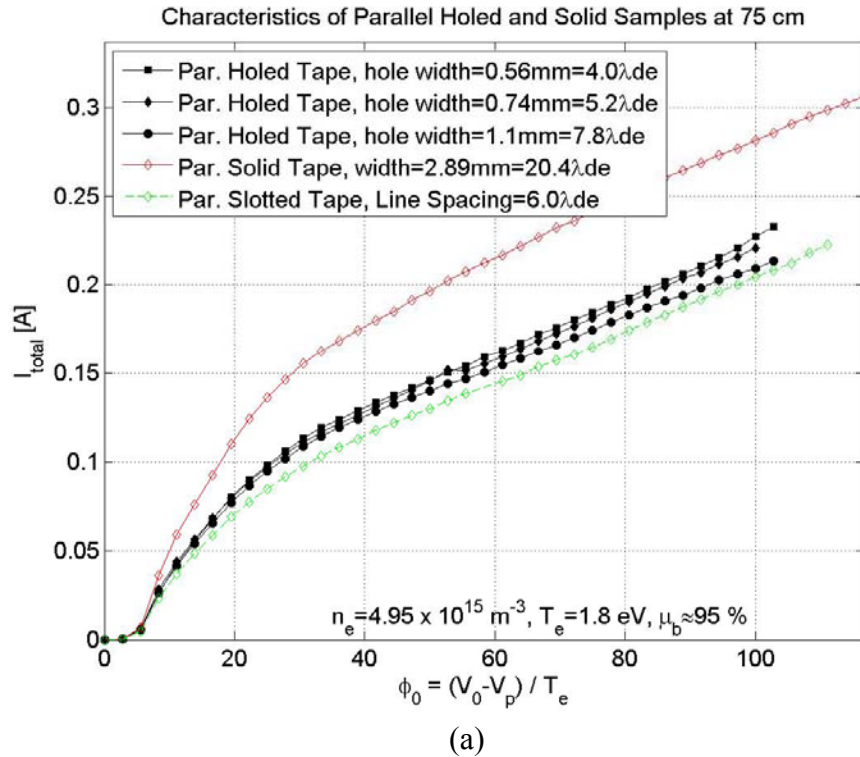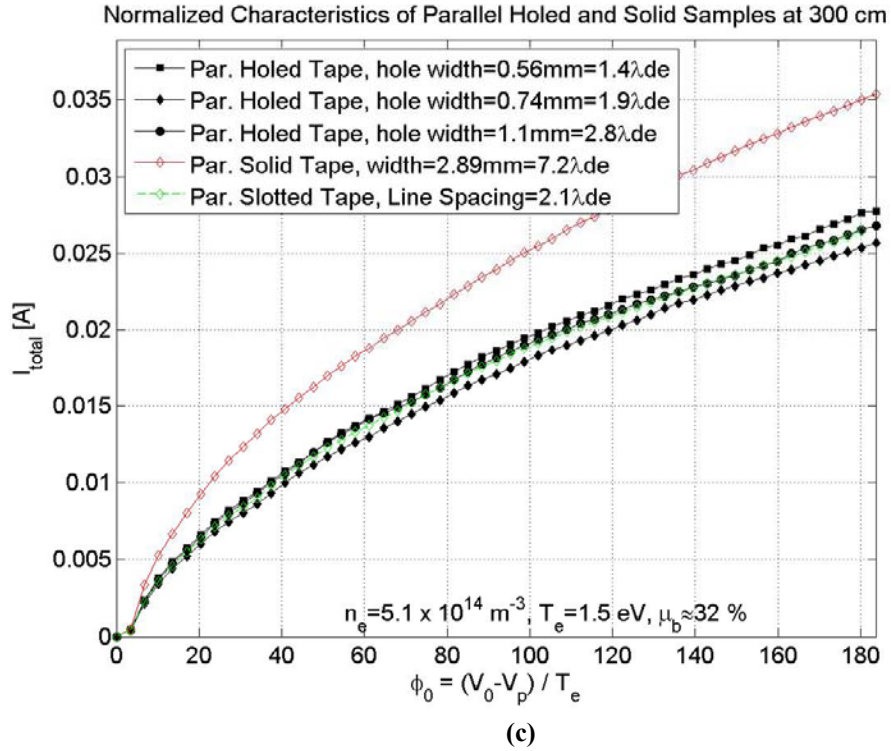
Figure 4-13: Absolute current collected from small, medium, and large size holes compared to the equivalent width solid tape at a) 75 cm, b) 160 cm, and c) 300 cm distance.

Using the ratio of the current of the solid tape over 2 times the holed tape current (for equivalent mass) from Figure 4-11 and Figure 4-13, the F_i value can be calculated for a tether with the dimensions of this experiment, in Debye lengths. There are two different configurations, perpendicular and parallel, where the maximum and minimum collections exist. These configurations must be used to represent an entire 360º twist. To do this, an approximation is made to interpolate the current collected by a twisted tape using Eq. 4-3. The twisted tape is ~0.64·(w+l) for the 2-d surface area, which varies between the parallel and perpendicular orientations as it rotates. Using this correlation, an assumption is made such that the current collection is approximated at 0.64 between the current values at each orientation. This value is seen in Table 4-7 for normalized potentials, ϕ_0, of 50 and 100.[30]

---

[30] These values were taken as arbitrary normalized potential points for the purposes of comparing the F_i / F_d ratio.

Interpolated Current Collection
(0.64 interpolated between Parallel and Perpendicular Configurations)

ϕ_o	75 cm		160 cm		300 cm	
	solid [A]	holed [A]	solid [A]	holed [A]	solid [A]	holed [A]
50	0.221	0.336	0.058	0.088	0.017	0.027
100	0.315	0.505	0.087	0.141	0.025	0.042

Table 4-7: The interpolated current collected by the parallel and perpendicular small holed tape samples at 2 different normalized potential values.

From this experiment, the greatest F_i / F_d ratio, which was found to be the small holed tape, can be compared to that of an equivalently shaped solid tape. In Table 4-8, the F_i / F_d value is calculated based on a solid twisted tape equaling 1. This also assumes that the drag surface area of a twisted solid tape equals 1. This normalization is done because the drag and current collection of a solid tape will always be less efficient than that of a slotted or holed tape of equivalent width and mass. As a result, for comparison purposes, the solid tape lower bounds were set to 1. The theoretical best case occurs where the thickness of the tape equals zero. In this case, the surface area of the 50% porous holed tape would be exactly 0.5 of the solid tape as it revolves 360° about its axis. As the thickness of the tape increases and/or the size of the holes decreases, more of the revolution is effectively a solid tape, and thus approaches 1, as seen in Table 4-8.[31]

Surface Area	Normalized V	75 cm	160 cm	300 cm
0.5	50	3.03	3.02	3.25
	100	3.21	3.25	3.32
0.596	50	2.54	2.54	2.72
	100	2.69	2.72	2.78
0.75	50	2.02	2.02	2.16
	100	2.14	2.17	2.21
1	50	1.51	1.51	1.62
	100	1.60	1.62	1.66

Table 4-8: F_i / F_d ratio comparing the small holed tape to the solid tape for varying surface areas.

The thickness of the tape and the size of the holes in this experiment results in a surface area value of 0.596. This results in the true F_i / F_d value seen in Table 4-8, with respect to the solid tape on an equivalent mass comparison. Table 4-8 primarily serves to display the trends associated with this ratio calculation. Each sample will have its own

---

[31] It should be noted that the 75 cm case is likely the most applicable to actual space condition because it is nearly 100% flowing.

current collection and F_i / F_d value according to the size of the holes and the thickness of the tape. The surface area for large holes is lower than that of small holes. The current collection for the small holes, however, is greater than that of the larger hole sample. This current enhancement is greater than the benefit of the smaller surface area, and thus yields a larger F_i / F_d. This is why, from the tape samples measured in this experiment, the small holed tape is decidedly the best choice for a tether system assuming a given tape width and thickness. This claim is in addition to the previous conclusions that an OML collector (small or in the order of a Debye length) is the most efficient current collector. A final optimal tether design for efficient current collection must consider both factors.

It can be observed that there is a 1% or less difference between the 75 and 160 cm distance for each respective normalized potential. These two cases have the greatest plasma flow percentage. The 300 cm case is 7% larger than the closer cases. This can be attributed to both error and less of a flow percentage. As the flow percentage diminishes, an increasing amount of current will be collected by thermal collection. In addition, the low current collections values allow for a small measurement value difference to be a larger error. Another observation is that the F_i / F_d only differs from 2% to 7% between the 50 and 100 normalized potential, ϕ_0.

To put this into perspective, since $T_e = 0.1$ eV in the Earth's atmosphere, the normalized tether potential of 50 and 100 equates to 5 V and 10 V, with respect to the ambient plasma. This also suggests that the hole sizes being tested are 33 mm to 94 mm at $n_e = 1 \times 10^{10}$ m^{-3} and 3.3 mm to 9.4 mm at $n_e = 1 \times 10^{12}$ m^{-3}. The results here don't imply much for the 1×10^{10} m^{-3} case because they are much too large for a practical tether; however, the trends still hold. This shows that even if the drag on the holed tether is equivalent to that of the solid tape, the mass equivalent current collection will far surpass that of the solid tape.

An important observation shows that, it appears the major controlled constraint in a tether system would involve making the tape as thin as possible, while maintaining the structural integrity necessary for a given mission. This would ensure that the mass of the tape as well as the 2-d surface area would be minimized. Future experimentation should involve the collection capabilities of even smaller holes than that of this chapter. Once

the hole size and the porosity of the tape are identified, the most efficient F_i / F_d ratio can be calculated for all holed geometries. These geometries have been shown to be more efficient than slotted as well as solid tape geometries. In addition, the thinner the holed tape, the larger the F_i / F_d ratio that can be achieved. This is because it will maximize the porosity throughout an entire revolution, thus minimizing drag.   Further investigation to more and less than 50% porous tethers will reveal even more as to the most efficient tether geometry per unit mass. In addition, the resistive affects on an EDT system will have to be evaluated. Thinner tapes will result in increased resistance.

4.6　　　　Present Status and Conclusion

Several conclusions can be drawn from the analysis of the results.

1)　　　　Beyond a threshold bias close to the beam energy, holed tapes collect more current when oriented transverse (perpendicular) to the flow rather than parallel, as also seen in Choinière et al. for slotted and solid tapes[136]. The most efficient perpendicular configuration (medium hole) was more efficient per unit area than the best parallel orientation (large hole) by 18.5%, 20.0% and 6.5% for the 75 cm, 160 cm, and 300 cm, respectively.

2)　　　　Holed tapes are more efficient than both solid and slotted tapes in terms of collected electron current per unit area when oriented perpendicular with respect to the plasma flow. In the perpendicular orientation, the most efficient holed tape (medium hole) is more efficient than the solid tape by 11.1%, 16.5% and 21.8% at the 75 cm, 160 cm, and 300 cm positions, respectively. Similarly, slotted tapes always appear to be slightly more efficient than holed or solid tapes when oriented parallel with respect to the plasma flow.

3)　　　　The electron current collection efficiency per unit area on holed tapes in the parallel orientation decreases with increasing hole size until a minimum is attained, beyond which it starts increasing again. This effect is in the noise at 75 cm, but

distinctive at 160 cm and 300 cm. The opposite effect occurred when the holed probes were oriented transverse to the flow, where a maximum efficiency was obtained for a hole size somewhere between the small and large hole sizes tested.

4)   Trends have been experimentally shown to exist that identify a tether geometry that would maximize the boosting force to the drag force ratio (F_i / F_d). The major controlled constraint in a tether system would involve making the tape as thin as possible while maintaining the structural integrity necessary for a given mission. This implies that once the hole size, tape width, and the porosity of the tape is identified, the most efficient F_i / F_d ratio can be calculated for all holed geometries. These geometries have been shown to be more efficient than slotted as well as solid tape geometries.

Further experimentation is needed to quantify more completely the observed effects. In addition, larger and smaller width holed tapes should be tested in both the parallel and perpendicular orientations to verify the effects that have been displayed in this experiment. The porosity of the larger-width probes (as defined in [136]) designed should be 50% and 77% in order to mimic the approximate porosity of the slotted sample. Similarly, the smaller-width holed probes designed should be 50% and 31% porous. In addition, a probe could be made that would have larger holes than this experiment. This would verify the assumption made in item 3 of Section 4.5.4.

In addition, a plethora of various holed tape geometries could be tested for their current collection capabilities. The width, porosity, and hole size should be varied, and current tested throughout an entire tape revolution. This combined with the calculation of the surface area over a rotation would allow for an elaborate comparison between various tape designs without the use of a current collection assumption. Once the optimal tether geometries have been identified, they can have immediate application into the simulation of future missions. Having a known optimal geometry for most space system cases reduces the amount of design required for each mission. An important theoretical and design question that can possibly be answered is whether slotted or holed tape have a greater F_i / F_d than an OML wire. Ideally a tether small enough to be considered in the

OML regime would be a maximum collection value. Perhaps the geometry would still allow the tape to collect at OML currents and yet there would be less drag.

The results also indicate that alternative-geometry space tethers can potentially allow for efficient electron collection. The holed and slotted geometries have the advantage of collecting more current per unit area, thus reducing mass requirements. The holed tape has the further advantage of having better micrometeoroid impact resistance than the slotted tape, allowing for a practical implementation in space tethers. Future improvements in 3-D sheath theory will improve tether design capability and ultimately allow for the combined maximization of electron collection and minimization of mass requirements.

CHAPTER 5

EDT SYSTEMS ANALYSIS

There are multiple parameters that can be varied in an EDT system to observe changes in performance (recall Figure 3-3). Examples include tether resistance, electron density, and the high voltage power supply (HVPS) power. EDT system design could involve optimizing for boost time, power efficiency, and/or system mass. It is also useful to know what the optimal bare tether length and geometry is for a given mission when designing the system.

This chapter serves to identify and better describe and understand how elements of an EDT system can impact performance under varying circumstances in boosting and de-boosting scenarios with an emphasis to EDT system design. Based on this, for example, methods can be tested to determine the optimized bare tether amount for a given system. In addition, the impact of the varying bare tether geometries (from Chapter 4) on an EDT system will be considered.

5.1   The Reference EDT System

A reference EDT system was defined for the majority of simulations in order to better show consistencies between the results.

Figure 5-1 presents sketches of a typical non-rotating boost and de-boost EDT scenario. Each EDT system is still based on the more detailed description of Figure 3-3

and the reference tether system scenario applicable to both can be seen in Table 5-1. If certain variables deviate from this reference case, they will be specified in the next text.

Tether Length [m]	5000
Tether Sections [ ]	1000
Tether Resistance [Ω/m]	0.015
B-Field [T] ($\perp$ to L and v_{orb})	2×10^{-5}
Orbital Velocity [m/s]	7000
EMF Potential Difference [V]	700
Tether Radius [mm] (assume wire)	0.6
Electron and Ion Temperature [eV]	0.1
α and β (according to TSS-1R) [ ]	2.5 & 0.52
Spherical Endbody collector Radius [m]	0.5
Load Resistor [Ω]	0
HVPS Power [W]	3000
Electron Emitter	Hollow Cathode
HC Orifice Plasma Density [m^{-3}]	2×10^{20}
HC Plasma Temperature [eV]	3.9
HC Emission Percentage 'f' [%]	100
System Configuration	Grounded tip emitter: Figure 3-8a

Table 5-1: Assumptions made for a 'reference case'.
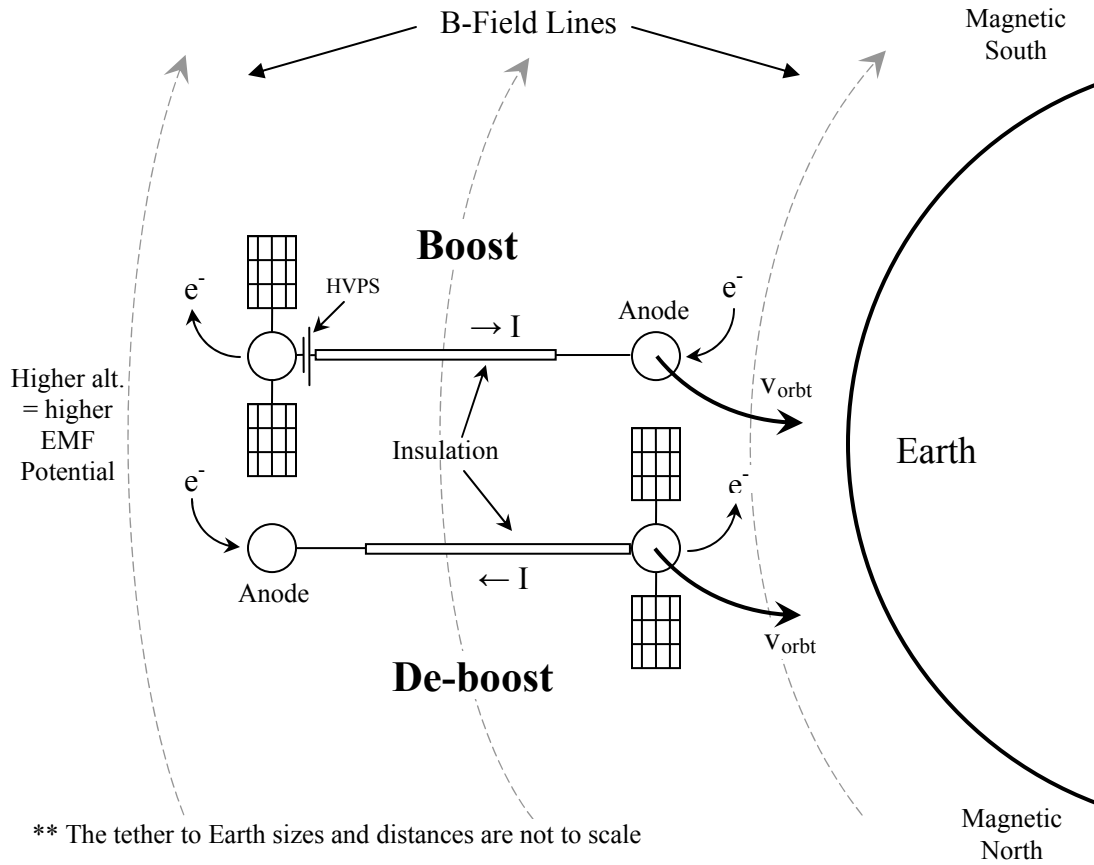
Figure 5-1: The physical orientation of a boost and de-boot EDT scenario.

The baseline tether length was chosen because it was the conductive length for the ProSEDS mission, which also serves as a conservative length for a typical EDT mission [135]. The radius was selected from the TSS-1 mission, since that was the same dimension of the conductive tether (10 strands of 34 AWG wire) [100]. The resistance was arbitrarily set to one half of the approximate value of the Hoytether desohned for the MXER mission to show what future designs with less resistance might yield [146]. This type of tether has been shown to be a strong design for future missions due to its potential for robustness from micrometeoroid survivability [7, 36]. The radius of the endmass was chosen to be slightly smaller than the TSS-1 mission (0.5 m instead of 0.8) as it was still a reference size. The number of bare tether sections for the simulation was arbitrarily chosen to be 1000 because this allowed for accurate results, while not requiring an overabundance of computing power. The B-field, electron and ion temperatures, and electron densities were chosen based on typical day time ranges for a 300 km altitude

circular orbit [78, 79]. The α and β were used as the calculated values from the TSS-1R mission [31]. The orbital velocity was acquired by using the x-axis component of v_{orbt} (subtracting the v_{Corot} term) in Eq. 3-5, and rounding. The EMF was found using the given values and Eq. 1-1. The HVPS power was chosen to be slightly less than the International Space Station (ISS) power as a conservative value for a typical EDT mission [6]. Finally, the HC and its respective values were decided upon because of their versatility with possible high current emissions as well as established reliability [119]. The configuration of the HC can be seen in Figure 5-2a, called the grounded tip/emitter.
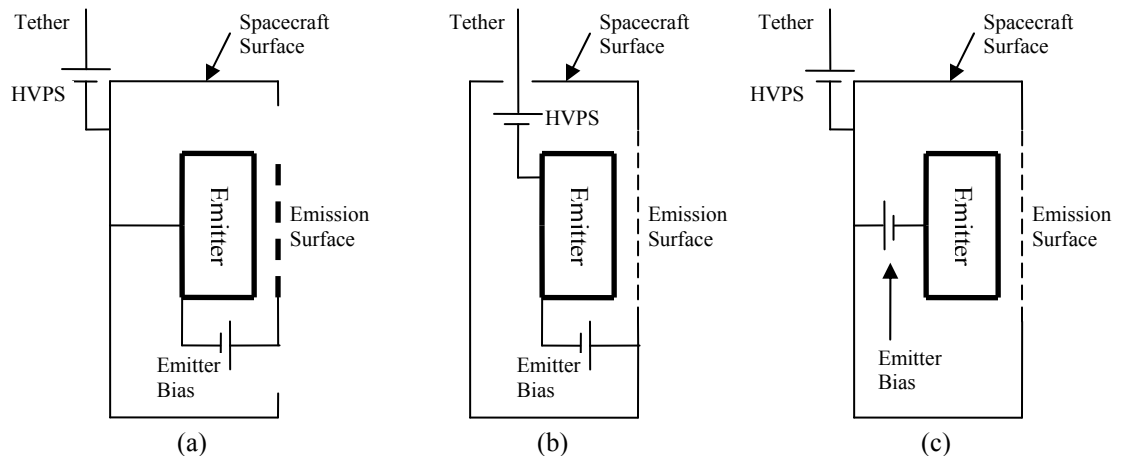
Figure 5-2: Possible electrical configurations of the electron emitter with the tether and high voltage power supply (HVPS): Grounded tip/emitter (a) grounded gate (b) and grounded gate, isolated tether (c) configurations. Same figure as Figure 3-9.

For the purposes of all the simulations conducted in this thesis, the grounded gate configuration was used in the floating potential mode. This configuration was chosen, as explained in Section 3.4, to minimize the input power because the V_{emf} would be used to drive the electron emitter. The assumption used in the simulations was that the potential of the electron emitter could not exceed its maximum design limit. This was 59 V for the FEA and 2500 V for the TC, which were chosen in Section 2.4.

5.2   Optimization of Bare Length

The amount of bare tether used in any tether system design will influence the amount of boosting force achievable. It turns out that in most de-boosting scenarios, an

almost entirely bare tether will yield the maximum electrodynamic force, compared to one that is insulated. This phenomenon will be explained thoroughly in Sections 5-3 through 5-5. The amount of bare tether must be determined when designing an efficient system for given mission objectives in order to maximize boosting capabilities. It is important to understand how the optimal amount of bare tether changes with the alteration of nearly every system variable. However, in order to limit the number of simulations required for comparison to a reasonable number, an arbitrary reference value was found that could be used for the simulations of this thesis.

To begin, a boost case simulation was conducted using approximate day and night electron density conditions of 1 x 10^{12} and 1 x 10^{10} m$^{-3,}$ respectively, in order to show the typical extreme conditions encountered throughout an orbit. The system setup was the reference case. Figure 5-3 shows the results of this simulation plotting boosting force versus bare tether length (total tether length held constant at 5 km). It is clear that the optimal bare tether distances are quite far apart between day (~1800 m) and night (~4000 m) conditions. An important note is that the boosting force drops after its maximum value because of the increasing exposed conductive tether. This increased bare tether length drives the anode potential increasingly negative, which collects ions instead of electrons. It is important to understand this relation to maximize the boosting capabilities across an entire orbit. This will be discussed further in the case studies of Chapter 6.
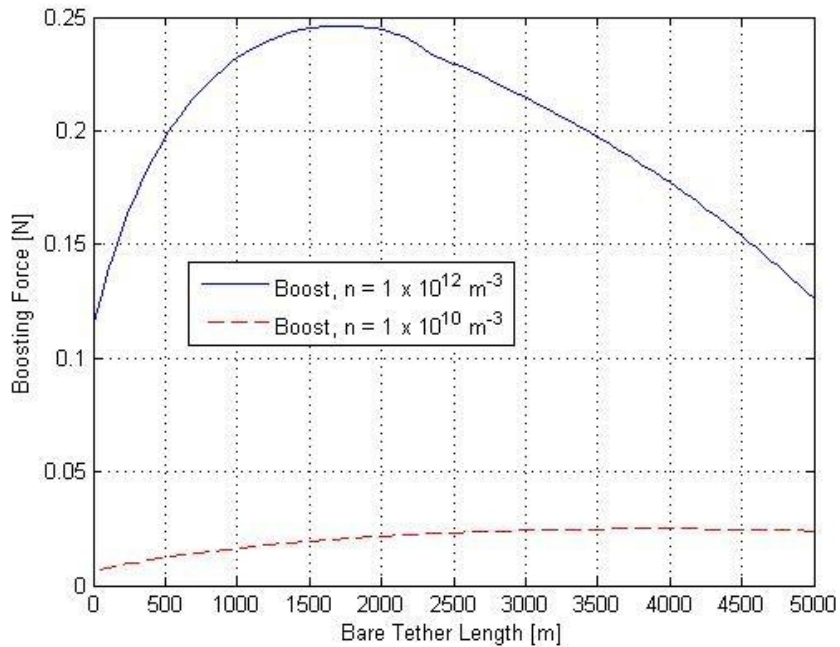
Figure 5-3: Plot describing the associated IxB·L forces involved with a certain bare tether length for typical day and night electron density extremes in the 'reference' system.

This difference in the optimal ideal bare tether length over the course of an orbit can be an important issue when attempting to determine the ideal system design. A possible solution that was investigated determined what would happen if the power was turned off during the low electron density times, such as the night, and left on during the day when the density, and thus boosting force, was much higher.

A simulation, using TEMPEST, was conducted in boost mode for the reference conditions, which turned off the HVPS when the system was in the shadow of the Earth. The simulation date chosen was February 3, 2004, and the ballistic coefficient were 1131 kg and 26 kg.m^2, respectively. These values were chosen to correspond with previous work from the ProSEDS mission [135]. Due to the altitude of the orbit (300 km), the daytime period is slightly more than 50% of the time. Figure 5-4 shows how the altitude of the orbit is affected by this reduction in power. The maximum apogee altitude gain for the case where the power is off for half the time is ~40 km, as compared to the case where the power is on all the time, which is a ~50 km gain. These results present a potentially serious flaw, however. The elipticity of the orbit becomes large, even over just one week of time. When boosting occurs just during the day, a ~35 km altitude

127

difference from apogee to perigee results, as opposed to a ~14 km difference in the constant boost case. For many applications this may not be acceptable.
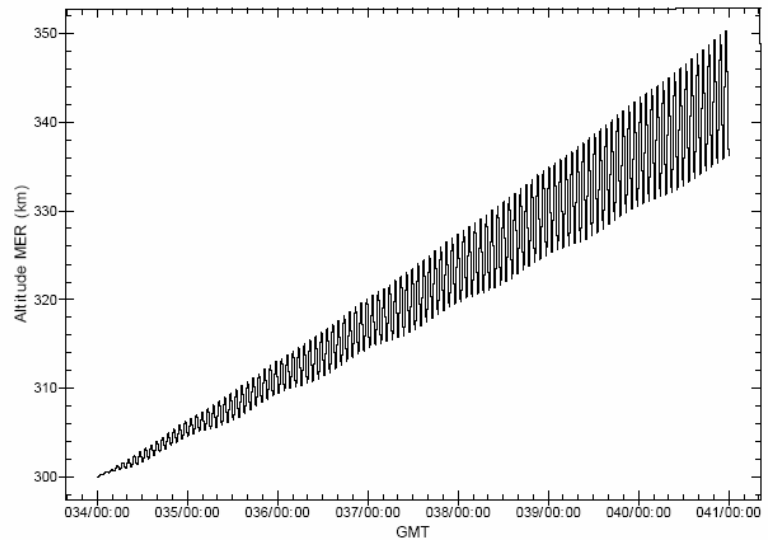
(a)
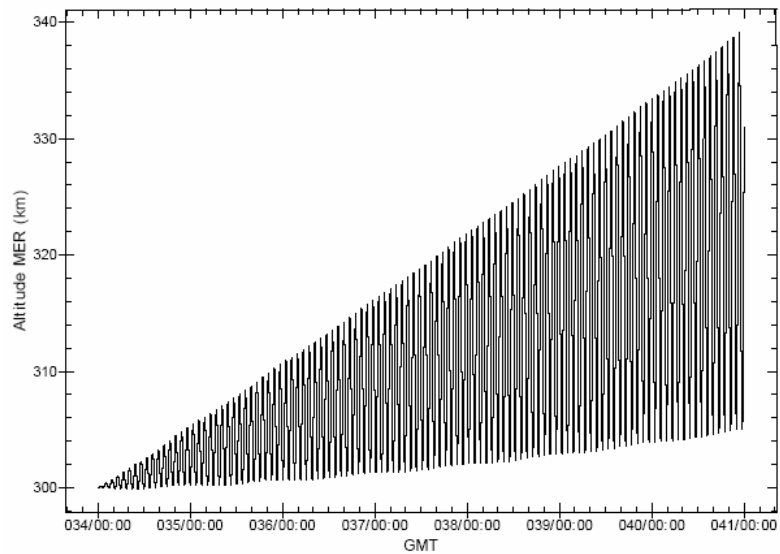
(b)

Figure 5-4: Orbit altitude plots versus time for one week with (a) the power on all the time and (b) with the power off when in the shadow of the Earth. The system was the boosting case using the reference conditions.

Since the EDT-Survey code is not capable of orbital dynamics it was assumed that leaving the power on all the time was the best option. The next step towards obtaining an optimal system design would be to find the best power efficiency, highest average boosting force, and total impulse across an entire orbit. Assuming the reference conditions and the same date as the elipticity simulation, another scenario was tested for a

single orbit. The magnetic, atmospheric, and ionospheric values were obtained using IGRF-2010 (International Geomagnetic Reference Field), MSIS-E-90 (Mass Spectrometer Incoherent Scatter-Empirical), and IRI-2001 (International Reference Ionosphere). Every minute of the orbit (93 minutes total for the 300 km altitude), the necessary variables were obtained from the before mentioned models and the EDT system was solved. For each minute of the orbit, the system forces and efficiencies were obtained and then averaged. This process was then conducted for each of the indicated bare tether lengths for the TC, FEA, and HC emitters. The TC and FEA emitters were run in the floating grounded gate configuration (Figure 5-2b).

Figure 5-5 details how boosting impulse varies as a function of bare tether length for each of the electron emitters over the course of an entire orbit. The units of impulse were used because they exhibit the total amount of force imparted to the system over the course of the entire orbit time. For this particular case, using a total tether length of 5000 m the optimal bare tether length was ~2500 m when using either the HC or FEA emitters, while with the TC the optimal length was ~1000 m of bare tether. Again, these results are for the 'reference' system that is detailed in Section 5.1. It can also be deduced from Figure 5-5 that the TC is not capable of producing as much impulse.
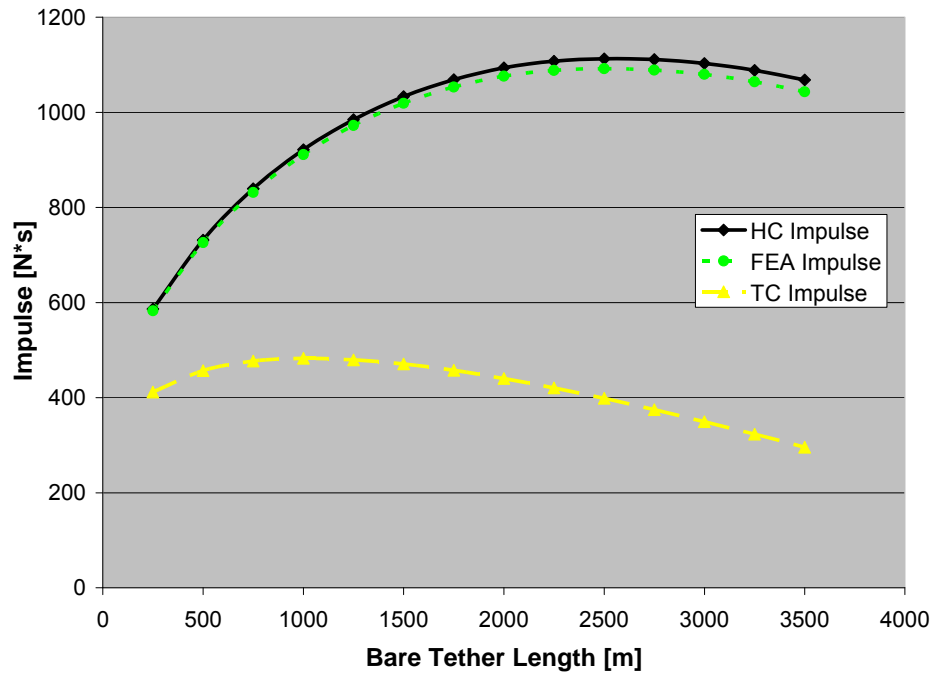
Figure 5-5: Total boosting impulse over an entire orbit for different bare tether lengths. An HC, FEA, and TC were compared at the reference conditions.

The differences between the emitters, shown in Figure 5-5, are the result of the potential requirements in the emission process. HCs require the least amount of potential to emit the greatest amount of current while the TC requires the most. Since the system configuration is the grounded gate (seen in Figure 5-2b) and the electron emitter is in floating potential mode, the electron emitter draws the potential necessary for emission directly from that available in the system (rather than its own independent power source). As a result, after solving KVL and KCL for the system (Eq. 3-6 & Eq. 3-8), the increased $V_{emitter}$ from the TC results in lower potentials to collect and drive current across the system. This in turn reduces the boosting forces of the system. Emitter performance differences will be discussed in further detail in Section 5.5. It should be noted, however, that the maximum force occurs when the bare tether is 50% bare for the FEA and HC electron emitters and 20% bare for the TC electron emitter.

5.3 General Behaviors and Trends of EDT Systems

A number of simulations were conducted in order to show the general trends that a tether system would result in when various elements were changed. The purpose of this was to understand what physically happens to the EDT system as design parameters are altered.

Since there are an abundance of variables that can be altered, a select few had to be chosen that could adequately represent as many cases as possible. The tether resistance, power supply, and electron density were altered in order to show the amount of boosting force obtained by these changes.

Using the reference condition and optimal bare tether amount, found in the previous section (2500 m bare tether for non-ideal HC[32]), tether cases were solved with respect to the electron density, tether resistance, and HVPS. The respective boosting and de-boosting thrust produced by altering these conditions was then plotted. In addition, the insulated tether system (as derived earlier in Section 3.3) and the 500 m bare tether cases were also plotted for the same conditions to compare and contrast the results. It

---

[32] The non-ideal HC refers to the HC description in Section 2.4.3. This is opposed to an ideal HC, which assumes infinite current emission past a particular keeper to ambient plasma potential difference.

may be useful to refer to Figure 5-1 to gain a better understanding of the physical orientation in orbit of the EDT system.

5.2.1   Deboosting: Vary n_e and R_t

Figure 5-6 and Figure 5-8 display the results for bare and insulated tethers for the de-boosting case of the reference scenario mentioned in Section 5.1. It can be seen in Figure 5-6a that the general trend is for the de-boosting force of the tether system to increase with decreasing tether resistance. The trends observed can be physically explained. According to Ohm's law, as the tether resistance decreases, the potential from the resistive loss of the tether must diminish as well. Then, using KVL (Eq. 3-7), the V_{emf}, $V_{emitter}$, and $V_{cathode}$ either don't change or vary less than the HC potential (< 26.5V in this case). This means that if V_{tether} is reduced, the V_{anode} must be increased for KVL to hold. The V_{anode} potential is also positive with respect to the plasma potential, resulting in an increase in the electron current, seen in Figure 5-6a. The change in thrust with respect to resistance is seen to drop off more drastically for a system that contains more bare tether, as seen in Table 5-2.
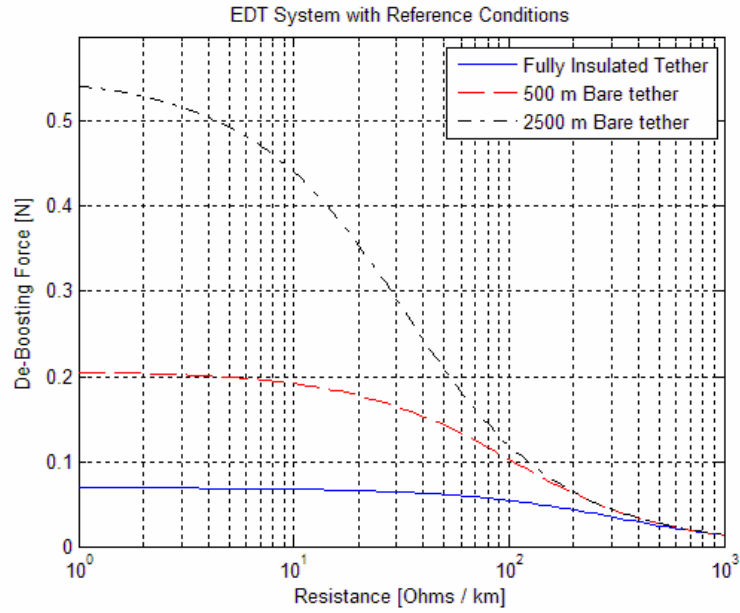
(a)
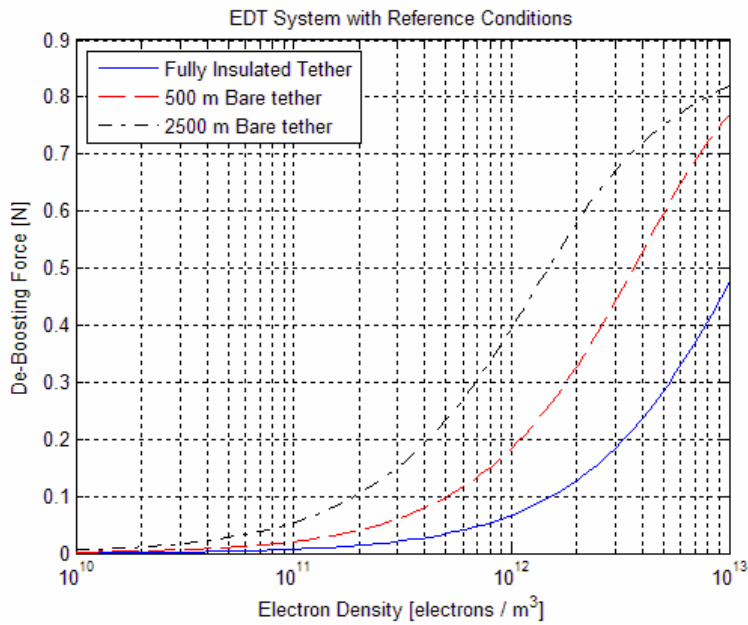
(b)

Figure 5-6: Plots of the force versus (a) tether resistance and (b) electron density. These plots are for the de-boost case with a reference EDT system.

Increase %	Resistance Change [Ω/km]			Plasma Density Change [m^{-3}]		
Bare tether Length [m]	1 to 10	10 to 100	100 to 1000	10^{10} to 10^{11}	10^{11} to 10^{12}	10^{12} to 10^{13}
2500	-19	-73	-88	800	631	108
500	-6	-47	-86	900	825	316
0	-3	-19	-74	600	857	610

Table 5-2: Percent changes in thrust for each tether as tether resistance and plasma density are changed for the de-boosting case.

132

An important note is that the V_{anode} in the de-boosting cases can never become zero. This is because electrons are collected in the higher altitude / higher potential (wrt. plasma) end of the tether.[33] This means that, if the current is not collected at the upper end of the tether for the de-boost case, then no current is collected at all, therefore no electrodynamic forces would be created in the tether.

As the bare tether length increases, from 0 to 500 m to 2500 m, the de-boosting force increases as well. The reason for this is because the increased bare tether surface creates more collection area and more current is collected. In addition, Table 5-3 illustrates the percentage increase in the thrust force of the bare tethers compared to the insulated tether.

De-boost % Above Insulated	Resistance Change [Ω/km]				Plasma Density Change [m^{-3}]			
	1	10	100	1000	10^{10}	10^{11}	10^{12}	10^{13}
2500	686	558	120	0	500	671	490	72
500	197	187	89	0	100	186	176	62

Table 5-3: Percent difference between the given bare tether amount and the insulated tether comparing across thrust and resistance variables for the de-boosting case.

Figure 5-6b details the total thrust produced as the electron density in the ionosphere changes. The general trend shows that the more electrons there are to collect in the higher densities, the greater the force produced. The physical mechanism behind this occurrence starts with the increase in density. This allows more current to be collected for a given surface area, and as can be seen, the more bare the tether, the faster the collection occurs. Then, following KVL, as mentioned for the resistance case above, the tether potential drop increases. The changing potentials and currents involved in this process can be seen in Figure 5-7. Also, Figure 5-8a and b detail the results of varying both electron density and tether resistance versus the thrust in a 3-dimentional plot.

---

[33] In a typical west to east orbit around Earth.
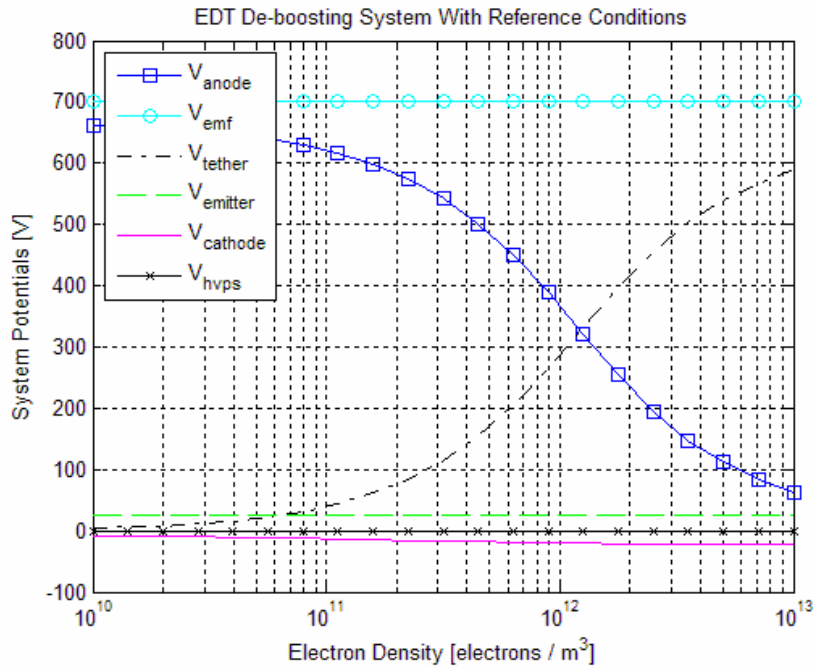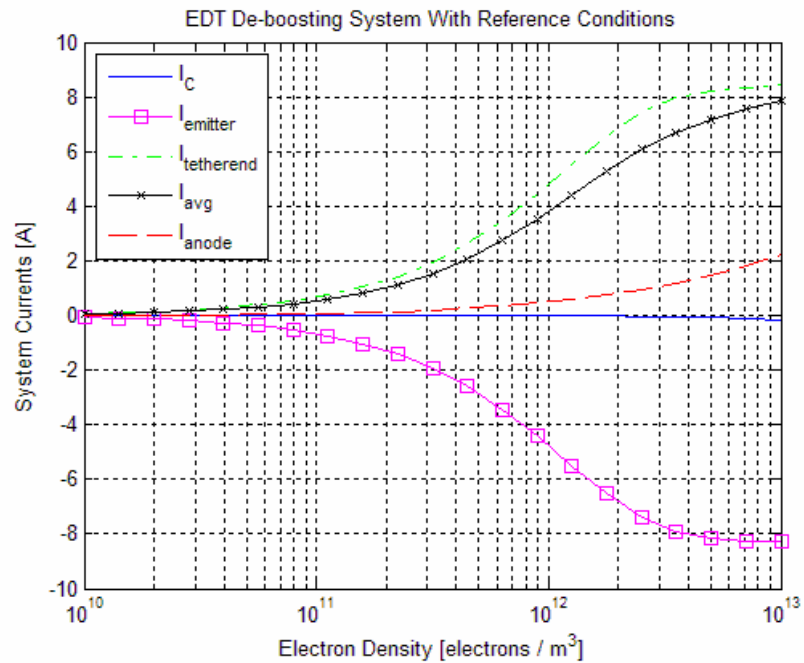
Figure 5-7: The system a) voltage and b) current profiles of a de-boosting scenario with reference condition, varying density.
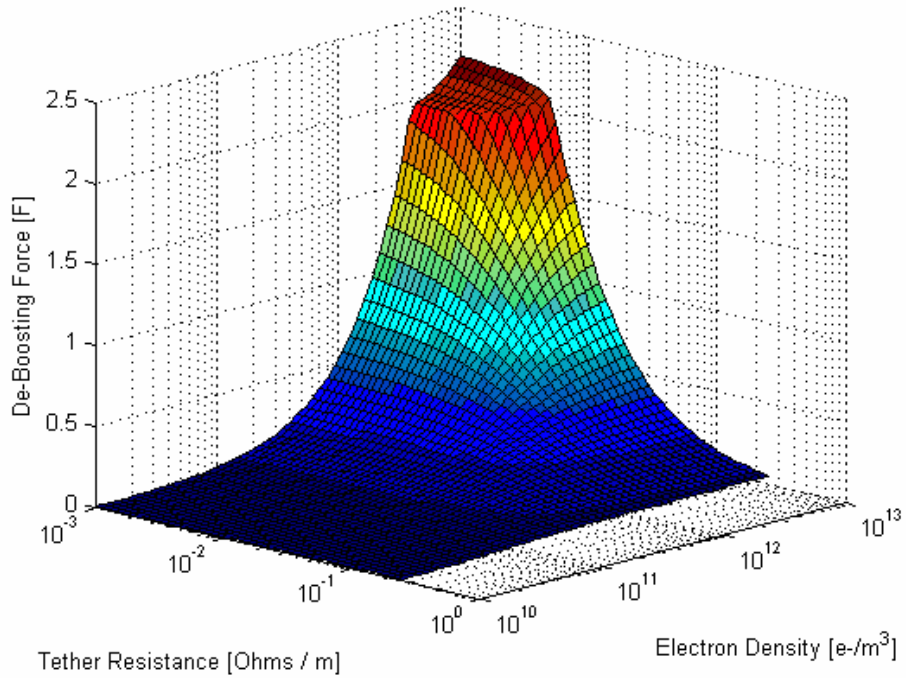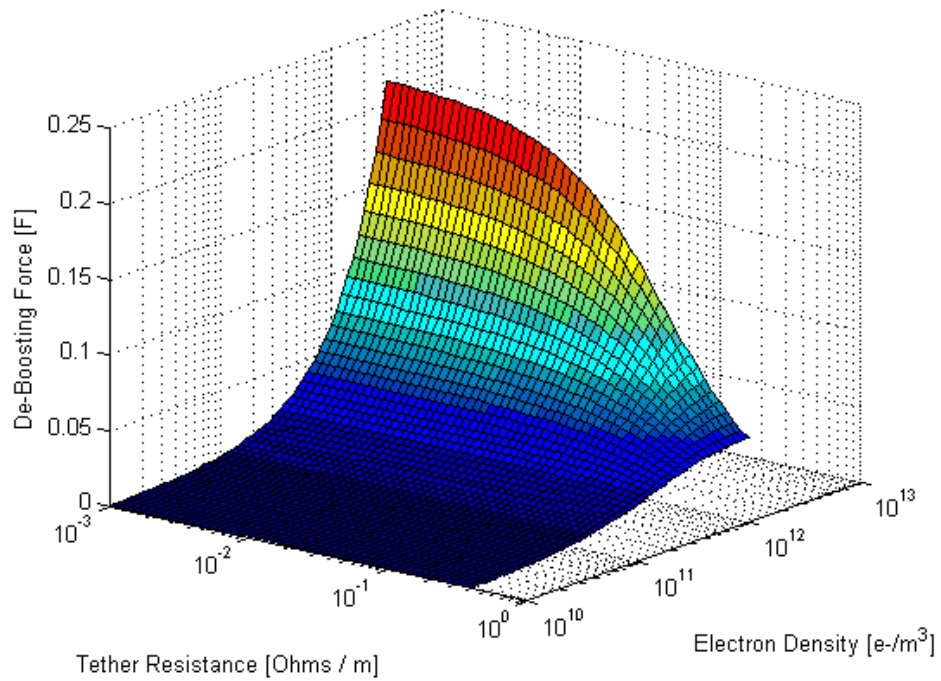
Figure 5-8: 3d-Plots of the tether resistance versus electron density versus the de-boosting power for (a) a 2500 m bare tether anode and (b) a completely insulated tether.

5.2.2   Boosting: Vary P_{hvps}, n_e, R_t

Figure 5-9 details the cases varying the HVPS, the tether resistance, and the electron density versus the resulting boosting force. As with the de-boosting cases, the system configuration is the reference case, and only the variables mentioned are changing. In addition, the HVPS case is presented in this boosting analysis as it is an essential component to this setup, and not commonly used in a de-boosting case.

(a)

(b)

EDT System with Reference Conditions
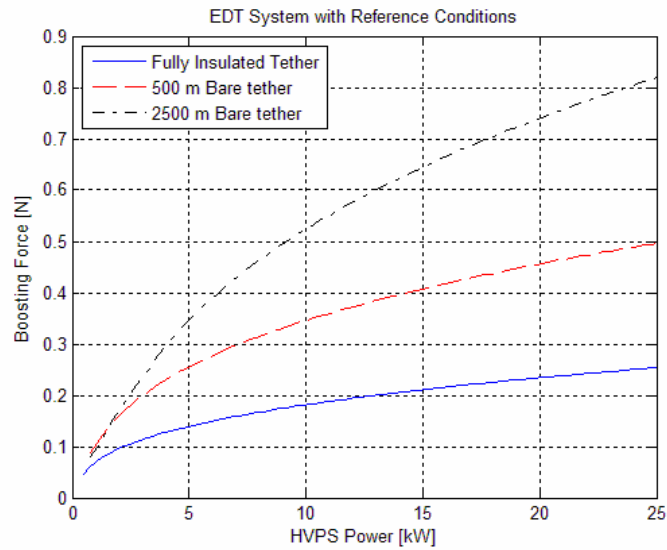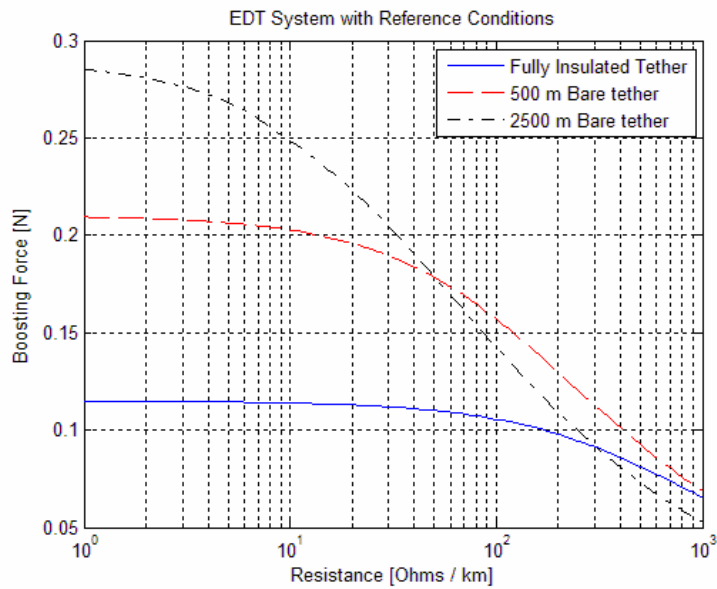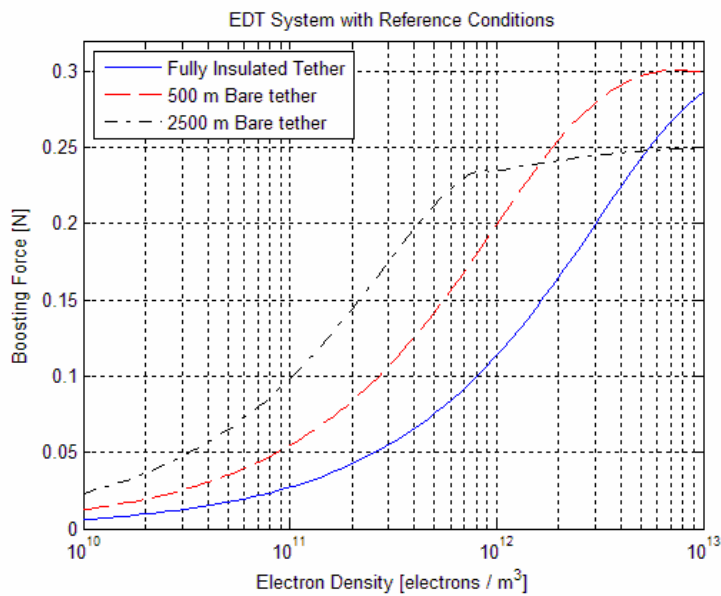
Figure 5-9: Plots of the force versus unit and then the change in thrust per change in unit versus unit where the units are (a) HVPS power, (b) tether resistance, and (c) electron density, respectively. These plots are for the boost condition.

In each of the plots of Figure 5-9 for the 2500 m bare tether condition, the potential at the endbody collector end of the tether system transitions from positively biased to negatively biased with respect to the plasma. This occurs because the bare tether is capable of collecting all the necessary current to complete the KVL and KCL for the system. The tether system becomes more positively biased (with respect to the ambient plasma) the further up the tether, until it becomes positive again. This phenomenon can be observed to occur on only the 2500 m bare tether condition (for the simulations conducted) at 3.5 kW, 0.006 Ω/m, and 9 x 10^{11} m^{-3} for the HVPS, R_t, and n_e, respectively. After these points, increases in the R_t and n_e and decreases in the P_{HVPS} result in endbody collector potential beginning at increasingly negative values. This also produces an observable decline in the boosting performance.

This phenomenon can be observed using the current collection and potential profiles for the reference case seen in Figure 5-10. At 0 m,[34] the endbody collector is negatively biased (-20 V) with respect to the plasma and is thus collecting ions, or a positive current. Around 150 m the V_{emf} drives the potential positive, and the tether begins to collect electrons. This continues until it reaches 2500 m, where it becomes

---

[34] For the boosting system, the anode is the lower altitude end.

137

insulated for the remainder of the tether. The I x B · L forces produced by the electron current (orbit raising force) is more than enough to overcome the small forces created by the ion collection (de-orbit force) and as a result yields an overall boosting force for the system in this configuration.

(a)

(b)
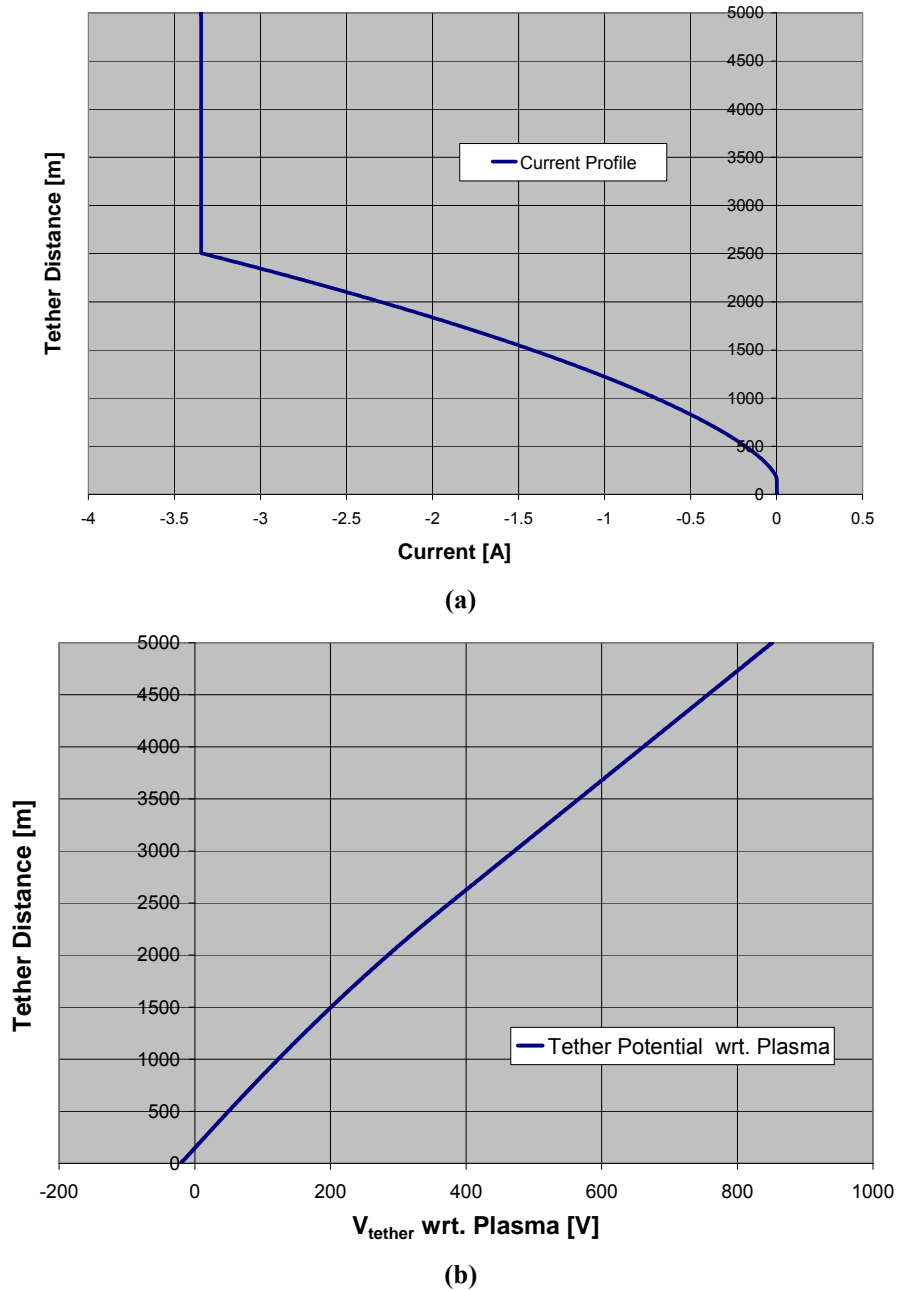
Figure 5-10: The a) current and b) potential profile of the reference configuration. This shows that the end body is biased negatively for the reference case.

The phenomenon is not as observable for the 500 m bare and fully insulated cases because the transition from negative to positive potential with respect to the plasma occurs at values beyond the range used in Figure 5-9. Also, in the case of the insulated tether, there is essentially no transition region at all.

In Figure 5-9a, it can be seen that any increase in the HVPS power on an EDT system will result in an increase in the boosting force because of the increase in driving potential. Also, in Figure 5-9b, it can be seen that the system always boosts less with increasing tether resistance because increasing the resistance of the tether increases the potential required to drive current across it.

Figure 5-9c displays the boosting force results for a changing electron density. Since the collected current is increased, the V_{HVPS} decreases and V_{tether} increases, according to Eq. 3-23 and Eq. 3-24, respectively. Now, in order to equate the system using KVL in Eq. 3-6, the V_{anode} must decrease. The changing potentials and currents for this scenario can be seen in Figure 5-11.
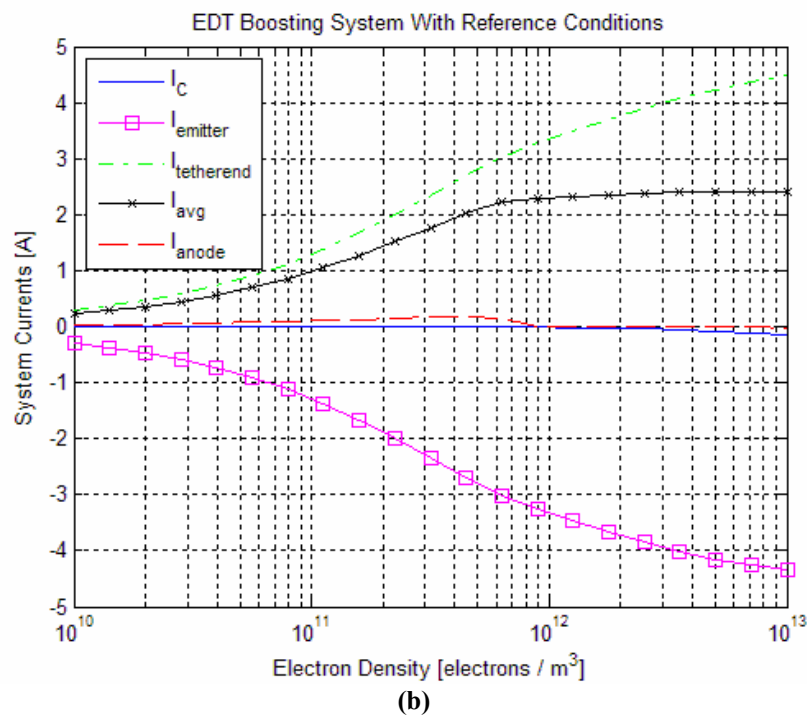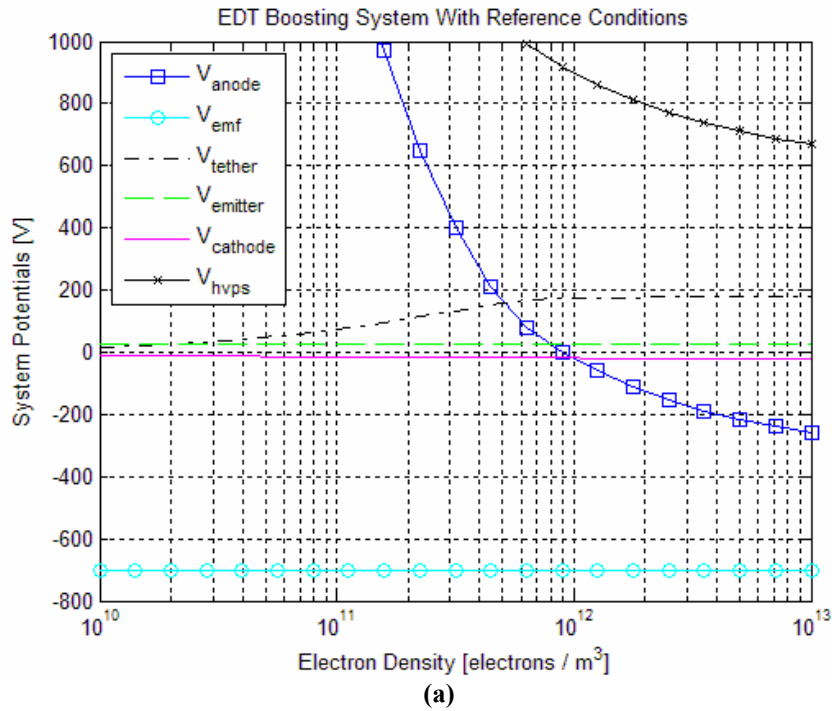
Figure 5-11: The a) potential and b) current profiles of a boosting scenario varying density.

A notable observable difference occurs where the boosting force of the 500 m and insulated case exceed the force of the 2500 m case (around 50 Ω/km and 300 Ω/km, respectively), as seen in Figure 5-9b. This is due to the fact that there is a transition from positive to negative V_{anode} within the 2500 m solution as explained earlier in this Section.

This change causes the decline in boosting force to occur more rapidly than the insulated or 500 m bare case because the endbody is collecting ions rather than collecting electrons.

Figure 5-12 displays the results for bare and insulated tethers for the boosting case. It can be seen where the density begins to maximize the thrust in Figure 5-12a; however, the maximum is not achieved in the insulated tether case for the electron densities given and shown in Figure 5-12b. Table 5-4 reviews the percentage differences for the cases in Figure 5-9 within tethers, for the HVPS, the tether resistance, and the electron density of the boosting case. The data reveals exactly how much more boosting force one case exhibits over another for this particular setup.

HVPS Power vs. Density vs. Boosting Force for a Reference Tether System
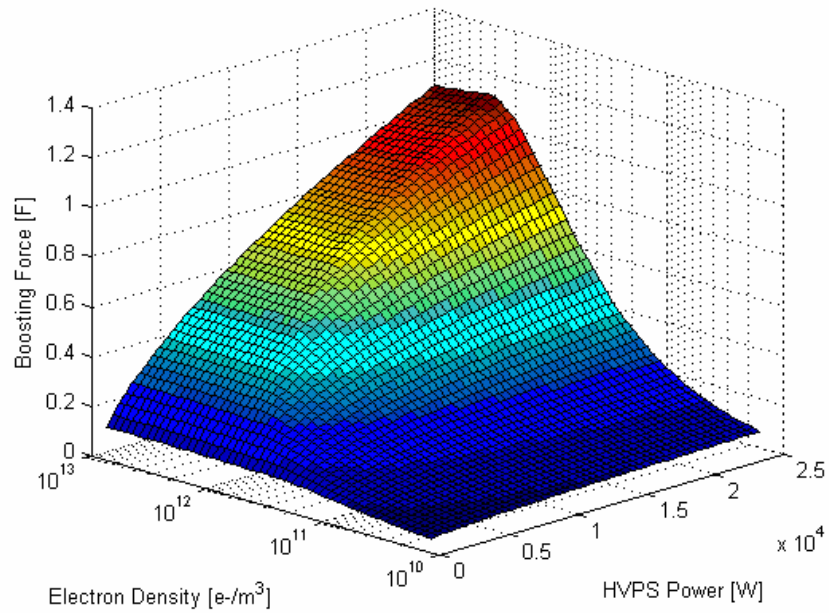
(a)

HVPS Power vs. Density vs. Boosting Force for an Insulated Reference Tether System
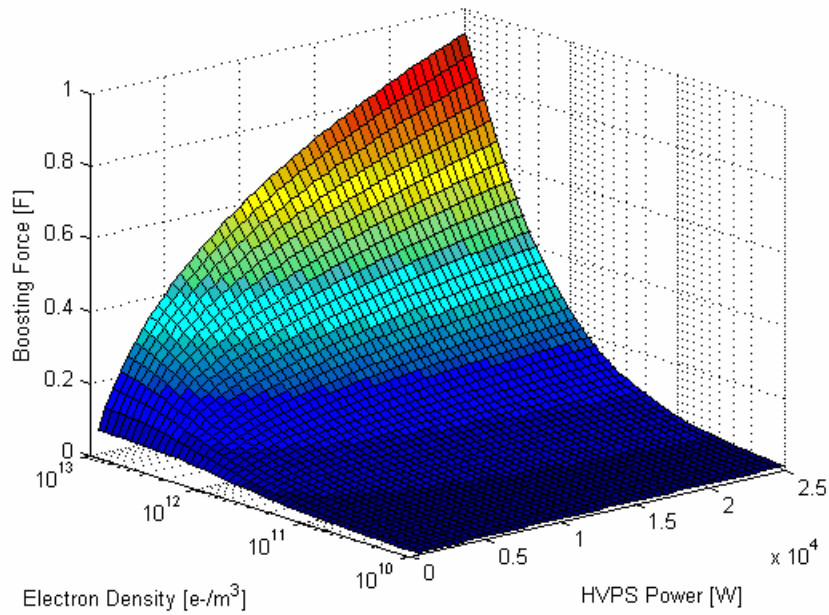
(b)

Figure 5-12: 3d-Plots of the tether resistance versus electron density versus the boosting power for (a) a 2500 m bare tether endbody collector and (b) a completely insulated tether.

142

Boost	Resistance Change [Ω/km]			Plasma Density Change [m^{-3}]		
Bare Tether Lengths	1 to 10	10 to 100	100 to 1000	10^{10} to 10^{11}	10^{11} to 10^{12}	10^{12} to 10^{13}
2500	-13	-42	-63	330	137	6
500	-3	-23	-56	358	262	50
0	-1	-7	-39	350	319	154

Bare Tether Lengths	High Voltage Power Supply Change [kW]				
	0.8 to 5	5 to 10	10 to 15	15 to 20	20 to 25
2500	339	51	23	15	11
500	190	36	18	12	9
0	128	31	16	11	9

Table 5-4: Percent changes in thrust for each tether as tether resistance, plasma density, and power are changed for the boosting condition.

5.3 Vary the Length and compare across emitters

The next simulation was to discover the implications of altering the total length of the tether in the system, while maintaining the fraction that is bare. It was observed in Section 5.2 that there was an optimal length of bare tether for the particular tether system chosen across the three differing emitters for the reference system configuration. In these simulations, the tether is always kept half bare for the HC and FEA cases, and one fifth bare for the TC cases. This is because, as discussed in Section 5.2, the maximum force for the reference system using a TC electron emitter was found at this bare tether length. In order to understand the physical effects occurring, the reference system configurations for each emitter will be analyzed with variations in the density and tether resistance for both the boosting and de-boosting cases. In addition, for the boosting case, the high voltage power supply will also be analyzed. An important fact to recall throughout this section is that the V_{emf} increases linearly as the length increases, according to Eq. 1-1. Also, the basic understanding behind the effects of varying the density, resistance, and P_{HVPS} are explained by the descriptions given in Section 5.3.2. This section focuses on discussing the added parameter of increased bare tether length.

5.3.1　　Hollow Cathode Emitter: De-boosting and Boosting

Figure 5-13a and b show the de-boosting thrust of the reference system configuration as a function of total tether length, with density and tether resistance as parameters. It can be observed in the de-boosting case that the forces vary linearly with increasing tether length for certain situations. As the tether length is initially increased (e.g. $0 - 3$ km for $n_e = 1$ x 10^{11} m^{-3}), the V_{emf} also increases along with the physical collection area. This allows the tether to also collect more current. Using KVL from Eq. 3-7, the variables that make a significant change are the V_{anode}, V_{tether}, and V_{emf}.[35] It can be seen in Figure 5-13a that as the bare tether length increases, the tether system continuously increases in de-boosting force. The longer tether increases the V_{emf}, according to Eq. 1-1. From KVL, the V_{anode} and V_{tether} are shown to increase, as seen in the I-V plots of Figure 5-14. As the bare tether length initially increases, this causes the increase in the V_{anode}, and the system collects more current. This causes the V_{tether} to increase because the average current is increasing, as explained in Eq. 3-23. As the tether length continues to increase (e.g. > 3 km for $n_e = 1$ x 10^{11} m^{-3}), less current is needed from the spherical endbody collector because of the increased exposed conducting tether. As a result, the V_{anode} reaches a maximum potential point and remains virtually constant, shown in Figure 5-14. Using KVL, since the V_{anode} is nearly constant, the only variables significantly shifting are the V_{emf} and V_{tether}. The magnitude of the average tether current does not change much; however, this average is held along a continuously longer length of tether as the total length increases. This produces the linear increase in thrust seen in Figure 5-13. Figure 5-13 varies the bare tether length up to 100 km; however, for this particular scenario, the important effects occur within the first 10 km, so that amount is magnified for observation purposes.

---

[35] There is no V_{load}; V_{emit} is a constant 26.5 V; $V_{cathode}$ is ~30 V for HCs (see Figure 2-22).
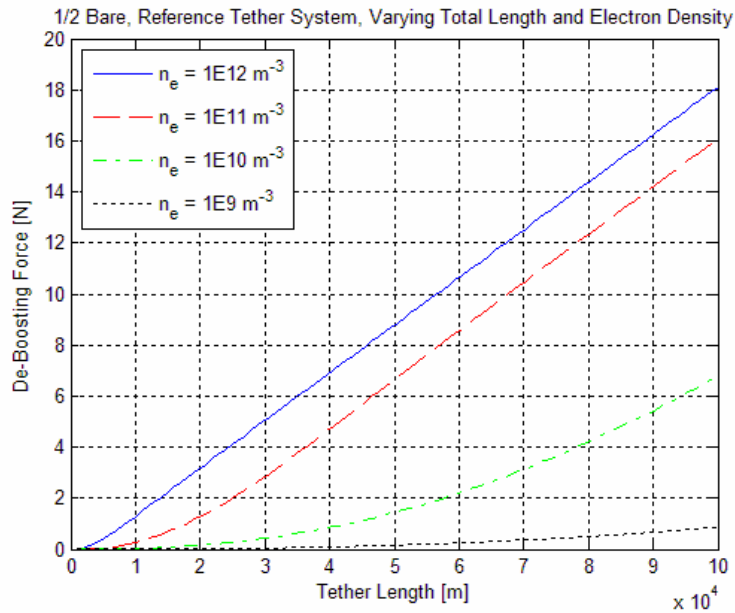
(a)
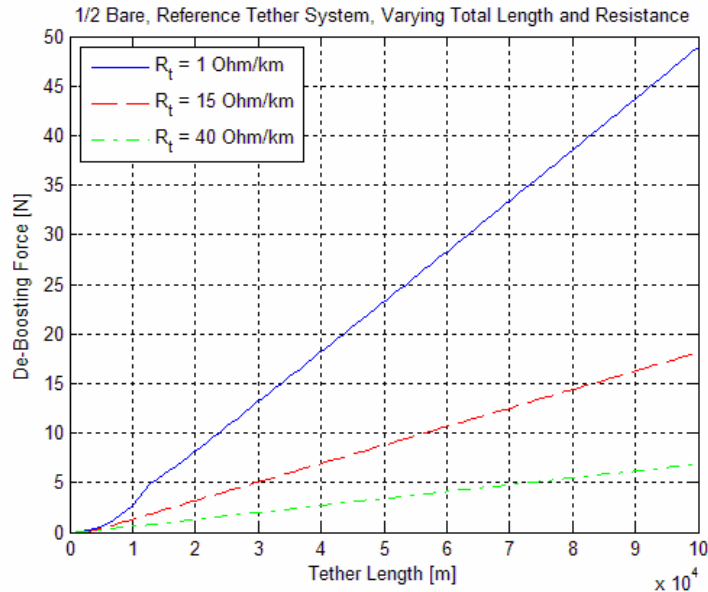
(b)

Figure 5-13: Hollow cathode de-boosting cases for a reference system configuration (while maintaining a 50% bare tether) varying tether length and comparing (a) density and (b) tether resistance.
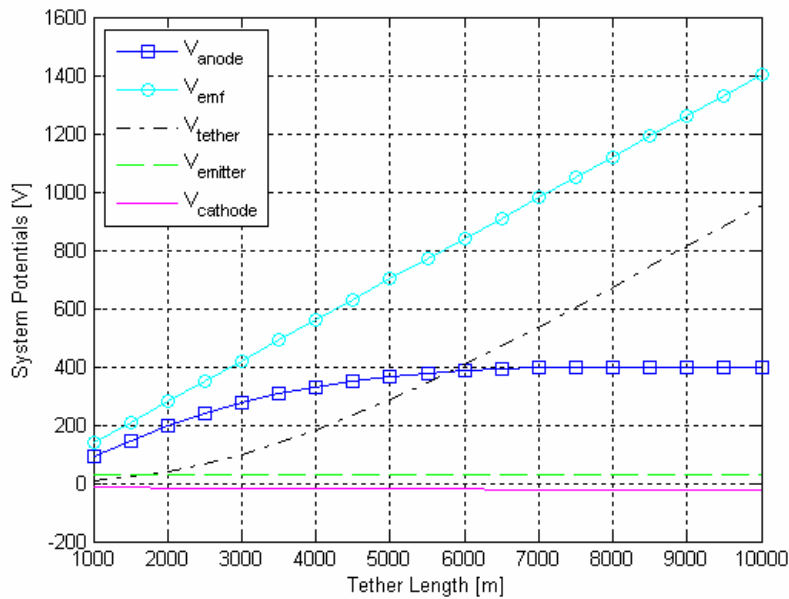
(a)
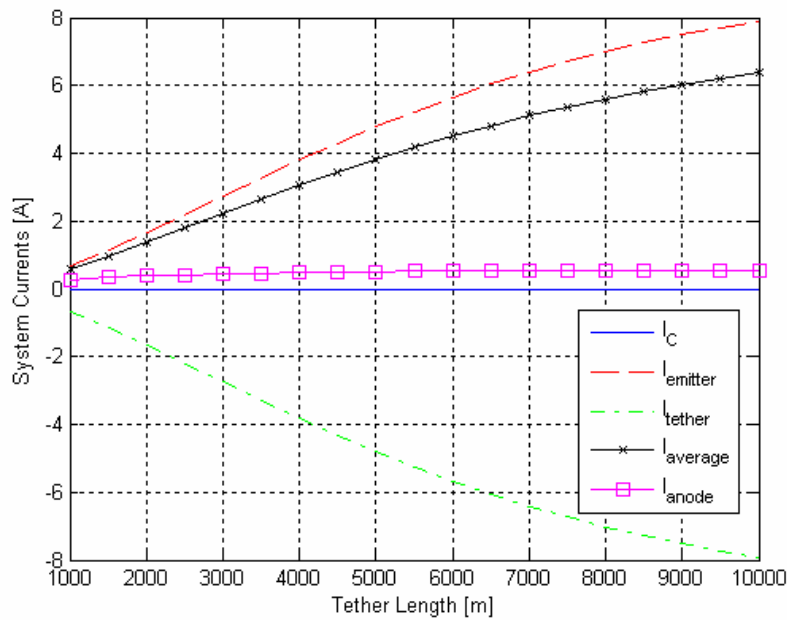
(b)

Figure 5-14: A (a) potential and (b) current profile for an HC de-boosting scenario as the tether length increases for a reference system configuration (while maintaining a 50% bare tether).[36]

A point of interest can be seen in the first 13 km of tether for the 1 Ω/km test case in Figure 5-13b. In this case the same process initially occurs as the reference case,

---

[36] The tether length x-axis scale is reduced to 1,000 m to 10,000 m to visually see the changes better. The plotted lines remain relatively constant from 10,000 to 100,000 as plotted in Figure 5-13.

previously explained. The system, however, collects much more current because of the reduced loss from the small tether resistandce. As a result, the current is capped at 25 A because that is the electron emission limit of the HC.

A reference boosting tether system is shown in Figure 5-15 with density, tether resistance, and P_{HVPS} used as parameters. As before, when the length is increased, the bare tether surface area and the V_{emf} linearly increase. Initially, the increased surface area allows the tether to draw more current. The increase in resistive tether length, as well as the average current, causes the V_{tether} to escalate. In addition, from Eq. 3-18, the increase in current also causes the HVPS potential to decrease (in a constant power mode). The $V_{cathode}$ and HC $V_{emitter}$ don't have a significant effect as in the de-boost case. KVL shows that the V_{anode} needs to drop, since the increase in tether surface area accounts for the additional current collected from the endbody collector. This is similar to the de-boost case. This current and voltage relationship for a reference system that maintains a 50% bare tether can be seen in Figure 5-16. This same reference system can be seen in Figure 5-15 as a) the $n_e = 1 \times 10^{12}$ m^{-3} case, b) the R = 15 Ω/km case, and c) the $P_{HVPS} = 3000$ W case.
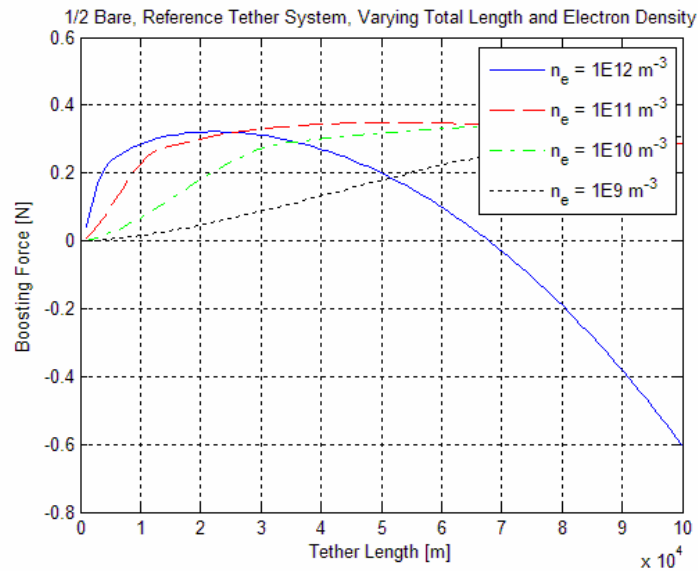
(a)
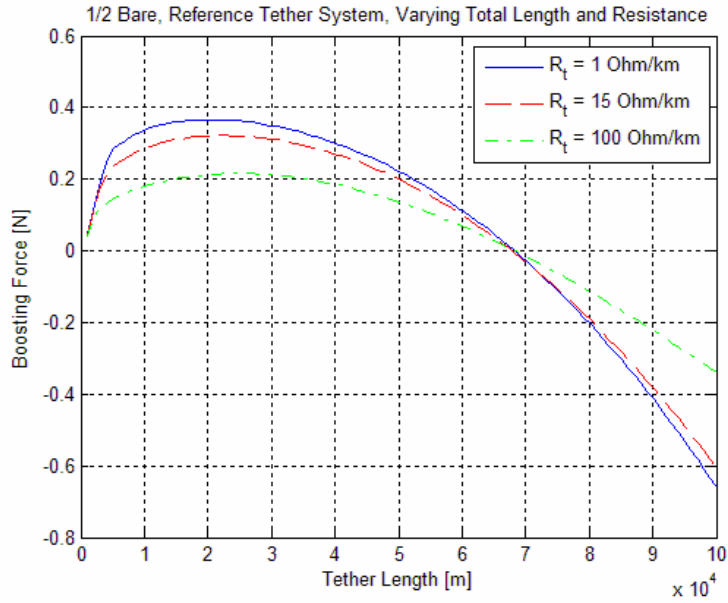
(b)
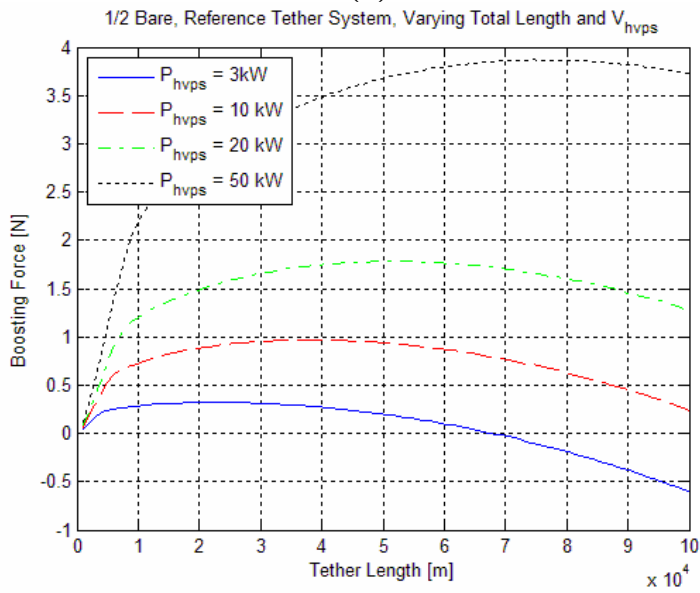
(c)

Figure 5-15: HC boosting cases varying tether length for (a) density, (b) tether resistance, and (c) the high voltage power supply for a 50% bare tether.

148
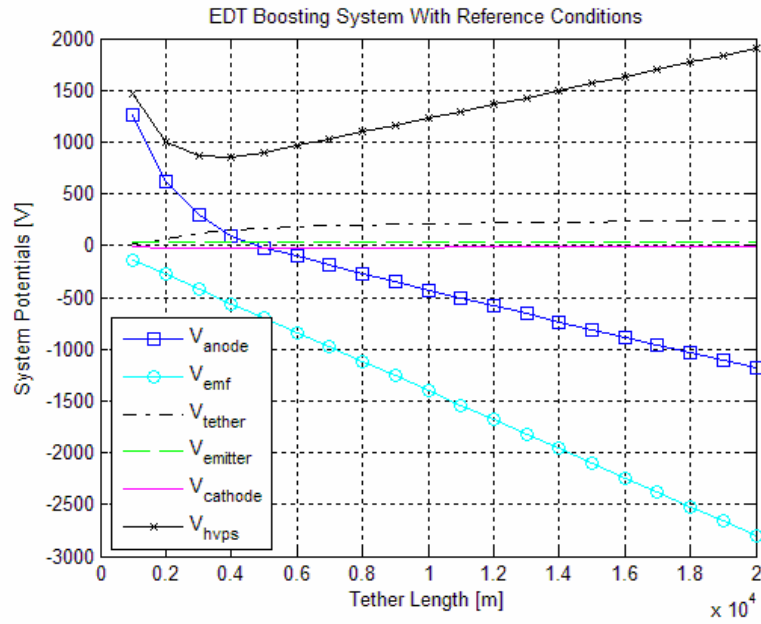
(a)
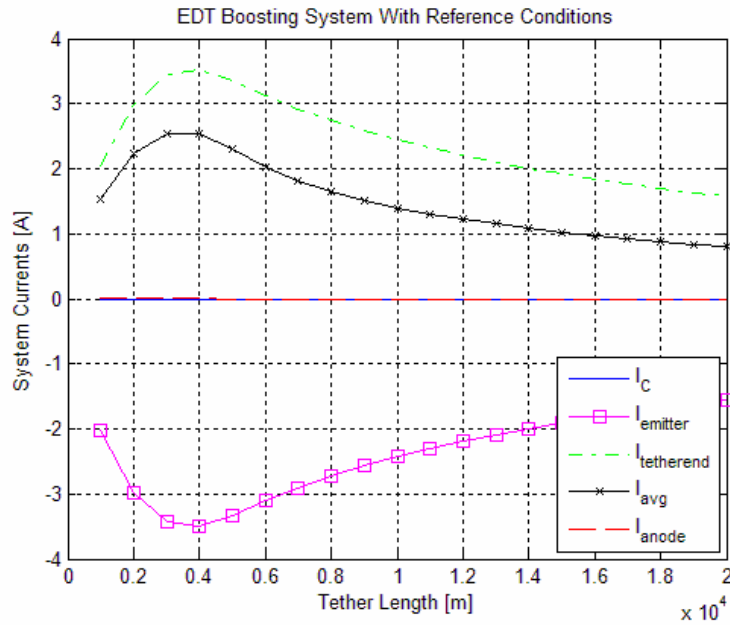
(b)

Figure 5-16: A typical (a) potential and (b) current profile for a HC and FEA boosting scenario (while maintaining a 50% bare tether).

Eventually, increasing the bare tether length reaches a point where the total current collection begins to decrease, as seen in Figure 5-16 because the tether end potential becomes negative reducing the net current collected. For this simulation the total HVPS power remains constant. Initially using KVL, the increase in V_{emf} results in

the reduction of V_{anode} since there was less potential to drive the current across an increasingly longer resistive tether. The increase in conductive surface area still allowed for the collected current to increase. The V_{emf} continues to grow with the increasing tether length, and the decreased average current collection causes the V_{HVPS} to increase, since the power supply is constant. These conditions continue until the tether system can no longer maintain a boosting force.

5.3.2   FEA: De-boosting and Boosting

The same de-boosting system setup was simulated as in the HC case previously discussed in Section 5.3.1, except an FEA was used for electron emission. The particular FEA configuration used here is called the grounded gate, as seen in Figure 5-2b, and the emitter is allowed to float to whatever potential the end of the system results in with the FEA chosen. The only restriction is that the potential from the gate to the tip cannot exceed ~59 V, as seen in Section 2.5.3, since that will damage the emitter. It is assumed that a potential monitor will be used to prevent this from occurring. The de-boosting force versus the variations in electron density and tether resistance over a tether system as the length increases results in nearly identical performance to that of the HC data. This is because the physics of the system do not change, only the values associated with the emission. The FEA requires from 0 to ~59 V gate bias, whereas the HC is set at ~27 V for its bias. The maximum current emission capability of the FEA chosen for this analysis was set to a maximum of ~10 A, whereas the HC chosen was set at a maximum of 25 A. This indicates that any time a system requires the electron emitter to release more than its maximum amount of current, it will be capped unless multiple emitters are used. Another limiting factor is the space charge limit, as discussed in Section 2.3. Since the spacecraft is allowed to float, the $V_{cathode}$ will usually be at floating potential, or ~0 V with respect to the plasma, as seen in Figure 5-16.

The boosting condition for an identical FEA system was also found to be nearly identical to the HC case. The only difference observed in the boosting case, which was similar to that of the de-boosting case, was that the maximum current emitted by the FEA

was also sometimes capped due to the lower maximum current emission. This issue was also addressed by using multiple emitters.

Overall, the FEA biased tether system had nearly identical performance when compared to the HC. The energy required to operate the two systems is also nearly equivalent. The only energy difference would be that required to initiate the thermionic process (which begins the electron emission in an HC). In addition, the hollow cathode requires consumables in order to operate, while the FEA does not.

5.3.3   Thermionic Cathode Emitter: De-boosting and Boosting

The TC electron emitter case was subjected to the same simulations as the HC and FEA. The major difference for this setup was the proportion of bare tether. It was determined in Section 5.4 using Figure 5-5 that the optimal amount of bare tether was found to be approximately 20% bare for the system designed in that section. It was also determined that the optimal amount of bare tether varies according to many variables. However, in order to maintain the consistency of the simulations with the original optimal determination, the analysis for the TC presented here was also kept at 20% bare as the total length increased.

The system setup configuration is the same as used for the FEA analyses, called the "floating grounded gate", as shown in Figure 5-2b. Other differences with the thermionic cathode emitter is the emission potential required to operate it. While the FEA and HCs selected for these analyses requires up to 59 V and ~27 V to operate, the TC selected requires up to 2500 V to operate.

The de-boosting scenario using the TC, as seen in Figure 5-17, behaves slightly different to the hollow cathode and FEA cases. The non-linear phenomenon occurring in the shorter tether lengths are more emphasized for the TCs. The boosting increases until it hits a critical point, at which point it continues a linear de-boosting force increase with the increasing tether length. The potentials and currents involved interact in slightly different ways, however.
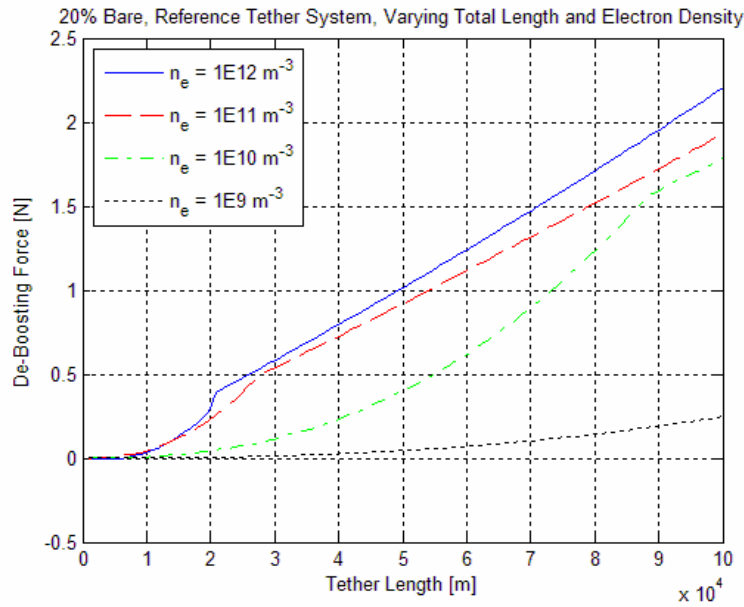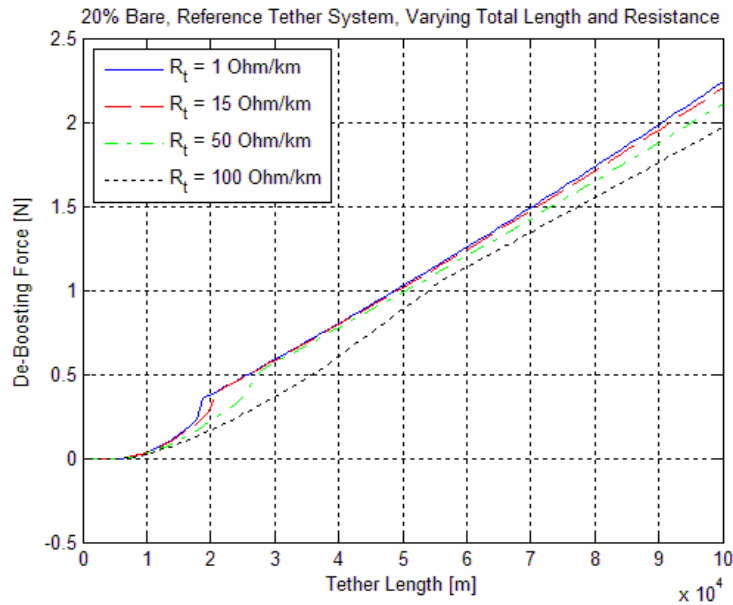
Figure 5-17: Thermionic cathode de-boosting cases varying tether length for (a) density, and (b) tether resistance for a 20% bare tether.

As seen in Figure 5-18, as the tether length increases I_{avg} increases because of the increasing bare collecting surface area increase and the V_{emf} increases. At smaller tether lengths, below ~5 km, the de-boosting force is shown to be negligible in Figure 5-17. This is because the potential required to emit the electrons from the TC (which is driven by the V_{emf} using KVL) is too great to yield much current. On longer tethers, as the V_{emf}

152

continues to increase, the V_{anode} increases and collects more current until it becomes a positive potential. From here, the $V_{emitter}$ begins to rise as the current needed to be emitted increases (from 0.02A @ 900 V and 7 km tether length to 0.92 A @ 2500 V and 22 km tether length for this reference system configuration), as seen in Figure 5-18. This increase occurs until the emitter abruptly hits its maximum emission potential of 2500 V. The $V_{cathode}$ now increases in order to compensate for the emitter potential remaining constant to satisfy KVL. After this point, the same phenomenon occurs as the other two emission devices. The V_{emf} continues to increase and the average current remains approximately the same. However, since the tether length increases, the amount of tether length with this higher current increases. This increases the total thrust.
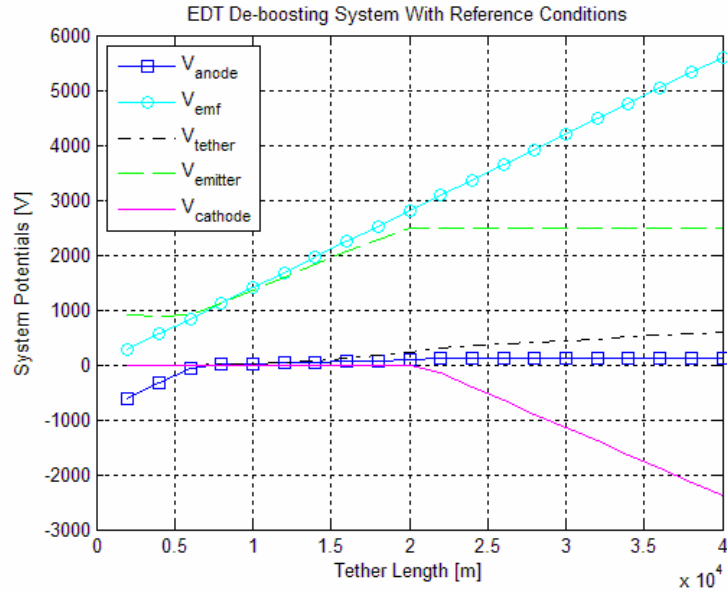
(a)
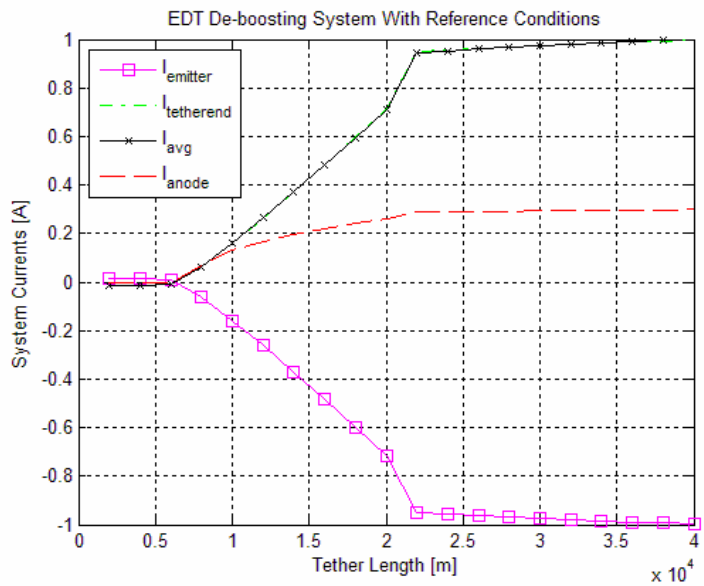
(b)

Figure 5-18: A typical (a) potential and (b) current profile for a de-boosting reference system configuration using a TC with a 20% bare tether.

The boosting cases for the TC emitter scenarios also behave slightly differently compared to the HC and FEA cases; however, the same mechanisms are at work. Figure 5-19a, b, and c display the results of the comparative analysis using the 20% bare TC emitter in a reference system configuration. The major reason for the differences in the trends is because only $1/5^{th}$ of the tether is insulated. If the plots were extended to 200

km, then an identical trend would be observed. The only minor discrepancy results from a larger emitter potential, which drives up the HVPS potential.

Overall, the TC power efficiency is lower than the HC and FEA, as seen in Figure 5-5. In addition, the energy required to emit the current is much greater than the other systems. The current emitted is also smaller since common TC emitters used in industry are only capable of emitting 1 to 3 A continuously for long periods of time. The potentials required to operate these emitters range from 2500 V for 1 A to up to 20,000 V used in some of the larger TC models [5]. There is also energy required to heat the cathode for its operation that must be accounted for.
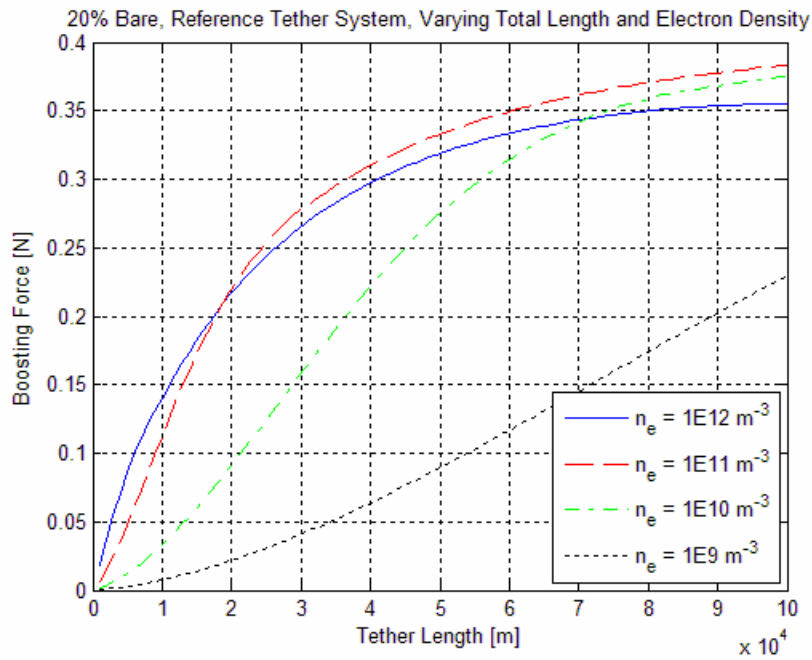
(a)
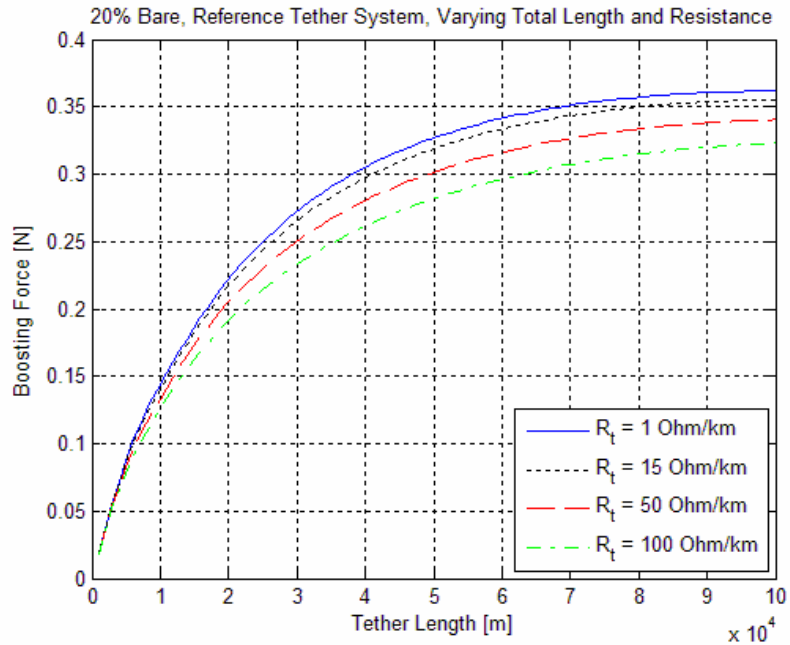
(b)
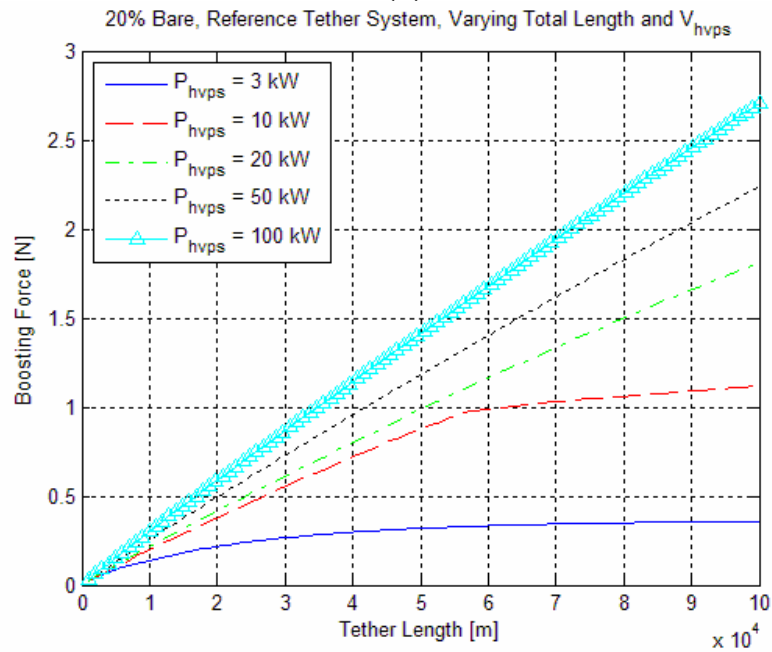
(c)

Figure 5-19: Thermionic cathode boosting cases varying tether length for a 20% bare reference system configuration altering the (a) density, (b) tether resistance, and (c) the high voltage power supply.

5.4 EDT Endbody Collection Comparison

Trying to discern what type of endbody collector a tether system could benefit most from is an important aspect that can determine whether the system will be heavy, complex, or consumable dependant. HCs, various size endbodies, and no endbody will be discussed as they apply to the reference EDT configuration for boosting and de-boosting cases.

5.4.1 De-boosting

Figure 5-20 displays the variation of de-boosting force versus bare tether length for various passive spherical endbody collector sizes as well as an HC endbody collector, all used in a reference system configuration for the de-boosting case. It can be seen that the increasing bare tether length increases the amount of boosting force by allowing more exposed conducting surface area that can collect current. This fact is consistent with all other de-boosting cases presented in this chapter. As the endbody collector size increases, it requires less V_{anode} to collect an equivalent amount of electron current due to the increased surface area. This continues to occur until all the electron current that the cathode end can emit is collected by the endbody and bare tether, and an increase in bare tether length has no effect (as indicated by the 10 m and 20 m radius endbody collectors in Figure 5-20). The hollow cathode endbody collector chosen for this case is shown to produce enhanced de-boosting effects over the 1 m radius endbody collector, but less than that of the 5 m radius endbody collector, as seen in Figure 5-20.
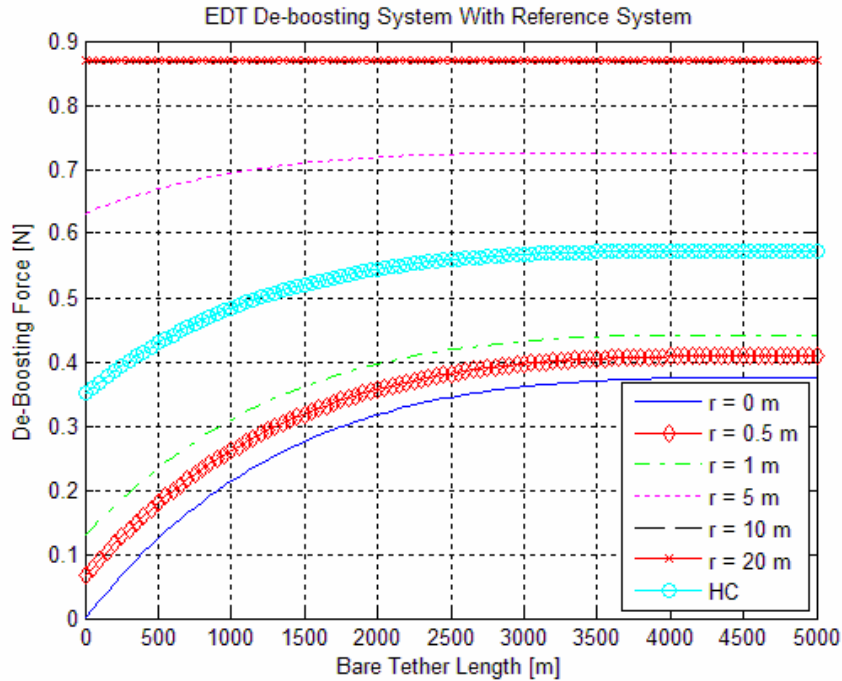
Figure 5-20: De-Boosting forces resulting from different endbody collectors across a variable bare tether length on a reference system configuration.

Figure 5-21 displays the potential and current profiles for the reference system configuration de-boosting case. In this case the current collected by the endbody collector is less than 1 A, and the potential is above 300 V. Increasing the radius size of the spherical endbody collector will cause the V_{anode} to decrease until it reaches the floating potential and stops collecting electron current. The V_{tether} then increases until it approaches the V_{emf}. This results in an increasing average current that becomes constant as the tether becomes fully bare, as seen in Figure 5-21.
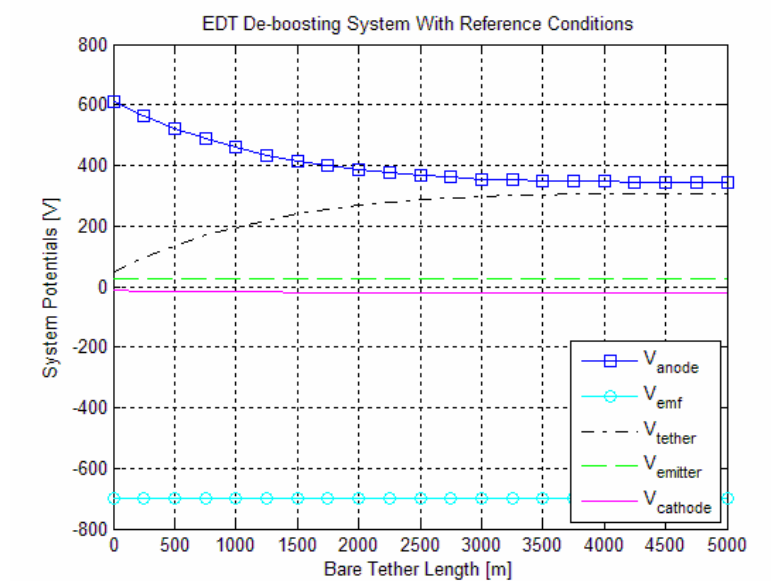
(a)
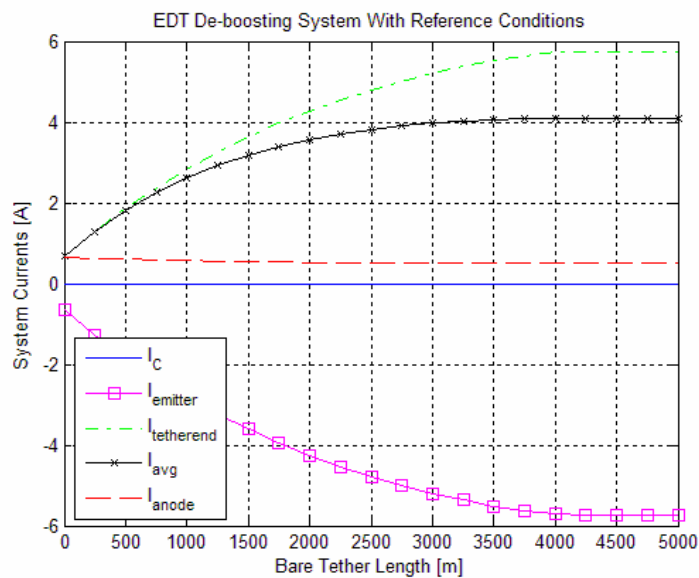
(b)

Figure 5-21: A (a) potential and (b) current profile for a HC de-boosting reference system configuration.

5.4.2 Boosting

Figure 5-22 displays the results for various size spherical endbody collectors, as well as an HC endbody collector used in a reference system configuration for the boosting case. In this scenario, a similar phenomenon is occurring where the increasing bare tether length and set power supply (the HVPS in this boosting case) predominantly

determine the results. In the boosting case, the endbody collector is capable of becoming negative, unlike the de-boosting case.
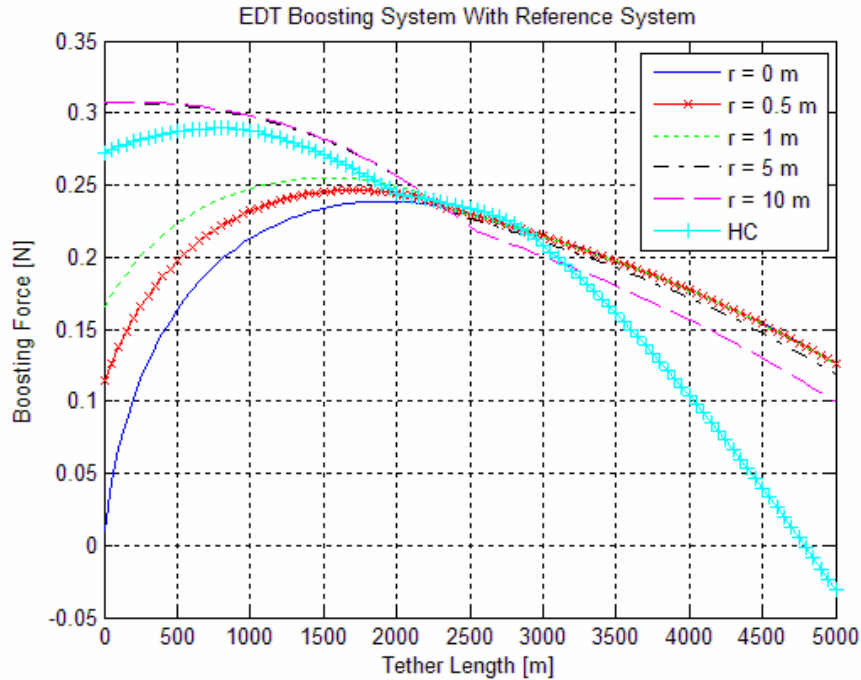
Figure 5-22: Boosting forces resulting from different endbody collectors across a variable bare tether length.

There are various trends that occur across the endbody collectors. In Figure 5-22, for bare tether lengths shorter than 2500 m the V_{anode} is positive. Here, the size of the endbody collector makes a difference up until a certain radius. Similar to the de-boosting cases, the larger the spherical endbody collector, the more boosting force results at lower bare tether lengths. As the endbody collector size continues to increase, a maximum boosting force will be reached. This can be seen in the 5 m and 10 m plots. For these large spheres, all the current that the EDT system can collect will be accomplished at the endbody collector. Any increase in the bare tether amount will only serve to reduce the boosting force. In addition, as in the de-boosting case, the larger the endbody collector the lower the endbody collector potential needed to collect that current.

For each EDT system, the V_{anode} becomes zero between about 2000 m and 3000 m of bare tether. As a result, each of the cases boost an equivalent amount at that zero potential point. The slight difference is due to the passive ion current that is being collected by the sphere now that it is negative. For each of the tether cases, once the

spherical endbody collector becomes negative, after about 3000 m of bare tether the boosting force drops off at similar rates. For passive spheres, the factor that determines the rate of boosting force decrease is the radius of the sphere. Larger radius spheres collect more ion current when the V_{anode} is negative. In the case of the hollow cathode where the potential of the keeper, with respect to the plasma, approaches zero, there is a range where it emits little to no current. This can be seen when the bare tether length of the HC endbody collector case in Figure 5-22 is between ~2000 m and ~2700 m. After that point, when the HC keeper is biased negative with respect to the plasma, it begins to rapidly emit electrons. This mechanism is what causes the more rapid decline in boosting force for the HC endbody collector EDT system as the bare tether length increases.

The potential and current profiles for the reference system configuration as the bare tether length increases are shown in Figure 5-23. The I_{avg}, I_{anode}, and I_{end} currents all begin at the same point when the tether is completely insulated. As the bare tether length increases, the V_{anode} required to collect the I_{anode} becomes less. Aside from the V_{anode}, V_{emf} and V_{HVPS}, all the remaining potentials are small and unchanging as the bare tether length increases.
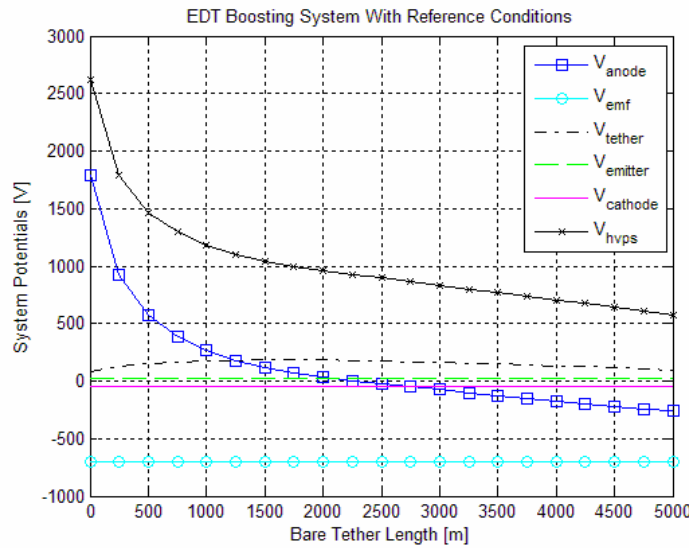
(a)
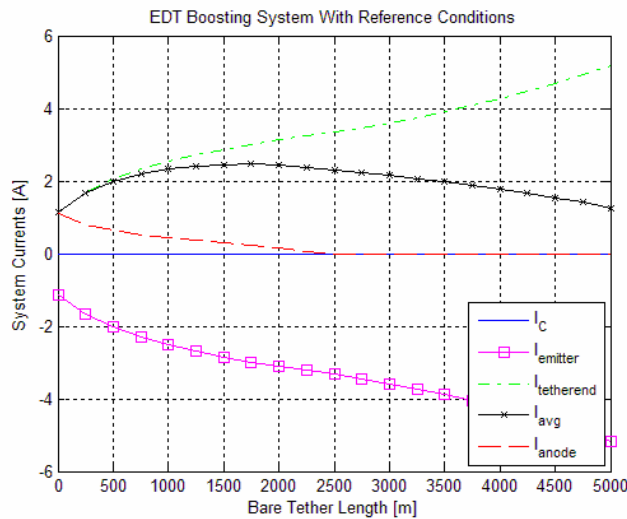
(b)

Figure 5-23: A typical (a) potential and (b) current profile for a HC boosting scenario with a 0.5m endbody collector.

In certain cases when the V_{anode} is driven to zero, it would reduce the system mass and improve boosting performance without an endbody.[37] It can be seen in Figure 5-22 that this is in fact true in certain circumstances. When the bare tether length is greater than ~2500 m, in this particular case, the endbody collector begins to collect ions rather than electrons and the thrusting trends reverse. The smaller the endbody collector, the larger the boosting force, but by only a few percent. In addition, it can be seen that for

---

[37] An endmass is still required to maintain the gravity gradient force which keeps the tether taught, defined by Eq. 6-2.

endbody collector sizes up to 1 m in radius, the boosting forces are within 1% of each other.

Due to the high electron emission capabilities of HCs, they appear to behave similarly to a spherical endbody collector between 1 m and 5 m, as seen in Figure 5-22, up until about 2500 m of bare tether. As the amount of bare tether increases, it is seen to drop off rapidly in thrusting capability. Around 4800 m of bare tether length, the HC endbody collector system ceases to even boost the system.   The reason for this discrepancy between the HC endbody collector and the spherical endbody collector stems from its ability to rapidly emit electrons when it is negatively biased with respect to the plasma.

Figure 5-24 shows that when the potential of the keeper with respect to the plasma for an HC is less than zero, the hollow cathode emits electrons at a much more rapid rate than a passive sphere can collect ions. This figure displays the passive collection current profile with the HC profile of Figure 2-11, as explained in Section 2.5.1. Figure 5-25 displays an example of the current along the length of a tether for the HC endbody collector system (seen in Figure 5-22) when 3500 m of the tether is bare. In this plot, all of the electrons collected by the bare tether are being emitted from the HC at the endbody collector side of the tether. From the endbody collector to the point where the current equals 0, (around 1500 m) the resulting force is a de-orbiting force. The total force produced by the flow of current on the remainder of the tether, however, is still enough to overcome the de-orbiting force, as seen in Figure 5-22.
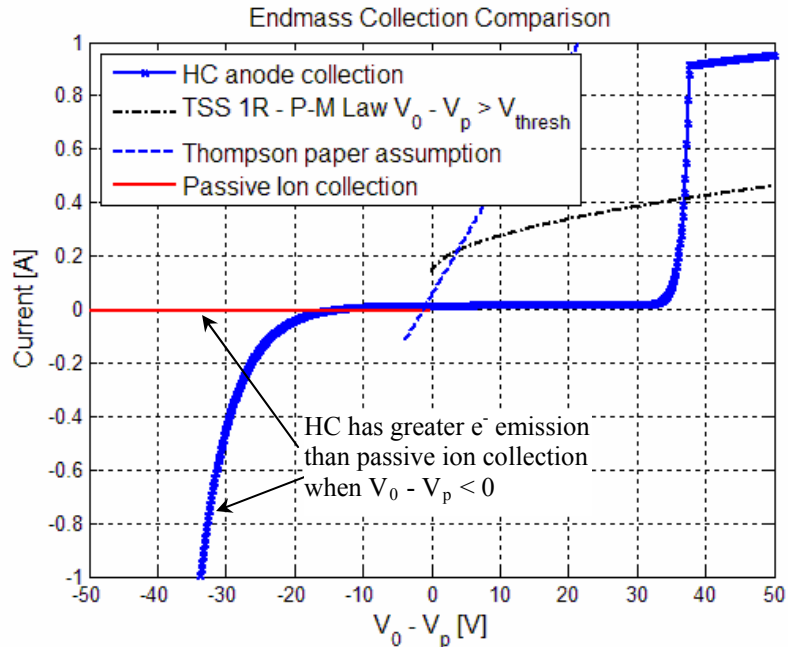
Figure 5-24: Comparison of a HC (as described in Section 2.2.4) and a 1 m passive sphere (as described in Section 2.5.1) current collection using reference ambient conditions
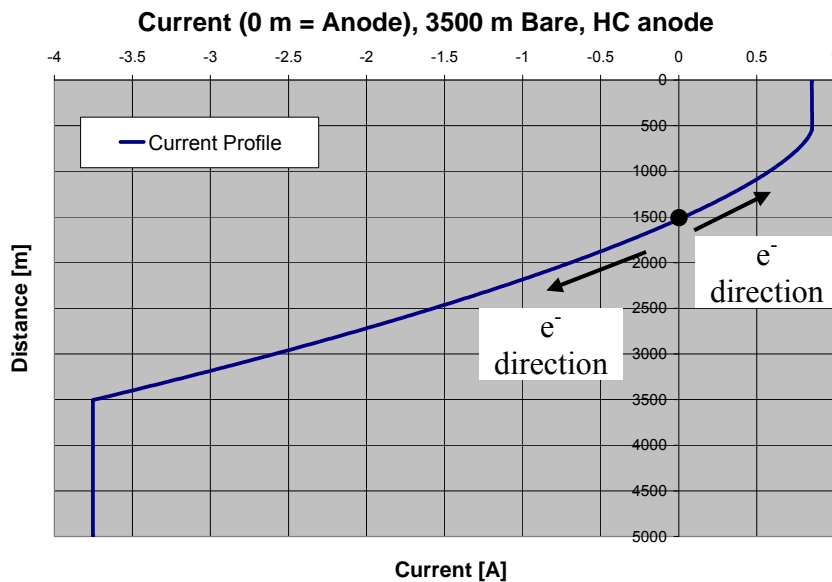
Figure 5-25: Current profile for a reference case using an HC endbody collector with 3500 m of bare tether

The constantly changing ambient conditions throughout an orbit cause the thrusting condition to vary significantly as well. The HC produces a much more rapid deterioration in thrust than a bare tether or spherical endbody collector, when the V_{anode} is negative. The HC, however, can also offer an enhancement to the tether boosting thrust

over that of a bare tether alone or small collecting endbody. In addition, larger spheres produce much more atmospheric drag, according to Eq. 4-2. These factors must be considered when determining the best endbody collector for the system.

5.5 Simulating Various Tether Geometries

From the experimental data obtained in Chapter 4, it was possible to compare actual electron collection tether geometries and orientations with respect to a particular Debye length. The perpendicular and parallel oriented (with respect to the flowing plasma) holed tape geometries were compared to a thin wire reference cylinder ~1 Debye length in radius. In order to compare values useful for system trades, the values of the experiment were adjusted to compare an equivalent mass tether system. The atmospheric drag and lifetime of the tether design are important considerations that will be discussed as well. The goal of this simulation is to use experimental values for electron current collection in a flowing plasma to predict the electrodynamic tether system performance, in order to understand the system tradeoffs involved.

In order to design a useful simulation, the dimensions of the tethers must be similar with respect to the Debye length. It was assumed that at the 75 cm experimental test case the plasma was 95% flowing. This is the closest test case to the actual ionospheric flowing plasma (100%), and thus was chosen for the simulations of this section. At 75 cm, the plasma density of the experiment was 4.95 x 10^{15} m^{-3} and the electron temperature was ~1.8 eV, which produced a Debye length of 0.14 mm. In the ionosphere at approximately 300 km, the typical extremes for electron density can range from ~1 x 10^{10} m^{-3} to ~1 x 10^{12} m^{-3} on a daily basis. The electron and ion temperatures, however, remain close to 0.1 eV. Using the measured tape dimensions in Debye lengths from Table 4-2 and Table 4-3, the equivalent dimensions of the medium holed tape, large holed tape, slotted tape, solid tape, and reference cylinder can be calculated for the ionosphere. These values can be seen for electron densities of 1 x 10^{10} m^{-3} and 1 x 10^{12} m^{-3} in Table 5-5. The dimensions of width, W, thickness, T, and surface area, SA, are displayed. The surface area is given in units of m^2 of tether per meter length of tether. The perpendicular medium holed tape and parallel large holed tape geometries were

chosen because they were the most efficient collectors for their respective orientations. An important system trade to investigate is the results of a system using equivalent mass. As a result, since the slotted and holed tapes were 50% porous, it took two of them to equal the mass of a solid tape. Since there are two tapes, assuming that there are spaces far enough apart so there are no sheath interactions, they will collect twice as much current as a single tape. In the case of the reference cylinder, it was found that the holed tape samples were approximately 4.7 times more massive per meter than the reference wire. In order to compare an equivalent mass tether using an integer number of wires, dimensions were obtained such that 5 tethers equaled an equivalent mass. This is done because the radii of these 5 tethers are all slightly smaller than the original reference cylinder in the experiment. It is shown by Choiniere that all cylinders that are smaller than ~1 Debye length collect according to OML theory [66]. Similar to the slotted and holed tapes, the current collection of the reference wires will therefore need to be multiplied by 5 in order to account for an equivalent mass. This also assumes that these wires are spaced far enough apart so that proximity doesn't interfere with established OML collection amounts.

5000 m tether No endbody collector	Experiment			$n_e = 1 \times 10^{10}$ m^{-3}			$n_e = 1 \times 10^{12}$ m^{-3}		
	W [mm]	T [mm]	SA each (total) [m^2/m]	W [mm]	T [mm]	SA each (total) [m^2/m]	W [mm]	T [mm]	SA each (total) [m^2/m]
2 ⊥ Medium Holed Tapes	2.89	0.1	0.0039 (0.0078)	485.2	16.8	0.665 (1.330)	48.52	1.68	0.065 (0.133)
2 ∥ Large Holed Tapes			0.0037 (0.0074)			0.613 (1.226)			0.061 (0.123)
2 ⊥ Slotted Tapes			0.0035 (0.0070)			0.591 (1.182)			0.059 (0.118)
2 ∥ Slotted Tapes									
1 ⊥ Solid Tape			0.0060 (0.0060)			1.004 (1.004)			0.100 (0.100)
1 ∥ Solid Tape									
5 Reference Cylinders	r = 0.14		0.00085 (0.00425)	r = 23.5		0.143 (0.715)	r = 2.35		0.014 (0.072)

Table 5-5: Equivalent dimensions of probes for various Debye lengths. The values represent those of an individual tape.

Using the calculated surface areas of Table 5-5 and the experimental results in Figure 4-7a, the collected electron current can be found for an equivalent system in the ionosphere. Instead of assuming OML collection along the tether, the EDT simulation

code developed uses the values obtained from the experiment in Chapter 4 to estimate the actual current collected for the simulated conditions.

For the simulation, the current collection outside the range of experimental results must be used. In order to account for this, best fit curves were found for each of the tether types using Figure 4-7a. An example of the best fit line, along with the experimental data for the reference probe, the perpendicular oriented holed tape, and the parallel oriented holed tape are shown in Figure 5-26. The equations for the curve fits and R^2 values for all the tether types can be seen in Table 5-6.[38] An important note is that, once the EDT normalized potential (V/T_e) value is outside the range of the experimental data, there will always be an inherent unknown associated with the results. The best fit lines assume an exponential increase in normalizing current until a 'knee' is reached, at which point the tape collects approximately linearly. This transition point where the equation of the curve changes, is also detailed in Table 5-6. The tapes are expected to collect approximately at $V^{0.5}$ at higher potentials (beyond the range of this experiment) as demonstrated by Gilchrist et al. [137]. Linear plots were used because they achieved a closer best fit line. For the purposes of this particular simulation, this approximation will do because the normalized potentials encountered lie within the range shown.

---

[38] R^2 is the measure of how well a regression line approximates real data points.
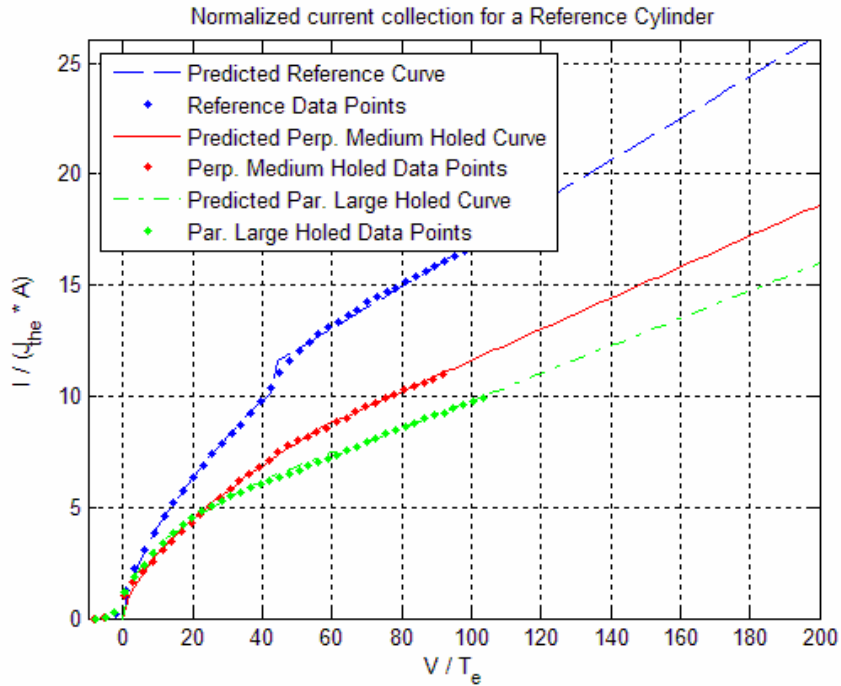
Figure 5-26: The best fit curve and experimental data of the reference wire and medium holed tape.

	Equation	R^2	Transition Point (V/T_e)
Reference Cylinder	$y = 0.962 \cdot x^{0.629}$ $y = 0.095 \cdot x + 7.36$	0.9986 0.9901	43
Perp. Medium Holed Tape	$y = 0.676 \cdot x^{0.628}$ $y = 0.070 \cdot x + 4.59$	0.9978 0.9982	59
Paral. Large Holed Tape	$y = 1.07 \cdot x^{0.473}$ $y = 0.062 \cdot x + 3.56$	0.9965 0.9994	43
Perp. Slotted Tape	$y = 0.767 \cdot x^{0.583}$ $y = 0.059 \cdot x + 4.87$	0.9982 0.9991	73
Paral. Slotted Tape	$y = 0.975 \cdot x^{0.485}$ $y = 0.070 \cdot x + 2.93$	0.9990 0.9990	42
Perp. Solid Tape	$y = 0.792 \cdot x^{0.582}$ $y = 0.044 \cdot x + 5.89$	0.9966 0.9955	61
Paral. Solid Tape	$y = 1.06 \cdot x^{0.466}$ $y = 0.049 \cdot x + 3.85$	0.9940 0.9985	37

Table 5-6: Equation of the best fit line for the reference cylinder and the perpendicular medium holed tape. The transition point between the two equations is also stated.

168

For this data analysis, a modified model for current collection along the tether was used in the *EDT-Survey* and *EDT-Trades* simulation tools. To produce the equivalent currents in the ionosphere, the potential of the tether at each element, along with the known T_e, is input to determine the V/T_e of Figure 5-26. Then, using the equations in Table 5-6, the normalized current, $I / (J_{the} \cdot A)$, is determined. Finally, after using Table 5-5, the current collected at each element of the tether can then be acquired and output into the EDT software.

The system setup for the simulation conducted involved the reference system configuration, with the exception of having no collecting endbody[39]. This setup was chosen to demonstrate the effects of just the tether. The results of these simulations are demonstrated in Figure 5-27. Despite the increased current collection efficiency (per unit area), the reference cylinder boosts less than the slotted and holed tether. The reference boosting still outdoes that of the lower efficiency solid tapes despite their greater surface area. The perpendicularly oriented holed tape results in the most boosting because it collects more current than the reference cylinder as a result of its larger surface area.

---

[39] The resistances were calculated based on the cross sectional area of each other and assuming an equal amount of total power was transmitted across the tethers. (For example, 3 kW went through the solid tape, 1.5 kW went through each slotted and holed sample and 600 W went through each of the 5 reference cylinders.) Thr resulting boosting force of each tether was then summed together to yield the total system boosting force.
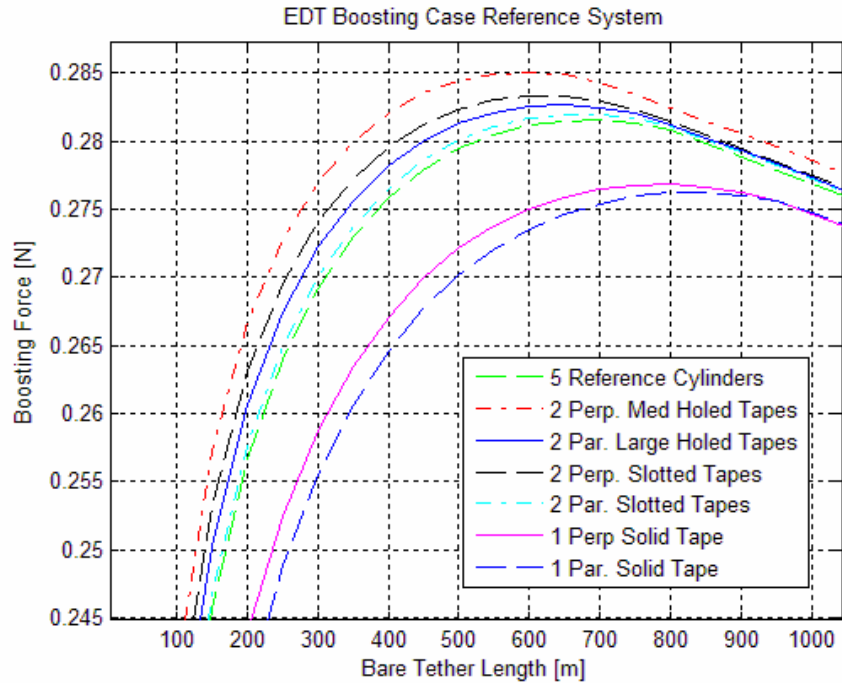
(a)
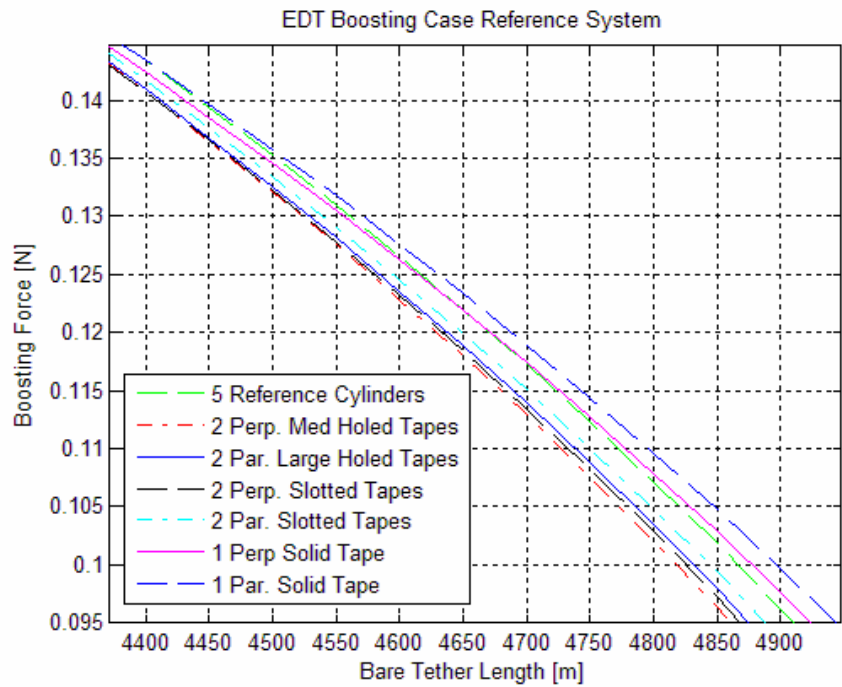
(b)

Figure 5-27: Boosting forces resulting from different tethers (size and geometry) and plasma density across a variable bare tether length in a reference system configuration excluding the 0.5 m endbody collector. The tether size was scaled to be consistent with experimental results of Chapter 4. A blow up of (a) the maximum boosting point and (b) a point where the boosting trends are reverse to that of the max boosting case.

The trends encountered in Figure 5-27 are consistent with phenomena encountered in previous simulations of Section 5.5.2. In the higher electron density case, all three tethers are shown to collect the current rapidly within the first few hundred meters of bare tether. The perpendicular oriented medium holed case was shown initially to collect the most electron current, while the parallel solid tether collected the least, shown in Figure 5-27a. The initially higher boosting perpendicular oriented medium holed tape drops off in thrust more rapidly than the other cases, as the bare tether length increases. At the same time, the parallel oriented solid tape becomes the best boosting tether, shown in Figure 5-27b. This occurs for the same reason described in Section 5.6.2, where the potential of the endbody collector, in addition to the initial sections of the bare tether, becomes negative. As a result, they collect ion current, and reduce the boosting force of the system.

An issue encountered with plotting this scenario stems from the physical size of the tether geometries. As the electron density changes from 1×10^{10} m^{-3} to 1×10^{12} m^{-3}, in order to retain the same experimental proportions, the physical size of the tether must change as well since it is dependant on the Debye length. This factor makes the feasibility of the tether structure relatively unphysical for the 1×10^{10} m^{-3} case, since the tether must be almost 0.5 m wide, as seen in Table 5-5. The drag from that would vastly outweigh the boosting force. As a result, the simulations explored in this section will focus on electron densities of 1×10^{12} m^{-3}.

Another factor that must be considered when evaluating the different tether geometries is the amount of atmospheric drag associated with each tether. The calculation for drag can be seen in Eq. 4-2. At an altitude of 300 km, the average ρ is 1.95×10^{-11} kg/m^3, a typical C_D is 2.2 [18], and the velocity with respect to the co-rotating atmosphere is ~7240 m/s.[40] For a 5 km long tether, the values for the surface area and drag at different densities are described in Table 5-7. The values presented by each of the perpendicular and parallel orientations are the extremes in drag that can be encountered by each respective tether geometry. Throughout the course of a tether mission, the tether will most likely be twisting somewhat due to dynamical forces, as

---

[40] The atmosphere co-rotates with the Earth at 300 km (similar to the B-field), and Table 3-2 is used, assuming a 0º latitude., 0º inclination orbit.

seen in Figure 4-12. In Chapter 4, using Eq. 4-3, the surface area of this twisting affect is calculated and shown in Table 5-7.

ne = 1 x 1012 m-3 (Equivalent Mass)	2-D Cross Sectional Area [m]	Atmospheric Drag [N]
5 Reference Cylinders	117.5	0.13
2 Slotted & Holed or 1 Solid Perpendicular Tape	242.6	0.27
2 Slotted & Holed Parallel Tapes	16.8	0.019
1 Solid Parallel Tape	8.4	0.009
2 Twisted Slotted & Holed or 1 Twisted Solid Tape	159.8	0.18

Table 5-7: The surface area and drag associated with the various tether geometries at 2 different densities.

It is interesting to note that the atmospheric drag of the parallel oriented large holed tape is almost a factor of 15 less than the perpendicular medium holed case, and almost a factor of 7 less than the reference cylinder case. The resulting boosting forces, after the atmospheric drag has been factored in, can be seen in Figure 5-28. In addition, using the method shown in Section 4.6, the approximate current collection between the perpendicular and parallel oriented case was calculated for a twisting tether.
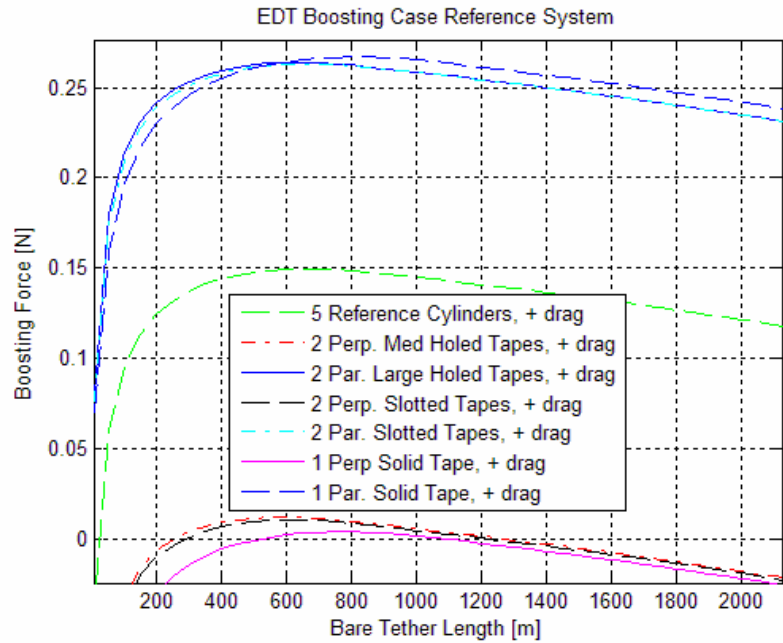
(a)
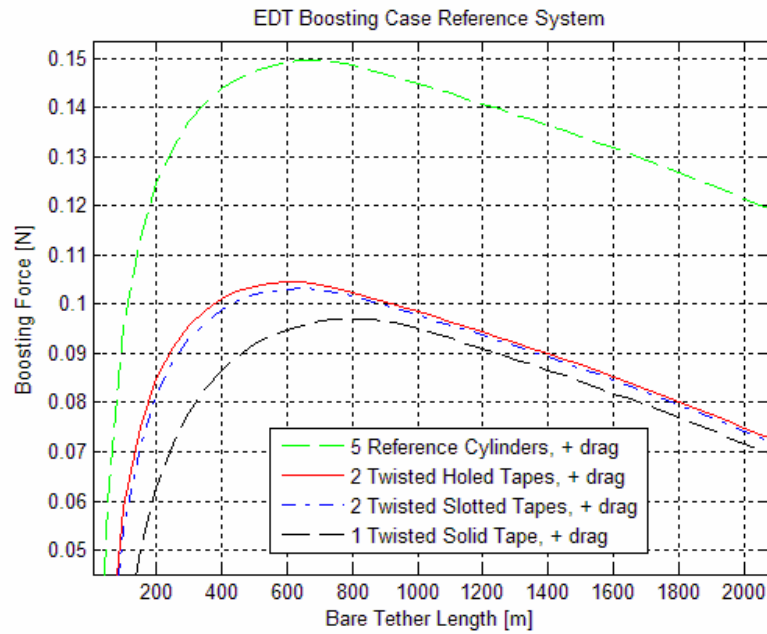
(b)

Figure 5-28: The resulting boosting force from various equivalent mass tether geometries including the atmospheric drag at $n_e = 1 \times 10^{12}$ m^{-3} for a reference system configuration excluding the 0.5 m endbody collector. The (a) perpendicular and parallel orientations are broken up as well as (b) shown for an entire twisting tether.

Even though the reference cylinder and perpendicular holed cases collect more per unit area, the parallel holed tape produces the best boosting effects overall, after

considering the atmospheric drag. In fact, the perpendicularly oriented cases barely even collect enough current to maintain a boosting system, shown in Figure 5-28a. The full twisting tether cases demonstrate the total effects of each tether geometry. The holed tether geometry collects the most followed closely by the slotted tether and the solid tether geometries. The reference cylinders exhibit a maximum system collection case. If tapes can be kept smaller than the Debye length, and far enough apart so there are no sheath interactions, then this optimal boosting geometry will result. It can also be seen that, as reference cylinders get closer together, they will result in system boosting forces similar to the slotted geometry.

CHAPTER 6

CASE STUDIES

The objective of this case studies section is to implement the knowledge and innovation of this thesis toward representative mission scenarios. The main reasons for applying EDT technology into current space missions, depending on its application, is because it can significantly reduce the cost and the mass over that of conventional propulsive devices. For example, the reduction in consumables alone for drag make-up can save up to a billion dollars in launch costs over time, as in the case of the International Space Station (ISS), which will be described later. In addition, this Section will explore the system design for maintaining the orbit of a large LEO scientific payload, Gamma ray large Area Space Telescope (GLAST), while minimizing mass, and adhering to other mission objectives. Finally, EDT thrusting at high ionospheric altitudes are analyzed for the Momentum eXchange Electrodynamic Reboost (MXER) system [7].

Every EDT system has a number of sub-systems that must be considered in order to obtain the optimal design for a particular mission. These include: the electron emission and electron collection devices; the tether material; the geometry; the length; the inclusion of an HVPS or an electrical load; and the conductive surface areas electrically connected to the tether system. Each subsystem will be investigated to obtain the optimal case for each mission discussed.

6.1   System Design Aspects

The mission requirements must first be obtained in order to begin the design process. These include orbital parameters such as the expected mission dates (solar,

ionospheric conditions), altitude, inclination, and eccentricity. These values enable us to predict parameters such as plasma density, electron temperature, magnetic field, etc. This directly determines the forces produced by the system. Next, the constraints of the mission must be determined in order to set boundaries from which to design. Some of these values include available power, system mass, microgravity effects, and mission lifetime.

In order to test the extreme cases here that an EDT system might encounter, the solar maximum and minimum neutral atmosphere values must be acquired. To do this, the National Oceanic and Atmospheric Administration (NOAA) website was consulted [147, 148]. The Space Environments Center (SEC) Space Weather Operations (SWO), Brussels international sunspot numbers (RI), the source 10.7 cm radio flux, and the geomagnetic activity (A_p) values were obtained. These monthly mean values for the extremes of the solar cycle, can be seen in Table 6-1.

Date	Sunspot Numbers				Radio Flux		Geomagnetic	
	Observed		Smoothed		Ob-served	Smoothed	Ob-served	Smoothed
	SWO	RI	SWO	RI	F10.7 cm		A_p	
June 1, 1996 (Solar Min.)	18.8	11.8	13.5	8.5	69.6	71.8	5	9.4
Dec. 1, 2001 (Solar Max.)	217.5	132.2	184.5	114.6	235.6	193.9	9	12

Table 6-1: List of the sunspot numbers, F 10.7 values and A_p values for the solar maximum and solar minimum points.

It was found that the solar maximum and minimum occurred during the month of December 2001 and June 1996, respectively. For the purposes of simulation, the first day of each respective month was used to acquire the atmospheric data[41].

The power requirements of the HVPS affect many system aspects. The mass of the power supply can be a significant portion of the total system mass, and thus the cost. This also influences the boosting capabilities of the system, as was seen in Chapter 5. Additional power supplies may also be needed depending whether any electron emission device requires one.

---

[41] June 1 = day 153 and December 1 = day 335

Another factor to be aware of when designing an EDT system is the ballistic coefficient. This value determines the rate at which an orbiting body changes due to an outside force. This value can be seen in Eq. 6-1.

$$\beta_{cf} = \frac{m}{C_d \cdot SA2d}$$ **Eq. 6-1**

The higher the coefficient, the more momentum it takes to alter the course of the orbiting body.

The tether is assumed to twist numerous times along its entire length. For a cylindrical wire, twisting does not have an impact on the total surface area, since it is symmetrical about the long axis. For tape geometries, the 2-d surface area changes as the tape rotates from its thickness to its width, as seen in Figure 4-3. In order to determine drag, defined in Eq. 4-2, an accurate approximation of this value needs to be obtained. Using Eq. 4-3, this 2-d surface area can be obtained [6]. The more times that the tape tether twists, the more accurate the equation becomes.

In order for the tether system to remain taut there must exist a particular size mass at either end of the tether system so a gravitational force gradient exists between them. This force is shown in Eq. 6-2 [18].

$$F_{gg} = 3 \cdot L \cdot m \cdot \omega_o^2 \quad \text{where} \quad \omega_o^2 = \frac{G \cdot M_{Earth}}{r_o^3}$$ **Eq. 6-2**

Here, the L is the length of the tether, G is the gravitational constant, and r is the distance from the center of mass of the Earth to the center of mass of the EDT system.

6.1.1 Recent Contributions to Case Study Analysis

An enhancement in tether simulations can result from the utilization of the change in resistance of a tether. This change is due to temperature fluctuations throughout an orbit. The warmer in temperature an object becomes, the larger the resulting resistance. Finding the equilibrium temperature of the tether is beyond the scope of this thesis, however once it is acquired, the implication on the rest of the system can be determined.

The resistivity, ρ_o, and the temperature coefficient, α, of the tether material is given. Once the temperature of the sample, T, is known, the actual resistivity, ρ_{res}, of the sample can be determined[42] from Eq. 6-3 and Eq. 6-4 [149].

$$\rho_{res} - \rho_o = \rho_o \cdot \alpha \cdot (T - T_o) \qquad \text{Eq. 6-3}$$

$$R = \frac{\rho_{res}}{A} \left[\frac{\Omega}{m} \right] \qquad \text{Eq. 6-4}$$

In order to verify the calculation of an accurate resistance value for a tape tether, previous mission data was used. In the TSS-1R mission, 10 copper cylindrical wire tethers were used, each with a radius of 0.16 mm. It was found that the average tether resistance was 0.083 Ω/km [133]. Using Eq. 6-4 and the material constants for copper, the same value was calculated, and thus verified [149]. The resistance measured in the experiment was found to be at room temperature. According to Eq. 6-3, for copper, a 1.4 degree drop in temperature results in approximately a 1% drop in the resistance.

As the width of the tape increases, the more the electron collection on the tape surfaces deviate from OML theory as mentioned in Section 2.1.2. In order to accurately portray the collection effects, the study Eric Choiniere performed was used [66]. From Figure 2-4 it can be seen how the collection percent of a widening tape changes. This curve can be mapped and the equation that fits best can be found using $Matlab^{TM}$'s curve fitting toolbox. The equation found is listed as Eq. 6-5.

$$f(x) = p_1 \cdot x^6 + p_2 \cdot x^5 + p_3 \cdot x^4 + p_4 \cdot x^3 + p_5 \cdot x^2 + p_6 \cdot x + p_7$$

$$where \quad p_1 = -1.092x10^{-9} \quad p_2 = 1.875x10^{-7} \quad p_3 = -1.269x10^{-5} \qquad \text{Eq. 6-5}$$

$$p_4 = 4.204x10^{-4} \quad p_5 = -6.481x10^{-3} \quad p_6 = 1.422x10^{-2} \quad p_7 = 0.992$$

The R^2 value was found to be 0.9996 for this equation. Figure 6-1 displays the raw data points and plots the best fit curve.

---

[42] T_o is defined as the room temperature, which equals 293 K.
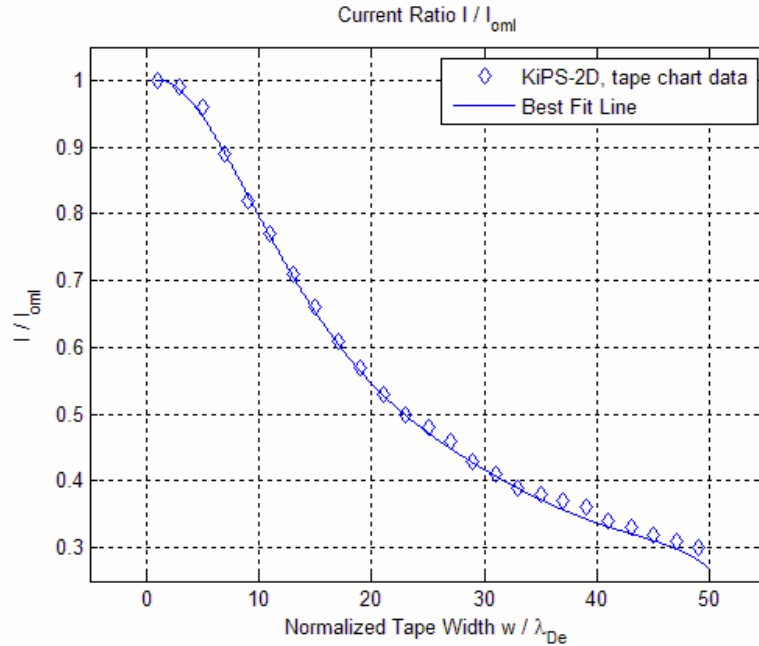
Figure 6-1: Finding the best fit curve for the simulated data describing how the tether width effects current collection that is normalized to OML theory.

Using this equation, the width of the tether can be mapped to the respective collection efficiency, and used to calculate the actual electron collection. Eq. 6-5 is only accurate in the range presented in Figure 6-1, since the best fit curve was developed for that range. Data will have to be calculated from KiPS-1d in order to acquire an efficiency percentage for normalized tape widths greater than 50. The simulations conducted in this thesis all fell within the range of the plot, however [150].

Another phenomenon, which is used for the simulations of this chapter, concerns current calculation pertains to the proximity of similar thin probes. It was found that as two probes are separated in an unflowing plasma, their ability to collect current is greatly reduced from what they would collect alone [66]. This profile is shown in Figure 2-5. It can be seen that if multiple tethers, each equal to or greater than 1 λ_{De}, are used in a system, they must be separated by many hundreds of Debye lengths in order to collect according to OML theory. Employing this design technique will be shown to be useful in systems that are capable of spacing multiple tethers many hundreds of Debye lengths apart. Not only does this technique improve the redundancy of the system, but it increases the current collection efficiency. Some designs have already been developed that employ similar techniques, such as the Hoyt Tether [36].

179

Another important factor involving the geometry of the tether is the boosting force of the tether with respect to the force of the drag (F_i / F_d). In Chapter 4 it was determined that the most efficient tether geometry of the experiment was the 50% porous, holed geometry. This analysis showed that there must exist a geometry where a particular hole diameter and thickness will optimize F_i / F_d. For the purposes of the case studies, the results of the experiment in Chapter 4 will be assumed. This assumption is that holed tapes will collect ~81% the current of an equal width solid tape, but will have 50% the drag and the mass. Another assumption drawn from the previous conclusion is that an equal mass holed tape will collect ~162% of the current to that of a solid tape. Points to consider with thinner tapes are that they are more resistive. In addition, as the tape design becomes thinner, there will come a point where it will not be able to withstand the stresses and strains of the system. The lifetime of the tether must be considered as well. Micrometeorites are one of the primary causes for a tether system breakage. The wider the tether, the greater the survivability [36], but unfortunately, the larger the drag.

6.1.2   System Design Process and Tradeoffs

Depending on the mission objectives, there are a number of items that must be considered in order to adequately design for the most efficient mass for any given system. If the mission requires higher boosting forces, then there must also be a correspondingly larger endmass, as determined by Eq. 6-2. A possible alternative to this decision would be to increase the length of the tether system, or the altitude of the mission. Increasing the tether length also adds mass to the system, however that mass is used to enhance the boosting capabilities. In addition, if the endmass is used as a passive current collection device, it could add another enhancement to the system that must be considered.

The power supply is a large factor in the total system mass. Assuming a mass to power ratio of 28 kg/kW for a power supply [151], a small power increase greatly affects the mass. Other ways to try and reduce the power requirements are to try and reduce the resistance of the tether, the effects of which are demonstrated in Chapter 5. Other tether system variables can be manipulated in order to optimize the thrust, and thus reduce the

power requirements as well. These variables include the tether length, material, and geometry.

Using an HC can have a sizable mass requirement compared to other electron emission techniques. For longer term missions, the mass of the consumable that a hollow cathode requires can become a burden. For example, if the hollow cathode used in the simulation is continuously running for 1 year, the consumables[43] required would equal ~17 kg.

The width of the tether is also of great concern when attempting to limit the total system mass. The wider the tether, the more current collection results, due to the increase in surface area, and thrust. Negative aspects, however, are increases in the system mass, as well as the drag. In addition, the tether would begin to collect current outside of the OML regime, and thus the efficiency would be reduced, as seen in Figure 6-1.

A typical general design process for identifying the most efficient system for a given mission may involve the following steps:

1.   Identify all relevant system requirements and constraints.

        Ex. Required altitude and inclination range and tolerances, subsystem mass limits, etc.

2.   Quantify the possible range for environmental conditions during the mission, e.g. neutral atmosphere, ionosphere, magnetic field. This may require understanding long-term variation (solar max, solar min) or minute-to-minute variation along a given orbit.

3.   For simulation, determine the ranges that need to be analyzed from all remaining system variables that are not constrained in order to satisfy objectives.

        Ex. A power range of 1 kW to 10 kW, or a tether width range from 1 cm to 4 cm, or the tether length can be from 5 km to 20 km long.

4.   Identify the requirements on tether width and geometry based on lifetime and practical limitations.

5.   Ascertain drag values of the system for each mission scenario to compare with EDT boosting and predict total boosting force on system.

---

[43] The average mass flow rate is 5.5 sccm for the HC used, as seen in Table 2-6.

6. Run simulation for optimizing the bare tether amount for each case. This requires the knowledge of approximate environmental conditions per time throughout an orbit (See step 2).

7. Throughout simulations, identify if there are any commonalities within runs to reduce the amount of total case study runs needed.

    Ex. Using an FEA or HC doesn't change results much, so just simulate HC, or an endbody that is 0.5 m radius has the same affect as a 2 m radius endbody, so just simulate 0.5 m radius endbodies.

8. During simulation identify how further alterations will affect system once mission objectives are met. (This step is not necessary, but useful to understand in case minor alterations in the system are necessary in the future.)

    Ex. How will the system be altered if 0.5 N more thrust is needed? Common important system values include: power, thrust, impulse, mass, mission time frame, and lifetime.

9. For system mass trade, calculate all aspects that affect mass within each run (HVPS, tether mass, anode, cathode) and keep track of results within each simulation.[44]

10. Identify how resulting EDT forces affect orbital path.

    Ex. How will the altitude and inclination of the orbiting system change over time as thrust is generated? Will this produce a highly elliptical orbit?

11. Estimate in-plane and out-of-plane forces and their likely impact to possible tether instabilities.[45]

    Ex. Causes for 'skip-rope effect' and librations

12. Select the design that best achieves the primary mission objectives.

---

[44] In depth analysis outside the scope of this thesis.
[45] In depth analysis outside the scope of this thesis

6.2   GLAST Systems Analysis

The Gamma ray large Area Space Telescope system is a pair-production high-energy (20 MeV < x < 300 GeV) gamma-ray telescope that is being built by an international partnership of astrophysicists and particle physicists for a 2006 launch to study a wide variety of high-energy astrophysical phenomena [152].

This particular mission could partially benefit from an EDT system to (1) extend the lifetime of the mission through orbital maintenance without mass consumption, and (2) support de-orbit requirements. To meet de-orbit requirements the spacecraft shall have an 85% probability of successful controlled re-entry and safe ocean disposal compliant with NSS 1740.14. Previous work determined that in order to achieve a landing site with a ± 500 km tolerance, the system would optimally require an EDT / hydrazine hybrid based approach [151].

Some of the major obstacles encountered in preparing an EDT system for the GLAST mission have been to reduce the time spent in the South Atlantic Anomaly (SAA) in order to minimize the increased interference of energetic particles[46]. In addition, another objective for the mission was to maintain the required orbit lifetime of 5 years, with a goal of 10 years. In addition, the thrust can not be greater than the gravity gradient force as seen in Eq. 6-2, and defined by Gilchrist et al.. System values that are important for an EDT design can be seen in Table 6-2.

GLAST system properties (excluding tether)	
System mass [kg]	4460
Surface Area [m^2]	29
Instrument Power [W]	1715

Table 6-2: Physical constants of the GLAST system excluding the EDT

This section begins by defining the previous work that has been accomplished for the GLAST mission, and what new additions will be simulated. The simulation work of this thesis is then verified against a particular case analyzed in the work by Gilchrist et al.

---

[46] The South Atlantic Anomaly is the region where Earth's inner van Allen radiation belt makes its closest approach to the planet's surface. The result is that, for a given altitude, the radiation intensity is higher over this region than elsewhere. The SAA is produced by a "dip" in the Earth's magnetic field at that location, caused by the fact that the center of Earth's magnetic field is offset from its geographic center by 450 kilometers [195].

The optimization techniques employed by the new simulations of this thesis are then explored for the boosting case. Finally the de-boost EDT case is explored and discussed.

6.2.1   New Contributions and Setup:

Unique simulations that are presented in this section investigate the issues that were not covered in the initial simulation work by Gilchrist et al. [151]. For this case study, the orbit inclination was analyzed at 5˚, instead of 28.5˚ to reduce the time spent in the SAA. A more complete simulation using different width porous tethers was also conducted using the experimental results found in Chapter 4. The most power efficient orbit maintenance scenario was then identified. For verification, the results from Gilchrist et al. [151] were compared to the tether collection models of this thesis.

The constraints for the simulation of this mission were to test; tether lengths of 2, 3, and 5 km; 50% porous aluminum tape widths of 25, 30, and 35 mm wide[47], and 1 mm thick; and tether boosting times of 5, 10, and 20 minutes. The power required to achieve the necessary orbit maintenance for the respective boosting times was then obtained. In addition, the tension due to the gravity gradient force was chosen to be two times the thrust value for dynamic stability. A 30% contingency was then added to account for any discrepancies in the final design.

6.2.2   Simulation Verification

According to Eq. 4-3, and the tether dimensions mentioned in the previous analysis [151] (1 mm x 25 mm), the 2-d surface area for a twisting tether was found to equate to 16.55 m^2 / km. The mass of the aluminum tether with the corresponding dimensions is 6.75 kg / km for a solid tape. As mentioned in Chapter 4, when calculating the drag of a 50% holed tether with a thickness to width ratio of 1:25, the holed tape drag will be 0.60 times the drag of the solid tape, or 9.86 m^2 / km. The current collection will

---

[47] The tether widths of 30 and 35 mm were different than that of the original simulations performed by Gilchrist et al. [151]. This is due to the fact that current collection differences between the varying widths are now understood better, and can be accounted for.

be different than the experiment however, since the Debye lengths, and sheath sizes, are different.

The electron density, magnetic field strength, electron and ion temperatures, orbital velocity, and the atmospheric drag values were obtained using the IRI-90, IGRF-91, and MSIS-86 models. In addition, the mass and surface area of tethers for a solid case and a 50% porosity case are displayed in Table 6-3.

EDT	2 km tether	3 km tether	5 km tether
Surface Area, solid [m^2]	33.10	49.65	82.76
SA 50% porous [m^2]	16.55	24.83	41.38
Mass, solid [kg]	12.62	18.93	31.55
Mass 50% porous [kg]	6.31	9.46	15.77

Table 6-3: 2-d surface areas and masses of solid and 50% porous aluminum holed tethers

Verification involved reproducing the results of previous work, which involved integration of tether systems into the GLAST mission [151]. In this research, a 2 km long, 100 m bare, 1 mm x 25 mm tether orbiting at 400 km on a 28.5° inclination orbit was simulated to maintain the orbit. It did this by thrusting for 20 minutes during the maximum electron density point of each orbit. During a solar maximum case[48], simulations were conducted to determine how much power a 20 minute impulse every orbit would require in order to make up for the drag and to maintain a relatively circular orbit. The average drag force for solar maximum during the given orbital specifications was obtained by simulating a system with the physical characteristics seen in Table 6-3. The average drag for 1 orbit was obtained using the MSIS-86 model and can be seen in Table 6-4. An important note is that Gilchrist et al. [151] had the HC emitter operating with 135 W at all times except during the 20 minute maximum power period for each orbit. The total impulse produced throughout the orbit is calculated from the 20 minute period of the orbit plus the impulse from the remainder of the orbit (135 W base power) must equal 117.1 N·s.

28.5° Inc., 2 km	November 2000
Avg. Drag [N]	2.67×10^{-2}
Impulse / Orbit [N·s]	117.1

Table 6-4: Impulse and average Drag created by the spacecraft and holed tether system that must be overcome to maintain orbit for a 28.5° inclination orbit

---

[48] This was determined to be November 1, 2000 (day 305) in the Gilchrist et al work.

The final step was to simulate the 100 m bare tether length using the defined mission constraints. Since the goal of this case study is to optimize the power necessary to overcome drag, and thus maintain an orbit, the power was varied across multiple bare tether lengths to calculate its respective impulse in these simulations. The impulse generated during the time when GLAST was at the base power (73 min) was calculated to be 51.7 N·s, as shown in Figure 6-2b,. This result indicates that the 20 minute boost must generate 65.4 N·s in order to overcome the atmospheric drag. In Figure 6-2a, point 'A' indicates the verification point, where using 100 m of bare tether equals the necessary impulse of 65.4 N·s. Through linear interpolation, it can be estimated that the power necessary to emit the orbit maintaining impulse at 100 m of bare tether is 530 W.

(a)
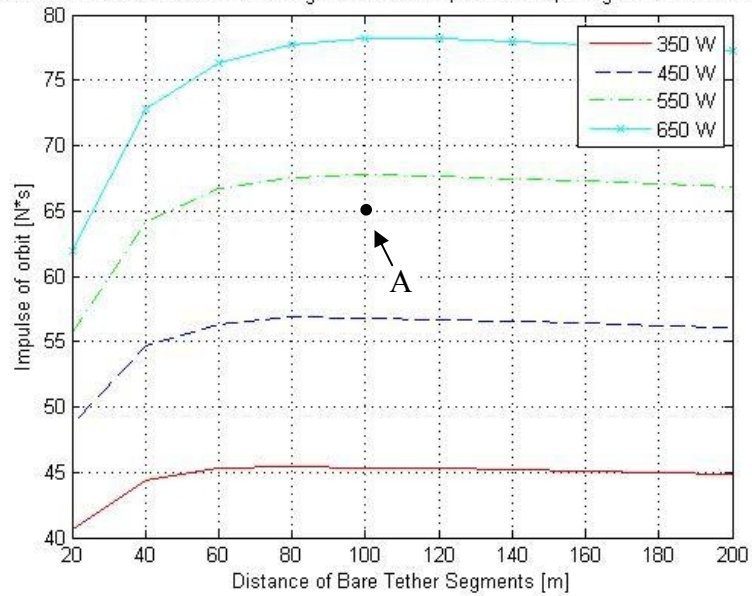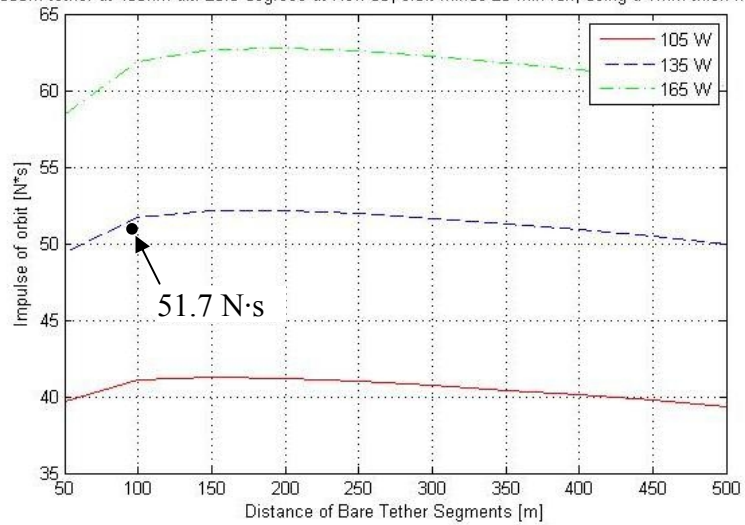
(b)

Figure 6-2: Simulations conducted to verify original work by Gilchrist et al. The power is varied to show the resulting impulse on the system, and the amount of bare tether required to obtain it. The total impulse is shown for a) the 20 minute max power, and b) the 73 minute base power period.

The results indicate that 530 W are required for the system to maintain the orbit as opposed to the previously calculated 550 W by Gilchrist et al. Possible discrepancies are the result of the average power value given from the previous work. A days worth of orbits (~15.5 orbits) were simulated with changing atmospheric values by Gilchrist et al.. This could cause different parts of each orbit to yield different electrodynamic thrusts.

Only one orbit was used to calculate the comparison in this verification. In addition, the simulation code uses only the B_y field instead of the B_x and B_y field to determine the forces. It was calculated and discussed in Section 3.1.2 that a 28.5º orbit using this assumption would yield ~+3.8% error. This error results in a 21 W underestimate in the required force and nearly accounts for the entire discrepancy. This verifies that using the developed *EDT-Survey* simulation for determining the orbital maintenance of an EDT system is accurate with respect to previous orbital dynamic models, such as TEMPEST.

6.2.3   New Simulation Work

Recent additions have been made to the current collection code, which were not employed in the work by Gilchrist et al.. The developed *EDT-Survey* and *EDT-Trades* simulations account for the reduction in OML collection as the tape gets wider as discussed in Section 6.1.1. This would result in a higher power requirement to produce an equivalent current collection, and thus thrust. In addition, the developed simulations do not assume the 50% holed tethers collect as a solid tether, as Gilchrist et al. This also results in the necessity for more power to overcome the drag. There is another 19% collection reduction associated with that fact as shown in the results of Chapter 4.

Similar simulations were conducted for the 5˚ inclination orbit for 2 km, 3 km, and 5 km tethers for the solar maximum and solar minimum cases under varying tape widths. This inclination was recommended by Gilchrist et al. [151] as aother potential orbit in hopes of minimizing the time in the SAA. The altitude used in the simulations of this section was however, 400 km instead of the suggested 550 km. The 400 km altitude does not reduce the time outside the affects of the SAA by much. However, the goal of this section is to show the method of obtaining a most efficient bare tether amount, which is accomplished.

Using Table 6-3, the average drag force could be obtained for each respective EDT system, and thus the impulse that needs to be overcome through boosting in order to maintain the orbit. An important note is that the system had a base power of 0 W when it was not undergoing the primary thrust, as opposed to the 135 W base power in the verification. The 'corrected' impulse was obtained by dividing the calculated drag

impulse[49] by a correction factor of 0.81. This correction factor is due to the experimental knowledge (from Chapter 4) that a 50% porous tether collects ~81% of the current to that of a comparable width solid tape. This correction is conducted because the *EDT-Survey* and *EDT-Trades* simulations use a solid tape, and the current collection and thrust differences must be accounted for. These values can be seen in Table 6-5.

5° Inc. 25 mm width	Solar Maximum (December 2001)			Solar Minimum (June 1996)		
	2 km	3 km	5 km	2 km	3 km	5 km
Avg. Drag [N]	1.51E-02	1.89E-02	2.64E-02	9.76E-03	1.22E-02	1.71E-02
Corrected Impulse [N·s]	102.9	128.7	180.2	66.5	83.2	116.5

Table 6-5: Impulse and average drag that must overcome by the spacecraft and tether system to maintain a 5° inclination orbit

The analysis of the system system performance was completed and shown in Table 6-6 through Table 6-9. To demonstrate the extreme cases in a solar cycle, the solar maximum and solar minimum were simulated for the 25 mm wide tape at all three boosting times and tape lengths. Then, to see the effects of a growing tape width, only the solar minimum case was simulated to reduce the number of simulation runs. The same set was then run for 30 mm and 35 mm width tapes also using the solar minimum case. As an example of the simulations conducted, Figure 6-3 displays the 10 minute boosting time of a 3 km tether at the solar maximum. In this case using Table 6-5, an impulse of 128.7 N·s needs to be achieved. The optimal lowest power is seen to be 1992 W at 315 m of bare tether.

---

[49] Impulse equals average drag [N] * time [s], or in this case 20 minutes boosting time
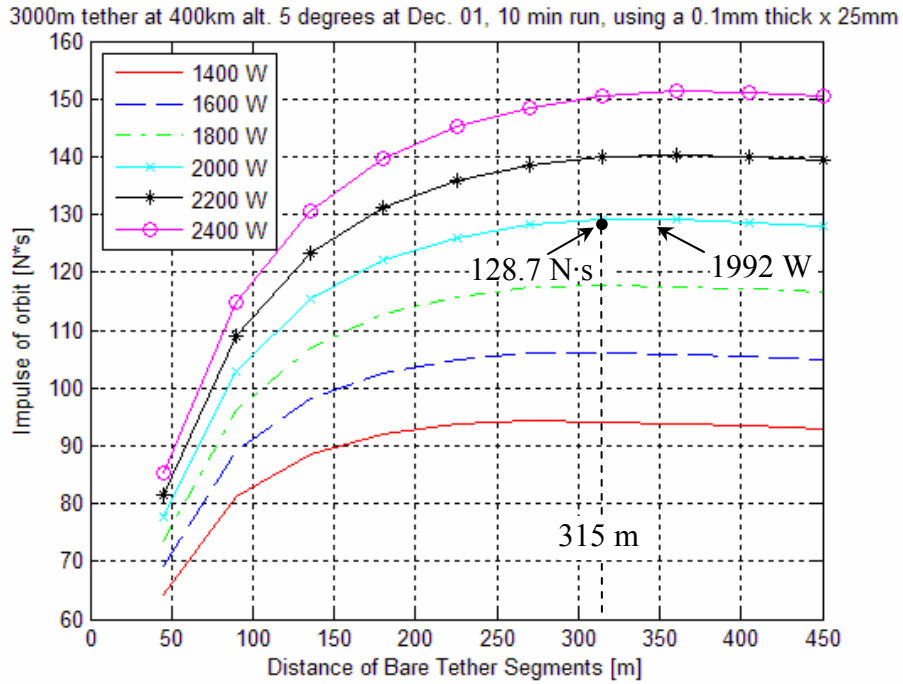
Figure 6-3: The impulse versus bare tether length of the solar maximum case with a boosting time of 10 min on a 3 km tether.

Boosting time [min]: Tether Length [m]	Power Required [W]	Bare Tether Amount [m]	Energy Required [kJ]	Power Mass [kg]	Endmass [kg]	Total EDT System Mass [kg]
5 : 2000	4337	560	1301	124.0	90.1	297.6
5 : 3000	4572	540	1372	130.8	75.1	291.0
5 : 5000	5680	500	1704	162.4	63.1	324.8
10 : 2000	1792	360	1075	51.3	45.1	144.4
10 : 3000	1992	315	1195	57.0	37.6	146.3
10 : 5000	2556	300	1534	73.1	31.6	167.6
20 : 2000	803	240	964	23.0	22.5	78.4
20 : 3000	921	225	1105	26.3	18.8	82.0
20 : 5000	1207	200	1448	34.5	15.8	96.9

Table 6-6: System values for the solar maximum case using a 25 mm wide 1 mm thick tape in a 5° inclination circular orbit. The boosting time was varied from 5 to 20 minutes, and the tether length was varied from 2 to 5 km.

Boosting time [min]: Tether Length [m]	Power Required [W]	Bare Tether Amount [m]	Energy Required [kJ]	Power Mass [kg]	Endmass [kg]	Total EDT System Mass [kg]
5 : 2000	2468	480	740	70.6	58.2	186.7
5 : 3000	2699	360	810	77.2	48.6	186.8
5 : 5000	3451	400	1035	98.7	40.8	212.9
10 : 2000	1084	200	650	31.0	29.1	97.4
10 : 3000	1236	240	742	35.3	24.3	100.9
10 : 5000	1614	250	968	46.2	20.4	118.1
20 : 2000	504	120	605	14.4	14.6	56.9
20 : 3000	563	180	676	16.1	12.1	60.1
20 : 5000	776	150	931	22.2	10.2	73.7

Table 6-7: System values for the solar minimum case using a 25 mm wide 1 mm thick tape in a 5° inclination circular orbit. The boosting time was varied from 5 to 20 minutes, and the tether length was varied from 2 to 5 km.

There were many observable trends across these simulations. The difference between the maximum and minimum solar cycle results at 25 mm was that an increase in power was required to maintain the same orbit maintaining boost. In these cases, the solar maximum has a greater amount of plasma density, so thrust increased, but there is also an increase in atmospheric density that causes an increase in drag. This extra drag is greater than the collection enhancement, and as a result requires more power to maintain the orbit. Since the goal lifetime is 10 years, however (almost an entire solar cycle of 11 years), all ranges should be accounted for. A comparison between the 25 mm tape across solar maximum and solar minimum from Table 6-6 and Table 6-7 can be seen in Figure 6-4. In addition, a comparison between the the varying tape widths at solar minimum from Table 6-7 through Table 6-9 are shown in Figure 6-5. For both Figure 6-4 and Figure 6-5 the system mass and the HVPS power is compared for each scenario.

Boosting time [min]: Tether Length [m]	Power Required [W]	Bare Tether Amount [m]	Energy Required [kJ]	Power Mass [kg]	Endmass [kg]	Total EDT System Mass [kg]
5 : 2000	2388	420	716	68.3	58.2	185.4
5 : 3000	2640	360	792	75.5	48.6	187.1
5 : 5000	3387	300	1016	96.9	40.8	214.6
10 : 2000	1070	240	642	30.6	29.1	98.5
10 : 3000	1221	225	733	34.9	24.3	102.8
10 : 5000	1598	225	959	45.7	20.4	121.6
20 : 2000	500	200	600	14.3	14.6	58.4
20 : 3000	582	180	698	16.6	12.1	63.2
20 : 5000	772	150	926	22.1	10.2	77.6

Table 6-8: System values for the solar minimum case using a 30 mm wide 1 mm thick tape in a 5° inclination circular orbit. The boosting time was varied from 5 to 20 minutes, and the tether length was varied from 2 to 5 km.

Boosting time [min]: Tether Length [m]	Power Required [W]	Bare Tether Amount [m]	Energy Required [kJ]	Power Mass [kg]	Endmass [kg]	Total EDT System Mass [kg]
5 : 2000	2330	400	699	66.6	58.2	184.9
5 : 3000	2591	360	777	74.1	48.6	187.8
5 : 5000	3339	300	1002	95.5	40.8	217.0
10 : 2000	1056	240	634	30.2	29.1	99.6
10 : 3000	1210	225	726	34.6	24.3	104.8
10 : 5000	1586	200	952	45.4	20.4	125.3
20 : 2000	496	160	595	14.2	14.6	59.9
20 : 3000	580	180	696	16.6	12.1	65.6
20 : 5000	769	150	923	22.0	10.2	81.6

Table 6-9: System values for the solar minimum case using a 35 mm wide 1 mm thick tape in a 5° inclination circular orbit. The boosting time was varied from 5 to 20 minutes, and the tether length was varied from 2 to 5 km.
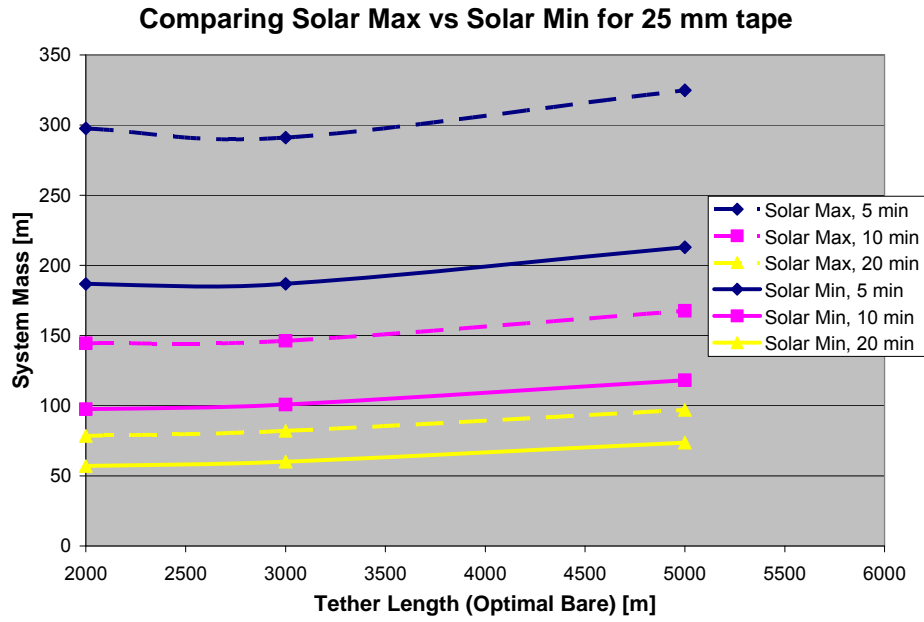
(a)
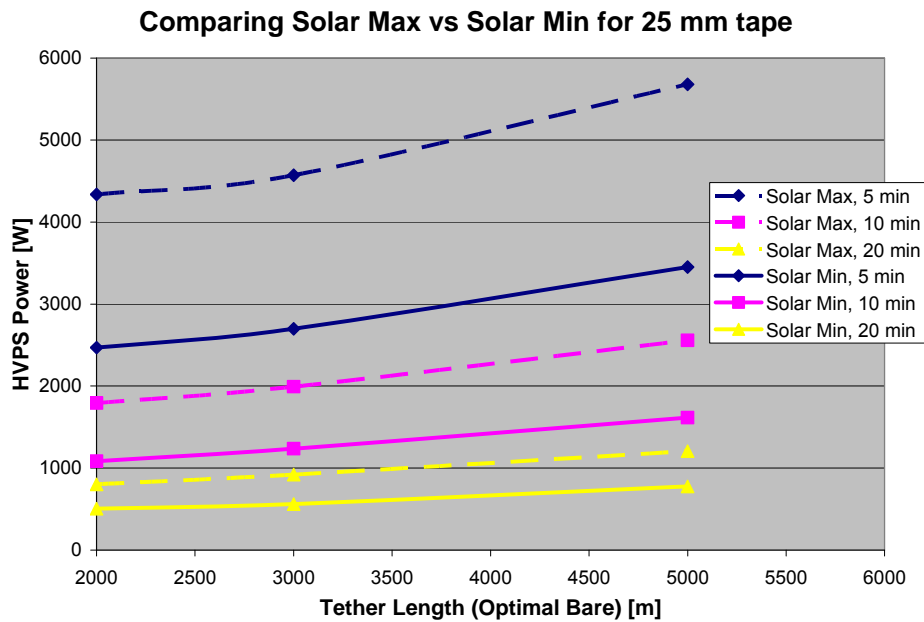
(b)

Figure 6-4: Plot of the data seen in Table 6-6 and Table 6-7 detailing the differences between the solar maximum and solar minimum cases across (a) system mass and (b) HVPS power.

Comparing Various Tape Widths for Solar Min

(a)

Comparing Various Tape Widths for Solar Min
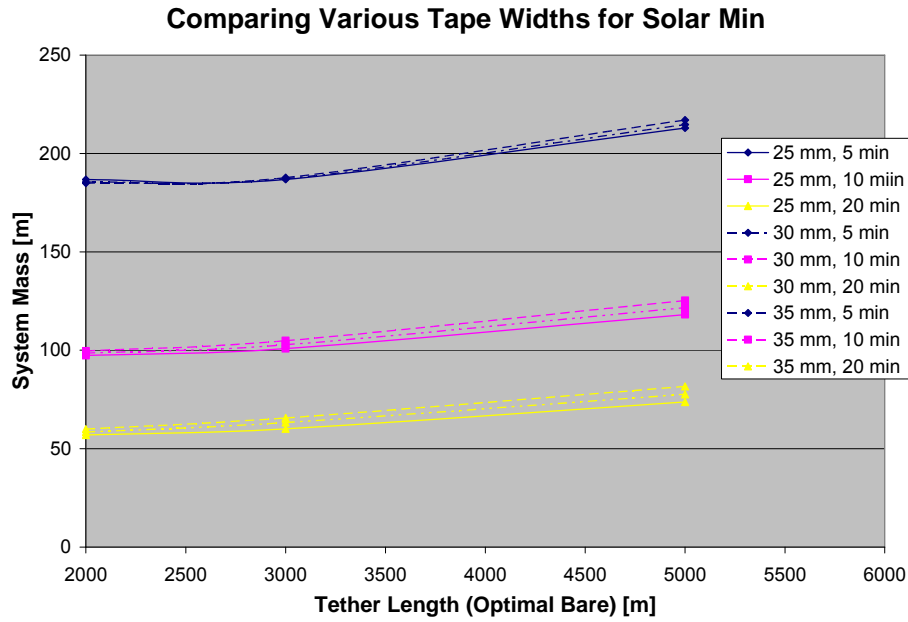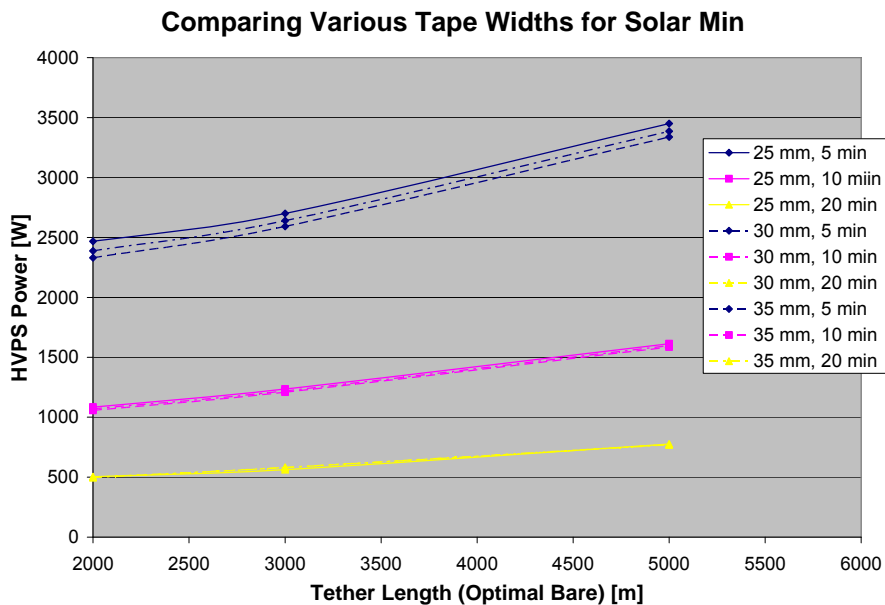
(b)

Figure 6-5: Plot of the data seen in Table 6-7 through Table 6-9 detailing the differences between the tape widths at solar minimum across (a) system mass and (b) HVPS power

There are also overall trends that pertain to all cases. As the power requirement increases, the system mass increases. Similarly, as the tether length increases, the total system mass increases. An important, but not surprising, observation shows that the system mass and energy decrease as the boosting period increases. This indicates that even longer boosting periods would be more beneficial. This increase in boosting time

will only work to a certain extent because the longer the boosting period (without a peak power boosting interval), the more elliptical the orbit becomes as shown in Gilchrist et al. [151]. Also, as the tape width increases, it can be seen that the required power decreases, while the total system mass increases (for all cases except the 5 minute boosting, 2 km length case). This is due to the increase in tether mass being greater than the decrease in required power sub-system mass. For the 5 minute, 2 km case, this trend was not true because the decrease in power is greater than the increase in mass. This is a system trade that must be evaluated by the designer basd on specific constraints. A decrease in power means that there is more remaining for the other systems to use. A decrease in mass means that the total cost to launch will go down dramatically, since the current average price is approximately $20,000 per kg [153].

It appears that the optimal boosting design under the given constraints for the GLAST mission would be one that employs a 2 km, 25 mm width porous tether with a 20 minute boost per orbit. The optimum point is not found with the preceding simulations, however as there are limitations to simulations beyond these values. Evidence shows that narrower, shorter tethers that boost for longer periods of time will yield even lighter systems that require less power. The limiting factor on the tether width will be the mission lifetime. Once it becomes too narrow, the chances that a micrometeoroid will sever it will rise sharply. Also, as shown in Section 5.4.1, the boosting capability will drop off as the tether becomes shorter until the point where the power to overcome the orbital drag will cause the system weight to be too great. Finally, as mentioned before, if the boosting time becomes too great, then the elipticity of the orbit will increase.

6.2.4 De-boosting Conditions

The other objective for pursuing tethers for the GLAST mission is the ability to de-boost the system in a more mass and cost effective way. Since the developed *EDT-Survey* and *EDT-Trades* simulations, described in Section 3.4, did not include orbital dynamics, only certain aspects of the scenario could be explored. One of the comparisons given by Gilchrist et al. [151] is the average de-boosting force profile as the tether system de-orbits from 550 km to 150 km. The system in the Gilchrist et al. study

[151] is a 3 km tether that is 25 mm wide and 50% porous. The average de-boosting force is ~0.3 N, with a peak around 0.68 N. To compare the work of this thesis with previous work by Gilchrist et al. [151], the results for the de-boosting capabilities of the EDT system using the previous tapes, can be seen in Table 6-10. In the de-boosting mode, the power supply is not used because the system de-orbits itself without the addition of energy. As a result, the only changing variable is the amount of bare tether that was solved for in the boosting cases. The table details the bare tether range that was obtained from Table 6-6 through Table 6-9, and the corresponding orbit boosting time (20 min. to 5 min.). The total simulated de-boosting average thrust as well as the total imparted impulse is given with respect to the orbiting period. The 10 minute case was not detailed because the maximum and minimum thrusting cases for each system configuration are of interest.

	Tether Length [m]	Bare Range [m] 20 – 5 min	Average Thrust [N] 20 min	Average Thrust [N] 5 min	Impulse [N·s] 20 min	Impulse [N·s] 5 min
Dec '01	2000	560 - 240	0.54	0.32	3000	1800
25 mm	3000	540 – 225	1.00	0.57	5500	3100
Solar Max.	5000	500 – 200	2.01	1.11	11100	6100
June '96	2000	480 – 120	0.39	0.14	2200	800
25 mm	3000	360 – 180	0.63	0.37	3500	2100
Solar Min.	5000	400 – 150	1.42	0.69	7800	3800
June '96	2000	420 – 200	0.47	0.26	2600	1400
30 mm	3000	360 – 180	0.75	0.45	4100	2500
Solar Min.	5000	300 – 150	1.41	0.83	7800	4600
June '96	2000	400 – 160	0.49	0.25	2700	1400
35 mm	3000	360 – 180	0.88	0.52	4800	2900
Solar Min.	5000	300 - 150	1.65	0.97	9100	5300

Table 6-10: Average Thrust and Impulse induced by the tether system in a de-boost scenario. The bare tether range is defined by the calculated best cases determined in the boosting scenario.

It can be seen that the EDT de-boosting force improves as: the bare tether amount increases; the total tether length increases; the tape width increases; and the electron density increases (or becomes closer to solar maximum conditions). In addition, the atmospheric drag enhances the de-boosting capabilities as the tether width and length increases. The negative aspect of these results is that they are exactly opposite to the conditions that allow the system to be a good boosting system. In order to determine

what boosting / de-boosting scenario is more beneficial, more needs to be known concerning the orbital mechanics. The orbital mechanics for the de-boost scenario is discussed in Gilchrist et al. [151].

Overall, the analysis presented here describes that which was not presented in the original analysis, specifically, the 5˚ inclination at a 400 km orbit. It was also discovered that there is enough new updated information implying it would be beneficial to redo much of the previous work by Gilchrist et al. [151]. More work still needs to be accomplished in order to identify the best overall scenario, however. The work here primarily focuses to detail some of the steps involved in implementing an EDT system to other missions using the advanced EDT technology and systems optimization of this thesis.

6.3 International Space Station (ISS) Systems Analysis

The international space station has a great need for inexpensive orbit maintenance and maneuvering. The station maintains an orbit that decays between ~350 and ~450 km over a few years, it needs to be constantly reboosted. There have already been several investigations to assess the use of tethers on the ISS to account for this decay [6, 10, 154] as well as other electromagnetic effects [155, 156]. This particular study employs unique attributes never before investigated to implement an EDT system for use on the ISS. Variables such as the tether width, tether porosity, anode type and cathode type will be introduced as new system parameters to be explored. Previous addressed variables such as altitude, system power, and mission date will be also be used

The work presented in this section seeks to guide the user toward optimizing the tether design for the ISS through theuse of the tools presented earlier in this thesis. Various trade-offs will be explored to exemplify typical results if various design directions were pursued.

6.3.1   Setup

According to Vas et. al., there are certain requirements and constraints that the system must follow if an EDT system is to be implemented correctly. The approximate altitude profile of the ISS over time is given in Figure 6-6a. In addition, the atmospheric drag of a combined ISS and a 11 mm x 0.6 mm x 7 km tether, are defined in Figure 6-6b and c, respectively. To calculate the tether drag, the surface area for a solid tape follows Eq. 4-3 for a twisted tape. The variable range chosen to be manipulated in this study are detailed in Table 6-11. It can be seen that many variables are still open to evaluation. Tape widths were chosen at the width Vas et al. [6] analyzed, and then increased by increments of 5 and 10 mm. The HC, and a range of conducting sphere endbody collector sizes were investigated determine the optimal electron collection method. The FEA and the HC electron emission cathode technologies were investigated, even though the current emission required is beyond the range of present FEA technology. Thermionic cathodes are not pursued, since they were shown to require excessive power, in Chapter 5 for the required emission current levels in this case (several Amperes). The two tape geometries experimentally investigated in Chapter 4, solid and holed, are implemented in this study as well. The altitude to be investigated was shown, in Figure 6-6a, to be within the ranges of 350 and 450 km. The HVPS was stated as being limited at 10 kW by Vas et al. [6]. As a result, power levels above and below that were simulated to cover a broader range of possibilities. Finally, since the ISS is a long term mission, it is important to simulate both solar maximum and minimum conditions.

	Tape Width [mm]	Endbody collector Type	Cathode Type	Tape Type	Altitude [km]	Power [kW]	Dates
Range / Types	11, 16, 21, 31, 41	HC Bare Tether Sphere: r = 0.5, 2, 5, 10 m	HC FEA	Solid Holed	350, 450	5, 10, 15 kW	July 1996 (solar max) Dec. 2001 (solar min)

Table 6-11: The manipulated variables tested by the simulation

(a)

(b)

199

(c)
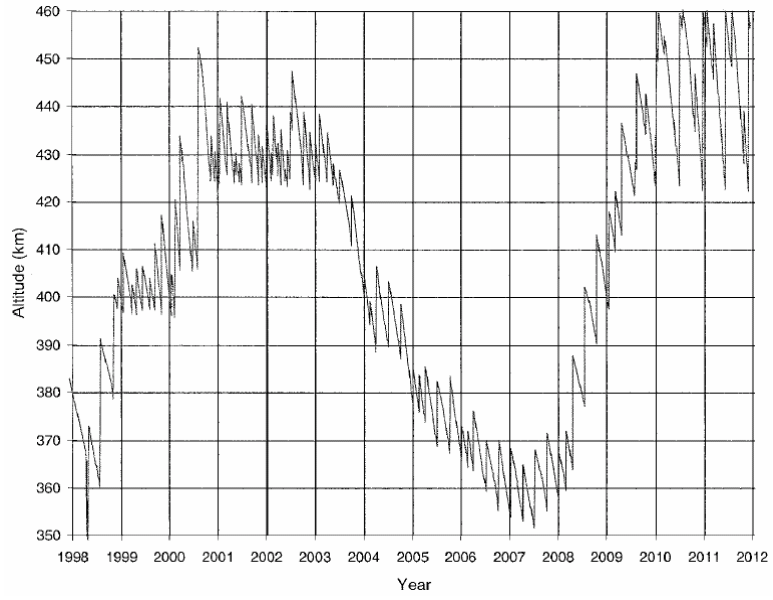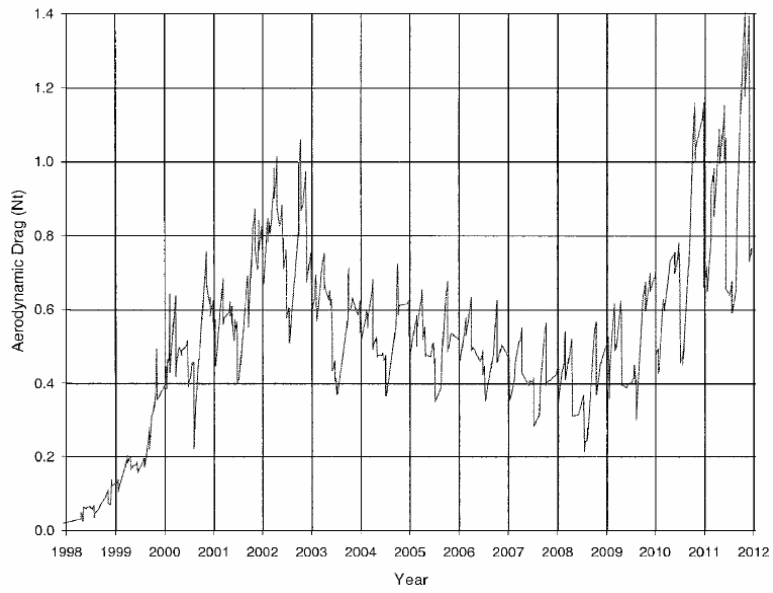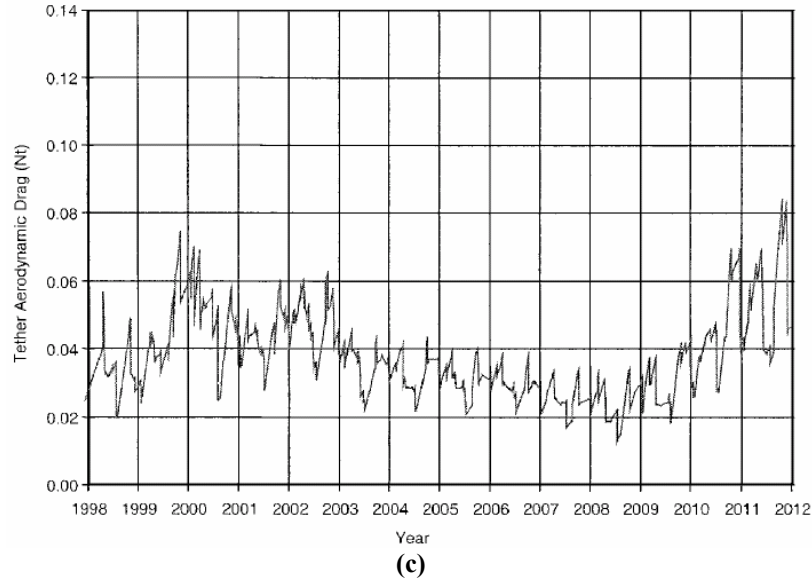
Figure 6-6: The (a) planned altitude of the ISS, as well as (b) aerodynamic drag produced by the body of the ISS and (c) the drag produced by the 0.6 mm thickness, 11 mm width, 7 km length twisted solid length tether [6]

The mass of the tether was calculated using values previously determined [154]. The density was determined for this case, and then applied to the other tape sizes tested in this case study to keep the tethers' equivalent. The surface area, tether mass, ballistic coefficient using Eq. 6-1, and tether resistance using Eq. 6-4, were also determined, and are shown in Table 6-12 and Table 6-13. To account for the holed tether geometries the same simulations were run, except for the surface area being 0.596 times as great (detailed in Section 4.6.1), and the tether mass equaling one half that of the solid tape.

Solid Tape (all 0.6mm thick)	11 mm 7 km	16 mm 7 km	21 mm 7 km	31 mm 7 km	41 mm 7 km
Surface Area [m^2]	51.7	74.0	96.3	140.8	185.4
Tether mass [kg]	116.6	169.6	222.6	328.6	434.6
Ballistic Coef. [kg/m^3]	1.23	1.25	1.26	1.27	1.28
Tether Resistance [Ω/km]	2.57	1.77	1.35	0.91	0.69

Table 6-12: Physical characteristics of the tethers used in the simulations for the 7 km tether

Solid Tape (all 0.6mm thick)	11 mm 10 km	16 mm 10 km	21 mm 10 km	31 mm 10 km	41 mm 10 km
Surface Area [m^2]	73.8	105.6	137.5	201.2	264.8
Tether mass [kg]	166.6	242.3	318.0	469.5	620.9
Ballistic Coef. [kg/m^3]	1.23	1.25	1.26	1.27	1.28
Tether Resistance [Ω/km]	2.57	1.77	1.35	0.91	0.69

Table 6-13: Physical characteristics of the tethers used in the simulations for the 10 km tether

200

In order to verify the drag values TEMPEST calculated, Figure 6-6c was used from the Vas et al. [6], along with the mass, inclination of the orbit, and C_d of the station[50]. The equivalent atmospheric drag values were compared for the dates: December 1st of 2000, 2001, and 2006, and found to be equivalent. This verification ensures that the atmospheric density and orbital velocity calculations from Vas are comparable to the TEMPEST values. Vas et al. [6] also stated that a tape of 7 km x 11 mm x 0.6 mm would result in a drag difference of ~6% of the ISS itself. The ISS atmospheric drag values can now be calculated. The average atmospheric drag values for all tether widths and lengths, at both altitudes, at the solar maximum and minimum, are shown in Table 6-14 and Table 6-15[51].

Average Drag [N]	11 mm	16 mm	21 mm	31 mm	41 mm	ISS Drag
Solar min, 350 km	0.028	0.043	0.057	0.084	0.111	0.467
Solar min, 450 km	0.005	0.008	0.010	0.015	0.020	0.083
Solar max, 350 km	0.042	0.066	0.085	0.126	0.167	0.700
Solar max, 450 km	0.008	0.013	0.016	0.024	0.032	0.133

Table 6-14: Drag associated with each respective tether and altitude for a 7 km tether

Average Drag [N]	11 mm	16 mm	21 mm	31 mm	41 mm
Solar min, 350 km	0.040	0.062	0.081	0.120	0.159
Solar min, 450 km	0.007	0.011	0.014	0.021	0.028
Solar max, 350 km	0.060	0.094	0.122	0.180	0.238
Solar max, 450 km	0.011	0.018	0.023	0.034	0.045

Table 6-15: Drag associated with each respective tether and altitude for a 10 km tether

6.3.2   Analysis: Trends

A number of tests were performed to determine the optimum amount of bare tether required to produce the maximum amount of thrust over the course of an entire orbit. These tests include varying the power, anode, cathode, tether width, length, and solar cycle. By observing these results it is possible to determine optimal performances based on different mission constraints. The simulations conducted accurately portray a full day-night cycle of ionospheric conditions by taking a data point each minute over an entire orbit and then averaging the results. Also, as noted in Section 3.1.2, if an

---

[50] The inclination = 51.6º, and the C_d = 2.35 (worst case of low density free molecular flow) [6].
[51] Drag values shown in the graphs are taken at the respective altitudes ±1 km.

assumption of just accounting for the B_y field is used for the 51.6º inclination at 350 km and 450 km altitude, the results yield a ~+18.3% and a ~+15.4% difference for the 350 km and 450 km altitudes, respectively. These ISS simulations account for the B_x and B_y magnetic fields to give a more accurate prediction of the in-plane boosting force, and will not have this error.

As the simulations began, it was observed that the FEA electron emitter produced near identical results to that of the HC electron emitters, as described in Section 5.4. These emitters each require an equivalent amount of power to operate. These results can be seen in Figure 6-7 where the lines are almost indistinguishable from one another. As a result, it can be assumed that future runs would behave in the same manner, so further FEA cathode runs were not performed.

An important note concerning these simulations was that in order for the HC and FEA to function in the system, it was required that they be large enough to emit all of the current traveling through the tether. As a result of this fact, during the FEA tests (10 kW and above) it was necessary for 2 FEA's, that could each emit 10 A, be used in order for the system to solve properly (this issue is discussed in Section 3.4). The HC design used for these simulations had a maximum value of 25 A, and only one was required for all the tests presented here.
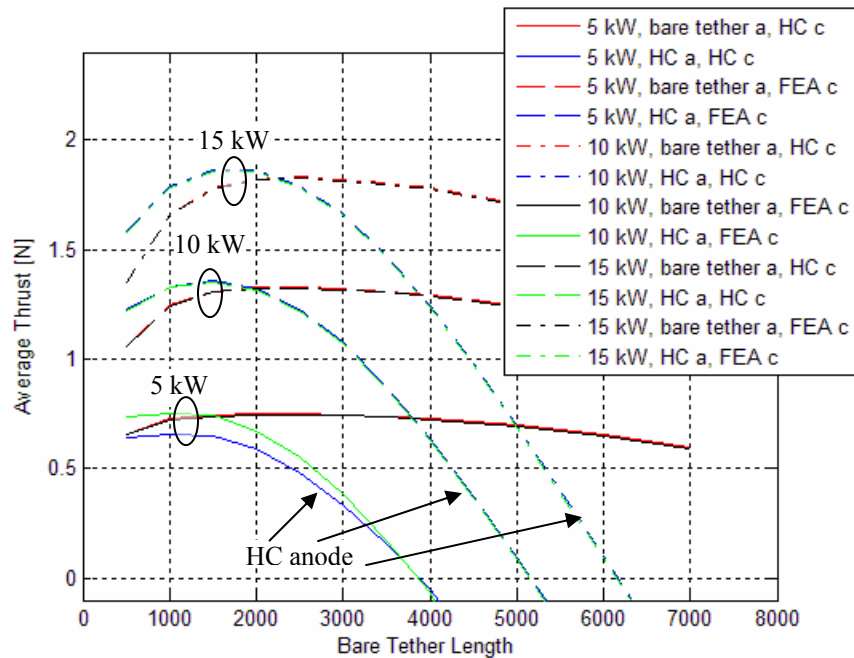
Figure 6-7: Bare tether length vs. average thrust for a 10 km tether system comparing HC and FEA e- emitters at 350 km altitude during solar minimum for a 0.6 mm thickness, 11 mm width tether

The next simulation pertains to the endbody collector effects on the system, and can be seen in Figure 6-8. The bare tether and the various sized spherical endbody collectors have very little affect on the maximum average thrusting point. It took a sphere with a 10 m radius to collect enough current to yield a system boost that surpasses the other endbody collectors, and then by only 0.05 N. In addition, the hollow cathode was found to have a maximum boosting force equivalent to a spherical endbody collector slightly smaller than the 5 m case. The HC, however, resulted in a system that dropped off rapidly as the bare tether length increased. The rapid thrusting drop off by the HC (with increasing bare tether length) is due to its electron and ion current collection characteristics. This phenomena is explained in Section 5.4.2. In the case of the bare tether with no spherical endmass or HC, the OML theory collection dictates the rate of electron or ion emission, because it is a thin wire with respect to the Debye length. Since the HC and spherical endbody collectors add complexity and weight to the system, and have minimal effects on the overall results, future analyses were done excluding these cases. In addition, the HC endbody collector limits where the tether optimal performance would occur to a small bare tether length. As parameters change in a mission, such as the HVPS, the altitude, and the date, the optimal bare tether amount changes. For the ISS, a systes must be chosen that performs well under a wide range of orbital and system parameters. The bare tether endbody collector can operate near optimal thrusting performance under a wider range of conditions.
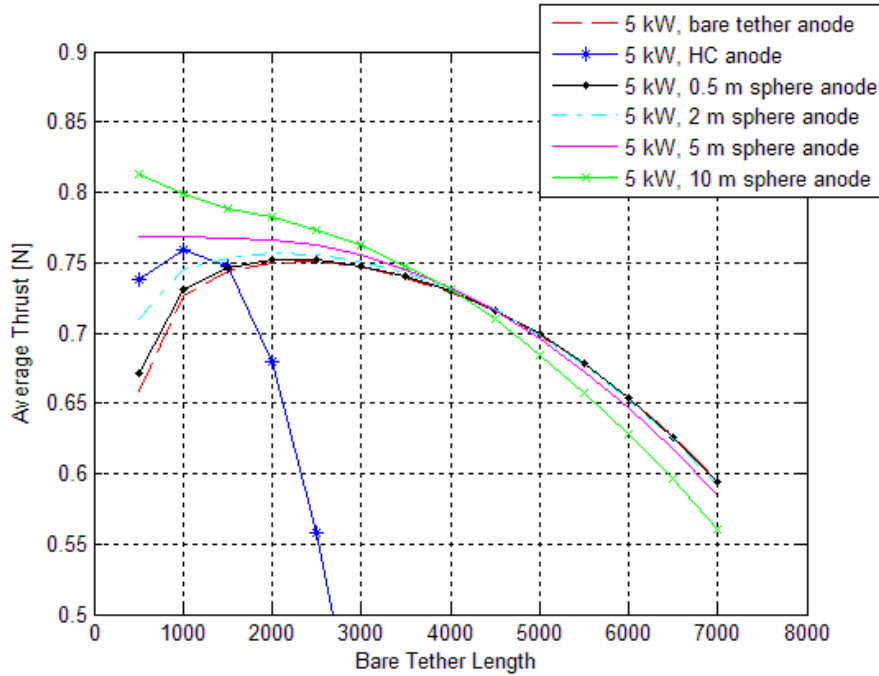
Figure 6-8: Bare tether length vs. average thrust for a 10 km tether system with an HC e- emitter at 350 km altitude during solar minimum comparing various endbody collectors for a 0.6 mm thickness, 11 mm width tether

Figure 6-9 displays only the bare tether and the HC as endbody collectors for various tether lengths and power supplies. It can be seen that for all power levels, the HC has a maximum point of ~0.05 N greater than the bare tether max, but for differing bare tether amounts. This HC endbody collector maximum point is found to drop very quickly compared to the bare tether endbody collector similar to Figure 6-8, which remains at a comparable thrust all the way through 7000 m of bare tether. Another observation is that the thrust of each case can be extrapolated based on the power increase. As shown in Figure 5-9a and discussed in Setion 5.2.2, for a particular bare tether length there exists as profile for the thrust versus HVPS. Using this type of plot, further HVPS values can be predicted in Figure 6-8.
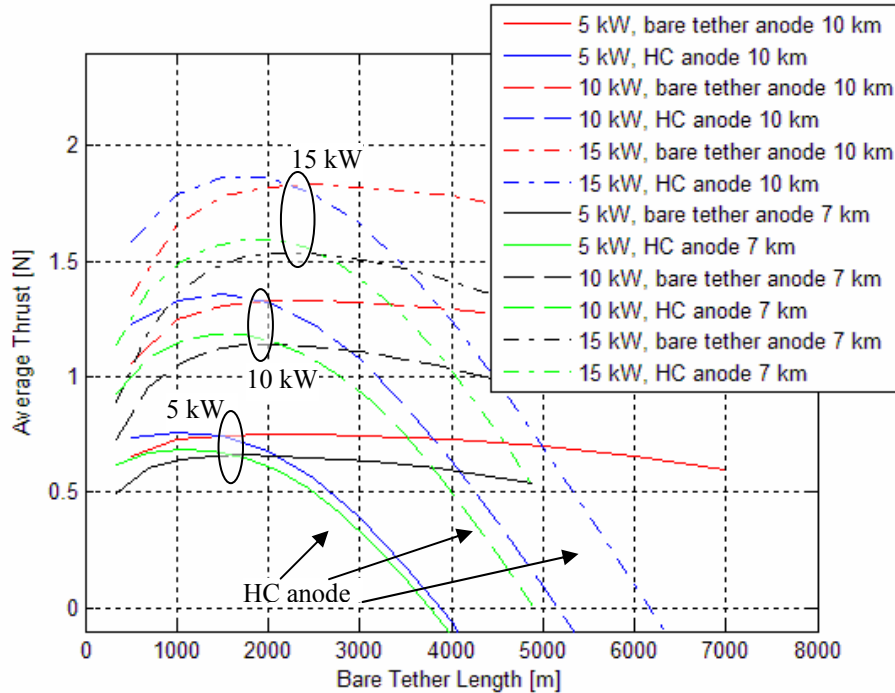
Figure 6-9: Bare tether length vs. average thrust with an HC e- emitter at 350 km altitude during solar minimum comparing various power supplies and endbody collectors for a 0.6 mm thickness, 11 mm width tether

Next, the differences between solar minimum, July 1996, and solar maximum, Dec. 2001, for both 350 km and 450 km altitude, were assessed at the 11 mm tether width, and 7 km and 10 km lengths. It is shown from both the 7 km tether case in Figure 6-10 and the 10 km case in Figure 6-11 that the differences in thrust are 15% between solar maximum and solar minimum cases.
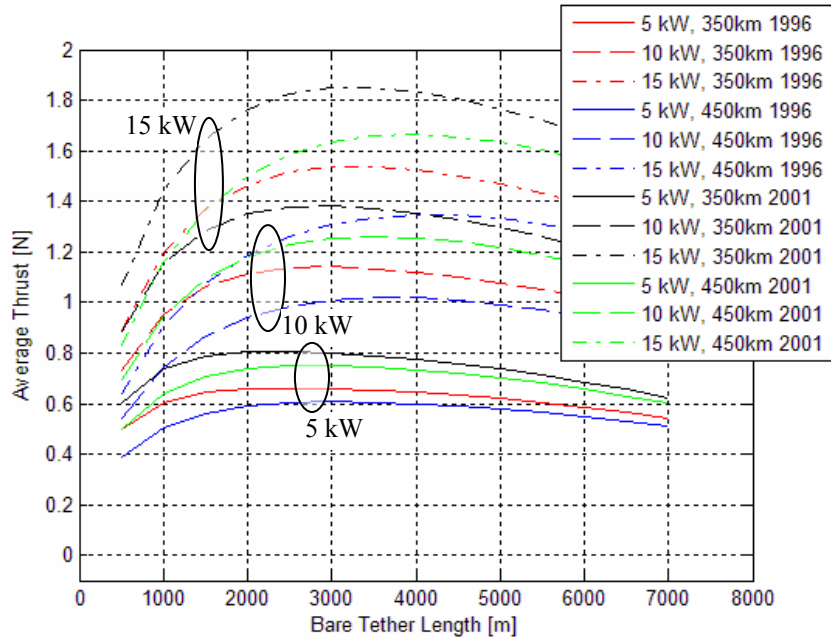
Figure 6-10: Bare tether length vs. average thrust for a 7 km tether system with an HC e-emitter comparing various dates and altitudes for a 0.6 mm thickness, 11 mm width tether
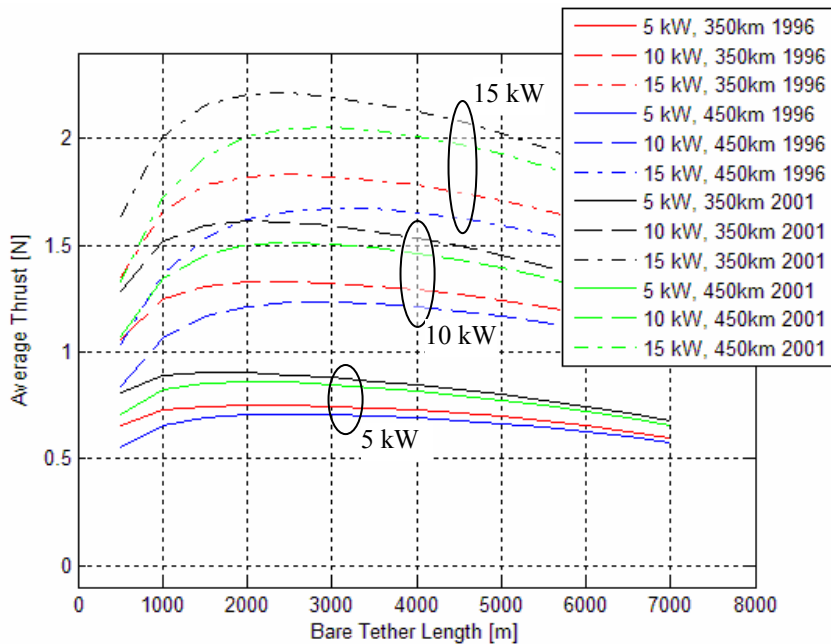
Figure 6-11: Bare tether length vs. average thrust for a 10 km tether system with an HC e- emitters comparing various dates and altitudes for a 0.6 mm thickness, 11 mm width tether

A significant observation shown in Figure 6-9 and Figure 6-10 is that the optimum bare tether length occurs at nearly the same point despite changes in the altitude and solar cycle point. This trend holds well for the 5 kW system, but varies slightly as the solar cycle has no significant impact on the optimum bare tether length at all powers.

206

This affect likely occurs because despite the overall electron densities being different at various points in the solar cycle, the day to night thrusting relationship (shown in Figure 5-3) is relatively consistent.

The next analysis was to compare different width tethers. This was conducted for the bare tether at 5 and 10 kW power supplies because it was shown earlier that larger powers could be extrapolated. The 7 km tether simulations are seen in Figure 6-12 and 10 km tether cases in Figure 6-13. These simulations display the fall off in collection efficiency from OML as the width gets larger, as described in Section 2.1.2 The thrust does increase as the width of the tape increases despite the increasing drag. It can be seen that this thrust increase diminishes as the width increases. If the tether continues to become wider, then the increase in drag will more than outweigh the thrust enhancement, and their thrust will begin to drop.
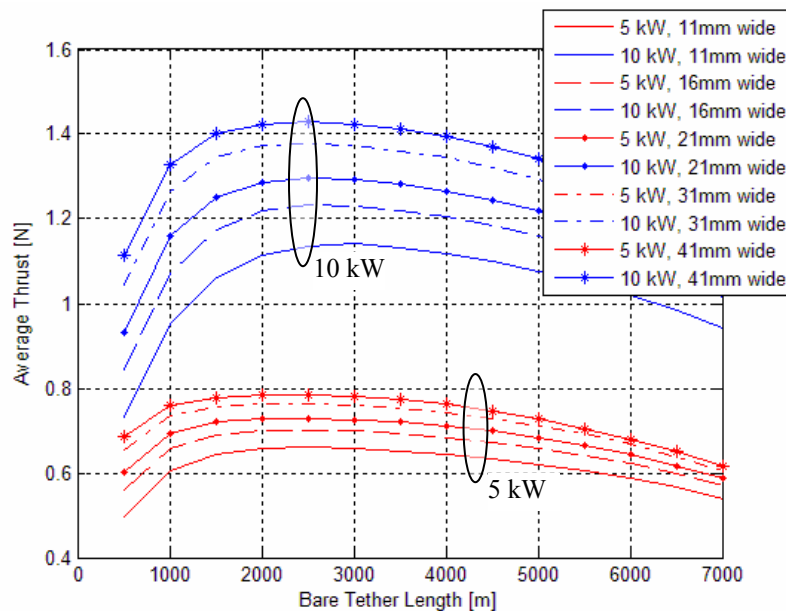
Figure 6-12: Bare tether length vs. average thrust for a 7 km tether system with an HC e- emitter at 350 km for a 0.6 mm thickness tether comparing various width tethers
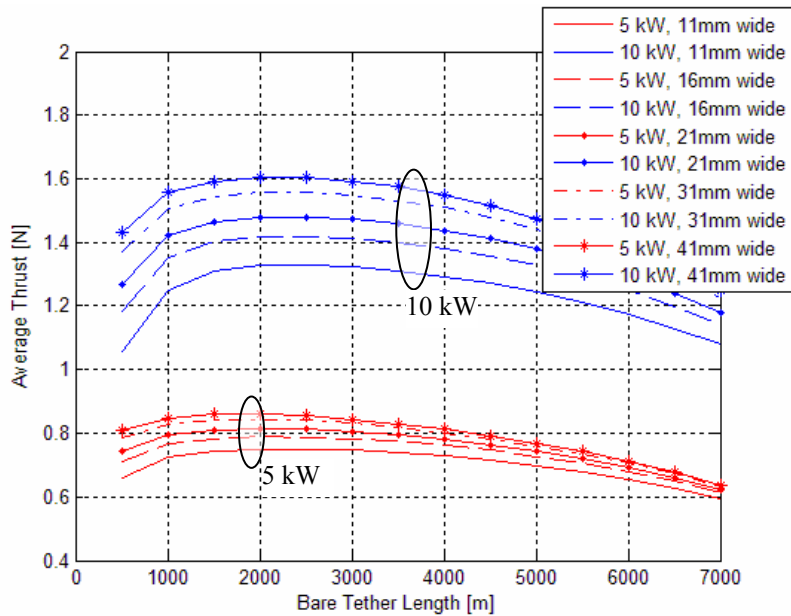
Figure 6-13: Bare tether length vs. average thrust for a 10 km tether system with an HC e- emitter at 350 km for a 0.6 mm thickness tether comparing various width tethers

The discussions of the simulations performed thus far pertain to the average boosting value. The density can vary by up to a factor of 100 from day to night in some typical extreme cases. It has been shown in Figure 5-3 that the boosting ability of the EDT system varies by over a factor of 10 throughout this density range because of the increase in available electrons to be collected, explained in Section 5.2.1. It is also known that if one particular point in the orbit is boosted much more than another, an elliptical orbit will result shown in Section 5.1. As a result, it is important to know what thrust a continuous boost can occur.

The only way to maintain a constant boost force throughout an entire orbit is to use the lowest force encountered in that orbit using the maximum amount of power. This is because every other point in that orbit will be able to achieve that same thrust by simply reducing the HVPS. To obtain this lowest force value, the minimum density and magnetic field encountered over a typical orbit for each respective date and altitude, was acquired and simulated. These minimum values can be seen in Table 6-16, and the respective simulations are shown in Figure 6-14. The particular EDT system configuration used was the 10 kW, 21 mm width, 10 km, solid tape system, using a bare tether endbody collector and a HC cathode.

Min Thrust	450 km Max	450 km Min	350 km Max	350 km Min
n_e [m^{-3}]	9.43×10^{10}	2.54×10^{10}	1.23×10^{11}	3.56×10^{10}
B [T]	6.58×10^{-6}	9.12×10^{-6}	6.84×10^{-6}	9.22×10^{-6}

Table 6-16: Values used to obtain the lowest boosting force for each respective orbit
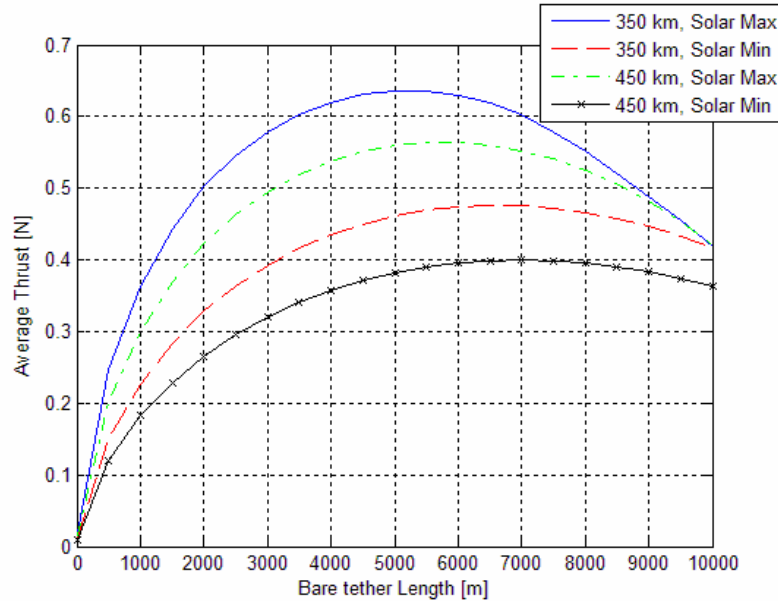
Figure 6-14: Minimum boosting force versus bare tether length for a 10 kW, 21 mm width, 10 km, solid tape system. Varying altitudes and dates are plotted.

Each orientation at their respective date is capable of a uniform thrust over an entire orbit at the particular bare tether length the maximum value is found. A constant boost throughout the entire orbit is achievable through appropriate regulation of power. It should also be noted that the figure serves as a minimum bounds to the uniform thrust value. Similar plots can be made for each EDT configuration. This merely serves to present the constant boosting scenario.

6.3.3 Analysis: Optimization Methods

Different ISS system powers and altitudes were used to demonstrate what the resulting boosting force would be. For the remainder of this section the system under test contains a bare tether anode with an HC cathode[52]. All other system variables will be detailed in the text. The first data set presented in this section details boosting forces without accounting for drag using a solid tape and averaging solar maximum and

---

[52] As detailed in Section 5.3.2, an FEA cathode will produce near identical results as an HC, only the FEA technology has not been experimentally verified for currents necessary for this tether system.

minimum. Averaging was done for the charts of this section to reduce the amount of data. The total thrust produced by solar maximum and minimum is approximately ±0.05 N from the values seen in Table 6-17 and Table 6-18. Several trends can be identified within these results as summarized in Table 6-17 and Table 6-18. The optimal bare tether amount is seen to decrease as the tether width increases. This phenomenon is similar to that seen in the GLAST mission. Since the tapes are getting wider, there exists more exposed conductive surface area for electron collection. As a result, it takes less exposed tether to acquire all the necessary electron collection for the system. The bare tether amounts can be seen to jump by groups of 350 m or 500 m. This is the result of simulations being taken at those particular points. In reality, the optimum point is gradually changing with each particular EDT case, however to save in simulation time, fewer points were taken.

7 km Tether		11 mm	16 mm	21 mm	31 mm	41 mm
350 km 5 kW	Force [N]	0.736	0.771	0.806	0.841	0.864
	Bare [m]	1750	1400	1400	1400	1400
350 km 10 kW	Force [N]	1.261	1.367	1.437	1.518	1.577
	Bare [m]	2100	1750	1750	1750	1400
450 km 5 kW	Force [N]	0.677	0.736	0.759	0.806	0.829
	Bare [m]	2100	1750	1750	1400	1400
450 km 10 kW	Force [N]	1.145	1.215	1.332	1.437	1.495
	Bare [m]	2450	2450	2100	1750	1750

Table 6-17: The optimal force and bare tether length for a 7 km tether for 5 and 10 kW over 350 and 450 km altitude orbits using solid tapes averaging solar maximum and minimum

10 km Tether		11 mm	16 mm	21 mm	31 mm	41 mm
350 km 5 kW	Force [N]	0.829	0.864	0.888	0.911	0.934
	Bare [m]	2000	2000	1500	1500	1500
350 km 10 kW	Force [N]	1.460	1.565	1.624	1.705	1.752
	Bare [m]	2000	2000	2000	2000	1500
450 km 5 kW	Force [N]	0.783	0.829	0.853	0.888	0.911
	Bare [m]	2000	2000	2000	1500	1500
450 km 10 kW	Force [N]	1.390	1.483	1.542	1.635	1.682
	Bare [m]	2500	2500	2000	2000	2000

Table 6-18: The optimal force and bare tether length for a 10 km tether for 5 and 10 kW over 350 and 450 km altitude orbits using solid tapes averaging solar maximum and minimum

An observable trend displayed within Table 6-17 and Table 6-18 is that the total boosting force increases with increasing tether width. As expected, this occurs due to the increasing surface area of collection. This increasing area allows for more current to be

collected more rapidly, resulting in an enhanced boost for an equivalent amount of power. The rate of growth in the EDT force diminishes with larger tape widths because the collection deviates from OML theory as seen in Figure 6-1. Also, as expected, the 10 km tether boosts more than the 7 km case in every instance due to the current traveling a longer distance, as explained in Eq. 1-2. It is important to note that thicker and longer tethers also have more mass and drag associated with them. In addition, there will be a change in the resistance as the tether cross sectional surface area is altered, according to Eq. 6-4. This resistive effect will affect the boosting force similar to Figure 5-9b. Also, increasing the thickness of the tether will not have an affect on the current collection until it becomes larger than a Debye length.

All of the cases simulated thus far can be applied to holed tapes using an approximation. From the experiment detailed in Chapter 4, it was found that the total current that was collected for normalized potentials $[(V_0 - V_p)/T_e]$ of 50 and 100 were approximately 75% and 81% of the total solid tape collection, respectively. In the ionosphere at the altitudes mentioned, the experiment translates to a tether to plasma potential difference of 5 V and 10 V. Since the potentials encountered in a typical EDT system can be up to several kV, depending on the amount exposed and the environmental conditions, this is not a reference value. It does suggest, however, that as the tether to plasma potential increases, the greater the percentage of the current collection the holed tapes come to the solid tapes. For this analysis, the 81% factor was applied as a conservative estimate until more experimentation can be accomplished to verify higher voltage values. This assumption is weak at best, however is the best that can be dine given the small amount of experimental and theoretical data.

In order to assess the total amount of system boosting force each respective tether sample results in, the total drag must be accounted for and subtracted out. It was found that for the 350 km altitude simulations, as observed in Figure 6-15, a maximum value can be discerned. These maximum points at 350 km, 5 kW are ~21 mm and ~16 mm width for the 7 km and 10 km tethers, respectively. A maximum also exists for the 350 km altitude for 10 kW at ~31 mm. The remaining cases exhibit a similar behavior, where a total thrust maximum value is being approached but not attained. This indicates that tapes of increasing width improve total boosting force only to a point before the drag

exceeds the thrusting of the tether. This data can also be seen in Figure 6-15. Optimum points will be obtained if even larger width tapes are used, but as will be explained in the next section, wider tethers will be shown to be too massive and far beyond the necessary thrust for a practical system.

Total Force vs. Solid Tether Width for a 7 km Tether

(a)

Total Force vs. Solid Tether Width for a 10 km Tether
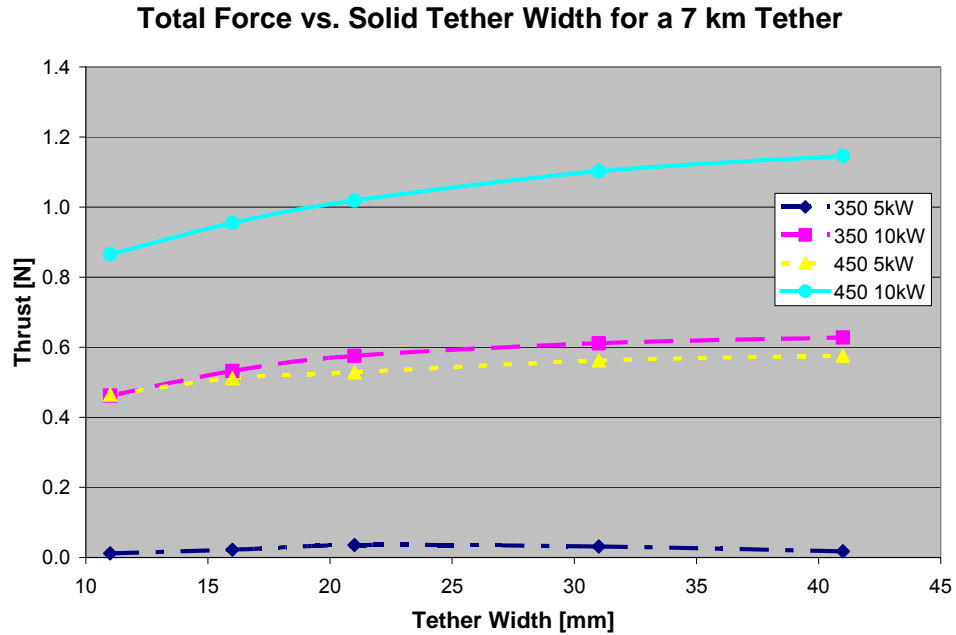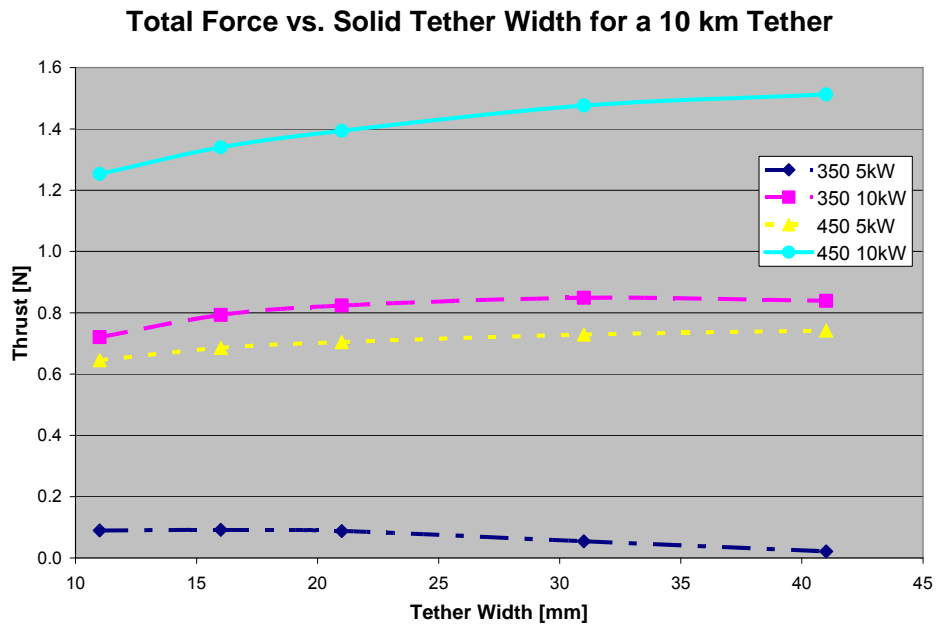
(b)

Figure 6-15: The change in thrust with the change in width for an a) 7 km and a b) 10 km tether system.

As the tape gets wider, more total thrust is obtained, however at an increasingly less efficient rate, as described earlier in this section. That, combined with the increase in atmospheric drag eventually resultsin a point where a wider tether yields less thrust. The primary factors that affect the outcome of the optimal point are:

- Higher altitudes have less atmospheric drag (MSIS model)
- Wider tethers collect less efficiently (Section 2.1.2)
- Increased power allows for more collection (Section 5.2.2)
- Longer tethers allow for greater thrust (Section 5.3)

The next value to be analyzed is the impact an equal mass OML tether will have on the system analysis.

The most current that a tape can collect would be according to OML theory. However, as the tape becomes wider, the electron current collection deviates from this theory according to Figure 6-1 [66]. The tapes are now divided into 10 equal sections which are each small enough to be in the OML regime. These narrower tapes would also have the same V_{emf} across them as the larger width tapes, because they are all in a parallel connection. The resistance for each section, however, will increase by a factor of 10, according to Eq. 6-4. These results can be seen in Figure 6-16, which analyze the 7 and 10 km cases for both the solid tapes and the holed tapes. Also, the bare amount of tether necessary to achieve the results in these figures can be seen in Table 6-17 and Table 6-18. For this case, it is shown in Figure 6-16 that the performance is always significantly better than the single, wider tether, as was predicted by OML theory. In Figure 6-16, similar color lines are of equivalent mass.

7 km Solid Tape: Equal Mass Thrust
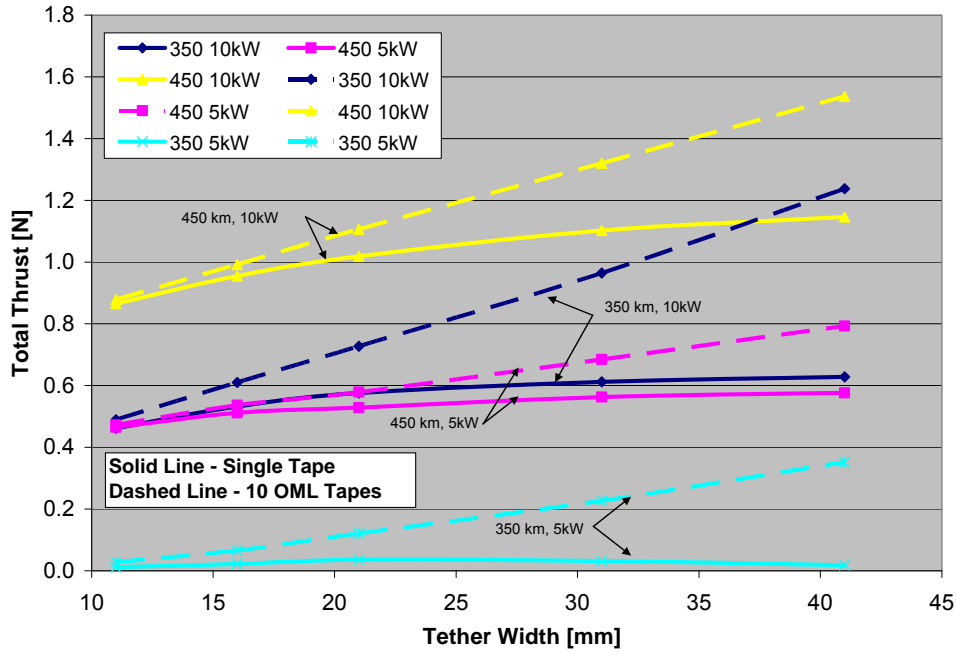
(a)

10 km Solid Tape: Equal Mass Thrust
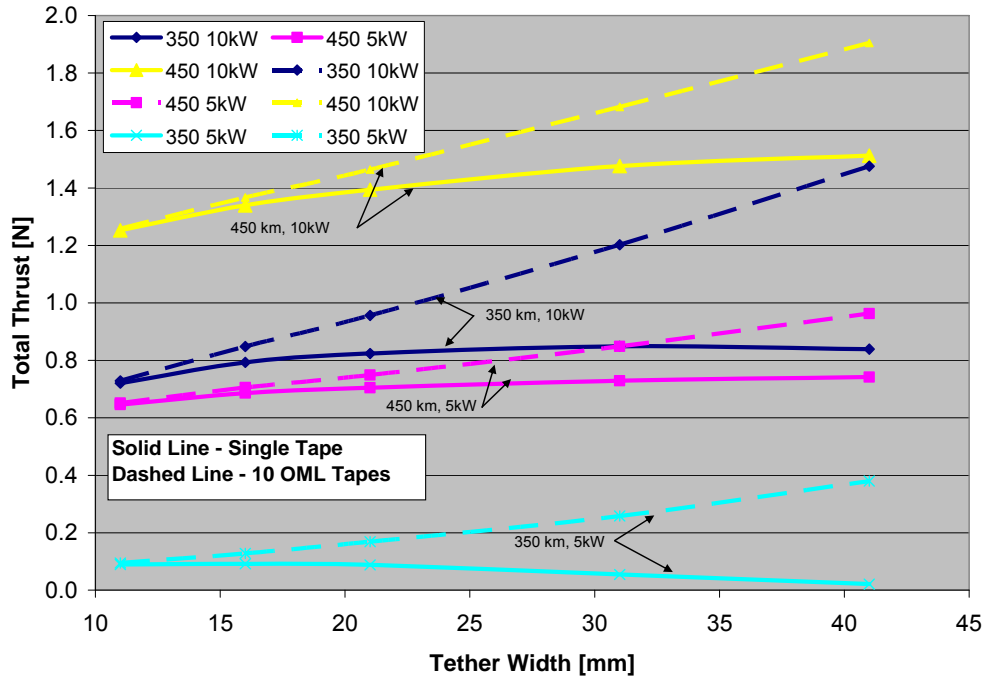
(b)

7 km Holed Tape: Equal Mass Thrust
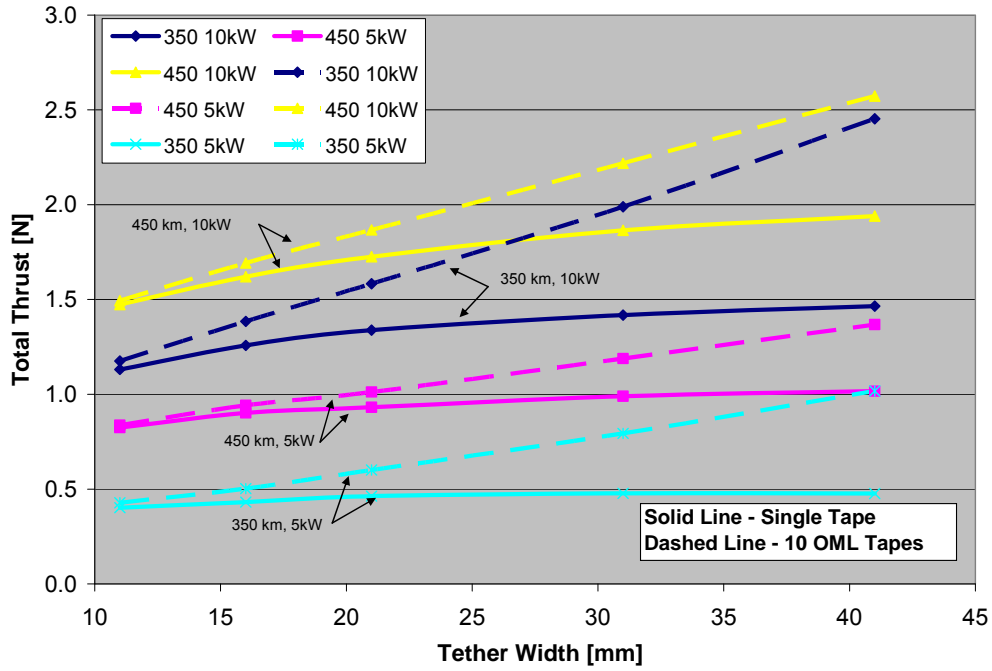
(c)

10 km Holed Tape: Equal Mass Thrust
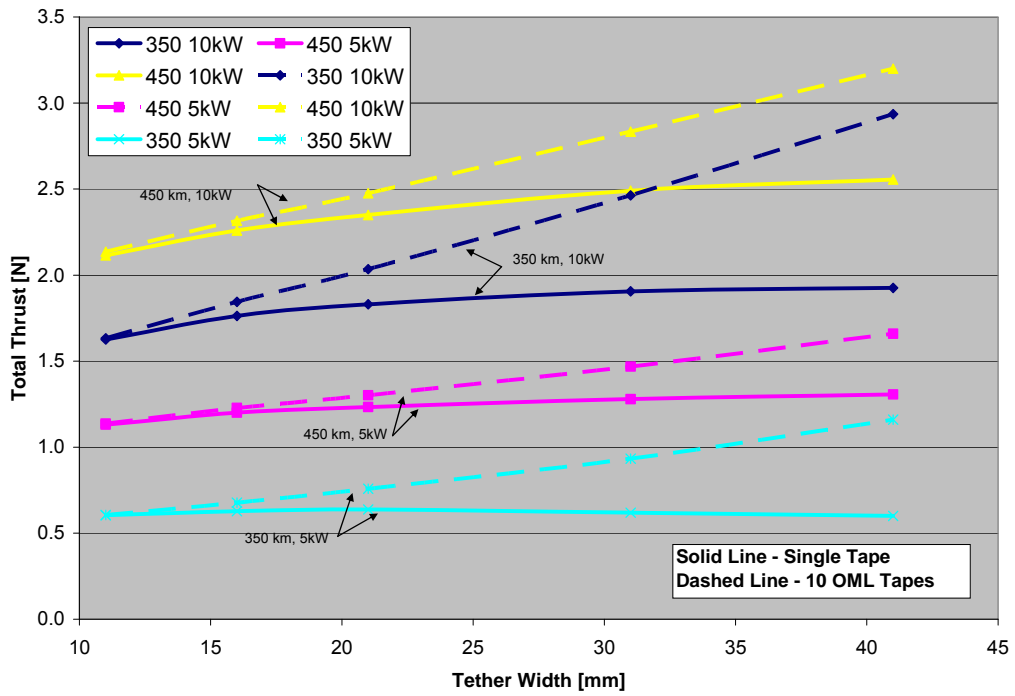
(d)

Figure 6-16: Comparison between a single wide tape tether and a 10 equivalent mass tethers, which are small enough to collect under OML theory at a) 7 km solid, b) 10 km solid, c) 1 km holed, and d) 10 km holed tether lengths

215

6.3.4 ISS Conclusion

Overall, it appears that the highest total thrust results in the 450 km 10 kW system using the 10 km long, 41 mm wide, holed tape, which is bare for 2 km. This system produces a net thrust of 1.9 N (which accounts for the drag of the ISS and the tether). Ideally the best case overall would be to have multiple tether lines, where each individual tether is in the OML regime. This would greatly enhance the performance of all tether widths. The only issue with this is that the tethers would have to be several hundred Debye lengths apart to take full advantage of this fact, as described in Section 2.1.2.

The hollow cathode was used as the electron emitter of the tether system presented here. It was shown in Figure 6-7 that the field emitter array can yield results equivalent to that of the HC, except for the fact that no gas consumable will be required to run it. The FEA technology required for this simulation is still a number of years into the future. When it is developed, it will be the optimal choice for the tether system.

Powers larger than 10 kW would also enhance the system performance, however 10 kW was the design condition limit. Similarly, a longer tether would be better, but is limited at 10 km.

A bare tether was used as the electron collection mechanism. For this 10 km system, there would need to be an endbody of ~52 kg according to Eq. 6-2, in order to keep the tether taught. If a payload is not on this endbody, then it may be used to contribute toward the electron collection as a conductive body. This would enhance the electron collection and increase the maximum boosting force. It would also alter the optimized bare tether amount, as described in Section 5.4.2.

Possible errors in this calculation would result from the estimation made where the holed tape collection efficiency was 81% to that of a solid tape of equal width. More experimental data will be needed in order to determine the actual current collection as detailed in Section 6.3.3. In addition, the boosting capabilities of the holed tether in ionospheric conditions under realistic potentials will need to be tested. In addition, the process used to determine the optimal amount of bare tether could be refined to determine

the exact optimal amount, rather than a data point every 500 m. This would also enhance the thrust calculation slightly.

The results here are not as conclusive as they could be. This is due to the fact that more refined questions need to be answered before a total analysis can be conducted. For example, the best case described above tried to yield the highest thrust. This resulted in a system that could produce much more boosting force than was necessary for an orbital maintenance application. A smaller value would save on power consumption as well as system mass, and thus cost. Also, the lifetime of the ISS can affect the width of the tether necessary. Thicker tethers will be required for longer missions. In addition, the available surface area on the ISS, for EDT sub-system will be important. FEA's and multiple strand tethers will require a lot of space in order to operate at their maximum efficiency. These particular design conditions need to be investigated and specified in order to acquire a complete analysis.

To summarize, the conditions for this work on the ISS are:

- The highest total thrust system tested is a 450 km 10 kW system using a 10 km long, 41 mm wide, holed tape, which is bare for 2 km
- FEA is best e^- emitter, once it is experimentally proven, otherwise HC is equivalent
- Multiple tethers are best, however need to be spaced $> 300 \, \lambda_{De}$
- More system objectives need to be determined for optimal system
    - How much thrust is necessary past maintenance thrust?
    - Mission lifetime
    - Available surface area

6.4   Momentum eXchange Electrodynamic Re-boost (MXER) Systems Analysis

Future EDT technologies may involve orbits that are not exclusively within a high plasma density ionosphere. As a result there must be an understanding as to what the

system will encounter while operating in these conditions. The MXER system is one such mission that follows an elliptical orbit that ventures out to an altitude of approximately 8200 km.

A specific realization of the MXER concept, described by Hoyt et. al. [7] uses a long, high strength rotating tether placed in an elliptical, equatorial orbit. Its rotation is timed such that the tether is oriented vertically below the central facility (side where the tether is stored and deployed during launch) and swings backwards when the system reaches perigee. At that point, a grapple mechanism, located at the tether tip, can rendezvous with and capture a payload. Half a rotation later, the tether releases the payload, tossing it into a higher energy orbit. This concept is termed a momentum exchange tether because when the tether system captures and then larer releases the payload, it transfers some of its orbital energy and momentum to the payload, resulting in a drop in the tether system's apogee and slowing of its rotation. In order for the tether system to accomplish this task multiple times, an EDT system is used to restore its orbital energy and momentum after each payload transfer operation. By properly controlling the tether current during an orbit, the tether system can re-boost itself to its original orbit, as illustrated in Figure 6-17.
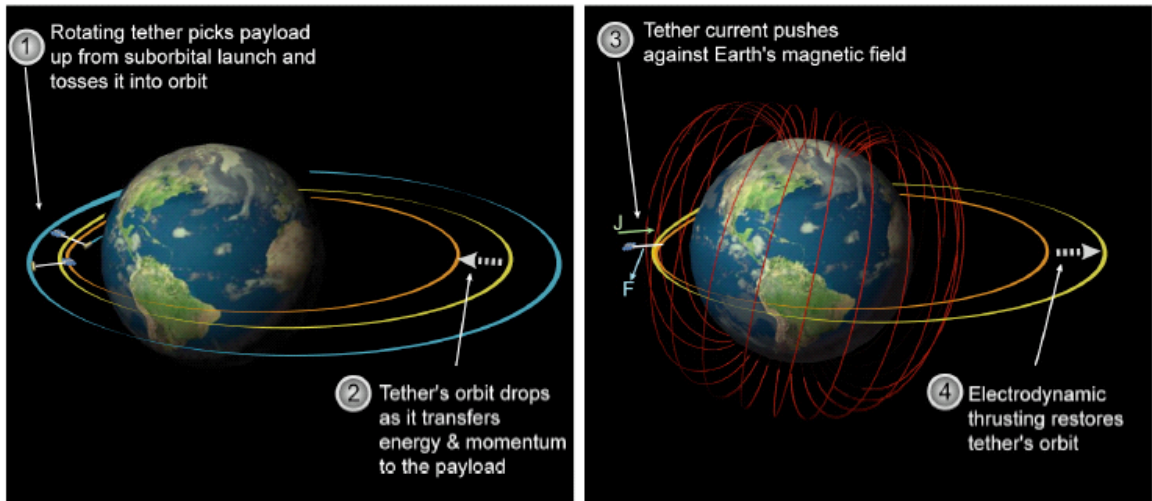
Figure 6-17: The MXER Tether Launch Assist Concept [7]

One particularly versatile technology on the EDT system is the Hollow Cathode. Its electron current collection and emission techniques, as mentioned earlier in Section 2.4.3, would be able to perform well within the regime of low electron densities and

magnetic fields. In order to understand the effects an HC would have on an Earth based MXER EDT system, knowledge of the atmospheric, ionospheric, and magnetic conditions must be obtained. Once this is known, it will be applied to simulations to identify performance enhancements.

This section will employ the EDT system simulations and techniques developed in this thesis to identify potential enhancements in the MXER system from that of previous work. The higher altitude environmental conditions will be discussed as well as their impact on the system. The MXER system bare tether amount will then be optimized according to the electron collection device below 2000 km. Finally, various high current HCs will be explored in hopes of improving the average thrust above and below 2000 km. A major issue concerning this system is if it can generate enough of an impulse during the perigee of the orbit, where the density is the greatest, so it can raise the apogee in a reasonable time frame. The goal of these simulations will be to determine if there is a way to enhance the thrusting on MXER such that it can reboost from post momentum exchange to pre-momentum exchange conditions (step 4 in Figure 6-17) in a reasonable time frame.

6.4.1   Space Environment

A number of significant changes occur above the ionosphere[53]. The ambient plasma gradually becomes hydrogen, which has a molecular weight of 1 amu, from 16 amu atomic oxygen at 300 km. This value directly affects the ion thermal current collection. Lower molecular weight plasma serves to enhance the ion collection, according to I_{thi} in Eq. 2-2. This means that a negatively biased tether will passively collect ions at a faster rate for a given potential. Also, the atmospheric drag falls off by five orders of magnitude between 300 km and 8300 km. This effectively eliminates all atmospheric drag effects over much of the orbit. The orbital velocity is also changing significantly. The further away from the Earth a satellite travels, the slower the velocity. From Eq. 1-1, it can be seen that the V_{emf} is reduced as well, by a factor of ~100 within the MXER's orbit as well. In the boosting mode, the V_{emf} is a value that must be overcome by the HVPS. This means that the HVPS has an easier time overcoming the

---

[53] The ionosphere is commonly defined as the region between 60 km 1000 km altitude [72].

opposing potentials, and thus has more potential to drive the electrons. This, in turn, enhances the boosting ability. The magnetic field also drops by a factor of ~10. This reduces the total boosting force, as seen in Eq. 1-2, by a factor of ~10. It also increases the gyro-radius of the incoming electrons and ions. This is a factor that must be kept in mind because if the circular end-bodies becomes smaller than the gyro-radius then it will no longer collect according to the TSS-1R corrected Parker Murphy law (Eq. 2-9).

It can be seen in Figure 6-18b that the electron and ion temperature changes by a factor of ~10 from 300 km to 8300 km. This also serves to further enhance the electron and ion thermal collection abilities. In addition, Figure 6-18a details the profile of the electron and ion density with respect to altitude. These values were both obtained using the previous IRI model up to ~2000 km. The IRI model used was an average value between solar maximum and solar minimum during the daytime. Models by Rycroft & Jones, and Gallagher, were used for values at higher altitudes [78, 79, 157-160]. The values were obtained graphically during summer conditions. As a result, there is approximately a ±2-5% tolerance on these plots. It can be seen that the differing models, shown in Figure 6-18 at 2000 km altitude, did not line up exactly, but the results allowed for an adequate simulation. This is because each model is likely to be slightly the actual value, and these models are the best predictions available. The remainder of the atmospheric, ionospheric, and geomagnetic values can be obtained from the MSIS and IGRF models, respectively.

IRI & Rycroft & Jones:
Electron Density vs. Altitude

(a)

IRI & Rycroft & Jones:
Electron Temp. vs. Altitude
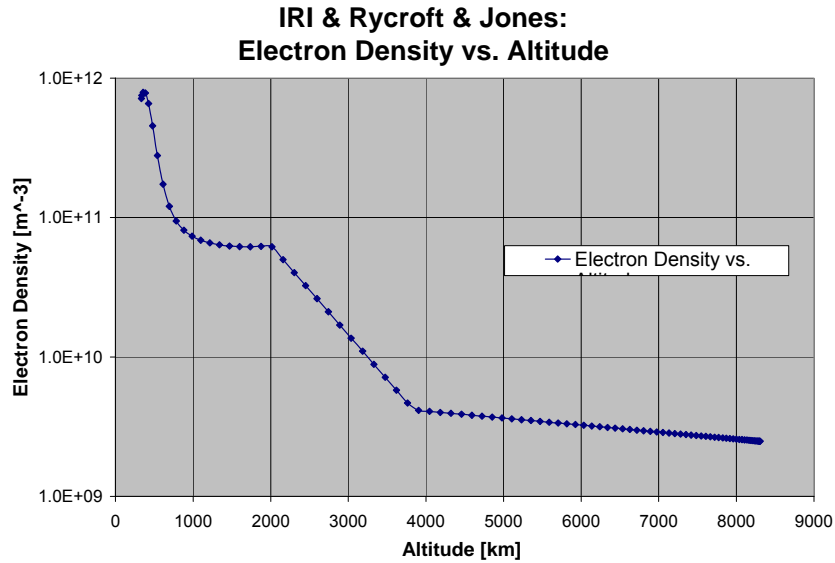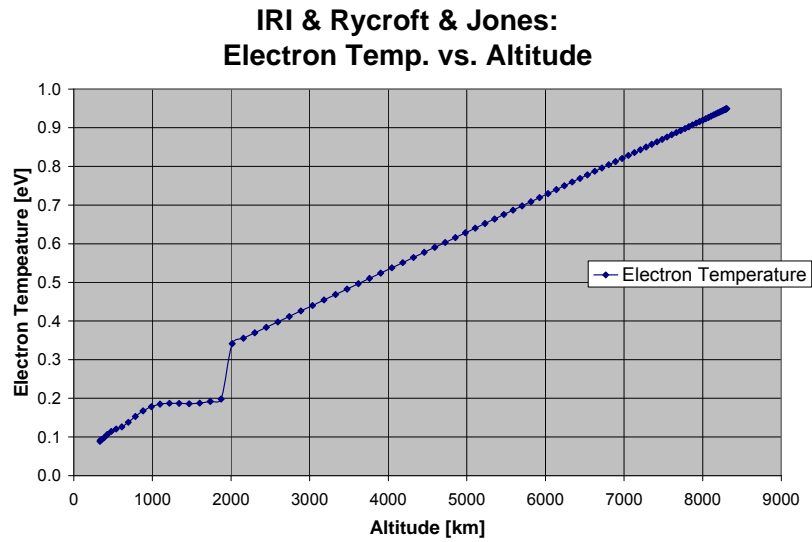
(b)

Figure 6-18: Description of the (a) Electron density and (b) Electron Temperature
using the IRI Model and Rycroft & Jones

6.4.2   Systems Analyses

According to Hoyt et al. [7] a probable MXER tether system will be composed of 80 km of conductive wire mesh called Hoyt Tethers. For the purpose of the tether system simulation a wire tether was used similar to the 'reference' wire used in the Chapter 5 simulations. Also, the Hoyt tether has approximately 30 Ω/km resistance [146], and the wire simulated was also set at this resistance. The MXER system also used an average of 60.5 kW to power the tether, as defined by Hoyt.

The elliptical orbit for MXER takes 184 minutes to complete. The time that the system is below 2000 km is ~39 minutes. Using the average HVPS power from Hoyt's work (constant 60.5 kW), if all the energy of the system for a 184 minute orbit was used during this 39 minute period, then the average power equates to a constant ~285 kW. This system would draw currents over 11.5 A, and as a result, rules out the use of FEAs (for near term use) and TCs (too much power expenditure). Hollow cathodes will be employed as the electron emission technology for the following simulations.[54] The two remaining EDT system aspects which could potentially be altered are the electron collection technology and the amount of bare tether. As a result, these are the variables that were simulated. A simulation was then conducted comparing various electron collection techniques, similar to that of Section 5.4.2, yielding results with equivalent trends and explanations. It can be seen in Figure 6-19 that the maximum thrust and total impulse for the region under 2000 km is best for the bare tether endbody collector. This plot is similar to the discussion of varying endbody collectors in Section 5.4, since the HC endbody collector tends to drop off much faster than the bare tether. In addition, the bare endbody collector, 1 m sphere, and 5 m spheres all produce approximately the same average thrust. This again implies that the bare tether is the best option as the endbody collector for the system since it requires less mass and complexity. Also, it can be seen that the optimal bare tether length for this bare tether anode system is ~12 km of the 80 km tether system.

---

[54] As displayed in Chapter 5.3.2, if an FEA was capable of emitting such crrents, then it would perform near identically to the HC electron emitter.
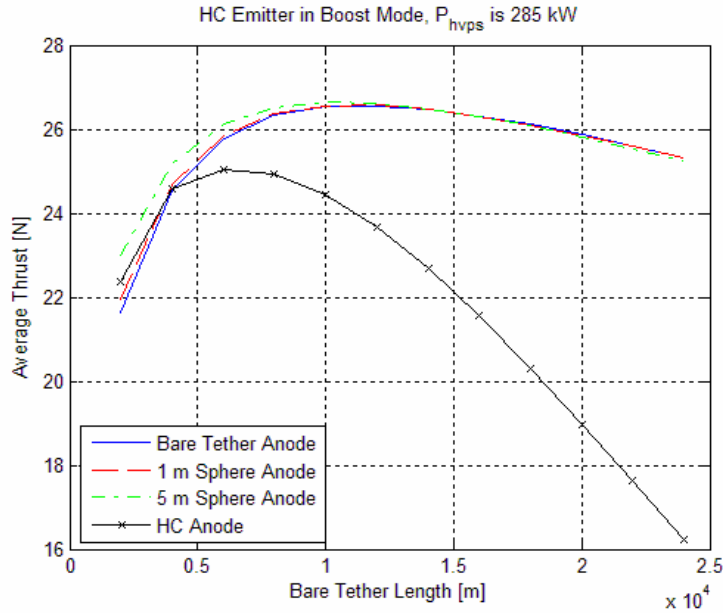
(a)
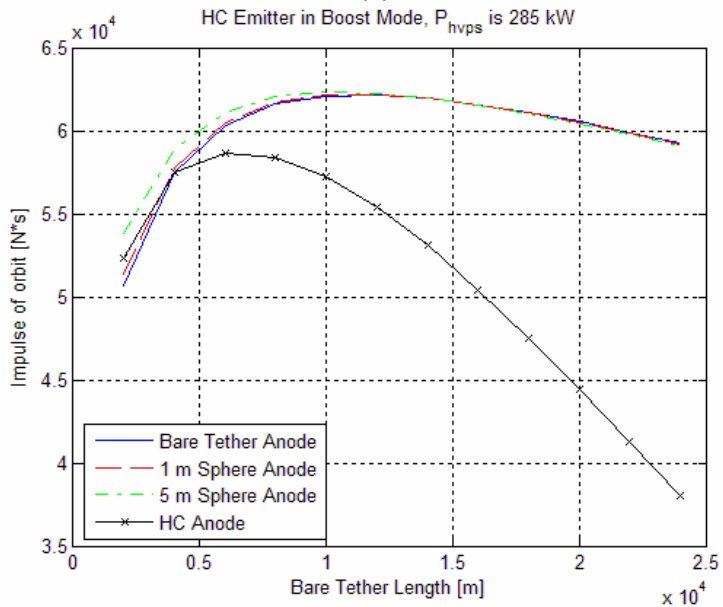
(b)

Figure 6-19: The (a) average thrust and (b) total impulse imparted to the orbiting system by the EDT. The EDT system used 285 kW, was 80 km long, used an HC emitter, and had a tether resistance of 30 Ω/km. This thrusting takes place throughout the time the system was below 2000 km (~39 min.).

The goal of this next simulation investigation deals with the enhancement of EDT boosting below 2000 km altitude. Since the electron density drops off significantly, bare tethers will lose effectiveness as an electron collector the higher the altitude. As a result, various HC technologies will be investigated for application in ranges up to 1000 km above the ionosphere.

223

The significant variables that affect the performance on an HC are the electron density, electron temperature, and magnetic field. Using the IRI and IGRF models the electron density, electron temperature, and magnetic fields for a typical average orbit at 2000 km are $n_e = 6.6 \times 10^{10}$ m^{-3}, $T_e = 0.34$ eV, and a B-field of 1.2×10^{-6} T. Using these values it can be seen in Figure 6-20 how an HC would perform under varying output ion currents. The ion current values given assume that each respective output value is singly ionized xenon. There must also be enough neutral xenon output such that the 'ignition' can take place as described in Section 2.4.3. The current conversion for the mass flow rate equates to 0.072 A / sccm, or 13.96 sccm / A. [55] This conversion assumes that the flow is singly ionized, and is independent of the particle species. The mass conversion for xenon equates to 0.098 mg/s per sccm. This value is dependant on the species. This implies, for example, that in order to achieve the electron collection profile indicated in Figure 6-20e, or 52 A, 726 sccm, or 71 mg/s of xenon must be emitted. This equates to 2245 kg per year if the HC was capable of performing at that rate for an entire year.

---

[55] sccm = standard cubic centimeters per minute
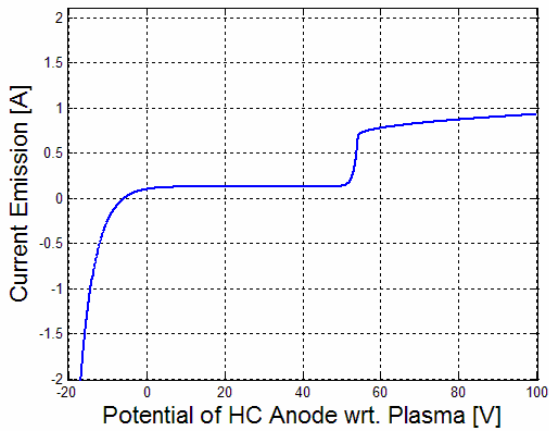
(a)
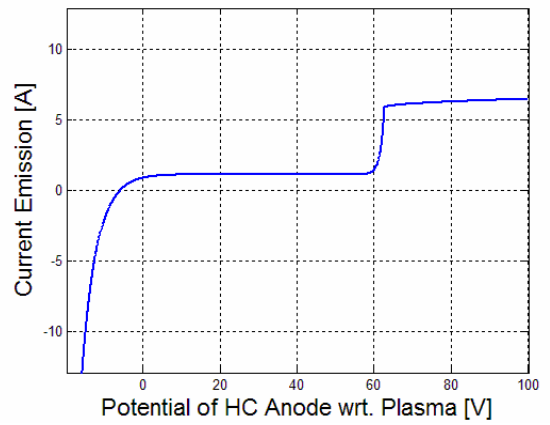
(b)
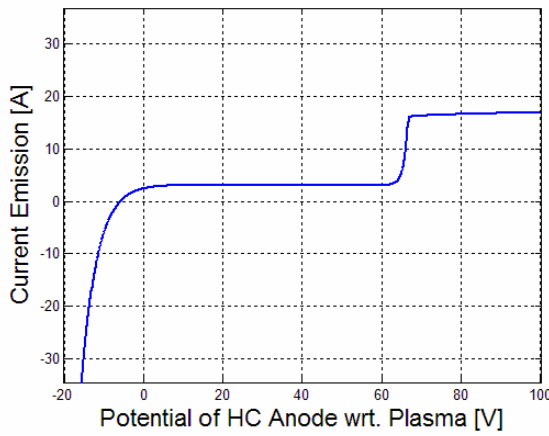
(c)
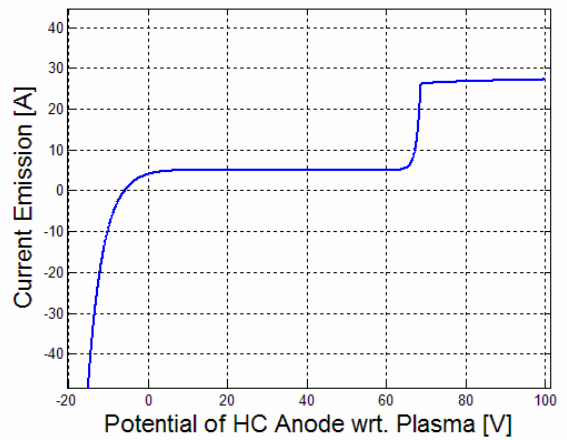
(d)
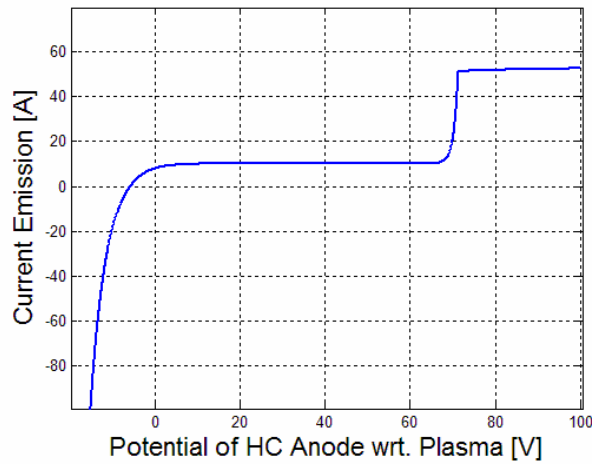
(e)

Figure 6-20: Details of the HC capabilities for an $n_e = 6.6 \times 10^{10}$ m^{-3}, $T_e = 0.34$ eV, and a B-field of 1.2×10^{-5} T. The HCs vary in their output ion current from a) 0.13 A to b) 1.13 A to c) 3.13 A to d) 5.13 A to e) 10.13 A

From the values in Figure 6-20, it can be seen that larger HC ion emission rates, I_o, result in larger electron collection values. [56] At the same time, this also increases the maximum electron emission capability when the ambient plasma is biased positive with respect to the keeper. The figure cuts off the maximum electron emission value for visual purposes. Following Eq. 2-20, these maximum electron current emission values are 25.0, 220.7, 612.1, 1003.6, and 1982.2 A for HC xenon ion currents of 0.13, 1.13, 3.13, 5.13, and 10.13 A, respectively. Further explanation of high current HC operation can be found in the Appendix C.

The ion emission currents, seen in the above HCs, are then applied to the example MXER system, as the endbody collector for altitudes under 2000 km[57]. The EDT system cathode is also an HC, however it has the original properties defined in Section 2.5.1. The anode part of the EDT system is simulated using the HC ion emission values of Figure 6-20. The 39 minute section of orbit below 2000 km altitude is tested using a 285 kW HVPS (similar to the previous simulation). The resulting total impulse and average thrust can be seen in Figure 6-21.

---

[56] A positive current value in Figure 6-20 indicates electron collection and ion emission.
[57] The values seen in Figure 6-20 are for the conditions at 2000 km. This profile will change as the environmental conditions, and thus altitude changes, throughout an orbit.
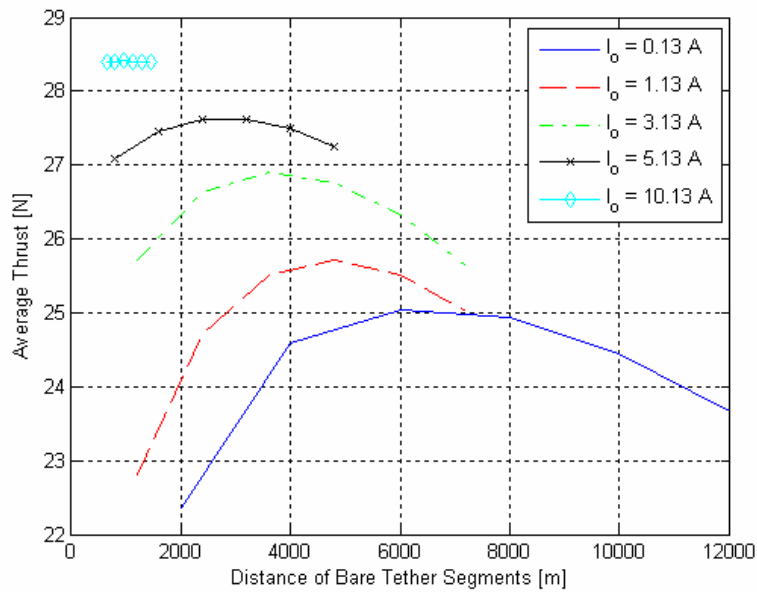
(a)
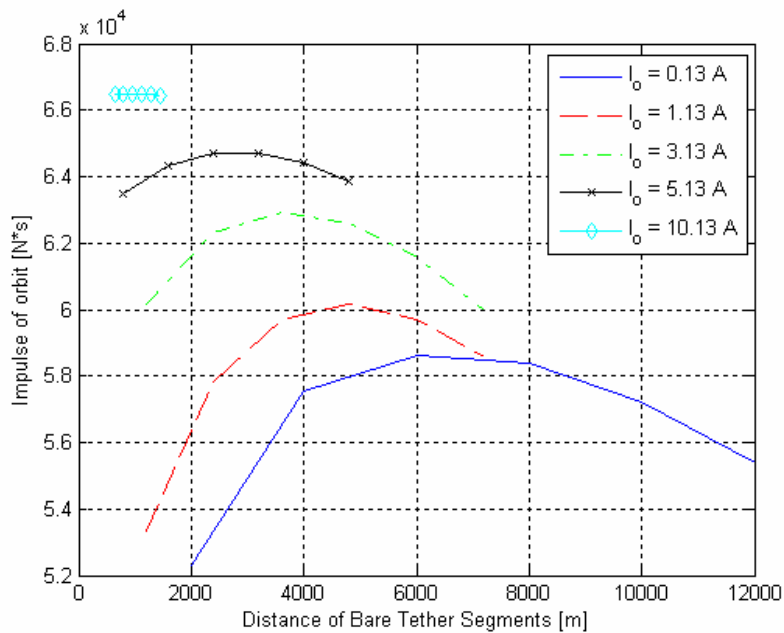
(b)

Figure 6-21: The (a) average thrust and (b) total impulse imparted to the orbiting system by the EDT. The EDT system used 285 kW, was 80 km long, used an HC emitter, and was 30 Ω/km. This thrusting takes place throughout the time the system was below 2000 km (~39 min.).

HCs with higher ion currents can be seen to yield EDT systems with higher average thrusts, while using an equal HVPS power supply. When comparing the optimal bare tether amounts of the HC anodes in Figure 6-19 with that of Figure 6-21 it can be seen that an HC anode using 10.13 A of ion current only out performs a bare tether

system by ~1.75 N, or ~6 % more thrust.[58] This occurs at the expense of about 2245 kg of xenon per year. As a result, it appears that the expense of the increase in boosting force may not be worth the added cost.

It can also be observed for MXER systems below 2000 km that the increased HC ion current does enhance the boosting capabilities of the system compared to that of lower I_o anode HCs. The increasing ion current results in diminishing returns, however. It can be seen in the 5.13 A to 10.13 A cases that the increase in boosting is ~ 1 N for a 5 A increase in I_o. The increase from 0.13 A to 1.13 A is also ~ 1 N for only a 1 A increase. Another observation shows that the optimal amount of bare tether decreases as the HC ion current increases. The optimal points were found to be 6000 m, 4800 m, 3600 m, 2400 m, and 960 m of bare tether for the 0.13 A, 1.13 A, 3.13 A, 5.13 A, and 10.13 A of I_o, respectively.

The resulting thrust and impulse increase is due to the enhanced electron collection and ion emission aspects of the HC as seen in Figure 6-20. In order to identify the particular causations of the improvement, the current and potential profiles are shown at their respective optimal bare tether amounts for each HC ion emission amount. These plots can be seen in Figure 6-23 through Figure 6-27. The 'Point in Orbit' refers to the altitude at which the simulation ran, as seen in Figure 6-22. It takes ~19 minutes to reach the apogee at 2000 km, and ~19 more minutes to return back to 300 km. Since the rise and rall in altitude plots are essentially symmetrical, just the 300 km to 2000 km range was plotted. The average thrust and impulse plots in Figure 6-21 are obtained from the full 39 minute orbit.

---

[58] Figure 6-19 and Figure 6-21 plot the same variables; however they are separated for visual clarity between the anode methods.
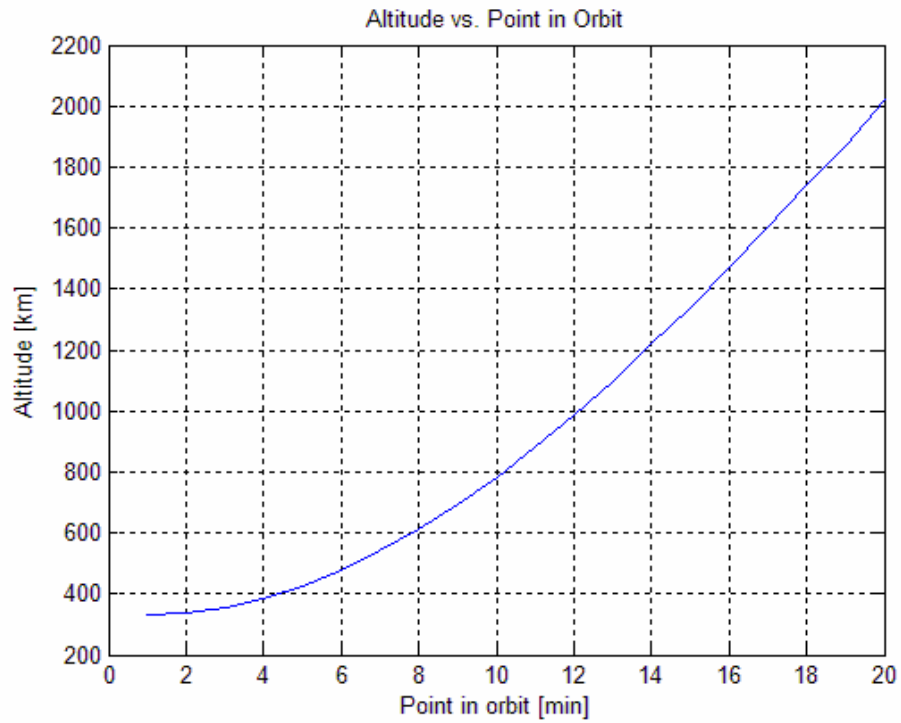
Figure 6-22: The Altitude of the MXER system according to the time in the orbit.

(a)

(b)
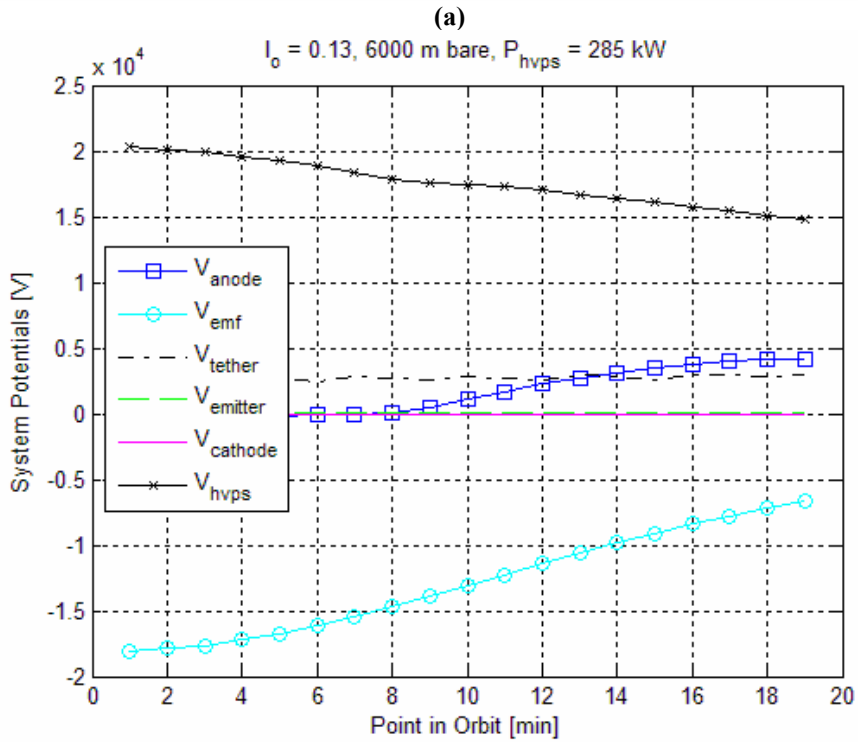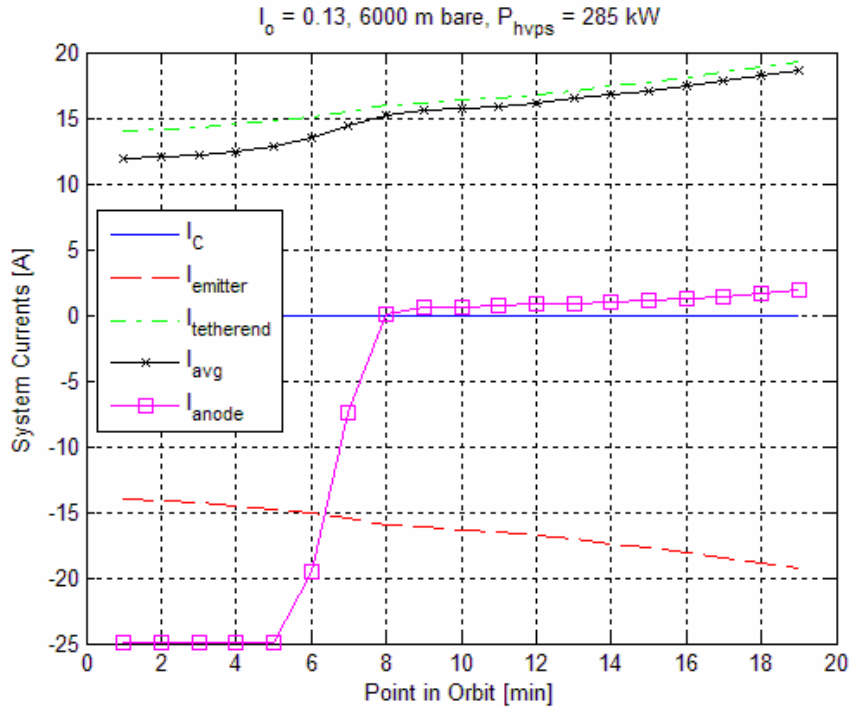
Figure 6-23: The a) Current and b) Potential Profiles for an HC Ion Emission of 0.13 A at the optimal bare tether point of 25 km. This is all shown at each particular point in the orbit from 300 km to the apogee of 2000 km and back down to 300 km.
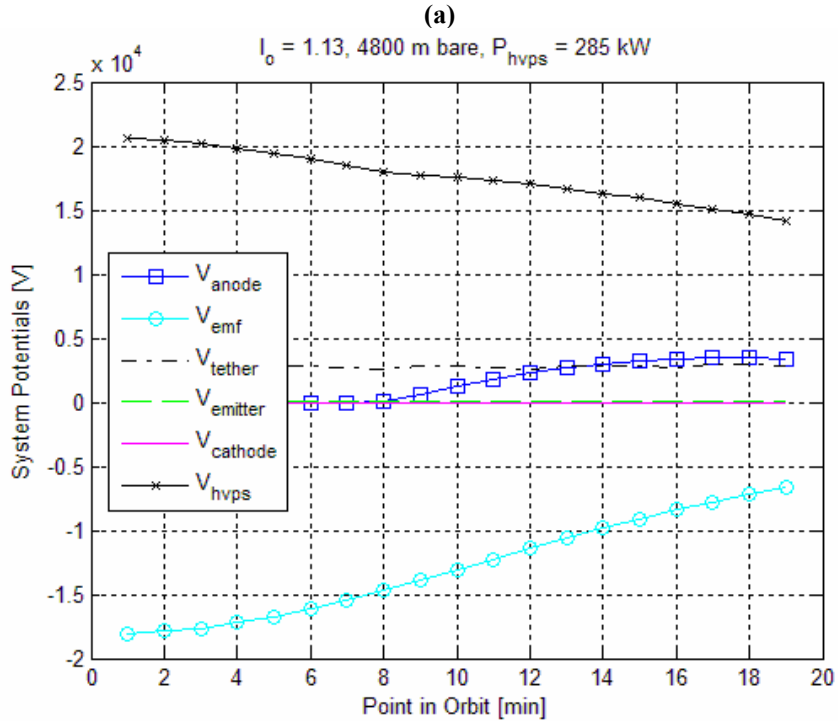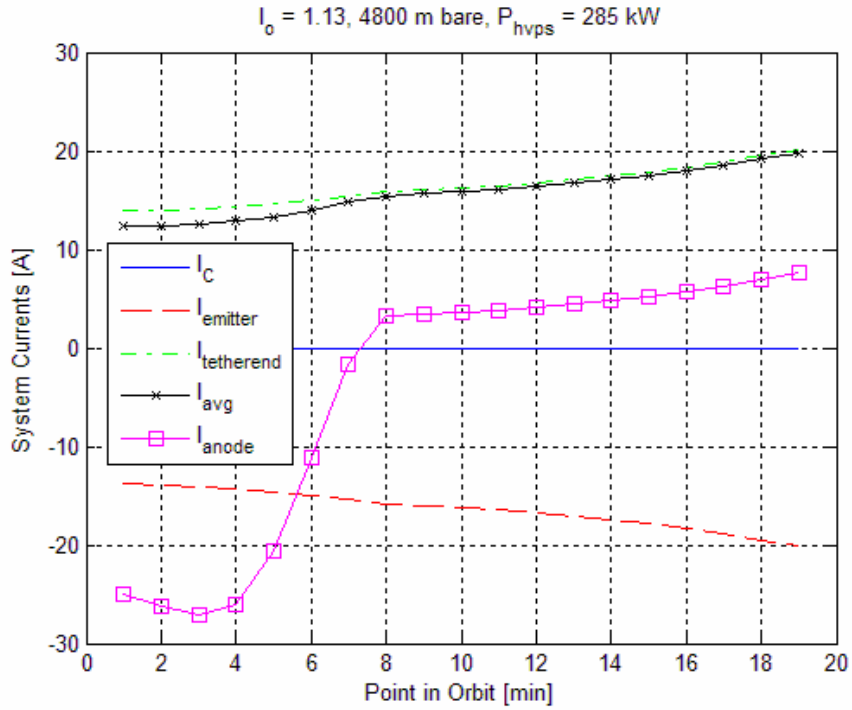
Figure 6-24: The a) Current and b) Potential Profiles for an HC Ion Emission of 1.13 A at the optimal bare tether point of 20 km. This is all shown at each particular point in the orbit from 300 km to the apogee of 2000 km and back down to 300 km.

(a)

(b)
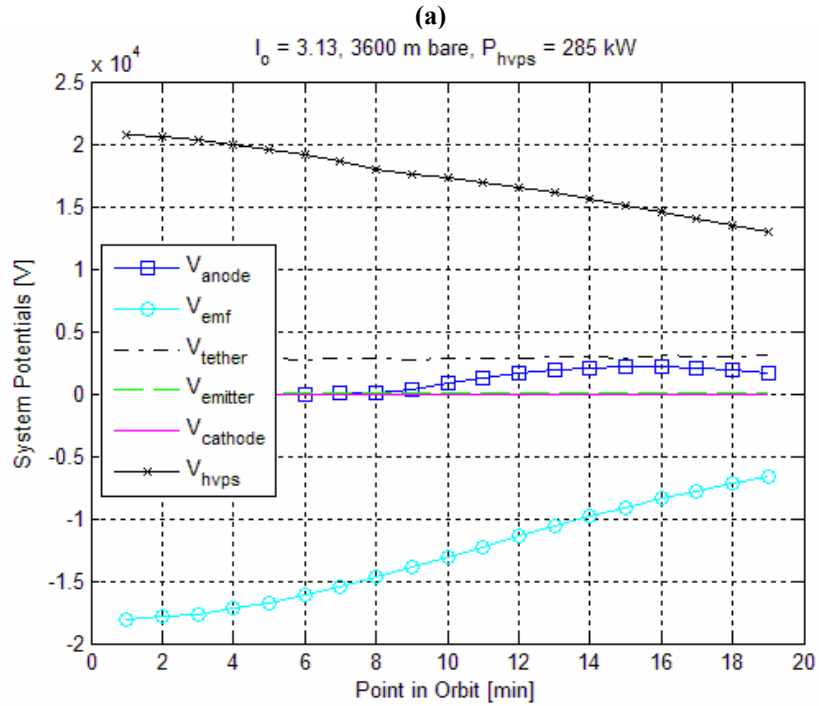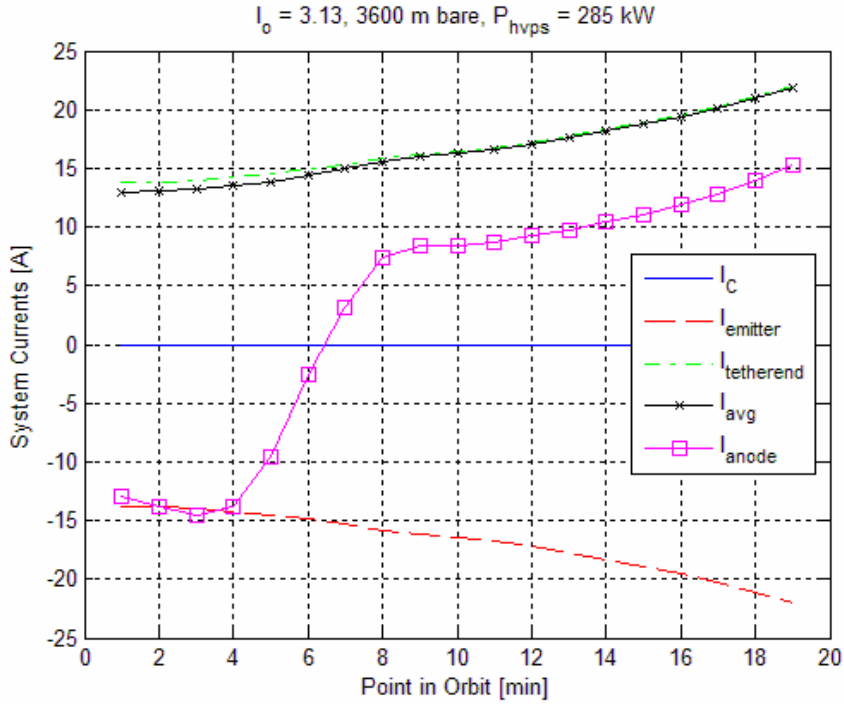
Figure 6-25: The a) Current and b) Potential Profiles for an HC Ion Emission of 3.13 A at the optimal bare tether point of 10 km. This is all shown at each particular point in the orbit from 300 km to the apogee of 2000 km and back down to 300 km.
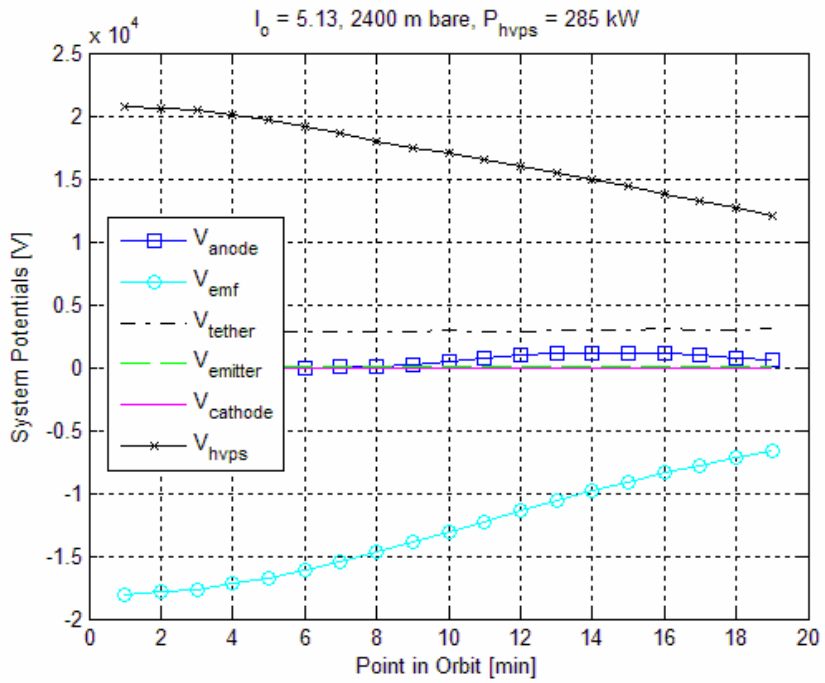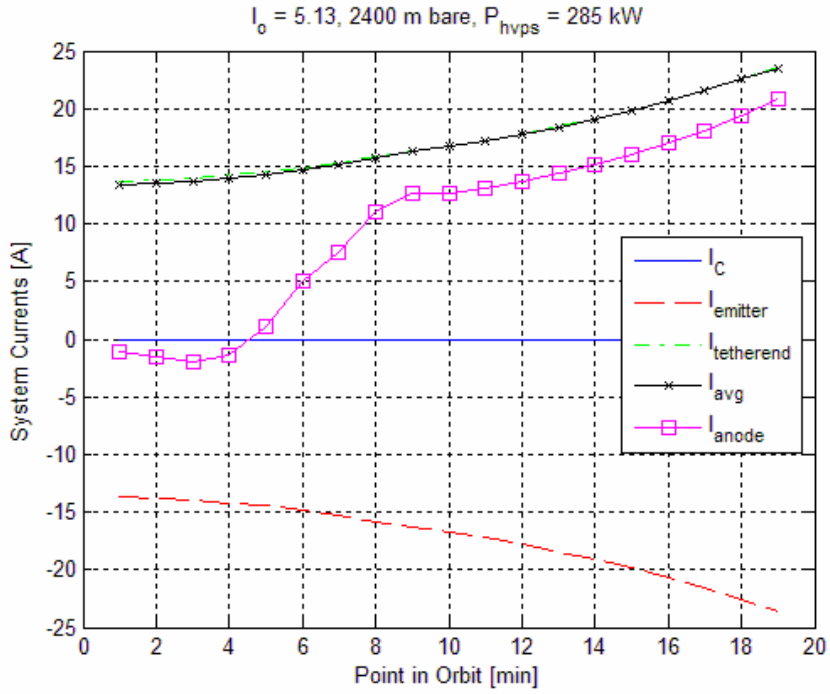
Figure 6-26: The a) Current and b) Potential Profiles for an HC Ion Emission of 5.13 A at the optimal bare tether point of 5 km. This is all shown at each particular point in the orbit from 300 km to the apogee of 2000 km and back down to 300 km.

233
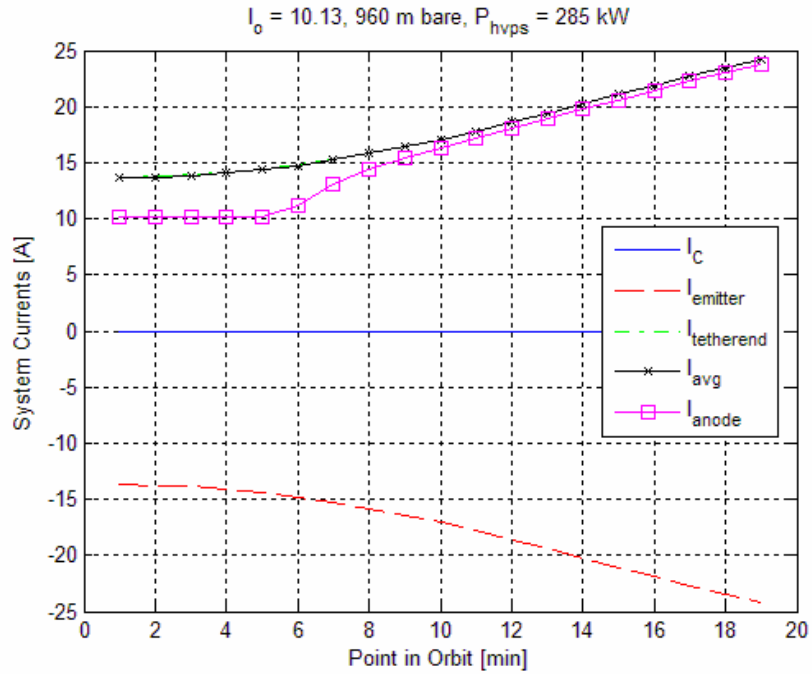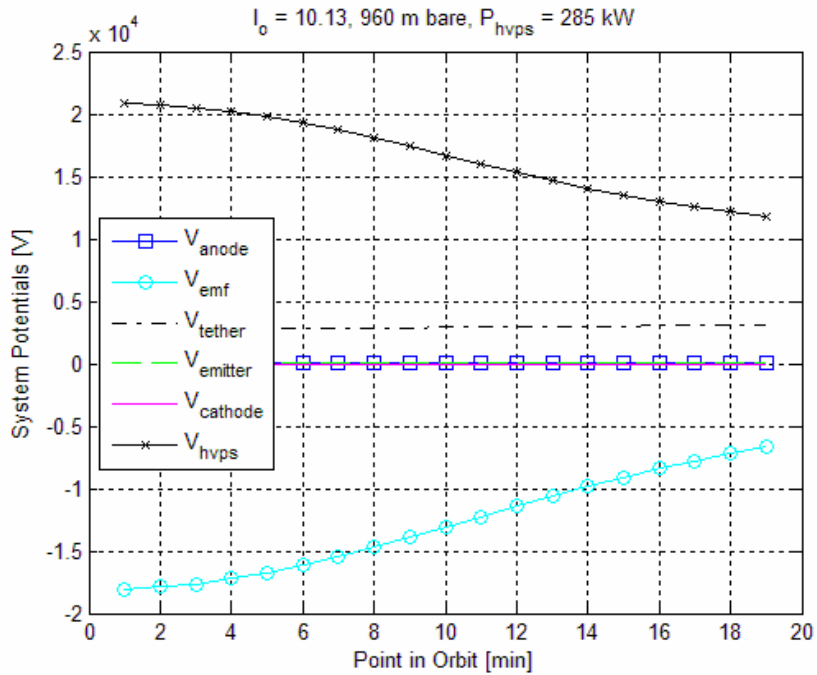
Figure 6-27: The a) Current and b) Potential Profiles for an HC Ion Emission of 10.13 A at the optimal bare tether point of 2.5 km. This is all shown at each particular point in the orbit from 300 km to the apogee of 2000 km and back down to 300 km.

A particular observation that can be made is the gradual increase in anode current with increasing HC ion emission current. At an I_o = 0.13 A the maximum average current starts at approximately 2 A, as seen in Figure 6-23a. This increases to a

maximum value of ~24 A, as the HC ion emission current increases to 10.13 A, as seen in Figure 6-27a. As I_o increases, a longer portion of the orbit operates at a higher anode current, and thus average tether current (which directly determines the system boost). The increase in I_o allows for an increasing amount of electron current to be collected with a smaller amount of V_{anode}. Figure 6-23a through Figure 6-26a display that the initial part of the orbit still requires that the HC endbody collector collect electron current in order to satisfy the KCL and KVL of the system. Ideally, the HC would be turned off during the times where it would be emitting electrons rather than collecting them. This would mean that the HC would need to be turned on and off once every 184 minutes, due to the constantly changing electron density from the changing altitude and day to night cycle. This means that much pre-mission calculation would have to be conducted ahead of time to determine the optimal place to cycle the power. As a result it was simulated being left on.

Also, using Eq. 3-18, it can be seen that the current driven by the power supply can be increased when the V_{hvps} is decreased. This allows for the increase in electron current collection by the endbody collector, and the overall tether current to be collected. This shows that as I_o is increased, the endbody collector current increases. This 24 A maximum current value, seen in Figure 6-27a, indicates that the mass flow rate must be at least 335 sccm, or 32.8 mg/s of xenon, assuming one can be made that will operate for these electron collection currents.

An important issue that must be addressed is the validity of the higher ion emission current HCs. In the electron collection mode of the HC, the ion plume must be large enough such that the ambient electrons that cross the plume 2d-surface area ($2 \cdot \pi \cdot r^2$) can equal the anticipated collected current. The lower the electron current density, the larger this plume area must be. As a result, the worst case scenario would be at the highest altitude, or at 2000 km in the previous simulation. The predicted plume radii and corresponding I-V curves can be seen for each of the HC ion emission values in Figure 6-28.

(a)

(b)

(c)

(d)

(e)

(f)

236
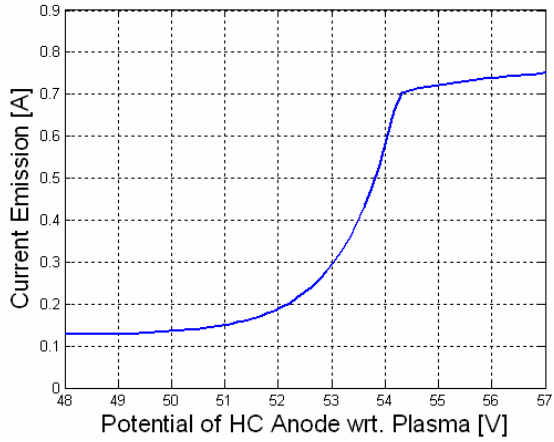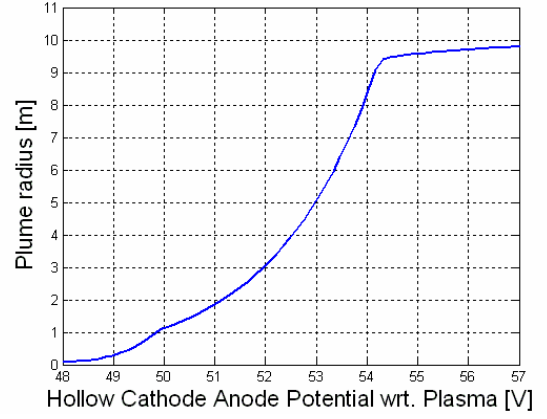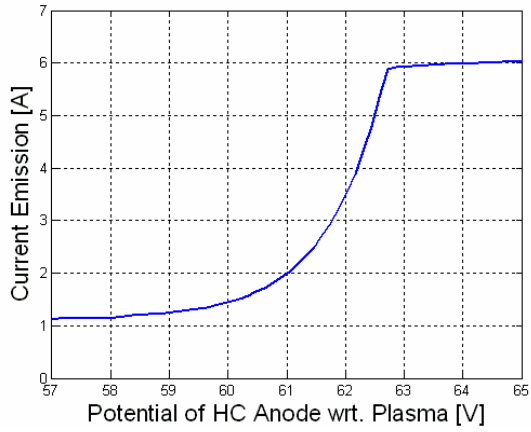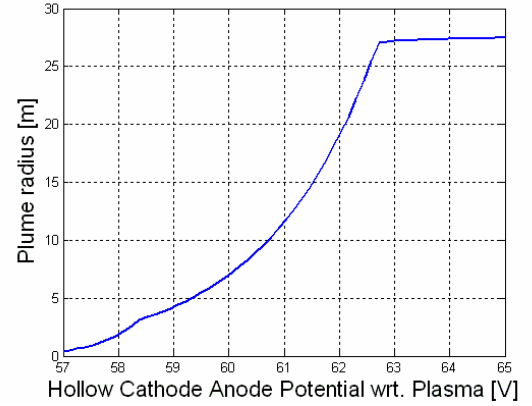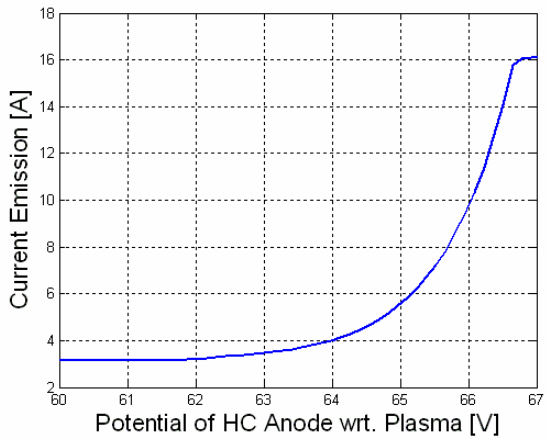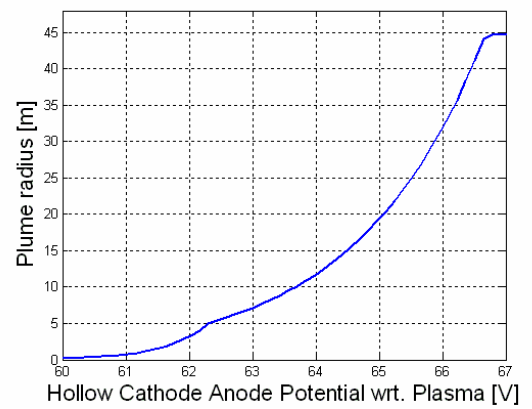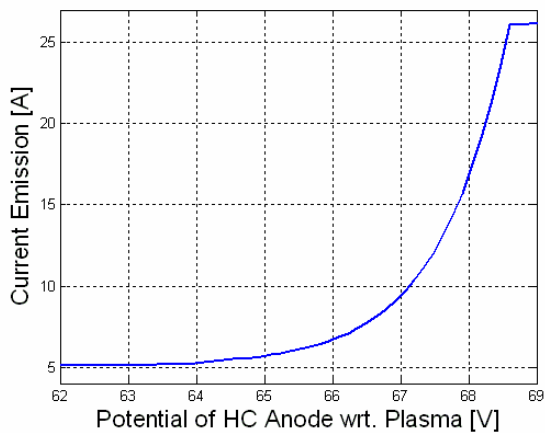
(g)
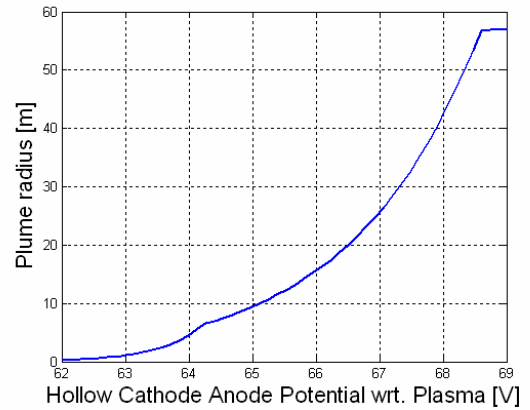
(h)
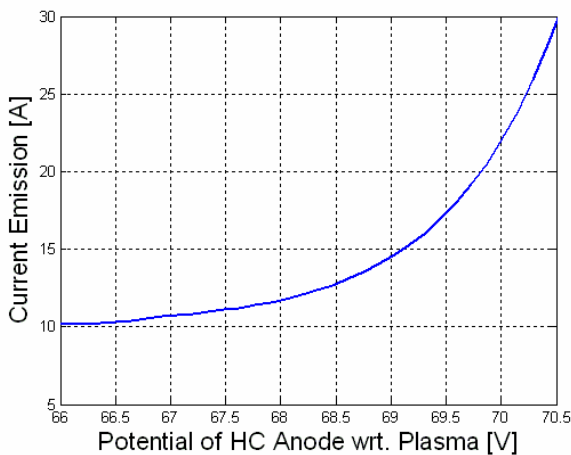
(i)
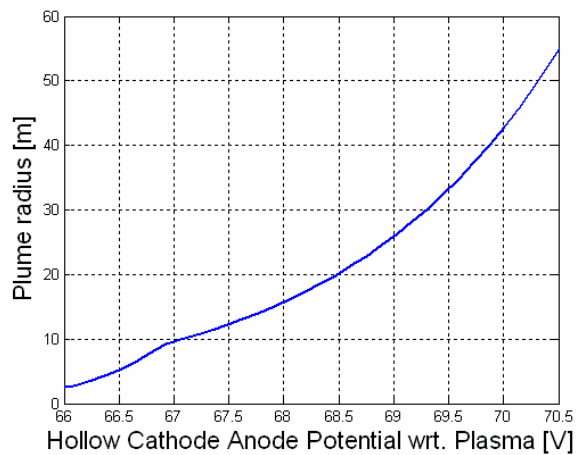
(j)

Figure 6-28: A blow up of the region in the HC plot where the electron current collection jumps as well as the corresponding plume radius. This data is from a HC operating at 2000 km during an average value between solar maximum and solar minimum for an I_o equal to (a,b) 0.13 A, (c,d) 1.13 A, (e,f) 3.13 A, (g,h) 5.13 A, and (i,j) 10.13 A.

It can be seen in Figure 6-28 that the plume radii have a small hump partially up the curve. This is the result of the expanding plume transitioning into the magnetically limited regime. The plume size must follow the restriction where the scattering frequency must remain larger than 0.1 times the plasma cyclotron frequency [112, 161]. This hump exists in the I-V curves, however is difficult to see due to the very slight change. In addition, the plume size predictions very close to zero can not be accurately predicted. The density of the outgoing ion current is several orders of magnitude larger than the ambient plasma. As a result the plume can only grow according to space charge limits. In addition, it has been shown with smaller HCs (around 0.75 A electron collection) that the ion emission density, which is several orders of magnitude larger than the ambient electron density, dissipates within a few cm of the orifice of the HC [116]. A

similar trend is assumed, however it cannot be determned until further experimentation is conducted inder similar conditions.

Using Figure 6-23 through Figure 6-26, the currents collected by the HC anode at 2000 km can be identified. The HC current collection is 2 A, 8 A, 15 A, 20 A, and 24 A at 0.13 A, 1.13 A, 3.13 A, 5.13 A, and 10.13 A ion emission currents, respectively. Using these values and Figure 6-28, the approximate plume radius can be identified for each scenario. For the 0.13 and 1.13 cases, the current collected required a current outside the viewable plot of Figure 6-28b and d. All the values necessary to obtain the plume radius at each HC scenario are detailed in Table 6-19.

2000 km HC ion emission [A]	Collected Current [A]	HC Potential for Collection [V]	Plume Radius [m]
0.13	2	1460	17
1.13	8	505	32.5
3.13	15	66.6	42.4
5.13	20	68.2	47.8
10.13	24	70.2	46.2

Table 6-19: The values used to find the plume radius at 2000 km altitude for various HCs

The plume radius values can be seen in Table 6-19 for the orbit of the MXER at 2000 km.   These values are much larger than any HC electron collection plume characterized through experimentation.   Previously recorded values for HC current collection plumes that have been only tenths of a meter [116]. It has not been tested enough to verify the sizes of plumes that have been predicted by the model used in this simulation, however there is no indication that the values seen in in Table 6-19 are incorrect.   Nonetheless the predicted values should be seen as a maximum value for collection. If a plume were to be as big as the predicted values it is likely that some of the incoming electrons that cross the surface area and impact the neutral ions would not be collected by a HC source such a distance away.

Another approach to this issue would be to use a lighter mass inert gas, such as helium, which is ~33 times less massive than xenon.   There has not been any experimentation to verify electron collection with other gasses, however barring that issue, predictions can still be made. Initial investigations reveal that in order to achieve similar electron collection values ti xenon, helium will require many times the flow rate,

and thus mass. Overall this seems to reduce the total mass required for the helium HC, however lack of experimental testing and physical understanding of this consumable prevents any verification of such a concept.

Further HC current collection work is outside the scope of this thesis. However, for the purposes of this analysis it merely shows that HC emission, even if performing to the magnitude of currents predicted is still not enough to provide a useful solution.

6.4.3   MXER Conclusion

The major assumption for these simulations is that the HC ion current can be simply raised to whatever ion emission value is necessary, provided the mass flow rate allows it. The HC must ionize the incoming neutral xenon gas within the orifice in order to obtain the I_o value. This current is then emitted along with the remaining un-ionized neutral gas. The physics involved in simulating such a process is still under investigation [162-164] It is important to note that the xenon feed gas HC used in the simulations is much greater than most industrial HCs have been tested for. Further simulation and experimentation is required in order to ascertain the feasibility, however.   Overall, it has been shown that below the 2000 km orbit of the MXER system that the bare tether endbody collector at ~12 km of bare tether will be the most efficient anode to the EDT system. It has been predicted that a HC using 10.13 A of ion emission current can produce thrusts 6% greater, however at the cost of an added 2245 kg of consumable mass per year. In addition, the predicted HC method uses unverified current collection values, and should be seen as a maximum value until further testing is accomplished. As a result the bare tether anode seems to be the optimal choice.

The implications of this work demonstrate that a bare tether anode is the optimal choice for the previously designed MXER system. In addition, the optimal amount of bare tether for this mission has been identified. EDT operations will likely be worthwhile in even higher altitude Earth orbits (for the MXER system) as the electron density does not drop off dramatically enough to disprove further investigation.   The work here represents an approximation of the average night and day values for the electron density and electron temperatures at an average solar maximum to solar minimum point.

As a result of the issues described above concerning large plasma plume sizes and lack of experimental data, other ion emission techniques may be worth investigating. Possible future investigations would include helicon antenna sources as they yield 100% ionization rates. Special attention will still need to be taken concerning the plasma acceleration and the space charge limits of this technology.

CHAPTER 7

CONCLUSIONS AND RECOMMENDATIONS FOR FUTURE RESEARCH

7.1   Conclusions for EDT Analysis

7.1.1   Technology and Theory Integration

This thesis has presented electron emitter and collector technology that is presently used, as well as that which is being developed. In addition, the latest theories for passive electron emission and collection have been discussed. Hollow cathodes, field emitter arrays, and thermionic cathodes have been evaluated for their actual and predicted effectiveness as electron emitters in an EDT mission.   The pros and cons of each individual technology are seen in Table 7-1.

Hollow Cathode	Field Emitter Array	Thermionic Cathode
+ Reliable & Proven	- Not Proven Yet	- Reliable and Proven
+ Robust	- Damageability	+ Robust
+ High Current capable	+ Medium Currents (possibly)	- Low Currents
+ Low Power	+ Medium Power	- High Power
- Consumes Fuel (mass)	+ No Consumables	+ No Consumables
	+ Redundancy	- Requires Electron gun

Table 7-1: Electron emitter comparisons.

It is clear that if FEAs prove reliable they will most likely be utilized into most of the future EDT missions. They have been shown to perform nearly identical to that of HCs, in theory. While HCs are still a very efficient and useful technology, the fact that they employ consumables may deter many long term missions from using them.   It has,

however, been demonstrated that presently hollow cathodes are the most useful and diverse technology for the electron emission needs of EDTs. In addition, for systems with larger current requirements (10+ A), HCs may be the only feasible electron emission option for a number of years. HCs have also been demonstrated to function as an effective electron collector in an EDT system.

For electron collection technologies, varying size conductive spheres, no endbodies, and HCs in electron emission mode were compared to one another. The general trend was for larger spheres to allow for greater de-boosting and boosting forces up to a point of diminishing returns. Depending on the size of the collecting sphere, the system design, and the atmospheric conditions, the HC anode could perform as well as relatively large spheres (~4 m radius in the simulations presented). The 'no endmass' anode resulted in the lowest system electrodynamic force. This force, however, was only a few percent less than the 'conductive sphere' anode.

Large spheres (>~5 m radius) may perform the best for systems in higher altitudes with low atmospheric drag or large systems. In addition, HCs and no endmass may be the best option for smaller systems or short term missions. It has been shown that HC technology is especially useful for systems that are smaller, require higher current levels, or are in regions of low electron densities.

7.1.2   Important EDT Variables

The theory presented identified many of the key variables associated with EDTs. For each of these variables, a thorough investigation as to the implications of their manipulations was presented. Particular variables of interest are the electron density, tether resistance, high voltage power supply, and total tether length. These values were discussed for both the boosting and de-boosting cases.

For the de-boosting cases, the general trend revealed that higher electron densities and lower tether resistances produce the greater forces. In addition, as the tether system increased in bare tether length, from 0 to 500 m to 2500 m (of a 5000 m tether), the de-boosting force continued to increase as well. Above ~300 Ω/km tether resistance and

below ~5 x 10^{10} m^{-3} electron density, the amount of bare tether in the system had negligible impact in the performance (for the particular system setup simulated).

For boosting cases, similar trends were seen for the resistance and the electron density. A small deviation from the de-boosting trend existed for tether resistances and electron densities where the optimal thrusting force changed as the bare tether length increased. There was a point where bare tether length resulted in a decline in performance. This factor depended on the atmospheric conditions and the tether system setup. Also, as the HVPS increased, the resulting boosting force increased no matter what the system setup or atmospheric conditions.

Studies were conducted increasing the tether length while maintaining the percentage of bare tether amount (50% bare, in the simulations of this thesis). Identical trends were observed to those of the de-boosting case when the electron density and tether resistance were varied. Larger densities and smaller resistances enhanced the de-boosting force despite the tether length. For the boosting scenarios, similar trends were observed to those of the changing bare tether amounts. There was a point where longer tethers resulted in a decline in performance for any given tether resistance, electron density, or HVPS.

7.1.3 Bare Tether Optimization

One of the major innovations of this thesis work was the ability to identify the optimal amount of bare tether a particular EDT system would require given the mission constraints. The amount of force a system generated was simulated across any variables of a system. Throughout this thesis, bare tether optimization was performed to find the values listed in Table 7-2.

Over an Entire Orbit	For a Particular Instance
Max, Min, and Avg Thrust	Anode Type
Impulse	System Potentials
Power Efficiency	System Voltages
	Tether Geometries

Table 7-2: List of the bare tether optimization conducted in this thesis.

In each of these cases, optimal performance data was obtained for comparison. The Matlab code developed to perform this simulation can be used across any system variable, and is an imperative tool developed for use in any EDT system design.

7.1.4 Tether Geometry Investigation

The experimental work presented in this thesis described and identified the relative efficiencies of various EDT geometries. Solid, slotted, and porous tape geometries in mesosonic flowing plasmas were investigated and shown to exhibit particular electron collection behaviors. A Hall thruster was used to create a high-speed (~8 km/s) flowing unmagnetized plasma in a large 6-m × 9-m vacuum chamber. Solid tape samples with widths spanning from 7.2 to 20.4 Debye lengths and slotted tapes with center-to-center line spacings spanning from 2.1 to 6.0 Debye lengths, from previous experimentation, were compared to holed tapes with hole diameters spanning from 1.4 to 9.4 Debye lengths. Several conclusions can be drawn from the analysis of the results:

1) Beyond a threshold bias close to the beam energy, holed tapes collected more current when oriented transverse (perpendicular) to the flow, just like solid and slotted tapes.

2) Holed tapes were more efficient electron collectors than both solid and slotted tapes in terms of collected electron current per unit area when oriented perpendicular to plasma flow. However, when oriented parallel to plasma flow, slotted tapes were more efficient than holed or solid tapes.

3) When the tapes were oriented parallel to the flow, the electron current collected on holed tapes decreased with increasing hole size until a minimum was attained, beyond which it started increasing again. The opposite effect occurred when the holed probes were oriented transverse to the flow, and a maximum efficiency was observed.

The conclusion was that the holed tethers, which also had a better structural stability, had electron collection capabilities greater than that of slotted tethers of similar mass and porosity as well as solid tethers of similar mass.[59]

7.1.5 Determination of Potential Optimal Tether Designs

Trends have been experimentally shown to exist that identify a tether geometry that would maximize the boosting force to the drag force ratio (F_i / F_d). By identifying the behaviors of porous collecting tether geometries, trends were observed that indicated electron collection current was maximized for a particular hole size. Also, smaller holes resulted in larger overall surface areas over an entire tether revolution. These measurements yielded a maximum value for F_i / F_d. Therefore, the major controlled constraint in a tether system will involve making the tape as thin as possible while maintaining the structural integrity necessary for a given mission. This is because it will minimize the 2-d surface area throughout an entire revolution, thus minimizing drag.

This implies that, once the hole size, tape width, and porosity of the tape is identified, the most efficient F_i / F_d ratio can be calculated for all holed geometries. These geometries have been shown to be more efficient than slotted as well as solid tape geometries. Experimentation will need to be conducted for each porosity and tape width over varying hole sizes in order to determine the maximum current collection.

This technique can be used for any geometry to determine a relative comparison between them, as well as indicate the optimal tether design. Since the least efficient method is a solid tape of similar width, the results are normalized to this geometry and are set to 1.

7.1.6 Efficient EDT System Design Technique

Any particular space mission commonly has a number of requirements for the propulsion system. Once these requirements are identified, a methodology is presented that employs the innovative results of this thesis in order to determine an optimal system.

---

[59] Solid samples are 0% porous.

A strong conceptual understanding of the trades involved in the system design, combined with the bare tether optimization technique, allow for improved EDT system design. This will significantly reduce the cost, mass, and travel times involved over that of previous design methods.

Case studies have been explored which identify what type of system setup will result in maintaining an orbit while minimizing mass, and adhering to other mission objectives. This has been accomplished for the Gamma ray large Area Space Telescope (GLAST) mission and the International Space Station (ISS). Simulations have also been run to explore possibilities of EDT thrusting outside common altitudes, as well as above the ionosphere. This work has been applied toward the Momentum eXchange Electrodynamic Reboost (MXER) system.

Every EDT system has a number of sub-systems that must be considered in order to obtain the optimal design for a particular mission. These include: the electron emission and electron collection devices; the tether material; the geometry; the tether length; the tether inclusion of an HVPS or a load resistor; and the conductive surface areas electrically connected to the tether system. These issues were addressed in this thesis, which yielded more efficient results compared with previous analyses for the GLAST, ISS, and MXER missions.

7.1.7   High Current Hollow Cathode Applications

Particular EDT applications were observed to require high electron emission currents up to 100 A. An investigation was performed to identify the current state-of-the-art theory and experimentation for hollow cathodes capable of such currents. Nearly all the research and development in high current hollow cathodes in the United States have come from three places: NASA - Glenn Space Center (predominantly), Colorado State University (which was contracted by NASA – Glenn), and NASA Jet Propulsion Laboratory (JPL). There are several companies and institutes that currently produce HCs which are capable of emitting 100 A of electron current, such as Busek, HeatWave Labs, the Jet Propulsion Laboratory, and NASA Glenn. The power required to run these HCs

mostly ranges between 1250 W and 2400 W, and they have mass flow rates ranging from 5 to 40 sccm.

There are issues associated with high electron emission current HCs which must be understood. The measurements from an electrostatic energy analyzer suggested that the majority of the ion current at the exit of the anode fall into the analyzer with an energy approximately equal to the discharge voltage (as predicted). The ion distribution, however, was found to be quite broad. There was a high energy tail on the distribution function that tended to grow with increasing discharge current. This tail can be several times the anode to cathode potential difference. This effect greatly increased sputter erosion rates. It was also discovered that the lifetime of the HC could be determined through an understanding of the barium evaporation and barium tungstate formation. A model was derived along with experimentation verification of 40 – 100 A electron emission HCs.

The electron collection mode was also investigated for high current applications. It was found that, to facilitate high electron current collection (100+ A), there needed to be a robust ion production rate on the order of 20 amperes (which exceeds present ion thrusters). In addition, there needed to be a lot of surface area for current collection, which came from the expanding ion plume. As the spacecraft ventured further out of the ionosphere, it would encounter plasma densities many orders of magnitude less than what is needed for ideal collection. As a result, this lack of electron collection through the ignition process would have to be replaced with an increasing amount of active ion emission. Assuming every atom of xenon from the mass flow is singly ionized, the minimum mass flow into the orifice must equal approximately 14 sccm per 1 A of emission current. This implied that a minimum of 1400 sccm of fuel would be required to collect 100 A of electron current. This equaled approximately 137 mg/s of Xe gas. Another option considered was the use of H instead of Xe as the mass flow input. The major difference in using H would be the total mass that would need to be stored on the system. Similar to the calculation earlier, 1400 sccm of H gas would equal just over 1 mg/s! The corrosive and flammable nature of the gas must be considered, however. In addition, the storage of H would require large cryogenic systems.

7.2   Recommendations for Future Work

7.2.1   Future Simulations

One possible future application for the EDT integration work conducted by the Matlab and Excel code would be the implementation into a more sophisticated code, or an all inclusive model. This ideal code would employ the use of orbital mechanics and tether dynamics into the EDT simulation. This would enable complete optimization to occur on a total system model.

In addition to this all inclusive model, other physical effects could be explored. Up until now, the only force assumed to be of significance is the $\overline{F} = I \cdot \int_{0}^{L} d\overline{L} \times \overline{B}$ force. The other Lorenz forces $\overline{F} = q(\overline{E} + \overline{v}_{orb} \times \overline{B})$ can be included into this extensive model to incorporate all aspects into the system. Here, the small atmospheric E-fields would be accounted for as well.

7.2.2   Experimental Recommendations

Further experimentation is needed to quantify more completely the observed effects. Particular future experiments that could be conducted to verify trends observed are:

1)   Larger and smaller width holed tapes at 50% porosity could be tested in both the parallel and perpendicular orientations. This would enable the verification of the maximum and minimum collection efficiency trends that have been observed in the experiment.

2)   The porosity of larger-width holed probes designed could be 50% and 77% in order to mimic the approximate porosity of the slotted samples. Similarly, the smaller-width slotted probes designed could be 50% and 31% porous. This would enable all three width slotted probes to be tested at all three porosities.

3) A holed probe could be made that would have larger diameter holes than this experiment. This would verify the observation made that the larger the holes, provided that the porosity remained the same, the closer they would mimic the slotted results.

4) A plethora of holed tape geometries could be tested for their current collection capabilities. The width, porosity, and hole size could be varied, and current collection tested throughout an entire tape revolution. This, combined with the calculation of the surface area over a rotation, would allow for an elaborate comparison between various tape designs.

Once the optimal tether geometries have been identified, they can have immediate application into the simulation of future missions. Having a known optimal tether geometry for most space system cases would reduce the amount of design required for each mission.

An important theoretical and design question that could possibly be answered is whether slotted or holed tapes have a greater F_i / F_d than an OML wire. Ideally, a tether small enough to be considered in the OML regime would have a maximum collection value. Perhaps the geometry would allow the tape still to collect at OML currents and yet have less drag.

7.2.3   Application into Future Missions and Beyond

There have already been EDT missions proposed to the moon, Mars, and even Jupiter [12, 15, 17, 165-167] The advanced tether analysis and optimizations can now be implemented from the work in this thesis. Updated enhanced results for the missions previously proposed can be obtained.

State-of-the-art electron emitter technologies and electron collection theories have been presented and integrated into this work; however, there are still more possibilities on the horizon. As more innovative devices emerge, the EDT capabilities will continue to advance. Perhaps EDT technology will become more thoroughly established so that many future missions can employ this versatile technology.

APPENDICES

APPENDIX A

CALCULATION FOR TETHER CURRENTS UP TO 100 A

Certain missions, such as the modulated spacecraft with integrated structural electrodynamic propulsion, proposed through NIAC, will need to collect and emit 100^+ amps of current [168]. As a result, an investigation was conducted to assess the current state of the art technology, as well as future possibilities to accomplish this feat. A major issue that must be addressed concerns operation of the modular spacecraft outside the ionosphere. Depending on the altitude, the electron density varies logarithmically from $n_e = 1 \times 10^{10}$ at 2600 km to $n_e = 1 \times 10^8$ at 19000 km [157, 158].[60] As a result, an unconventional approach to current collection and emission must be used.

A.1 Ion Collection – Electron Emission Evaluation

Hollow Cathodes

HCs (Hollow cathodes) are commonly used for electron emission in industry, and they have been verified experimentally and theoretically for various types of use. The major drawback for this device is that it needs to expend consumables in order to accomplish the desired effect. The basic schematic can be seen in Figure 2-21.

Numerous companies have been contacted to determine the current state of the art specifications of working hollow cathodes. Table A-1 describes a comparison of various HCs in the electron emission mode. It can be seen in this table that the power and mass

---

[60] The average density is equal for day and night at solar maximum and minimum at these altitudes

flow rate[61] required to obtain the same amount of emission current can vary greatly. This is due to the fact that geometry and design can play a major role in device efficiency.

Company	Mass Flow Rate [sccm]	Current [A]	Discharge Voltage [V]	Power [W]	Fuel Type
Busek [169]	40	100	25	2500	Xenon
Aerojet [170]	50	60	11	660	Xenon
HeatWave Labs [5]	10	100	100	10000	Xenon
HeatWave Labs	5	100	100	10000	Argon
JPL [171]	9.5	100	27	2700	Xenon
NASA Glenn [172]	20.5	100	12.5	1250	Xenon
JPL [173]	9	100	24	2400	Xenon

Table A-1: Industry Electron Emission HC Values

The mass flow rate is a limiting factor for this technology. Using the NASA Glenn HC, it would take approximately 20.5 sccm of consumables to emit 100 A worth of electrons[62]. Assuming all the input xenon atoms are singly ionized, it would take a minimum of ~2 mg/s worth of consumables to operate. An alternative method to emitting Xe atoms is the emission of hydrogen atoms. The purpose of HCs for this application is to emit current, not mass, so this would produce the equivalent effect as Xe. Using the fact that 1 sccm of H equals 7.4×10^{-4} mg/s it can be determined that only 0.015 mg/s are needed. This would greatly reduce the required mass of payload needed to emit 100 A of electrons. The annual fuel requirement for a Xe HC emitter is ~63 kg of Xe, while the same system only requires 0.478 kg for H. Issues associated with using H as an HC consumable are primarily its corrosive and flammable attributes.

Field Emitter Arrays

Theoretically proposed 10 A FEA's, described in Section 2.4.2 by Jenson [105], would work, however it would require a system of 10 FEA's to emit 100 A. In addition, the devices would need to be kept within 0.4 V of the plasma potential or else the SCL (space charge limits) would greatly limit the amount of emitted current. Assuming they

---

[61] 1 mg/s = 10.23 sccm of Xenon
[62] Assuming a supply of electrons is electrically connected to the HC

do operate, each device would also have to be far enough apart so that the SCL would not have any effect on it. The total power consumption for the system would be ~5860 W for 100 A of emission.   An important factor to remember is that an FEA system that emits 10 A is not going to be developed until many years into the future.

Thermionic Cathodes

This technology has been proven to work in the laboratory as well as in space aboard the TSS-1 mission [100]. A major benefit to this technology is that, unlike the FEA, it requires no consumables. Nothing on the scale of 100 A has ever been tested, however. Current technology, from HeatWave Labs Inc., is a 5.7 A TC setup, and the specifications can be seen in Chapter 2.4.2. This would imply that 18 emitters would be needed, each running at 20 kV, in order to emit the 100 A. Power for the heater of the thermionic emission process must also be supplied, but is a minor power concern.

The results would indicate that the TC system would require a power supply of ~2.1 MW to emit 100 A electrons. In addition, the emitters must all be within 1.25 V of plasma potential or they will be limited by the SCL. The power consumption of this technology would not allow TC's to be a viable solution to the current emission requirements of the modulated spacecraft system.

A.2   Ion Emission – Electron Collection Evaluation

HC's

HCs have theoretically been shown for electron collection and ion emission up to 100 A. Using HCs solely as an ion source is still being investigated as it is a very inefficient process. Hydrogen fuel is being investigated because the mass requirements are significantly less. Approximately 1400 sccm of consumables are required, or about 137 mg/s Xe or 1 mg/s H in order to produce 100 A of current. The description of HC electron collection and ion emission are presented in the Chapter 2.4.3.

Passive Electron Collection

Passive electron current collection is explained in Chapter 2.2. Different techniques are explored using a flat plate and a sphere. Despite there being no consumables required for this method, there are many difficulties to overcome.

A conducting sphere in typical atmospheric conditions of n_e = 1 x 10^{12}, B = 2.5 x 10^{-5} T, T_e = 0.1 eV was analyzed[63]. If a 1 m radius sphere was used, it would have to expend over 4.6 MW of power to collect 100 A, and the drag would be 6.6 mN (or 0.7 mN for a 90% porous sphere). In attempts to require less system power, the size of the sphere was used as the variable. In this case 1 MW of power will still be needed for a 2.29 m radius sphere. This would also have 35 mN of drag associated with it (or 3.5 mN for a 90% porous sphere).

In the case of a flat plate oriented parallel to flow direction there would still be 61.3 MW required for a 5 m^2 plate[64]. In attempts to reduce the power requirements, a 54.5 m^2 plate can be used, which would only require 545 kW of power. There will be 52.5 μN and 573 μN of drag for the small and large square cases, respectively. This assumes an orbital velocity of 7000 m/s and a thickness of 5 mm.

Overall, this method either requires too much power or too much surface area to collect 100 A of electron current. Also, the potential on the passive collectors, with respect to the plasma, can not be actively maintained at a particular potential. The current emission is at the discression of the ambient plasma and the tether system that it is attached to. Unless the dimensions of the conductive collector can be altered, passive collection is not a reliable method for maintained 100 A electron collection or emission current.

Ion Source / Ion Gun

This technology required a technique similar to the TC system. An ion source is required to extract the ions from the neutral gas, and then an ion gun is used for the emission. There are very few reasons to produce ion currents up to 100 A for any application, and as a result most ion emission systems designed in industry are for low

---

[63] Using the TSS-1R corrected Parker Murphy collection theory in section 2.2.1
[64] Using the electron thermal current collection accounting for sheath growth in section 2.2

currents. For example, HeatWave Labs Inc. has an ion emission system that can emit 1.2 mA at the expense of 10 kV. In order to achieve 100 A, 83,334 emitters will be needed as well as a power supply of 1 MW. Due to this fact ion emission physics needs to be investigated further in order to obtain some actual values for emission up to 100 A.

Ion Emission Physics

The ion emission technologies need to produce the ions they are emitting. Knowledge about the physics involved must be obtained in order to predict the powers required to ionize the neutral gas. According to Lieberman & Lichtenberg, the energy loss per electron-ion pair created is summed up in Eq. A-1 [65].

$$K_{iz}E_c = K_{iz}E_{iz} + K_{ex}E_{ex} + K_{el} \cdot \frac{3m_e}{M_i} \cdot T_e$$ **Eq. A-1**

The complete energy needed for each ion-electron pair is calculated by the sum of the energies needed for the ionization, the excitation, and the elastic scattering. 'K', is the rate constant [m^3/s], E is the energy, and ($3m_e/M_i$)T_e is the mean energy lost per electron for polarization scattering. Each of the terms is dependant upon the electron temperature, T_e, and can be calculated using reaction equations, as seen for argon and oxygen in the tables of Lieberman. The complete energy, E_c, for argon has been plotted over varying T_e values. For T_e values over 15 eV, the total E_c value is constant at about 20 V, and for T_e values between 1 and 15 eV, E_c ranges from 18 to 1000 V. (the ionization energy for argon is 15.76 eV). Typical T_e values inside an ion emitter will be over 40 eV, and as a result, the energy loss involved in creating an ion is ~20 eV.

Similarly for xenon, the ionization energy is 12.13 eV. Since it is a noble gas, it is expected to perform comparable to argon. A table with the reactions described will be required for an accurate assessment. The energy loss will be assumed at 16.5 V due to the 3.5 V less ionization energy than argon. As a result, 100 A of current, at 16.5 eV a collision, will result in ~1,650 W of power to maintain the constant ionization of that much current. Similarly, for 20 A of ion current production, 330 W of power will be required

There are other effects that must be considered, however, when ionizing a molecular gas such as Hydrogen. Additional collisional energy losses are present in these gasses, such as excitation of vibrational and rotational energy levels, molecular dissociation, and, for electronegative gases, negative ion formation. As a result, the E_c value can be a factor of 2 to 10 times greater than for a noble gas of the same T_e, when it is below ~20 V. In this case it would not affect the results as the temperatures being dealt with are above that threshold. The ionization energy for hydrogen is 13.9 eV, or about 1.8 eV greater than xenon, which results in a total power of 1830 W for 100 A. Again, the assumption made is for the energy loss to be 18.3 V per collision. A table of H reactions will be required to estimate a more accurate ionization energy.

SUMMARY

Emission	Device	Power	Notes
Electron Emission	TC + Electron Gun	2.1 MW	18 emitters, < 1.25 V for SCL
	FEA	5860 W	10 emitters, < 0.4 V for SCL
	HC	1250 W to 10 kW	Flow Rates & Ion Type 9 sccm to 40 sccm Xe
Electron Collection	Passive Sphere a	4.7 MW	1 m radius, 6.6E-3 N Drag 90% Porous = 6.6E-4 N
	Passive Sphere b	1 MW	2.29 m radius, 3.46E-2 N Drag 90% Porous = 3.46E-3 N
	Passive Plate a	61.3 MW	5 m^2 → 5.26E-5 N Drag
	Passive Plate b	1 MW	54.52 m^2 → 5.73E-4 N Drag
	HC	6150 W + 330 W (20 A ion prod.)	280 sccm fuel 27.35 mg/s Xe$^+$ or 0.21 mg/s H$^+$
Ion Emission	Ion Emission + Ion Gun	1 MW + 1650 W (100 A ion prod.)	83,334 emitters needed 137 mg/s of Xe$^+$ or 1.1 mg/s H$^+$
	HC	1000 W + 1650 W (100 A ion prod.)	1400 sccm fuel 137 mg/s of Xe$^+$ or 1.1 mg/s H$^+$

Table A-2: Comparison of emission and collection at 100 A

All the technologies can be summed up into Table A-2. Overall performance results and recommendations can be determined based on the presented material.

The TC seems to be a little costly for the power requirements and the number of emitters. Perhaps future TCs will be able to emit 100 A in one emitter, however the electron gun power required to overcome the SCL will always be substantial. If FEA technology is

proven past 1 cm^2 experimentally, as it has been theoretically, then this will most likely be the best choice, since it does not require any consumables.

HCs currently appear to be the best choice for all types of collection and emission. Not only has the electron emission mode been experimentally verified, but missions have flown in space that employed the electron collection and emission methods [112]. The major negative attribute is that it requires consumables. This may be avoided somewhat with the use of hydrogen because it is 131 times less massive. However, as mentioned previously, there are other negative factors to be aware of, such as hydrogen's corrosive and explosive nature. When the system is outside of the ionosphere, it appears that an HC in the ion emission mode will be the best possibility. Current investigations are being conducted to solve the issue concerning ion emission into a sparse plasma.

Ion emitters currently require too much power and too many emitters to produce the desired current emission. This technology should be reviewed every few years as it shows potential, however it is too uneconomical as of now.

Passive collection seems to require too much surface area or power for use in this project. In addition, as explained earlier, the emission can not be actively controlled. As a result, since the physics will not change with time, this electron current collection technique should be deemed unfeasible for this application.

A.3 High Current Hollow Cathode Analysis

Hollow Cathodes have the unique capability of emitting electrons, collecting electrons and emitting ions, as previously explained. Companies were contacted to assess the 'state of the art' technology they possessed for high currents, and to gather more information on the topic. In addition, other issues and potential models for HC use were evaluated through published literature.

Nearly all the research and development in high current hollow cathodes in the United States have been from three places: NASA – Glenn (predominantly), Colorado State University (who was contracted by NASA – Glenn), and NASA JPL. Seven companies were contacted that produce hollow cathodes. The information gathered from this search is in Table A-3, and is valid as of February 8, 2006. An important note is that no company develops HC electron collection emitters for commercial use.

Company	Highest e⁻ emission HC product [A]	Notes
Busek [169]	30 & 100	$20k and $30k, 25,000 hr. lifetime, 3.9 mg/s Xe
Aerojet [174]	60	20 – 50 sccm, paper [170]
Semicon Associates [175]	Make Inserts	Worked on TSS and for European Space Agency
Electric Propulsion Laboratory - NASA Glenn [176]	4000 & many 100+	Many published works. Facilities: http://facilities.grc.nasa.gov/epl/epl_caps.html
NASA – JPL [177]	1000 & 100	Focus on modeling (2-D) and experimentation from NEXIS project
HeatWave Labs Inc. [5]	50, scale to 100	Do mechanical/thermal design and fabrication, not application oriented design and testing
Veeco / Ion Tech Inc. (merger) [178]	17	5 A Ion emission also

Table A-3: Description of Industry 'state of the art' technology

High Current HC Electron Emission Issues

Certain phenomenon occurs when large electron currents are emitted from HCs. An issue of particular significance to the lifetime of an HC is the high energy (jet ion) ion emission phenomenon. The measurements from an electrostatic energy analyzer suggest that the majority of the ion current at the exit of the endbody collector falls into the analyzer with an energy approximately equal to the discharge voltage (as predicted). The ion distribution, however, was found to be quite broad. There was a high energy tail on the distribution function that tended to grow with increasing discharge current. This tail can be several times the anode to cathode potential difference. This effect greatly increases sputter erosion rates.

A particular 60 A electron emission erosion study has been conducted, resulting in a proposed structural depletion model [179, 180]. Other similar preliminary experimentation work on ion erosion at 10^+ A electron emission currents was completed and modeled [179-182]. Finally, an elaborate study of high energy ions during a 15 A electron emission HC test was conducted and discussed [183].

It was discovered that the lifetime of the HC could be determined through the understanding of the barium evaporation and barium tungstate formation. A model was derived along with experimentation verification of 40 – 100 A electron emission HCs

258

[184]. Another more chemical intensive derivation was also conducted resulting in a comparative model [185].

There have also been analytical models designed to evaluate the current emission properties of HCs. A 1-D model was developed and verified through experimental results by Katz [111, 186]. In addition, 2-D advanced models with experimental results up to 33.8 A electron emissions have been performed by Mikellides [162]. These tests have been accomplished for the NEXIS (Nuclear Electric Xenon Ion System) 25 kW thruster using software called OrCa2D (2-D Orificed hollow Cathode code) at JPL [163]. A detailed discussion of the theory for OrCa2D and its predecessor, IROrCa2D (2-D Insert Region of an Orificed Cathode code), are also presented [187]. Another study has been performed that produced models relating HC dimensions to output currents for HCs up to 300 A electron emission [188, 189].

High current electron emission hollow cathodes over 100 A have been tested and discussed in various published literature. Work has been done on electron beam emission up to 300 A [190]. Also, lifetime tests have been run at 100 A emissions [171]. Industry standard 28,000 hour lifetime tests have been initially conducted by Sarver-Verhey at 12 A [191, 192]. Overview studies of the technology have been performed by NASA Glenn in tests up to 100 A [172]. Plasma cathode electron gun tests have been shown to up to 200 A [119]. Finally, LaB_6 HCs are described in depth and tested from $10 - 100$ A [193].

Electron Collection / Ion Emission Mode

It was found that to facilitate high electron current collection (100+ A), there needs to be a robust ion production rate on the order of 20 amperes[65]. In addition, there needs to be a lot of surface area for current collection, which comes from the expanding ion plume.

Early work has been conducted to investigate the electron collection capabilities of HCs in the 'ignited' mode [116, 194]. An example of an active model for calculating the hollow cathode electron collection, as well as electron emission, can be found in Section 2.4.3.

---

[65] For atmospheric values of: $n_e = 1 \times 10^{12}$ m^{-3}, $T_e = 0.1$ eV, and $B = 2.5 \times 10^{-5}$ T, shown in Figure A-3

As the spacecraft ventures further out of the ionosphere, it will encounter plasma densities many orders of magnitude less than what is needed for ideal collection. As a result, this lack of electron collection through the ignition process, will have to be replaced with an increasing amount of active ion emission.

The total release of positive charge from the HC is the summation of two separate events. The ion emission from the orifice of the HC combined with the electron collection from the 'ignition' of the electrons, control this positive charge release. The electron collection of the device is greatly dependant on the plasma ambient conditions. Another factor that must be accounted for is the total mass flow for this requirement. In order to produce the electron collection currents indicated by the simulation, there must be enough neutral gas to allow the incoming ambient electrons to ionize them. Therefore, assuming every atom of xenon from the mass flow is singly ionized, the minimum mass flow into the orifice must equal approximately 14 sccm per 1 A of emission current. This implies that a minimum of 1400 sccm of fuel would be required to collect 100 A of negative charge. This equates to approximately 137 mg/s of Xe gas.

Another option considered was the use of H instead of Xe as the mass flow input. The major difference in using H would be the total mass that would need to be stored on the system. Similar to the calculation earlier, 1400 sccm of H gas would equal just over 1 mg/s! The corrosive and flammable nature of the gas must be considered as well.

The space charge limit is not a major problem with HCs as explained in the electron collection section. However, it is still under investigation as to whether this fact is true in sparse plasma. The major disadvantage with this device would be the amount of consumables needed for longer missions.

A.4 Simulations Involving B-Field effects

Simulation Work (*EDT-Survey* code)

Work has been conducted to assemble a HC model that will accurately simulate current collection and emission. The concepts for hollow cathode simulation were discussed in the write-up of the plasma contactor section of a program called Electronic Workbench, developed by SAIC (Science Applications International Corporation) [115].

This has been supplemented by the estimate of electron loss to the keeper structure based on geometric considerations [114].

The algorithm obtained represents a hollow cathode for electron emission and electron collection. Depending on the physical parameters of the device and a bias with respect to the surrounding plasma, a certain amount of electron current will be emitted or collected from it. The variables used are those detailed earlier in Section 2.4.3 for the HC, a density of 5 x 10^{11} m^{-3} and a magnetic field strength of 2.5 x 10^{-5}.

The result of this program is a plot of the total emission current versus the potential of the endbody collector with respect to the ambient plasma. The electron emission, as well as the electron collection currents can be seen in the Figure A-1, Figure A-2, and Figure A-3.

A particular issue that exists is the limiting factor that the ambient conditions can place on the electron emission. There can only be so much electron current collection across a sheath as dictated by the space charge limits and the Child Langmuir laws. In addition, the Earth's magnetic field can limit the current collected by the plasma contactor. Current can be collected if the scattering frequency is greater than the cyclotron frequency. If it isn't, the emitted ions would not form a spherical mass capable of expanding or contracting. Figure A-1 and Figure A-2 show how the limiting cases effect the electron collection.
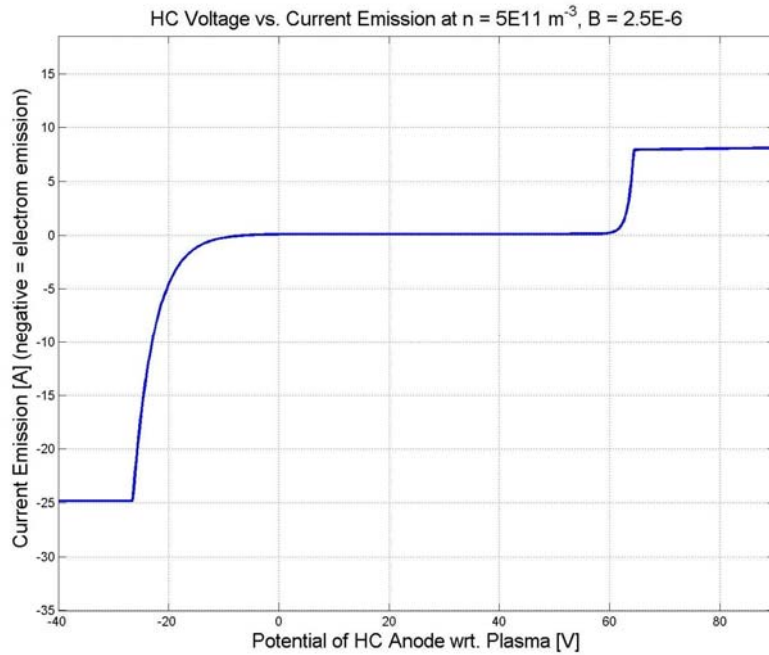
Figure A-1: Current collected from ambient across double layer sheath
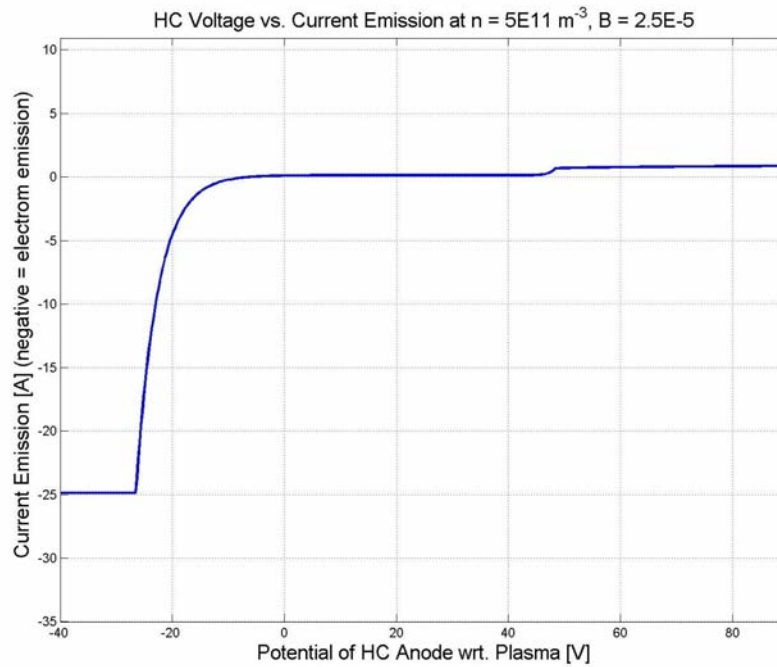
Figure A-2: Magnetic limited current collection

Figure A-1 displays the electron current being ignited by the ambient plasma temperature and density. This case is simulated using a magnetic field ten times less than the actual value for the 300 km altitude. It can be seen that the actual magnetic field around the Earth at that particular altitude produces the results seen in Figure A-2. This

indicates that the magnetic field is a major limiting factor to be considered. To lower the magnetic limiting effect, the HC can move to a higher altitude where there is less of a magnetic field. This idea also reduces the electron density thereby reducing the overall amount of collection and countering the original intent. It is important to be aware of these tradeoffs.
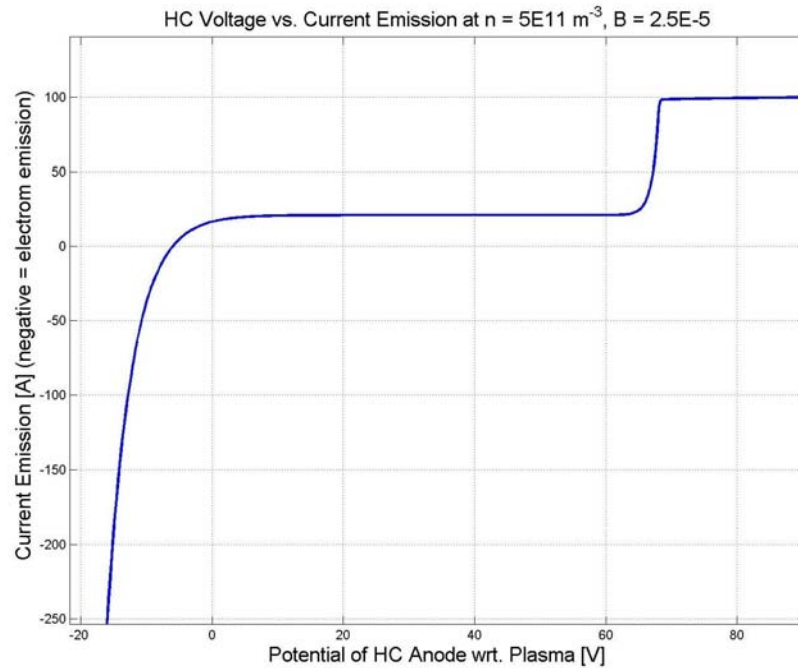
Figure A-3: 100 A HC electron collection condition

Figure A-3 displays the plot of an HC that collects 100 A of electron current. The conditions are the same as in Figure A-2 except 20 A of ion current is emitted from the orifice of the HC instead of the 0.124 A. This is similar to the previous two figures. The Earth's magnetic field is a significant hindrance to electron collection currents. If the B-Field was a factor of 10 or smaller, then the restraint would be from the space charge limit effect. This means that the altitude of the HC operation will play a significant role in its performance.

A.5   Hollow Cathode Diagram

Figure A-4 displays all the values associated with a typical HC. In addition, the potentials with circles around them are just potential differences. They are not physical

connections between the two endpoints. Similarly, the distance measurements are also not physical connections.
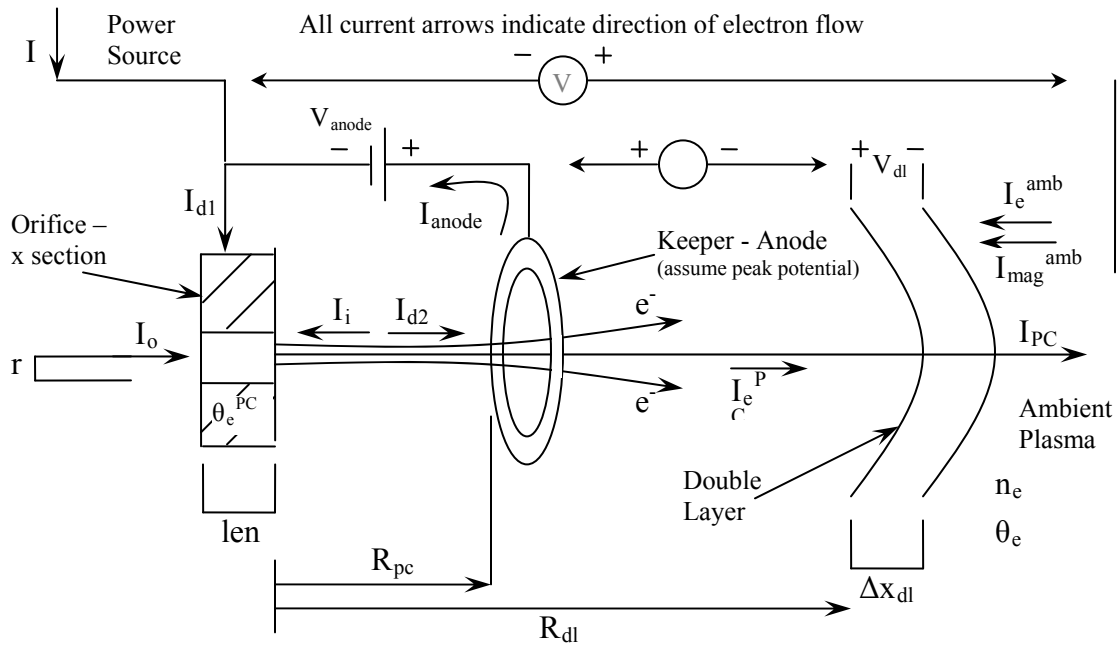
Figure A-4: Setup of an HC system detailing current paths and geometries

Δx_{dl} Child Layer estimate of double layer thickness [m]

$\Delta\varphi$ Potential difference for a double sheath layer with a potential drop equivalent to the source electron temperature. [V] – This is basically the potential difference between the HC keeper and the double layer.

f   Escape fraction of electrons moving beyond the keeper. This is based on the geometry of the keeper.

I   Electron Current [A] – Electron current brought into the system by an outside power source, in this case a tether.

I_{anode} Anode Current [A] – The amount of current that is collected by the keeper / anode and returned into the system. User can control either this variable or the V_{anode} by manipulating the power source.

I_{d1} Electron Entrance Current [A] – Electron current brought into the system by an outside power source and the keeper / anode power supply. ($I_{d1} = I + I_{anode}$)

I_{d2} Electron Discharge Current [A] - After passing through the Hollow Cathode the electron current could be limited by a maximum value, I_e^{max} . ($I_{d2} = I_e^{PC} + I_{anode}$)

$I_e{}^{amb}$ Current (due to the flow of electrons) collected from the Ambient Plasma through a Double Layer [A] This value must be checked to see it is less than $I_{mag}{}^{amb}$ to determine the limiting factor. Whichever is less is the current that is collected from the ambient plasma.

$I_e{}^{max}$ The maximum possible escaping electron current: $= f\sqrt{\dfrac{m_i}{2\pi \cdot m_e}} I_i$

$I_e{}^{PC}$ The current due to electrons flowing outward from the plasma contactor [A] – This value is limited: $\leq I_e{}^{max}$.

I_i Hollow cathode emitted ion current [A] - The neutral atoms are ionized and then emitted through ion thermal collection. This value must be less than I_o.

$I_{mag}{}^{amb}$ Magnetic limited current collected [A] – According to Parker Murphy the maximum impact parameter of charged particles that reach a sphere of a certain radius and potential can be calculated, which therefore shows that the current collected by the plasma contactor is limited by the magnetic field.

I_o Neutral molecular gas flow rate [A] – The amount of gas manually fed into the system converted to units of Amps: = Rate[sccm] * 0.07165.

I_{PC} Total current to (or from) the plasma contactor: $I_e{}^{PC} - I_i - min(I_e{}^{amb}, I_{mag}{}^{amb})$. [A]

len   Hollow cathode orifice length [m]

n_e Ambient plasma density [particles / m^3] : quasineutral

r   Hollow cathode orifice radius [m]

R_{dl} Radius at which the double layer occurs [m]

R_{pc} Radius of plasma contactor gas generation region [m]

θ_e Ambient plasma electron temperature [eV]

$\theta_e{}^{PC}$ Temperature of the electrons (and ions – it is in thermal equilibrium) as is exits the orifice. [eV] (solved for)

V   Potential of the plasma contactor with respect to the plasma (this variable is known from our tether system). [V]

V_{anode} Hollow cathode anode potential [V] - User can control either this variable or the I_{anode} by manipulating the power source.

V_{dl} Double layer potential drop [V]

APPENDIX B

DEVELOPED *MATLAB*^{TM} CODE: *EDT-SURVEY*

Small modifications were made to the EDT-Survey code in order for it to apply toward the variety of simulations that were conducted in this thesis. Variations of EDT-Survey were used for boosting and de-boosting cases all while varying the electron density, HVPS, tether resistance, and bare tether length, both across an orbit and at a static point in time. In addition, each of the GLAST, ISS, and MXER missions of Chapter 6 had their own unique aspect that the code had to be specially developed for. The particular differences between the differing variations of EDT-Survey involve where the repeating loops are located. Depending on the values and ranges of interest there will be several loops imbedded within one another.

Ideally, all of the different techniques applied by EDT-Survey used in this thesis would be included in one self-contained code. In addition, there are plenty of aspects that could be made more user-friendly and descriptive. However, due to the limitations of time and funding, this could not be achieved. Perhaps this could be future work.

Inputs:

       Environmental Conditions

       Physical Setup and Values

       Electron Emitter Values

       Electron Collector Value (if HC is chosen)

Options:

       Electron Emitter Type: HC (ideal or non-ideal), FEA, or TC

Configuration Type - Grounded tip/emitter, grounded gate, and grounded gate isolated tether – see Figure 3-7.

Mode – Electron emitter bias - Floating or User Defined

Electron Collector Type: Bare of HC

Outputs:

Breakdown and Plots of all Currents and Voltages Involved (Typical plots can be seen within this thesis in Chapters 5 and 6.

Breakdown of all Powers Involved

Impulse and Average Boosting Force

Can Obtain Nearly Any Value in the System for Further Analysis

```matlab
%Keith Fuhrhop
%1 - 28 - 05
%Solver

close all;
clear all;
format long g;

points = 21;                        %Number of points that the system plots
Baret = linspace (0,1000,points);       %The constant that is being varied

%These are for the PM module (and some for the tether segment module)
n = 1E12;                   %Density [charged particles/m^3]
rs = 0.5;                   %Radius of the endbody sphere [m]
B = 2E-5;                    %Magnetic Flux Density [T]
alpha = 2.5;                 %Constant used to siulate experimental results
beta = 0.52;                 %Constant used to siulate experimental results
vorb = 7000;                 %orbital velocity [m/s]
M = 16.0;                    %Molecular Weight if Ions
Te = 0.1;                    %Electron temparature [eV]
Ti = 0.1;                    %Ion temparature [eV]
jphoto = 2.4e-5;             %Photoemission current density [A/m^2]
rc = 2;                      %Radius of the cathode [m]
Tlength = 5000;              %Length of tether
dl = Tlength/1000;           %length of each segment
ro = 0.0006;                 %Radius of Tether [m]
Impedance = 0.015;           %Tether resistance [Ohms / m]
Vfloat = -0.000001;          %Floating potential of s/c
Load = 0;                    %Resistive load placed at end of tether [Ohms]

CollectionType = 0;          %The type of electron collection method - 0 = Parker Murphy (TSS-1R
corrected)
                    %and 1 = Hollow Cathodee electron collection
```

```matlab
if CollectionType == 0
    disp('The Type of ELECTRON COLLECTION in this setup is PARKER MURPHY (TSS-1R
corrected)');
elseif CollectionType == 1
    %Variables that are specific to the Non-Ideal Hollow Cathode on the Anode side
    Enumb = 1;                    %Number of HC's on the anode
    Tepcb = 3.889;                %Source Electron Temperature [eV]
    MMb = 131.29;                 %Molecular Weight if Ions (Xenon)
    Vanodeb = 26.5;               %Hollow Cathode Anode Potential {V}
    Iiab = 0.12774;               %Hollow Cathode Orifice Emitted Ion Current [A]
                            %Basically the percentage of the input
                            %neutral xenon is being ionized
    npb = 2E20;                   %Orifice density [particles / m^3] : quasineutral
    rb = 1.375E-3;                %Hollow Cathode Orifice Radius [m]
    defineIb = 1;                 %If user defines Ii then = 1, or if user
                            %defines np and Tepc then defineI = 0
    dkb = 4.675E-3;               %Diameter of keeper [m]
    tkb = 2.4E-4;                 %Thickness of keeper [m]
    lckb = 2.4E-4;                %Distance from orifice exit to beginning of keeper [m]
    definegb = 0;                 %0 if the dimensions, dk, tk, and lck are not defined
                        %(in this case f = 1) 1 if the dimensions dk, tk, and
                        %lck are known. (f is then calculated)
    disp('The Type of ELECTRON COLLECTION in this setup is HOLLOW CATHODE colletion');
else
    disp('The ELECTRON COLLECTION in this setup is not set correctly');
end

Psupply = 1;                  %Power Supply style - 0 = constanr potential, 1 = Constant Power
Vhvps = 2000;                 %High Voltage Power Supply Potential [V]
Phvps = 3000;                 %High Voltage Power Supply Power [W]

if Psupply == 0
    disp(sprintf('The HVPS in this setup is in CONSTANT POTENTIAL mode where V = %g V',Vhvps));
elseif Psupply == 1
    disp(sprintf('The HVPS in this setup is in CONSTANT POWER mode where P = %g W',Phvps));
else
    disp('The HVPS in this setup is not set correctly');
end

%These are for the tether segment module:
Induced_EMF = -vorb*B*dl;        %EMF change per segment [V]
A = 2*pi*ro*dl;                  %Surface Area of tether per segment[m]


%These inputs are for the emitter and load
%If emitter is 3 or 4 then Configuration and Mode do not need to be specified

Emitter = 4;                  %Determines the Electron Emissionn Technique
                        %1 = FEA, 2 = TC, 3 = Ideal HC, 4 = Non-Ideal HC

Configuration = 0;            %If Configuration = 1 then Mode does not need to be specified
                        %Determines if the TC or FEA is setup with a basic grounded
                        %gate (Config B) or a series grounded gate (Config C)
                        %0 = Config B, 1 = Config C

Mode = 0;                     %Determined what system setup is for FEA and TC in configuration B
```

```matlab
                        %0 = Floating, 1 = User determined

if Emitter == 1
    if Configuration == 0
        if Mode == 0
            disp('The ELECTRON EMISSION is currently set to FIELD EMITTER ARRAY emission');
            disp('    in the BASIC GROUNDED GATE configuration in the FLOATING mode.');
        end
        if Mode == 1
            disp('The ELECTRON EMISSION is currently set to FIELD EMITTER ARRAY emission');
            disp('    in the BASIC GROUNDED GATE configuration in the USER DETERMINED mode.');
        end
    end
    if Configuration == 1
            disp('The ELECTRON EMISSION is currently set to FIELD EMITTER ARRAY emission');
            disp('    in the SERIES GROUNDED GATE configuration.');
    end

elseif Emitter == 2
    if Configuration == 0
        if Mode == 0
            disp('The ELECTRON EMISSION is currently set to THERMIONIC CATHODE emission');
            disp('    in the BASIC GROUNDED GATE configuration in the FLOATING mode.');
        end
        if Mode == 1
            disp('The ELECTRON EMISSION is currently set to THERMIONIC CATHODE emission');
            disp('    in the BASIC GROUNDED GATE configuration in the USER DETERMINED mode.');
        end
    end
    if Configuration == 1
        disp('The ELECTRON EMISSION is currently set to THERMIONIC CATHODE emission');
        disp('    in the SERIES GROUNDED GATE configuration.');
    end

elseif Emitter == 3
    disp('The ELECTRON EMISSION is currently set to IDEAL HOLLOW CATHODE emission');

elseif Emitter == 4
    disp('The ELECTRON EMISSION is currently set to NON-IDEAL HOLLOW CATHODE emission');

else
    disp('The ELECTRON EMISSION in this setup is not set correctly');
end

%The solver
%Using a binary search, find the anode voltage that forces system
%electron collection to equal system electron emission.
%Return true if the system could be balanced.

for iii = 1:1:points;            %Start the process...

    number_of_bare_tether_segments = Baret(iii);
    number_of_insulated_tether_segments = (Tlength/dl)-number_of_bare_tether_segments;


    ERROR_TOL = 0.0001;              %How exact we want the answer to be
```

269

```
MIN_STEP_SIZE = 0.00000000000000001;          %Makes sure that it stops if the steps are getting too
small
MAX_ANODE_V = 100000.0;            %Max possible trial anode potential
MIN_ANODE_V = -100000.0;           %Min possible trial anode potential
anode_v_start = MAX_ANODE_V;       %Starting potential
span = MAX_ANODE_V - MIN_ANODE_V;  %How large the span of guessing is
error_v = MAX_ANODE_V;             %An Arbitrary large starting potential
error_i = MAX_ANODE_V;             %An Arbitrary large starting potential
xx = 1;


%-----------------------------------------------------------

%This section is if the emitter is a Field Emitter Array (Emitter = 1):

if Emitter == 1

%Variables that are specific to a particular field emitter array theoretically developed by Kevin Jensen
    Enum = 1;                 %Number of electron emitters in system (spaced adequately ...
                    %apart so SCL does not affect)
    Aemit = 6.5E-2;           %Surface Area of emitter array [m^2]
    BB = 2.8682E-6;           %Fowler - Nordheim Constant [A/V^2/tip]
    C = 962.5;                %Fowler - Nordheim Constant [V]
    tips = 1.3E10;            %Number of tips in the array
    eta = 1;                  %Tip efficiency - what percent of tips actually work
    Vfea = 58;                %Guess potential that is used for the field emitter array [V]
    Vmax = 58.75;             %Maximum value that the FEA can be.  Emitter must be limited to this or it
will break. [V]
    SCL = 1;                  %Set the SCL value to get things going
    first_time_through = 0;   %This is for config B, user define mode, if the program can not find
                    %the solution in the non-SCL mode.  Will now attempt in the SCL mode
    firstSCL = 0;             %Used to find the first time soluion is not SCL'ed
    lastSCLanode = 0;

    while abs(error_i) > ERROR_TOL

anode_start_check(xx) = anode_v_start;          %Check

    %Put the anode_v_start variable into the PM module to get collected current
    if CollectionType == 0
      [Node_Current]=PM_Passive_Collector(n,rs,B,alpha,beta,vorb,M,Te,Ti,jphoto,anode_v_start);
      anode_v_startb = anode_v_start;
    else

[Node_Current]=Hollow_Cathode_module(Tepcb,MMb,Enumb,Vanodeb,Iiab,npb,rb,defineIb,dkb,tkb,lckb
,definegb,anode_v_start,Te,n,B);
        anode_v_startb = anode_v_start - Vanodeb;
    end

Anode_current_check(xx) = Node_Current;         %Check
Potential_check(1) = anode_v_start;             %Check
Endpoint_current_check(1) = Node_Current;       %Check

    bare = 1;                 %Says that the tether is bare (beginning part)
```

```matlab
    %Put the current collected variable (Node_Current) from the PM module and the original
anode_v_start
    %variable into the Tether segment module

[Collected_current,Endpoint_current,Endpoint_voltage]=Tether_Segment(anode_v_startb,Node_Current,In
duced_EMF,Impedance,A,n,Te,Ti,M,bare,dl);
    Node_Current = Endpoint_current;

Current_collected_per_node(1) = 0;                  %Check
Current_collected_per_node(2) = Collected_current;      %Check
Potential_check(2) = Endpoint_voltage;              %Check
Endpoint_current_check(2) = Endpoint_current;         %Check

    %Call the resulting potential after the first element variable, v_anode
    %(so we can use this variable to manipulate while preserving anode_v_start).
    anode_v = Endpoint_voltage;

    for i = 1:(number_of_bare_tether_segments-1)

[Collected_current,Endpoint_current,Endpoint_voltage]=Tether_Segment(anode_v,Node_Current,Induced
_EMF,Impedance,A,n,Te,Ti,M,bare,dl);
        anode_v = Endpoint_voltage;
        Node_Current = Endpoint_current;

Potential_check(i+2) = Endpoint_voltage;            %Check
Endpoint_current_check(i+2) = Endpoint_current;       %Check
Current_collected_per_node(i+2) = Collected_current;   %Check

    end

    bare = 0;               %Says that the tether is insulater (end part)

    for i = 1:(number_of_insulated_tether_segments)

[Collected_current,Endpoint_current,Endpoint_voltage]=Tether_Segment(anode_v,Node_Current,Induced
_EMF,Impedance,A,n,Te,Ti,M,bare,dl);
        anode_v = Endpoint_voltage;
        Node_Current = Endpoint_current;

Potential_check(i+1+number_of_bare_tether_segments) = Endpoint_voltage;          %Check
Endpoint_current_check(i+1+number_of_bare_tether_segments) = Endpoint_current;      %Check
Current_collected_per_node(i+1+number_of_bare_tether_segments) = Collected_current;  %Check

    end

    %Potential loss from the resistor
    Resistive_load_potential = Endpoint_current * Load;

    %Potential (wrt. plasma) right before the emitter
    if Psupply == 0
        Vcathode = Endpoint_voltage - Resistive_load_potential - Vhvps;
    else
        %P = IV, so V = P/I or the power stated earlier / the I at the end of the tether
        Vcathode = Endpoint_voltage - Resistive_load_potential - (Phvps/Endpoint_current);
    end
```

```matlab
Endpoint_voltage_check(xx) = Endpoint_voltage;        %Check
Endpoint_current_check_a(xx) = Endpoint_current;      %Check
Vcathode_check(xx) = Vcathode;                        %Check

    if Configuration == 1     %Config C

first_time_through_check(xx) =  first_time_through;    %Check

        if first_time_through == 0
            if Vcathode - Vfloat > 0        %There are 3 solutions, this also ensures the correct one is
obtained
                Iemit = -9999;
                Vinput = 9999;
            elseif Vcathode + Vfea < -Vfea
                Iemit = 9999;
                Vinput = 0;
            else
                Vinput = Vcathode;

[Iemit,SCL,Imax,Ifea]=Field_Emitter_Array(n,rc,BB,C,tips,eta,M,Te,Ti,jphoto,Vinput,Aemit,Vfea,Vmax,
Enum,B,alpha,beta,vorb);

                if SCL == 1;
                    Iemit = 9999;
                end

                if SCL == 0 & firstSCL == 0        %Records only the first point where it becomes SCL'ed
                    firstSCL = 1;
                    lastSCLspan = 50;              %Broadens the search for the SCL solution (20 is arbitrary:
                                                   %just needs to be large enough so when it starts the search
                                                   %it selects a first point with a solution of the opposite sign)
                    lastSCLanode = anode_v_start;  %Makes sure the reset point is + (between the SCL
and
                                                   %non-SCL solutions) and in the non-SCL regime so it can
                                                   %go backwards to search the SCL regime
                end
            end
        elseif first_time_through == 1        %If the non-SCL case fails, then try the SCL case
            Vinput = Vcathode;

[Iemit,SCL,Imax,Ifea]=Field_Emitter_Array(n,rc,BB,C,tips,eta,M,Te,Ti,jphoto,Vinput,Aemit,Vfea,Vmax,
Enum,B,alpha,beta,vorb);
        end

SCL_check(xx) = SCL;                       %Check
FEA_check(xx) = Vfea;                      %Check
Vinput_check(xx) = Vinput;                  %Check
Iemit_check(xx) = Iemit;                   %Check

    end

    if Configuration == 0     %Config B

first_time_through_check(xx) =  first_time_through;    %Check

        if Mode == 0                        %Floating
```

```matlab
        if first_time_through == 0
          if Vcathode - Vfloat > 0          %There are 3 solutions, this also ensures the correct one is
obtained
             Vinput = 9999;
             Iemit = -9999;
          elseif Vcathode - Vfloat > -Vmax
             Vinput = Vfloat;
             Vfea = -Vcathode + Vfloat;

[Iemit,SCL,Imax,Ifea]=Field_Emitter_Array(n,rc,BB,C,tips,eta,M,Te,Ti,jphoto,Vinput,Aemit,Vfea,Vmax,
Enum,B,alpha,beta,vorb);
          else
             Vinput = -Vcathode + Vfloat;
             Vfea = Vmax;

[Iemit,SCL,Imax,Ifea]=Field_Emitter_Array(n,rc,BB,C,tips,eta,M,Te,Ti,jphoto,Vinput,Aemit,Vfea,Vmax,
Enum,B,alpha,beta,vorb);

             if SCL == 1;
                Iemit = 9999;
             end

             if anode_v_start < 1               %Just to make sure that a realistic solution is chosen
                Iemit = 9999;
             end

             if SCL == 0 & firstSCL == 0         %Records only the first point where it becomes
SCL'ed
                firstSCL = 1;
                lastSCLspan = 50;                %Broadens the search for the SCL solution (20 is
arbitrary
                                                 %- just needs to be large enough so when it starts the search
                                                 %it selects a first point with a solution of the opposite sign)
                lastSCLanode = anode_v_start;    %Makes sure the reset point is + (between the SCL
and
                                                 %non-SCL solutions) and in the non-SCL regime so it can
                                                 %go backwards to search the SCL regime
             end
          end
        elseif first_time_through == 1          %If the non-SCL case fails, then try the SCL case
          Vinput = Vcathode + Vfea;

[Iemit,SCL,Imax,Ifea]=Field_Emitter_Array(n,rc,BB,C,tips,eta,M,Te,Ti,jphoto,Vinput,Aemit,Vfea,Vmax,
Enum,B,alpha,beta,vorb);
        end

SCL_check(xx) = SCL;                      %Check
FEA_check(xx) = Vfea;                     %Check
Vinput_check(xx) = Vinput;                 %Check
Iemit_check(xx) = Iemit;                  %Check

      elseif Mode == 1        %User Defined
        if Vfea > Vmax
           Vfea = Vmax;
           disp('The emitter bias chosen is above the max.');
           disp('The emitter bias has been limited and set to the max value now.')
```

```matlab
            end

first_time_through_check(xx) =  first_time_through;    %Check

        if first_time_through == 0
            if Vcathode + Vfea > 0        %There are 3 solutions, this also ensures the correct one is
obtained
                Vinput = 9999;
                Iemit = -9999;
            elseif Vcathode + Vfea < -Vfea
                Vinput = 0;
                Iemit = 9999;
            else
                Vinput = Vfea + Vcathode;

[Iemit,SCL,Imax,Ifea]=Field_Emitter_Array(n,rc,BB,C,tips,eta,M,Te,Ti,jphoto,Vinput,Aemit,Vfea,Vmax,
Enum,B,alpha,beta,vorb);

            if SCL == 1;
                Iemit = 9999;
            end

            if SCL == 0 & firstSCL == 0            %Records only the first point where it becomes
SCL'ed
                firstSCL = 1;
                lastSCLspan = 50;                %Broadens the search for the SCL solution (20 is
arbitrary:
                                                 %just needs to be large enough so when it starts the search
                                                 %it selects a first point with a solution of the opposite sign)
                lastSCLanode = anode_v_start;           %Makes sure the reset point is + (between the SCL
and
                                                 %non-SCL solutions) and in the non-SCL regime so it can
                                                 %go backwards to search the SCL regime
            end
        end
    elseif first_time_through == 1        %If the non-SCL case fails, then try the SCL case
        Vinput = Vcathode + Vfea;

[Iemit,SCL,Imax,Ifea]=Field_Emitter_Array(n,rc,BB,C,tips,eta,M,Te,Ti,jphoto,Vinput,Aemit,Vfea,Vmax,
Enum,B,alpha,beta,vorb);
        end

SCL_check(xx) = SCL;                        %Check
FEA_check(xx) = Vfea;                       %Check
Vinput_check(xx) = Vinput;                  %Check
Iemit_check(xx) = Iemit;                    %Check

    else
        disp('The Mode was not selected properly')
        return
    end                            %end of mode statement
    end                            %end of configuration statement

    error_i = Endpoint_current - Iemit;

error_i_check(xx) = error_i;                %Check
```

274

```matlab
        span = span / 2.0;

span_check(xx) = span;                          %Check

    if first_time_through == 0
        if (error_i > 0)                        %Acquires the solution for the non-SCL case (negative slope)
            if Endpoint_current < 0
                %2nd constraint added because error_i can be incorrect sign when a number that low is used
                anode_v_start = anode_v_start + span;
            else
                anode_v_start = anode_v_start - span;
            end
        else
            anode_v_start = anode_v_start + span;
        end
    else
        if (error_i < 0)                        %Acquires the solution for the SCL case (positive slope)
            anode_v_start = anode_v_start - span;
        else
            anode_v_start = anode_v_start + span;
        end
    end

    if (span < MIN_STEP_SIZE)
        if first_time_through == 1 | lastSCLanode == 0
            Did_not_work = 1                    %Error, did not converge in the SCL or non-SCL condition
            if Endpoint_current > Imax
                disp(sprintf('The tether is collecting %g A and the FEA selected can only output %g A
max',Endpoint_current,Imax));
            end
            %Make an error message that says if the total current
            %collected by the tether is greater than the total the FEA
            %can output then an error will result - physiclaly explain
            %too!!!
            return;
        end

        if first_time_through == 0              %If the config B, user defined mode can not find a non-SCL
answer,
                                                %now go back to where it just became SCL'ed and try the SCL answer
            first_time_through = 1;
            span = lastSCLspan*2;
            anode_v_start = lastSCLanode;
        end
    end

    xx = xx + 1;
end                                             %End of the while loop

The_vanode_of_this_syetem_converges_to(iii) = anode_start_check(xx-1);    %State the answer
The_vcathode_of_this_syetem_converges_to(iii) = Vinput;

if Configuration == 0 & Mode == 0
    disp(sprintf('The potential of the FEA in this floating mode is %g V',Vfea));
end
```

```matlab
    if SCL == 0
        disp('This solution is NOT space charge limited');
    else
        disp('This solution is SPACE CHARGE LIMITED');
    end

%---------------------------------------------------------
%                  Power Analysis
%---------------------------------------------------------
    Collector_Power = anode_start_check(xx-1) * Anode_current_check(xx-1);
    IR_Loss_Power = sum(Endpoint_current_check(2:(Tlength/dl+1)).^2 * (Impedance*dl));
    Orbit_Power = (vorb*B*dl) * (Tlength/dl) * sum(Endpoint_current_check(2:(Tlength/dl+1))) /
(Tlength/dl);
    Resistor_Power = Endpoint_current_check(Tlength/dl+1)^2 * Load;
    if Psupply == 0
        HVPS_Power = Vhvps * Endpoint_current_check(Tlength/dl+1);
    else
        HVPS_Power = Phvps;
    end
    Element_Power = sum( Current_collected_per_node(2:(number_of_bare_tether_segments+1)) .*
Potential_check(2:(number_of_bare_tether_segments+1)) );
    Emitter_Power = Vfea * Ifea;
    End_Sheath_Power = -(Vinput - Vfloat) * Endpoint_current_check(Tlength/dl+1);
    Heating_Power = 0;

    HVPS_Power = HVPS_Power;
    if Configuration == 0
        Total_Power = Collector_Power + IR_Loss_Power + Orbit_Power + Resistor_Power +
Element_Power + Emitter_Power + End_Sheath_Power + Heating_Power;
    else
        Total_Power = Collector_Power + IR_Loss_Power + Orbit_Power + Resistor_Power +
Element_Power + End_Sheath_Power + Heating_Power;
    end

%-----------------------End of Power Analysis-----------------
    IIaverage(iii) = sum(Endpoint_current_check(2:1000+1)) / 1000;
    IIanode(iii) = Anode_current_check(xx-1);
    VVanode(iii) = anode_start_check(xx-1);
    VVemf(iii) = Induced_EMF * 1000;
    VVtether(iii) = Impedance * Tlength * IIaverage(iii);
    VVload(iii) = Load * Endpoint_current_check(1000+1);
    VVemitter(iii) = Vinput;
    VVcathode(iii) = Vcathode;
    VVhvps(iii) = Phvps/Endpoint_current_check(1000+1);

    Force(iii) = sum(Endpoint_current_check(2:1001)*B*dl);

    if iii>1
        dTdBare(iii)=(Force(iii)-Force(iii-1))/(Baret(iii)-Baret(iii-1));
    end
end

%End of ideal FEA solver

%---------------------------------------------------------
```

```matlab
%This section is if the emitter is a Thermionic Cathode (Emitter = 2):

if Emitter == 2

    Enum = 1;                       %Number of electron emitters in system (spaced adequately ...
                        %apart so SCL does not affect)
    Aemit = 3.33E-4;                %Surface Area of emitter array [m^2]
    %** Not sure of this emitter area... still looking**

    %Variables that are specific to thermionic cathodes
    phi = 4.54;                     %Work function [eV] (of Tungsten)
    pervs = 7.2E-6;                 %Perveance of emitter (depends on geometry) [pervs]
    eta = 0.97;                     %Efficiency of Device
    Veg = 1500;                     %The potential of the electron gun being tried [V]
    Vmax = 2500;                    %Electron Gun Maximum potential [V]
    Iset = 10;                      %Determines the temperature limit set by user [A]

    while abs(error_i) > ERROR_TOL

anode_start_check(xx) = anode_v_start;              %Check

        %Put the anode_v_start variable into the PM module to get collected current
        if CollectionType == 0
            [Node_Current]=PM_Passive_Collector(n,rs,B,alpha,beta,vorb,M,Te,Ti,jphoto,anode_v_start);
            anode_v_startb = anode_v_start;
        else

[Node_Current]=Hollow_Cathode_module(Tepcb,MMb,Enumb,Vanodeb,Iiab,npb,rb,defineIb,dkb,tkb,lckb
,definegb,anode_v_start,Te,n,B);
            anode_v_startb = anode_v_start - Vanodeb;
        end

Anode_current_check(xx) = Node_Current;                 %Check
Potential_check(1) = anode_v_start;                 %Check
Endpoint_current_check(1) = Node_Current;               %Check

        bare = 1;               %Says that the tether is bare (beginning part)

        %Put the current collected variable from the PM module and the original anode_v_start
        %variable into the Tether segment module

[Collected_current,Endpoint_current,Endpoint_voltage]=Tether_Segment(anode_v_startb,Node_Current,In
duced_EMF,Impedance,A,n,Te,Ti,M,bare,dl);
        Node_Current = Endpoint_current;

Current_collected_per_node(1) = 0;                  %Check
Current_collected_per_node(2) = Collected_current;          %Check
Potential_check(2) = Endpoint_voltage;              %Check
Endpoint_current_check(2) = Endpoint_current;           %Check

        %Call the resulting potential after the first element variable, v_anode
        %(so we can use this variable to manipulate while preserving anode_v_start).
        anode_v = Endpoint_voltage;

        for i = 1:(number_of_bare_tether_segments-1)
```

```matlab
[Collected_current,Endpoint_current,Endpoint_voltage]=Tether_Segment(anode_v,Node_Current,Induced
_EMF,Impedance,A,n,Te,Ti,M,bare,dl);
        anode_v = Endpoint_voltage;
        Node_Current = Endpoint_current;
        Potential_check(i+2) = Endpoint_voltage;            %Check
        Endpoint_current_check(i+2) = Endpoint_current;        %Check
        Current_collected_per_node(i+2) = Collected_current;    %Check
    end

    bare = 0;                 %Says that the tether is insulater (end part)

    for i = 1:(number_of_insulated_tether_segments)

[Collected_current,Endpoint_current,Endpoint_voltage]=Tether_Segment(anode_v,Node_Current,Induced
_EMF,Impedance,A,n,Te,Ti,M,bare,dl);
        anode_v = Endpoint_voltage;
        Node_Current = Endpoint_current;
Potential_check(i+1+number_of_bare_tether_segments) = Endpoint_voltage;            %Check
Endpoint_current_check(i+1+number_of_bare_tether_segments) = Endpoint_current;        %Check
Current_collected_per_node(i+1+number_of_bare_tether_segments) = Collected_current;    %Check
    end

    %Potential loss from the resistor
    Resistive_load_potential = Endpoint_current * Load;

    %Potential (wrt. plasma) right before the emitter
    if Psupply == 0
        Vcathode = Endpoint_voltage - Resistive_load_potential - Vhvps;
    else
        %P = IV, so V = P/I or the power stated earlier / the I at the end of the tether
        Vcathode = Endpoint_voltage - Resistive_load_potential - (Phvps/Endpoint_current);
    end
Endpoint_voltage_check(xx) = Endpoint_voltage;                        %Check
Vcathode_check(xx) = Vcathode;                            %Check

    if Configuration == 1     %Config C
        %Call the Thermionic Cathode function

[Iemit,Itc]=Thermionic_Cathode(n,rc,phi,pervs,eta,M,Te,Ti,jphoto,Vcathode,Aemit,Veg,Vmax,Enum,Iset,
B,alpha,beta,vorb);
        Vinput = Vcathode;
    end

    if Configuration == 0     %Config B
        if Mode == 0          %Floating
            if Vcathode > 0
                Iemit = -9999;
            elseif  abs(Vcathode) > Vmax
                Vinput = Vmax + Vcathode;
                Veg = Vmax;

[Iemit,Itc]=Thermionic_Cathode(n,rc,phi,pervs,eta,M,Te,Ti,jphoto,Vinput,Aemit,Veg,Vmax,Enum,Iset,B,a
lpha,beta,vorb);
            else
                Vinput = Vfloat;
```

```matlab
                Veg = Vfloat - Vcathode;

[Iemit,Itc]=Thermionic_Cathode(n,rc,phi,pervs,eta,M,Te,Ti,jphoto,Vinput,Aemit,Veg,Vmax,Enum,Iset,B,a
lpha,beta,vorb);
            end

        elseif Mode == 1        %User Defined
            if Veg > Vmax
                Veg = Vmax;
                disp('The emitter bias chosen is above the max.  The emitter bias has been limited and set to
the max value now.')
            end

            if Vcathode + Veg > 10
                Iemit = -9999;
            else
                Vinput = Veg + Vcathode;

[Iemit,Itc]=Thermionic_Cathode(n,rc,phi,pervs,eta,M,Te,Ti,jphoto,Vinput,Aemit,Veg,Vmax,Enum,Iset,B,a
lpha,beta,vorb);
            end
        else
            disp('The Mode was not selected properly')
            return
        end
    end

E_current_check(xx) = Endpoint_current;                    %Check
Iemit_check(xx) = Iemit;                       %Check

    error_i = Endpoint_current - Iemit;
error_i_check(xx) = error_i;                        %Check

    span = span / 2.0;
    span_check(xx) = span;

    if (error_i > 0)
        if Endpoint_current < 0
            %2nd constraint added because error_i can be incorrect sign when a number that low is used
            anode_v_start = anode_v_start + span;
        else
            anode_v_start = anode_v_start - span;
        end
    else
    anode_v_start = anode_v_start + span;
    end

    if (span < MIN_STEP_SIZE)
        if Mode == 1 & Configuration == 0
            disp(' ')
            disp('The potential chosen for the TC was too large.')
            disp('The tether can not collect enough current for this condition.')
            disp('The physical solution would be whatever current the system can emit that would')
            disp('cause it to result in ~0 potential at the end (after the HVPS)')
            %Should be able to output the approximate current value here as a future step...
        elseif Configuration == 1
```

279

```matlab
            disp(' ')
            disp('The potential chosen for the TC was too large.')
            disp('The tether can not collect enough current for this condition.')
            disp('The physical solution would be whatever current the system can emit that would')
            disp('cause it to result in ~0 potential at the end (after the HVPS)')
        else
            Did_not_work = 2            %Error, did not converge
        end
        return
    end

    xx = xx + 1;
end

if Configuration == 1 & Vcathode > 10
    disp(' ')
    disp(sprintf('The potential on the s/c is %g wrt. the plasma',Vcathode))
    disp('The potential chosen for the TC was too large.')
    disp('The attractive force of the + potential would pull some current back.')
    disp('The physical solution would be whatever current the system can emit that would')
    disp('cause it to result in ~0 potential at the end (after the HVPS)')
    return
end

The_vanode_of_this_syetem_converges_to(iii) = anode_start_check(xx-1);
The_vcathode_of_this_syetem_converges_to(iii) = Vinput;

if Endpoint_voltage > 0 & Configuration == 0
    disp(' ')
    disp(sprintf('The potential on the s/c is %g wrt. the plasma',Endpoint_voltage))
    disp('This means that the true answer is close to this but not exactly.')
    disp('The attractive force of the + potential would pull some current back.')
end

%--------------------------------------------------------
%                   Power Analysis
%--------------------------------------------------------
Collector_Power = anode_start_check(xx-1) * Anode_current_check(xx-1);
IR_Loss_Power = sum(Endpoint_current_check(2:(Tlength/dl+1)).^2 * (Impedance*dl));
Orbit_Power = (vorb*B*dl) * (Tlength/dl) * sum(Endpoint_current_check(2:(Tlength/dl+1))) / (Tlength/dl);
Resistor_Power = Endpoint_current_check(Tlength/dl+1)^2 * Load;
if Psupply == 0
    HVPS_Power = Vhvps * Endpoint_current_check(Tlength/dl+1);
else
    HVPS_Power = Phvps;
end
Element_Power = sum( Current_collected_per_node(2:(number_of_bare_tether_segments+1)) .* Potential_check(2:(number_of_bare_tether_segments+1)) );
Emitter_Power = Veg * Itc;
End_Sheath_Power = -(Vinput - Vfloat) * Endpoint_current_check(Tlength/dl+1);
Heating_Power = 0;

HVPS_Power = HVPS_Power;
if Configuration == 0
```

```matlab
        Total_Power = Collector_Power + IR_Loss_Power + Orbit_Power + Resistor_Power +
Element_Power + Emitter_Power + End_Sheath_Power + Heating_Power;
    else
        Total_Power = Collector_Power + IR_Loss_Power + Orbit_Power + Resistor_Power +
Element_Power + End_Sheath_Power + Heating_Power;
    end
    if Configuration == 0
        disp('Discrepancy in the total power is due primarily to the heating power value.')
    end
%------------------------End of Power Analysis-----------------
    IIaverage(iii) = sum(Endpoint_current_check(2:1000+1)) / 1000;
    IIanode(iii) = Anode_current_check(xx-1);
    VVanode(iii) = anode_start_check(xx-1);
    VVemf(iii) = Induced_EMF * 1000;
    VVtether(iii) = Impedance * Tlength * IIaverage(iii);
    VVload(iii) = Load * Endpoint_current_check(1000+1);
    VVemitter(iii) = Vinput;
    VVcathode(iii) = Vcathode;
    VVhvps(iii) = Phvps/Endpoint_current_check(1000+1);

    Force(iii) = sum(Endpoint_current_check(2:1001)*B*dl);

    if iii>1
        dTdBare(iii)=(Force(iii)-Force(iii-1))/(Baret(iii)-Baret(iii-1));
    end
end

%End of ideal TC emitter solver

%-------------------------------------------------------------

%This section is if the emitter is an ideal Hollow Cathode (Emitter = 3):

if Emitter == 3;

HC = -40;                        %Ideal Hollow Cathode Potential (all current is emitted)

    while abs(error_v) > ERROR_TOL

anode_start_check(xx) = anode_v_start;              %Check

    %Put the anode_v_start variable into the PM module to get collected current
    if CollectionType == 0
        [Node_Current]=PM_Passive_Collector(n,rs,B,alpha,beta,vorb,M,Te,Ti,jphoto,anode_v_start);
        anode_v_startb = anode_v_start;
    else

[Node_Current]=Hollow_Cathode_module(Tepcb,MMb,Enumb,Vanodeb,Iiab,npb,rb,defineIb,dkb,tkb,lckb
,definegb,anode_v_start,Te,n,B);
        anode_v_startb = anode_v_start - Vanodeb;
    end

Potential_check(1) = anode_v_start;                  %Check
Endpoint_current_check(1) = Node_Current;            %Check

    bare = 1;                %Says that the tether is bare (beginning part)
```

```matlab
    %Put the current collected variable from the PM module and the original anode_v_start
    %variable into the Tether segment module

[Collected_current,Endpoint_current,Endpoint_voltage]=Tether_Segment(anode_v_startb,Node_Current,In
duced_EMF,Impedance,A,n,Te,Ti,M,bare,dl);
    Node_Current = Endpoint_current;

Current_collected_per_node(1) = 0;                          %Check
Current_collected_per_node(2) = Collected_current;            %Check
Potential_check(2) = Endpoint_voltage;                    %Check
Endpoint_current_check(2) = Endpoint_current;               %Check

    %Call the resulting potential after the first element variable, v_anode
    %(so we can use this variable to manipulate while preserving anode_v_start).
    anode_v = Endpoint_voltage;

    for i = 1:(number_of_bare_tether_segments-1)

[Collected_current,Endpoint_current,Endpoint_voltage]=Tether_Segment(anode_v,Node_Current,Induced
_EMF,Impedance,A,n,Te,Ti,M,bare,dl);
        anode_v = Endpoint_voltage;
        Node_Current = Endpoint_current;

Potential_check(i+2) = Endpoint_voltage;                    %Check
Endpoint_current_check(i+2) = Endpoint_current;              %Check
Current_collected_per_node(i+2) = Collected_current;          %Check
    end

    bare = 0;                %Says that the tether is insulater (end part)

    for i = 1:(number_of_insulated_tether_segments)

[Collected_current,Endpoint_current,Endpoint_voltage]=Tether_Segment(anode_v,Node_Current,Induced
_EMF,Impedance,A,n,Te,Ti,M,bare,dl);
        anode_v = Endpoint_voltage;
        Node_Current = Endpoint_current;

Potential_check(i+1+number_of_bare_tether_segments) = Endpoint_voltage;              %Check
Endpoint_current_check(i+1+number_of_bare_tether_segments) = Endpoint_current;        %Check
Current_collected_per_node(i+1+number_of_bare_tether_segments) = Collected_current;    %Check

    end

    Resistive_load_potential = Endpoint_current * Load;


        %Potential (wrt. plasma) right before the emitter
    if Psupply == 0
        error_v = Endpoint_voltage - HC - Resistive_load_potential - Vhvps;
    else
        %P = IV, so V = P/I or the power stated earlier / the I at the end of the tether
        error_v = Endpoint_voltage - HC - Resistive_load_potential - (Phvps/Endpoint_current);
    end

    error_v_check(xx) = error_v;
```

```matlab
        span = span / 2.0;
        span_check(xx) = span;

        if (error_v > 0)
            if Endpoint_current < 0
                %2nd constraint added because error_i can be incorrect sign when a number that low is used
                anode_v_start = anode_v_start + span;
            else
                anode_v_start = anode_v_start - span;
            end
        else
            anode_v_start = anode_v_start + span;
        end

        if (span < MIN_STEP_SIZE)
            Did_not_work = 1           %Error, did not converge
            return
        end

        xx = xx + 1;
    end

    The_vanode_of_this_syetem_converges_to(iii) = Potential_check(1);
    The_vcathode_of_this_syetem_converges_to(iii) = HC;

%------------------------------------------------------------
%                   Power Analysis
%------------------------------------------------------------
%   Collector_Power = anode_start_check(xx-1) * Anode_current_check(xx-1);
%   IR_Loss_Power = sum(Endpoint_current_check(2:(Tlength/dl+1)).^2 * (Impedance*dl));
%   Orbit_Power = (vorb*B*dl) * (Tlength/dl) * sum(Endpoint_current_check(2:(Tlength/dl+1))) /
(Tlength/dl);
%   Resistor_Power = Endpoint_current_check(Tlength/dl+1)^2 * Load;
%   if Psupply == 0
%       HVPS_Power = Vhvps * Endpoint_current_check(Tlength/dl+1);
%   else
%       HVPS_Power = Phvps;
%   end
%   Element_Power = sum( Current_collected_per_node(2:(number_of_bare_tether_segments+1)) .*
Potential_check(2:(number_of_bare_tether_segments+1)) );
%   Emitter_Power = Veg * Itc;
%   End_Sheath_Power = (Vinput - Vfloat) * Endpoint_current_check(Tlength/dl+1);
%   Heating_Power = 0;
%
%   HVPS_Power = HVPS_Power
%   Total_Power = Collector_Power + IR_Loss_Power + Orbit_Power + Resistor_Power +
Element_Power + Emitter_Power + End_Sheath_Power + Heating_Power

%------------------------End of Power Analysis------------------
    Force(iii) = sum(Endpoint_current_check(1:(Tlength/dl))*B*dl);

    if iii>1
        dTdR(iii)=(Force(iii)-Force(iii-1))/(Impedancet(iii)-Impedancet(iii-1));
    end
end
```

```
%End of ideal HC emitter solver

%-------------------------------------------------------------

%This section is if the emitter is a Non-Ideal Hollow Cathode (Emitter = 4):

if Emitter == 4

    Enum = 1;                    %Number of electron emitters in system (spaced adequately ...
                            %apart so SCL does not affect)

    %Variables that are specific to the Non-Ideal Hollow Cathode
    Tepc = 3.889;                %Source Electron Temperature [eV]
    MM = 131.29;                  %Molecular Weight if Ions (Xenon)
    Vanode = 26.5;                %Hollow Cathode Anode Potential {V]
    Iia = 0.12774;                %Hollow Cathode Orifice Emitted Ion Current [A]
                            %Basically the percentage of the input
                            %neutral xenon is being ionized
    np = 2E20;                    %Orifice density [particles / m^3] : quasineutral
    r = 1.375E-3;                 %Hollow Cathode Orifice Radius [m]
    defineI = 1;                  %If user defines Ii then = 1, or if user
                            %defines np and Tepc then defineI = 0
    dk = 4.675E-3;                %Diameter of keeper [m]
    tk = 2.4E-4;                  %Thickness of keeper [m]
    lck = 2.4E-4;                 %Distance from orifice exit to beginning of keeper [m]
    defineg = 0;                  %0 if the dimensions, dk, tk, and lck are not defined
                            %(in this case f = 1) 1 if the dimensions dk, tk, and
                            %lck are known. (f is then calculated)

    while abs(error_i) > ERROR_TOL

anode_start_check(xx) = anode_v_start;                %Check

        %Put the anode_v_start variable into the PM module to get collected current
        if CollectionType == 0
            [Node_Current]=PM_Passive_Collector(n,rs,B,alpha,beta,vorb,M,Te,Ti,jphoto,anode_v_start);
            anode_v_startb = anode_v_start;
        else

[Node_Current]=Hollow_Cathode_module(Tepcb,MMb,Enumb,Vanodeb,Iiab,npb,rb,defineIb,dkb,tkb,lckb
,definegb,anode_v_start,Te,n,B);
        anode_v_startb = anode_v_start - Vanodeb;
        end

Anode_current_check(xx) = Node_Current;                %Check
Potential_check(1) = anode_v_start;                %Check
Endpoint_current_check(1) = Node_Current;                %Check

        bare = 1;            %Says that the tether is bare (beginning part)

        %Put the current collected variable from the PM module and the original anode_v_start
        %variable into the Tether segment module

[Collected_current,Endpoint_current,Endpoint_voltage]=Tether_Segment(anode_v_startb,Node_Current,In
duced_EMF,Impedance,A,n,Te,Ti,M,bare,dl);
```

```matlab
        Node_Current = Endpoint_current;
Current_collected_per_node(1) = 0;                  %Check
Current_collected_per_node(2) = Collected_current;          %Check
Potential_check(2) = Endpoint_voltage;              %Check
Endpoint_current_check(2) = Endpoint_current;           %Check

    %Call the resulting potential after the first element variable, v_anode
    %(so we can use this variable to manipulate while preserving anode_v_start).
    anode_v = Endpoint_voltage;

    for i = 1:(number_of_bare_tether_segments-1)

[Collected_current,Endpoint_current,Endpoint_voltage]=Tether_Segment(anode_v,Node_Current,Induced
_EMF,Impedance,A,n,Te,Ti,M,bare,dl);
        anode_v = Endpoint_voltage;
        Node_Current = Endpoint_current;
Potential_check(i+2) = Endpoint_voltage;            %Check
Endpoint_current_check(i+2) = Endpoint_current;         %Check
Current_collected_per_node(i+2) = Collected_current;    %Check
    end

    bare = 0;               %Says that the tether is insulated (end part)

    for i = 1:(number_of_insulated_tether_segments)

[Collected_current,Endpoint_current,Endpoint_voltage]=Tether_Segment(anode_v,Node_Current,Induced
_EMF,Impedance,A,n,Te,Ti,M,bare,dl);
        anode_v = Endpoint_voltage;
        Node_Current = Endpoint_current;
Potential_check(i+1+number_of_bare_tether_segments) = Endpoint_voltage;         %Check
Endpoint_current_check(i+1+number_of_bare_tether_segments) = Endpoint_current;      %Check
Current_collected_per_node(i+1+number_of_bare_tether_segments) = Collected_current;   %Check
    end

    %Potential loss from the resistor
    Resistive_load_potential = Endpoint_current * Load;

    %Potential (wrt. plasma) right before the emitter

    if Psupply == 0
        Vcathode = Endpoint_voltage - Resistive_load_potential - Vhvps;
    else
        Vcathode = Endpoint_voltage - Resistive_load_potential - (Phvps/Endpoint_current);
    end


E_current_check(xx) = Endpoint_current;                 %Check
Endpoint_voltage_check(xx) = Endpoint_voltage;              %Check
Vcathode_check(xx) = Vcathode;              %Check

    %Call the Ideal Hollow Cathode function

[Iemit]=Hollow_Cathode_module(Tepc,MM,Enum,Vanode,Iia,np,r,defineI,dk,tk,lck,defineg,Vcathode,Te,
n,B);

Iemit_check(xx) = Iemit;                %Check
```

```matlab
Current_emitted_by_HC(iii) = Iemit;                    %Check

    %This runs the PM module to find the passive current collection on the cathode
    [Icollect]=PM_Passive_Collector(n,rc,B,alpha,beta,vorb,M,Te,Ti,jphoto,Vcathode);

Current_emitted_by_Passive(iii) = Icollect;            %Check

    %Icollect is - for electron emission, and + for electron collection
    %Iemit is - for electron emission and + for electron collection
    %Current at bottom of tether will be + (because a lot of electrons
    %will need to be emitted)
    Iemit = -(Icollect + Iemit);
    error_i = Endpoint_current - Iemit;

Total_current_emitted_at_end(iii) = Iemit;                 %Check
Icollect_check(xx) = Icollect;                         %Check
Iemitwions_check(xx) = Iemit;                           %Check
error_i_check(xx) = error_i;                        %Check

    span = span / 2.0;
    span_check(xx) = span;

    if (error_i > 0)
      if Endpoint_current < 0 | (Vcathode + 2*Vanode) < 0
        %2nd constraint added because error_i can be incorrect sign when a number that low is used
        anode_v_start = anode_v_start + span;
      else
        anode_v_start = anode_v_start - span;
      end
    else
      anode_v_start = anode_v_start + span;
    end

    if (span < MIN_STEP_SIZE)
      Did_not_work = 1              %Error, did not converge
      return
    end

    xx = xx + 1;
  end
  The_vanode_of_this_syetem_converges_to(iii) = anode_start_check(xx-1);
  The_vcathode_of_this_syetem_converges_to(iii) = Vcathode;

%-----------------------------------------------------------
%              Power Analysis
%-----------------------------------------------------------
%   Collector_Power = anode_start_check(xx-1) * Anode_current_check(xx-1);
%   IR_Loss_Power = sum(Endpoint_current_check(2:(Tlength/dl+1)).^2 * (Impedance*dl));
%   Orbit_Power = (vorb*B*dl) * (Tlength/dl) * sum(Endpoint_current_check(2:(Tlength/dl+1))) /
(Tlength/dl);
%   Resistor_Power = Endpoint_current_check(Tlength/dl+1)^2 * Load;
%   if Psupply == 0
%      HVPS_Power = Vhvps * Endpoint_current_check(Tlength/dl+1);
%   else
%      HVPS_Power = Phvps;
%   end
```

286

```matlab
%   Element_Power = sum( Current_collected_per_node(2:(number_of_bare_tether_segments+1)) .*
Potential_check(2:(number_of_bare_tether_segments+1)) );
%   Emitter_Power = -Vanode * Iemit_check(xx-1);
%   End_Sheath_Power = -(Vcathode + Vanode - Vfloat) * Endpoint_current_check(Tlength/dl+1);
%   Heating_Power = 0;
%
%   HVPS_Power = HVPS_Power;
%   Total_Power = Collector_Power + IR_Loss_Power + Orbit_Power + Resistor_Power +
Element_Power + Emitter_Power + End_Sheath_Power + Heating_Power;
%%------------------------End of Power Analysis-----------------

    IIaverage(iii) = sum(Endpoint_current_check(2:1000+1)) / 1000;
    IIanode(iii) = Anode_current_check(xx-1);
    VVanode(iii) = anode_start_check(xx-1);
    VVemf(iii) = Induced_EMF * 1000;
    VVtether(iii) = Impedance * Tlength * IIaverage(iii);
    VVload(iii) = Load * Endpoint_current_check(1000+1);
    VVemitter(iii) = Vanode;
    VVcathode(iii) = Vcathode;
    VVhvps(iii) = Phvps/Endpoint_current_check(1000+1);

    Force(iii) = sum(Endpoint_current_check(2:1001)*B*dl);

    if iii>1
        dTdBare(iii)=(Force(iii)-Force(iii-1))/(Baret(iii)-Baret(iii-1));
    end
end

%End of Non-Ideal Hollow Cathode solver

 %----------------------------------------------------------------------
end

%barelength = number_of_bare_tether_segments*dl;

%subplot(2,1,1);
%[AX,H1,H2] = plotyy(Baret*5,Force,Baret*5,Efficiency,'plot');
%xlabel('Bare Tether Length [m]');
%set(get(AX(1),'Ylabel'),'String','Boosting Force [N]');
%set(get(AX(2),'Ylabel'),'String','Power Efficiency: (V_e_m_f*I_a_v_g) / P_h_v_p_s');
%%ylabel('Boosting Force [N]');
%title(sprintf('Bare Tether Length vs. Boosting Force for n = %g m^-^3 and P_h_v_p_s = %g
W',n,Phvps));
%orient landscape;
%grid on;
%
%subplot(2,1,2);
%plot(Baret(2:points)*5,dTdBare(2:points)*1000);
%xlabel('Bare Tether Length [m]');
%ylabel('dTdBare [mN/m]');
%title('Bare Tether Length vs. dTdBare');
%orient landscape;
%grid on;

subplot(2,1,1);
plot(Baret*dl,Force);
```

```matlab
xlabel('Bare Tether Length [m]');
ylabel('Boosting Force [N]');
title(sprintf('Tether Length vs. Boosting Force for a n = %g m^-^3, R_t = %g ohm/m, P_h_v_p_s = %gW
Bare Tether Boosting System',n,Impedance,Phvps));
orient landscape;
grid on;
%axis([1000 100000 -0.8 0.6]);

subplot(2,1,2);
plot (Baret(2:points)*dl,dTdBare(2:points)*1000);
xlabel('Tether Length [m]');
ylabel('dT/db [mN/m]');
title(sprintf('Tether Length vs. dT/dl for a n = %g m^-^3, R_t = %g ohm/m, P_h_v_p_s = %gW Bare
Tether Boosting System',n,Impedance,Phvps));
orient landscape;
grid on;
%axis([1000 100000 -0.03 0.07]);

figure(2);
plot(Baret*dl,VVanode,'b-s');
hold on;
plot(Baret*dl,VVemf,'c-o');
hold on;
plot(Baret*dl,VVtether,'k-.');
hold on;
%plot(Baret*dl,VVload,'r*');
%hold on;
plot(Baret*dl,VVemitter,'g--');
hold on;
plot(Baret*dl,VVcathode,'m-');
hold on;
plot(Baret*dl,VVhvps,'k-x');
hold on;

xlabel('Tether Length [m]');
ylabel('System Potentials [V]');
title(sprintf('Tether Length vs. System Potentials for a n = %g m^-^3, R_t = %g ohm/m, P_h_v_p_s =
%gW Bare Tether Boosting System',n,Impedance,Phvps));
%title('Electron Density vs. System Potentials for a 5000m, R_t = 1\omega/m, P_h_v_p_s = 3000W  Bare
Tether System');
legend('Anode','EMF','Tether','Emitter','Cathode','HVPS');
%legend('Anode','EMF','Tether','Load','Emitter','Cathode','HVPS',2);
orient landscape;
grid on;
%axis([1000 100000 -5000 3000]);

figure(3);
plot(Baret*dl,Current_emitted_by_Passive);
hold on;
plot(Baret*dl,Current_emitted_by_HC,'r--');
hold on;
plot(Baret*dl,Total_current_emitted_at_end,'g-.');
hold on;
plot(Baret*dl,IIaverage,'k-x');
hold on;
plot(Baret*dl,IIanode,'m-s');
```

```matlab
hold on;
xlabel('Tether Length [m]');
ylabel('System Currents [A]');
title(sprintf('Tether Length vs. System Currents for a n = %g m^-^3, R_t = %g ohm/m, P_h_v_p_s = %gW
Bare Tether Boosting System',n,Impedance,Phvps));
legend('Passive Current','Hollow Cathode','Tether End','Tether Average','Anode',2);
%legend('Anode','EMF','Tether','Load','Emitter','Cathode','HVPS',2);
orient landscape;
grid on;
%axis([1000 100000 -5 4]);

dTdBare_export = dTdBare(2:points);


save('Current_emitted_by_Passive_boost.mat', 'Current_emitted_by_Passive');
save('Current_emitted_by_HC_boost.mat', 'Current_emitted_by_HC');
save('Total_current_emitted_at_end_boost.mat', 'Total_current_emitted_at_end');
save('IIaverage_boost.mat', 'IIaverage');
save('IIanode_boost.mat', 'IIanode');

save('VVanode_boost.mat', 'VVanode');
save('VVemf_boost.mat', 'VVemf');
save('VVtether_boost.mat', 'VVtether');
save('VVemitter_boost.mat', 'VVemitter');
save('VVcathode_boost.mat', 'VVcathode');
save('VVhvps_boost.mat', 'VVhvps');
%
%save('Force_per_Bare_boost.mat', 'Force');
%save('dTdR_Force_per_Bare_boost.mat', 'dTdBare_export');
%save('dTdP_Force_per_Bare_xaxis.mat', 'Baret');

%subplot(4,1,3);
%plot (Impedancet*1000,The_vanode_of_this_syetem_converges_to);
%xlabel('Resistance [Ohms / km]');
%ylabel('V_a_n_o_d_e [V]');
%title(sprintf('Resistance vs. Anode Potential for a %gm Bare Tether System',barelength));
%orient landscape;
%grid on;

%subplot(4,1,4);
%plot (Impedancet*1000,The_vcathode_of_this_syetem_converges_to);
%xlabel('Resistance [Ohms / km]');
%ylabel('V_a_n_o_d_e [V]');
%title(sprintf('Resistance vs. Anode Potential for a %gm Bare Tether System',barelength));
%orient landscape;
%grid on;

 %
% Values that can be used for different altitudes...

% Numbers for Excel Tether Simulation for January 1, 2006 1AM (Solar Min, night time)

%Altitude [km]  Bmag [nT]   EMF [V] vorb [m/s]  Ion Temp. [eV]  Ele. Temp. [eV] Ne [#/m^3]  Avg Mol
Wt [amu]    Atm. Drag [N]
%199      25522.052  930.188    7282.006    0.05575    0.05668    4.19984E+09    24.96179    2.2816E-
01
```

```
%250       28066.994  1021.97   7275.087   0.05638   0.06792   4.27873E+10   20.4004     3.5172E-02
%300       27160.060  984.532   7242.609   0.05937   0.05939   4.60609E+10   16.57921    6.8496E-03
%400       26300.075  944.566   7175.815   0.06580   0.07700   3.55067E+10   15.699178   4.0537E-04
%500       25064.326  892.168   7111.914   0.07153   0.08490   2.56643E+10   14.91981    3.5698E-05
%750       22131.004  770.757   6958.446   0.08319   0.08747   1.76355E+10   8.483674    2.0668E-06
%1000  19915.024  678.777   6809.923   0.08608   0.08612   1.64358E+10   2.526702   6.3143E-07
%1500  16080.332  525.831   6533.518   0.08403   0.08406   1.63003E+10   1.187582   1.5421E-07
%2000  13169.591  413.852   6278.685   0.11113   0.11119   1.63649E+10   1.187582   7.0859E-08
```

%Numbers for Excel Tether Simulation for July 15, 2001 12:11:00 AM (Solar Max, day time)
%
%Altitude [km] Bmag [nT]   EMF [V] vorb [m/s] Ion Temp. [eV] Ele. Temp. [eV] Ne [#/m^3] Avg Mol Wt [amu]   Atm. Drag [N]

```
%200       36191.747  1323.950   7309.000   0.07593   0.11790   2.22783E+11   18.96   3.9323E-01
%250       34919.517  1271.500   7275.185   0.08296   0.17493   7.50991E+11   16.70   9.8153E-02
%300       32770.421  1186.360   7233.199   0.09066   0.19611   1.18158E+12   16.30   3.2725E-02
%400       29490.437  1049.250   7108.757   0.09934   0.10047   1.21393E+12   13.87   5.9515E-03
%500       26931.934  944.580   7007.565   0.10500   0.11478   9.12086E+11   11.53   1.5703E-03
%750       23776.199  816.101   6857.999   0.14717   0.14723   1.75802E+11   4.11   6.9105E-05
%1000  21383.602  718.337   6711.866   0.18160   0.18168   1.14127E+11   2.17   5.9598E-06
%1500  17499.965  564.032   6439.653   0.24450   0.24461   1.07352E+11   1.31   7.0763E-07
%2000  14456.003  447.783   6188.926   0.27988   0.28000   1.07158E+11   1.31   2.1545E-07
```

BIBLIOGRAPHY

BIBLIOGRAPHY

[1] Sanmartin, J.R., Martinez-Sanchez, M., and Ahedo, E., "Bare Wire Anodes for Electrodynamic Tethers," *Journal of Propulsion and Power,* Vol. 9, No. 3, 1993, pp. 353-360.

[2] Sanmartin, J.R., and Estes, R.D., "The orbital-motion-limited regime of cylindrical Langmuir probes," *Physics of Plasmas,* Vol. 6, No. 1, 1999, pp. 395-405.

[3] Stone, N.H., and Bonifazi, C., "The TSS-1R mission: Overview and Scientific Context," *Geophysical Research Letters,* Vol. 25, No. 4, 1998, pp. 409-412.

[4] Gilchrist, B.E., Johnson, L., and Bilen, S.G., "Space Electrodynamic Tether Propulsion Technology: System Considerations and Future Plans," *AIAA/ASME/SAE/ASEE Joint Propulsion Conference and Exibit,* 1999, pp. 1-8.

[5] Gunther, K., "Hollow Cathode / Ion Source Quotation," HeatWave Labs, Inc., 3968, Watsonville, CA, 2006.

[6] Vas, I.E., Kelly, T.J., and Scarl, E.A., "Space Station Reboost with Electrodynamic Tethers," *Journal of Spacecraft and Rockets,* Vol. 37, No. 2, 2000, pp. 154-164.

[7] Hoyt, R.P., Slostad, J.T., and Frank, S.S., "A Modular Momentum Exchange Electrodynamic Reboost Tether System Architecture," *39th AIAA/ASME/SAE/ASEE Joint Propulsion Conference and Exhibit,* AIAA, 2003, pp. 1-12.

[8] Whipple, E.C., "Potentials of Surfaces in Space," *Report of Progress in Physics,* Vol. 44, 1981, pp. 1197-1250.

[9] Chung, P.M., Talbot, L., and Touryan, K., "Electric probes in stationary and flowing plasmas: theory and application," Springer-Verlag New York Inc., New York, 1975, pp. 111.

[10] Johnson, L., Carroll, J., Estes, R.D., "Electrodynamic tethers for reboost of the International Space Station and spacecraft propulsion," *AIAA, Space Programs and Technologies Conference,* AIAA, Huntsville, AL, 1996, pp. 1-8.

[11] Forward, R.L., Hoyt, R.P., and Uphoff, C.W., "Terminator Tether: A Spacecraft Deorbit Device," *Journal of Spacecraft and Rockets,* Vol. 37, No. 2, 2000, pp. 187-196.

[12] Hoyt, R.P., "Design and Simulation of a Tether Boost Facility for LEO to GTO Transport," *36th AIAA/ASME/SAE/ASEE Joint Propulsion Conference & Exhibit,* AIAA, 2000, pp. 1-10.

[13] Levin, E.M., "MXER Simulation Study," NASA MSFC, STAR, Inc. report to NASA/MSFC, Marshall Space Flight Center, AL, 2005.

[14] Wilson, J., "The Vision For Exploration," Vol. 2007, No. 5/23, 2007, pp. 1.

[15] Hoyt, R.P., and Uphoff, C., "Cislunar Tether Transport System," *35th AIAA/ASME/SAE/ASEE Joint Propulsion Conference & Exhibit,* AIAA, 1999, pp. 1-16.

[16] Forward, R.L., and Nordley, G.D., "Mars-Earth Rapid Interplanetary Tether Transport MERITT System," *35th AIAA/ASME/SAE/ASEE Joint Propulsion Conference & Exhibit,* AIAA, 1999, pp. 1-18.

[17] Forward, R.L., "Tether Transport from LEO to the Lunar Surface," *AIAA/ASEE/SAE/ASEE 27th Joint Propulsion Conference,* AIAA, 1991, pp. 1-6.

[18] Cosmo, M.L., and Lorenzini, E.C., "Tethers in Space Handbook," NASA Marchall Space Flight Center, 1997, pp. 274-1-274.

[19] Fuhrhop, K.R., Gilchrist, B.E., Bilen, S.G., "System Analysis of the Expected Electrodynamic Tether Performance for the ProSEDS Mission," *39th AIAA/ASME/SAE/ASEE Joint Propulsion Conference,* AIAA, 2003, pp. 1-10.

[20] Johnson, L., Estes, R.D., Lorenzini, E.C., "Propulsive Small Expendable Deployer System Experiment," *Journal of Spacecraft and Rockets,* Vol. 37, No. 2, 2000, pp. 173-176.

[21] Lorenzini, E.C., Welzyn, K., and Cosmo, M.L., "Expected Deployment Dynamics of ProSEDS," *39th AIAA/ASME/SAE/ASEE Joint Propulsion Conference and Exhibit,* AIAA, 2003, pp. 1-9.

[22] Sanmartin, J.R., Charro, M., Lorenzini, E.C., "Analysis of ProSEDS Test of Bare-tether Collection," *39th AIAA/ASME/SAE/ASEE Joint Propulsion Conference and Exhibit,* AIAA, 2003, pp. 1-7.

[23] Vaughn, J.A., Curtis, L., Gilchrist, B.E., "Review of the ProSEDS Electrodynamic Tether Mission Development," *40th AIAA/ASME/SAE/ASEE Joint Propulsion Conference and Exhibit,* AIAA, 2004, pp. 1-12.

[24] Williams, S.D., Gilchrist, B.E., Aguero, V.M., "TSS-1R Vertical Electric Fields: Long Baseline Measurements using an Electrodynamic Tether as a Double Probe," *Geophysical Research Letters,* Vol. 25, No. 4, 1998, pp. 445-448.

[25] Gilchrist, B.E., Banks, P.M., Neubert, T., "Electron Collection Enhancement Arising from Neutral Gas Jets on a Charged Vehicle in the Ionosphere," *Journal of Geophysical Research,* Vol. 95, No. A3, 1990, pp. 2469-2475.

[26] Burke, W.J., Raitt, W.J., Thompson, D.C., "Shuttle Charging by Fixed Energy Beam Emissions," *Geophysical Research Letters,* Vol. 5, No. 25, 1998, pp. 725-728.

[27] Aguero, V.M., Gilchrist, B.E., Williams, S.D., "Current Collection Model Characterizing Shuttle Charging During the Tethered Satellite System Missions," *Journal of Spacecraft and Rockets,* Vol. 37, No. 2, 2000, pp. 212-217.

[28] Chang, C.L., Drobot, A.T., Papadopoulos, K., "Current-Voltage Characteristics of the Tethered Satellite System Measurements and Uncertainties Due to Temperature Variations," *Geophysical Research Letters,* Vol. 25, No. 5, 1998, pp. 713-716.

[29] Winningham, J.D., Stone, N.H., Gurgiolo, C.A., "Suprathermal electrons observed on the TSS-1R satellite," *Geophysical Research Letters,* Vol. 25, No. 4, 1998, pp. 429-432.

[30] Parker, L.W., and Murphy, B.B., "Potential Buildup on an Electron-Emitting Ionospheric Satellite," *Journal of Goephysical Research,* Vol. 72, No. 5, 1967, pp. 1631-1636.

[31] Thompson, D.C., Bonifazi, C., Gilchrist, B.E., "The current-voltage characteristics of a large probe in low Earth orbit: TSS-1R results," *Geophysical Research Letters,* Vol. 25, No. 4, 1998, pp. 413-416.

[32] Stone, N., "Electrodynamic characteristics of the Tethered Satellite System during the TSS-1R mission," *AIAA, Space Programs and Technologies Conference,* AIAA, 1996, pp. 1-12.

[33] Kawashima, N., Sasaki, S., Oyama, K., "Results from a tethered Rocket Experiment - CHARGE 2," *Advanced Space Research,* Vol. 8, No. 1, 1988, pp. 197-201.

[34] Mott-Smith, H.M., and Langmuir, I., "The Theory of Collectors in Gaseous Discharges," *Physical Review,* Vol. 28, 1926, pp. 727-763.

[35] VanNoord, J., and Sturmfels, R., "Electrodynamic Tether Optimization for the STEP-AIRSEDS Mission," *37th AIAA/ASME/SAE/ASEE Joint Propulsion Conference and Exhibit,* AIAA, 2001, pp. 1-9.

[36] Forward, R.L., and Hoyt, R.P., "Failsafe multiline Hoytether lifetimes," *31st AIAA, ASME, SAE, and ASEE, Joint Propulsion Conference and Exhibit,* AIAA, 1995, pp. 1-10.

[37] Leamy, M.J., Noor, A.K., and Wasfy, T.M., "Dynamic Simulation of a Tethered Satellite System using Finite Elements and Fuzzy Sets," *Computer Methods in Applied Mechanics and Engineering,* Vol. 190, No. 37-38, 2001, pp. 4847-4870.

[38] Fuhrhop, K.R., West, B., Choiniere, E., "Current Collection to Electrodynamic-Tether Systems in Space," *2nd International Energy Conversion Engineering Conference (IECEC),* AIAA, 2004, pp. 1-9.

[39] Hoyt, R., Slostad, J., and Twiggs, R., "The Multi-Application Survivable Tether MAST Experiment," *39th AIAA/ASME/SAE/ASEE Joint Propulsion Conference and Exhibit,* AIAA, 2003, pp. 1-7.

[40] Bangham, M.E., Lorenzini, E., and Vestal, L., "Tether Transportation System Study," NASA Center for AeroSpace Information, TP-1998-206959, Linthicum Heights, MD, 1998.

[41] Estes, R.D., Lorenzini, E.C., and Santangelo, A., "An Overview of Electrodynamic Tethers," *38th Aerospace Sciences Meeting and Exibit,* AIAA, 2000, pp. 1-12.

[42] Johnson, L., Estes, R.D., Lorenzini, E., "Electrodynamic Tethers for Spacecraft Propulsion," *AIAA, 36th Aerospace Sciences Meeting & Exibit,* AIAA, 1998, pp. 1-8.

[43] Santangelo, A., and Johnson, L., "Future Application of Electrodynamic Tethers tor Propulsion,"
36th AIAA/ASME/SAE/ASEE Joint Propulsion Conference & Exhibit, 2000, pp. 1-11.

[44] Iess, L., Bruno, C., Ulivieri, C., "Satellite De-Orbiting by means of Electrodynamic Tethers Part I: General Concepts and Requirements." *Acta Astronautica,* Vol. 50, No. 7, 2002, pp. 399-399-406.

[45] Iess, L., Bruno, C., Ulivieri, C., "Satellite De-Orbiting by means of Electrodynamic Tethers Part II: System Configuration and Performance," *Acta Astronautica,* Vol. 50, No. 7, 2002, pp. 407-407-416.

[46] Vannaroni, G., Dobrowolny, M., and DeVenuto, F., "Deorbiting with Electrodynamic Tethers-Comparison between Different Tether Configurations," *Space Debris,* Vol. 1, 2001, pp. 159-172.

[47] Vannaroni, G., Dobrowolny, M., and De Venuto, F., "Deorbiting of LEO Satellites with Electrodynamic Tethers," *38th Aerospace Sciences Meeting & Exibit,* 2000,

[48] Dobrowolny, M., "Electrodynamics of Long Metal Tethers in the Ionospheric Plasma," *Radio Science,* Vol. 13, No. 3, 1978, pp. 417-424.

[49]   Ahedo, E., and Sanmartin, J., "Analysis of Electrodynamic Tethers as Deorbiting Systems," *36th AIAA/ASME/SAE/ASEE joint Propulsion Conference & Exibit,* 2000,

[50]   Sanmartin, J.R., Charro, M., Pelaez, J., "Floating Bare Tether as Upper Atmosphere Probe," *2nd International Energy Conversion Engineering Conference,* AIAA, 2004, pp. 1-6.

[51]   Bilen, S.B., and Gilchrist, B.E., " Transient Plasma Sheath Model for Thin Conductors Excited by Negative High Voltages with Application to Electrodynamic Tethers," *IEEE Transactions on Plasma Science,* Vol. 28, No. 6, 2000, pp. 2058-2074.

[52]   Gilchrist, B.E., Voronks, N., and Bilen, S., "ProSEDS "Open Circuit" Characteristics: EMF Measurements and Currents," University of Michigan, 068-3033, Ann Arbor, MI, 1998.

[53]   Bilén, S.G., Gilchrist, B.E., Bonifazi, C., "Transient Response of an Electrodynamic Tether System in the Ionosphere: TSS-1 First Results," *Radio Science,* Vol. 30, No. 5, 1995, pp. 1519-1535.

[54]   Choiniere, E., and Gilchrist, B.E., "Electron Collection to Arbitrarily Shaped Electrodynamic Tethers in Flowing Plasmas: a Kinetic Model," *38th AIAA/ASME/SAE/ASEE Joint Propulsion Conference and Exibit,* 2002, pp. 1-9.

[55]   Choiniere, E., Gilchrist, B.E., and Bilen, S., "Enhancement of Electrodynamic Tether Electron Current Collection Using Radio Frequency Power: Numerical Modeling and Measurements," *37th AIAA/ASME/SAE/ASEE Joint Propulsion Conference and Exibit,* 2001,

[56]   Gilchrist, B.E., Bilen, S.G., Gallimore, A., "Current Collection to Long Conductors with Wide Geometries for Bare Electrodynamic Tether Applications: A Laboratory Update," *40th AIAA Aerospace Sciences Meeting and Exibit,* 2002,

[57]   Arnold, D.A., and Dobrowolny, M., "Transmission Line Model of the Interaction of a Long Metal Wire with the Ionosphere," *Radio Science,* Vol. 15, No. 6, 1980, pp. 1149-1161.

[58]   Estes, R.D., Sanmartin, J., and Martinez-Sanchez, M., "Performance of Bare-Tether Systems Under Varying Magnetic and Plasma Conditions," *Journal of Spacecraft and Rockets,* Vol. 37, No. 2, 2000, pp. 197-197-204.

[59]   Estes, R.D., and Lorenzini, E.C., "Performance and Dynamics of an Electrodynamic Tether," *38th Aerospace Sciences Metting & Exibit,* 2000,

[60]   Grossi, M.D., "Orbiting Tether's Electrodynamic Interactions," NASA - Goddard Space Flight Center, NAS5-25077, Greenbelt, MD, 1979.

[61] Finckenor, M., Vaughn, J., and Watts, E., "Changes in Polymetric Tether Properties Due to Atomic Oxygen," *42nd AIAA Aerospace Sciences Meeting and Exibit,* 2004,

[62] Voronka, N.R., and Hoyt, R.P., "Bare Tether Electromagnetic Propulsion Without the use of Endbody Plasma Contactors," *41st AIAA/ASME/SAE/ASEE Joint Propulsion Conference & Exhibit,* AIAA, 2005, pp. 1-7.

[63] Ferry, J.B., and Martinez-Sanchez, M., "Electron Collection by a Tether at High Potential in a Magnetized Plasma," *39th AIAA/ASME/SAE/ASEE Joint Propulsion Conference and Exhibit,* AIAA, 2003, pp. 1-12.

[64] Onishi, T., Martinez-Sanchez, M., Cooke, D.L., "Effect of Magnetic Field on Current Collection to a Bare Tether in LEO," *38th AIAA/ASME/SAE/ASEE Joint Propulsion Conference & Exibit,* 2002,

[65] Lieberman, M.A., and Lichtenberg, A.J., "Principles of Plasma Discharges and Materials Processing," Wiley-Interscience, Hoboken, NJ, 2005, pp. 757.

[66] Choinere, E., "Theory and Experimental Evaluation of a Consistant Steady State Kinetic Model for 2-D Conductive Structures in Ionospheric Plasmas with Application to Bare Electrodynamic Tethers in Space," 2004, pp. 1-313.

[67] Choiniere, E., Gilchrist, B.E., Bilen, S.G., "Measurement of Cross-Section GeometryEffects on Electron Collection to Long Probes in Mesosonic Flowing Plasmas," *39th AIAA/ASME/SAE/ASEE Joint Propulsion Conference and Exhibit,* AIAA, 2003, pp. 1-13.

[68] Choiniere, E., and Gilchrist, B.G., "Investigation of Ionospheric Plasma Flow Effects on Current Collection to Parallel Wires Using Self-Consistent Steady-State Kinetic Simulations," *41st AIAA/ASME/SAE/ASEE Joint Propulsion Conference and Exhibit,* AIAA, 2005, pp. 1-13.

[69] Parker, L.W., "Plasmasheath-Photosheath theory for Large High-Voltage Space Structures," edited by H.B. Garrett and C.P. Pike, Space Systems and their Interactions with the Earth's Space Environment, AIAA Press, 1980, pp. 477-491.

[70] Hutchinson, I.H., "Principles of Plasma Diagnostics," Camebridge University Press, Camebridge, United Kingdom, 2002, pp. 440.

[71] Bernstein, I.B., and Rabinowitz, I.N., "Theory of Electrostatic Probes in a Low-Density Plasma," *Physics of Fluids,* Vol. 2, No. 2, 1959, pp. 112-121.

[72] Gombosi, T.I., "Physics of Space Environments," Dessler, A.J. Houghton, J.T. and Rycroft, M.J. eds., Camebridge University Press, Camebridge, UK, 1998, pp. 1-339.

[73] Mariani, F., Candidi, M., Orsini, S., "Current Flow Through High-Voltage Sheaths Observer by the TEMAG Experiment During TSS-1R," *Geophysical Research Letters,* Vol. 25, No. 4, 1998, pp. 425-428.

[74] Cooke, D.L., and Katz, I., "TSS-1R electron Currents: Magnetic Limited Collection from a Heated Presheath," *Geophysical Research Letters,* Vol. 25, No. 5, 1998, pp. 753-756.

[75] Gunell, H., Larsson, M., and Brenning, N., "Experiments on anomalous electron currents to apositive probe in a magnetized plasma stream," *Geophysical Research Letters,* Vol. 27, No. 2, 2000, pp. 161-164.

[76] Singh, N., and Leung, W.C., "Numerical Simulation of Plasma Processing Occuring in the Ram Region of the Tethered Satellite," *Geophysical Research Letters,* Vol. 25, No. 5, 1998, pp. 741-744.

[77] Gregory, F.D., "NASA Safety Standard Guidelines and Assessment Procedures for Limiting Orbital Debris," NASA, NSS 1740.14, Washington D.C., 1995.

[78] Bilitza, D., "International Reference Ionosphere 2000," *Radio Science,* Vol. 36, No. 2, 2001, pp. 261-275.

[79] Bilitza, D., "International Reference Ionosphere - Status 1995/96," *Advanced Space Research,* Vol. 20, No. 9, 1997, pp. 1751-1754.

[80] Wertz, J.R., and Larson, W.J. eds., "Space Mission Analysis and Design," Microcosm Press & Kluwar Academic Publishers, El Segundo, CA, 1999, pp. 1-985.

[81] Aguero, V.M., "A Study of Electrical Charging on Large LEO Spacecraft Using a Tethered Satellite as a Remote Plasma Reference," *Stanford University, Space, Telecommunications and Radioscience Laboratory,* 1996, pp. 1-192.

[82] Stone, N.H., and Gierow, P.A., "A Preliminary Assessment of Passive End-Body Plasma Contactors," *39th Aerospace Sciences Meeting and Exibit,* AIAA, 2001, pp. 1-6.

[83] Stone, N.H., and Moore, J.D., "Grid Sphere Electrodes used for Current Collection at the Positive Pole of Electrodynamic Tethers," *45th AIAA/ASME/ASCE/AHS/ASC Structures, Structural Dynamics & Materials Conference,* AIAA, 2004, pp. 1-7.

[84] Khazanov, G.V., Krivorutsky, E., and Sheldon, R.B., "Solid and grid sphere current collectionin view of the tethered satellite systemTSS 1 and TSS 1R mission results," *Journal of Goephysical Research,* Vol. 110, 2005, pp. 1-10.

[85] Hastings, D., and Garrett, H., "Spacecraft - Environment Interactions," Camebridge University Press, New York, NY, 1996, pp. 292.

[86] Siegel, M.W., and Vasile, M.J., "New wide angle, high transmission energy analyzer for secondary ion mass spectrometry," *Review of Scientific Instrumentation,* Vol. 52, No. 11, 1981, pp. 1603-1615.

[87] Benninghoven, A., "Developments in Secondary-Ion Mass Spectroscopy and Applications to Surface Studies," *Surface Science,* Vol. 53, 1975, pp. 596-625.

[88] Benninghoven, A., "Surface Investigation of Solids by the Statistical Method of Secondary-Ion Mass Spectroscopy (SIMS)," *Surface Science,* Vol. 35, 1973, pp. 427-457.

[89] Benninghoven, A., and Mueller, A., "Secondary ion yields near 1 for some chemical compounds," *Physics Letters,* Vol. 40A, No. 2, 1972, pp. 169-170.

[90] Child, C.D., "Discharge From Hot CaO," *Physical Review (Series I),* Vol. 32, No. 5, 1911, pp. 492-511.

[91] Langmuir, I., "The Effect of Space Charge and Initial Velocities on the Potential Distribution and Thermionic Current between Parallel Plane Electrodes," *Physical Review,* Vol. 21, No. 4, 1923, pp. 419-435.

[92] Langmuir, I., "The Effect of Space Charge and Residual Gases on Thermionic Currents in High Vacuum," *Physical Review,* Vol. 2, No. 6, 1913, pp. 450-486.

[93] Luginsland, J.W., McGee, S., and Lau, Y.Y., "Virtual Cathode Formation Due to Electromagnetic Transients," *IEEE Transactions on Plasma Science,* Vol. 26, No. 3, 1998, pp. 901-904.

[94] Lau, Y.Y., "Simple Theory for the Two-Dimensional Child-Langmuir Law," *Physical Review Letters,* Vol. 87, No. 27, 2001, pp. 278301/1-278301/3.

[95] Luginsland, J.W., Lau, Y.Y., and Gilgenbach, R.M., "Two-Dimensional Child-Langmuir Law," *Physical Review Letters,* Vol. 77, No. 22, 1996, pp. 4668-4670.

[96] Humphries, S.J., "Charged Particle Beams," John Wiley & Sons, Inc., New York, 1990, pp. 834.

[97] Morris, D., "Optimizing Space-Charge Limits of Electron Emission Into Plasmas in space Electric Propulsion," *University of Michigan,* 2005, pp. 1-212.

[98] Gilchrist, B.E., Gallimore, A.D., Jensen, K.L., "Field-Emitter Array Cathodes (FEACs) for Space-Based Applications: An Enabling Technology," Not Published, University of Michigan, 2001.

[99] Dekker, A.J., "Thermionic Emission," *McGraw Hill Access Science Encyclopedia ,* Vol. 2004, No. 5 / 3, 2002, pp. 2.

[100] Dobrowolny, M., and Stone, N.H., "A Tecnical Overview of TSS-1: the First Tethered-Satellite System Mission," *Il Nuovo Cimento Della Societa Italiana Di Fisica,* Vol. 17C, No. 1, 1994, pp. 1-12.

[101] Bonifazi, C., Svelto, F., and Sabbagh, J., "TSS Core Equipment I - Electrodynamic Package and Rational for System Electrodynamic Analysis," *Il Nuovo Cimento Della Societa Italiana Di Fisica,* Vol. 17C, No. 1, 1994, pp. 13-47.

[102] Gomer, R., "Field emission," *McGraw Hill Access Science Encyclopedia*, Vol. 2005, No. July 1, 2002, pp. 2.

[103] Spindt, C.A., Holland, C.E., and Rosengreen, A. Brodie, I., "Field-Emitter Arrays for Vacuum Microelectronics," *IEEE Transcations on Electron Devices,* Vol. 38, No. 10, 1991, pp. 2355-2363.

[104] Spindt, C.A., "Spindt Emitter Measurements," *unpublished material Stanford Research Institute*, 2001, pp. 1.

[105] Jensen, K.L., "Field emitter arrays for plasma and microwave source applications," *Physics of Plasmas,* Vol. 6, No. 5, 1999, pp. 2241-2253.

[106] Jensen, K.L., "Field Emitter Array Calculation Spreadsheet," Vol. 3.0, 1996,

[107] Lapuerta, V., and Ahedo, E., " Dynamic model of a plasma structure with an intermediate double-layer, formed outside an anodic plasma contactor," *Physics of Plasmas,* Vol. 7, No. 6, 2000, pp. 2693-2703.

[108] Wells, A.A., "Current Flow Across a Plasma Double Layer in a Hollow Cathode Ion Thruster," *AIAA 9th Electric Propulsion Conference,* AIAA, 1972, pp. 1-15.

[109] Andrews, J.G., and Allen, J.E., "Theory of a Double Sheath Between Two Plasmas," *Proceedings of the Royal Society of London Series A,* Vol. 320, No. 1543, 1971, pp. 459-472.

[110] Prewett, P.D., and Allen, J.E., "The double sheath Associated with a Hot Cathode," *Proceedings of the Royal Society of London Series A,* Vol. 348, No. 1655, 1976, pp. 435-446.

[111] Katz, I., Anderson, J.R., Polk, J.E., "One-Dimensional Hollow Cathode Model," *Journal of Propulsion and Power,* Vol. 19, No. 4, 2003, pp. 595-600.

[112] Katz, I., Lilley, J. R. Jr., Greb, A., "Plasma Turbulence Enhanced Current Collection: Results from the Plasma Motor Generator Electrodynamic Tether Flight," *Journal of Geophysical Research,* Vol. 100, No. A2, 1995, pp. 1687-1690.

[113] Parks, D.E., Katz, I., Buchholtz, B., "Expansion and electron emission characteristics of a hollow-cathode plasma contactor," *Journal of Applied Physics,* Vol. 74, No. 12, 2003, pp. 7094-7100.

[114] Domonkos, M.T., "Evaluation of Low-Current Orificed Hollow Cathodes," *University of Michigan Ph.D. Dissertation,*1999, pp. 1-173.

[115] Maxwell Technologies, "Environment Work Bench," Vol. 5.0, 2003, pp. 12-11 to 12-23.

[116] Williams, J.D., and Wilbur, P.J., "Gound Based Tests of Hollow Cathode Plasma Contactors," *3rd International Conference on Tethers in Space - Toward Flight,* AIAA, 1989, pp. 77-87.

[117] Williams, J.D., "An experimental investigation of hollow-cathode-based plasma contactors," *Colorado State University Ph.D. Dissertation*, 1991, pp. 1-125.

[118] Williams, J.D., "Verification of Hollow Cathode Model for Electrodynamic Tether Simulations," Vol. Personal Communication Via E-mail, 2006, pp. 1.

[119] Goebel, D.M., Jameson, K.K., Watkins, R.M., "Hollow Cathode and Keeper-Region Plasma Measurements Using Ultra-Fast Miniature Scanning Probes," *40th AIAA/ASME/SAE/ASEE Joint Propulsion Conference and Exhibit,* AIAA, 2004, pp. 1-12.

[120] Dobrowolny, M., Vannaroni, G., and DeVenuto, F., "Electrodynamic Deorbiting of LEO satellites," *Nuovo Cimento,* Vol. 23C, No. 1, 2000, pp. 1-21.

[121] Dobrowolny, M., Colombo, G., and Grossi, M.D., "Electrodynamics of long conducting tethers in the near-earth environment," *Interim Report Smithsonian Astrophysical Observatory,* 1976, pp. 1-48.

[122] Hoyt, R.P., "Stabilization of Electrodynamic Tethers," *38th AIAA/ASME/SAE/ASEE Joint Propulsion Conference & Exibit,* 2002, pp. 1-9.

[123] Voronka, N.R., "TEMPEST Version 1.97," Vol. 1.97, 2001,

[124] Stenzel, R.L., and Urrutia, J.M., "Laboratory Experiments on the Electrodynamic Behavior of Tethers in Space," *AIAA 22nd Fluid Dynamics, Plasma Dynamics & Lasers Conference,* AIAA, 1991, pp. 1-9.

[125] Stenzel, R.L., Urrutia, J.M., and Rousculp, C.L., "Pulsed Currents Carried by Whistlers. Part I: Exc.itatian by Magnetic Antennas," *Physics of Fluids B,* Vol. 5, No. 2, 1993, pp. 325-338.

[126] Stenzel, R.L., Urrutia, J.M., and Rousculp, C.L., "Transport of Time-Varying Plasmaby Whistler Wave Packets," *IEEE Transactions in Plasma Science,* Vol. 20, No. 6, 1992, pp. 787-796.

[127] Donohue, D.J., "Plasma Wave Radiation Induced by a Conducting Tethered Satellite System," 1991, pp. 1-202.

[128] Bonometti, J.A., Sorensen, K.F., Jansen, R.H., "Free Re-boost Electrodynamic Tether on the International Space Station," *41st AIAA/ASME/SAE/ASEE Joint Propulsion Conference & Exhibit,* AIAA, 2005, pp. 1-7.

[129] Morris, D., Gilchrist, B.E., and Gallimore, A., "Integration of Field Emitter Arrays into Spacecraft Systems," *Space Technology and Applications International Forum,* AIAA, 2002, pp. 393-400.

[130] Gilchrist, B., and Morris, D., "Planning for the TOR3QUE Electron – Field Emission System (E-FES)," Unpublished, University of Michigan, 2004.

[131] Morris, D., and Gilchrist, B.E., "Electron Field Emission and the Space Charge Limit: Techniques and Tradeoffs," *Joint Propulsion Conference,* AIAA, 2003, pp. 1-9.

[132] Szuszczewicz, E.P., Blanchard, P., Wilkinson, P., "The first real-time worldwide ionospheric predictions network: An advance in support of spaceborne experimentation, on-line model validation, and space weather," *Geophysical Research Letters,* Vol. 25, No. 4, 1998, pp. 449-452.

[133] Gilchrist, B.E., Bonifazi, C., Bilén, S.G., "Enhanced electrodynamic tether currents due to electron emission from a neutral gas discharge: Results from the TSS-1R mission," *Geophysical Research Letters,* Vol. 25, No. 4, 1998, pp. 437-440.

[134] Fuhrhop, K.R.P., Choiniere, E., and Gilchrist, B.E., "Measurement of Electron Collection to Holed Tape Probes in a High-Speed Flowing Plasma," *unpublished IEEE Transactions in Plasma Science*, 2007, pp. 1-18.

[135] Johnson, L., Lorenzini, E., Gilchrist, B.E., "Propulsive Small Expendable Deployer System (ProSEDS) Experiment Mission Overview & Status," *39th AIAA/ASME/SAE/ASEE Joint Propulsion Conference and Exhibit,* AIAA, 2003, pp. 1-9.

[136] Choiniere, E., Gilchrist, B.E., Bilen, S.G., "Experimental Investigation of Electron Collection to Solid and Slotted Tape Probes in a High-speed Flowing Plasma," *IEEE Transactions on Plasma Science,* 2004, pp. 1-32.

[137] Gilchrist, B.E., Bilen, S.G., Choiniere, E., "Analysis of Chamber Simulations of Long Collecting Probes in High-Speed Dense Plasmas," *IEEE Transactions on Plasma Science,* Vol. 30, No. 5, 2002, pp. 2023-2034.

[138] Laframboise, J.G., and Parker, L.W., "Probe Design for Orbit-Limited Current Collection," *The Physics of Fluids,* Vol. 16, No. 5, 1973, pp. 629-636.

[139] Bilen, S.G., Domonkos, M.T., and Gallimore, A.D., "Simulating Ionospheric Plasma with a Hollow Cathode in a Large Vacuum Chamber," *Journal of Spacecraft and Rockets,* Vol. 38, No. 4, 2001, pp. 617-621.

[140] Choiniere, E., and Gilchrist, B.E., "Modeling Long Probes in Flowing Plasmas using KiPS-2D, a Novel Steady-State Vlasov Solver," *39th AIAA/ASME/SAE/ASEE Joint Propulsion Conference and Exhibit,* AIAA, 2003, pp. 1-11.

[141] Haas, J.M., Gulczinski, F.S., Gallimore, A.D., "Performance Characteristics of a 5 kW Laboratory Hall Thruster," *34th AIAA/ASME/SAE/ASEE Joint Propulsion Conference and Exhibit,* AIAA, 1998, pp. 1-8.

[142] Williams, G.J., Smith, T.B., Domonkos, M.T., "Laser-Induced Fluorescence Characterization of Ions Emitted from Hollow Cathodes," *IEEE Transactions in Plasma Science,* Vol. 28, No. 5, 2000, pp. 1664-1675.

[143] Smith, T.B., Herman, D.A., and Gallimore, A.D., "Laser-induced Fluorescence Velocimetry of Xe II in the 30-cm NSTAR-type Ion Engine Plume," *40th AIAA/ASME/SAE/ASEE Joint Propulsion Conference and Exhibit,* AIAA, 2004, pp. 1-17.

[144] Hoegy, W.R., and Wharton, L.E., "Current to a Moving Cylindrical Electrosatic Probe," *Journal of Applie Physics,* Vol. 44, No. 12, 1973, pp. 5365-5371.

[145] Choiniere, E., and Gilchrist, B.E., "Poisson-Vlasov Modeling of Parallel Cylinders in Ionospheric Plasmas," *40th AIAA/ASME/SAE/ASEE Joint Propulsion Conference and Exhibit,* AIAA, 2004, pp. 1-20.

[146] Hoyt, R.P., "Hoyt Tether Resistance," *Personal Communication,* 2006, pp. 1.

[147] National Oceanic and Atmospheric Administration, "Solar Cycle 23 Progression," http://www.sel.noaa.gov/SolarCycle/, Vol. 2005, 2007, pp. 1.

[148] National Oceanic and Atmospheric Administration, "Recent Solar Indices," http://www.sel.noaa.gov/ftpdir/weekly/RecentIndices.txt, Vol. 2005, 2007, pp. 1.

[149] Halliday, D., Resnick, R., and Walker, J., "Fundamentals of Physics," John Wiley and Sons, Inc., 2003, pp. 1000.

[150] Choiniere, E., "Analysis of high-voltage cylindrical sheaths in ionospheric plasmas using KiPS-1D and KiPS-2D," *unpublished IEEE Transactions in Plasma Science*, 2004, pp. 1-74.

[151] Gilchrist, B.E., Lim, B., Meckel, N., "The use of Electrodynamic Tethers for Orbit Maintenence and Deorbit of Large Spacecraft- A Trade Study of the NASA GLAST Mission," *38th AIAA/ASME/SAE/ASEE Joint Propulsion Conference & Exhibit,* AIAA, 2002, pp. 1-13.

[152] Gehrels, N., and Michelson, P., "GLAST: the next-generation high energy gamma-rayastronomy mission," *Astroparticle Physics,* Vol. 11, 1999, pp. 277-282.

[153] Turner, A.E., "Use of a Staging Orbit for Geosynchronous Orbit-Raising Involving Servicing," *AIAA/AAS Astrodynamics Specialist Conference and Exhibit,* AIAA, 2002, pp. 1-12.

[154] Johnson, L., and Herrmann, M., "International Space Station Electrodynamic Tether Reboost Study," NASA, TM--1998-208538, 1998.

[155] Ferguson, D.C., "vxB Effects on Space Station," *2nd International Energy Conversion Engineering Conference,* AIAA, 2004, pp. 1-7.

[156] Singh, N., "Electromagnetic Effects Induced by the Space Station," *Proceedings., Twenty-First Southeastern Symposium on System Theory,* IEEE, 1989, pp. 362-366.

[157] Gallagher, D.L., Craven, P.D., and Comfort, R.H., "An Emperical Model of the Earth's Plasmasphere," *Advanced Space Research,* Vol. 8, No. 8, 1988, pp. 15-24.

[158] Gallagher, D.L., Craven, P.D., and Comfort, R.H., "Global Core Model," *Journal of Geophysical Research,* Vol. 105, No. A8, 2000, pp. 18819-18833.

[159] Rycroft, M.J., and Jones, I.R., "A Suggested Model for the IRI Plasmaspheric Distribution," *Advanced Space Research,* Vol. 7, No. 6, 1987, pp. 13-22.

[160] Rycroft, M.J., and Jones, I.R., "Modelling the Plasmasphere for the International Reference Ionosphere," *Advanced Space Research,* Vol. 5, No. 10, 1985, pp. 21-27.

[161] Vannaroni, G., Dobrowolny, M., Melchioni, E., "Characterization of the Interaction Between a Hollow Cathode Source and an Ambient Plasma," *Journal of Applied Physics,* Vol. 71, No. 10, 1992, pp. 4709-4717.

[162] Mikellides, I.G., Katz, I., and Goebel, D.M., "Numerical Simulation of the Hollow Cathode Discharge Plasma Dynamics," *The 29th International Electric Propulsion Conference,* 2005, pp. 1-15.

[163] Mikellides, I.G., Katz, I., Goebel, D.M., "Hollow cathode theory and experiment. II. A two-dimensional theoreticalmodel of the emitter region," *Journal of Applied Physics,* Vol. 98, 2005, pp. 113303 - 113303-14.

[164] Mikellides, I.G., Katz, I., Goebel, D.M., "Theoretical Model of a Hollow Cathode Plasma for the Assessment of Insert and Keeper Lifetimes," *41st AIAA/ASME/SAE/ASEE Joint Propulsion Conference & Exhibit,* AIAA, 2005, pp. 1-24.

[165] Hoyt, R.P., Forward, R.L., Nordley, G.D., "Rapid Interplanetary Tether Transport Systems," *50th International Astronautical Congress,* AIAA, 1999, pp. 1-32.

[166] Hoyt, R.P., "Moon & Mars Orbiting Spinning Tether Transport," *NIAC Phase II Interim Report*, Report # 07600-034, 1999, pp. 1-156.

[167] Hoyt, R.P., "Design of a Tether Boost Facility for the Human Mars Mission," Tethers Unlimited, Inc., Seattle, WA, 1999.

[168] Voronka, N.R., Hoyt, R.P., Slostad, J., "Modular Spacecraft with Integrated Structural Electrodynamic Propulsion," NAS5-03110-07605-003-050, 2006.

[169] Pote, B., "Busek Hollow Cathode Information," *Personal Correspondance,* 2006, pp. 1.

[170] Beal, B., Grys, K., Welander, B., "Development of a High Current Hollow Cathode for high Power Hall Thrusters," *Joint Army Navy NASA Air Force Propulsion Meeting/Liquid Propulsion Subcommittee/Spacecraft Propulsion Subcommittee Conference,* 2005, pp. 1-8.

[171] Brophy, J.R., and Garner, C.E., "Tests of High Current Hollow Cathodes for Ion Engines," *AIAA/ASME/SAE/ASEE 24th Joint Propulsion Conference,* AIAA, 1988, pp. 1-11.

[172] Carpenter, C.B., and Patterson, M.J., "High-Current Hollow Cathode Development," *2001 International Electric Propulsion Conference,* 2001, pp. 1-8.

[173] Goebel, D.M., and Watkins, R.M., "High current, low pressure plasma cathode electron gun," *Review of Scientific Instruments,* Vol. 71, No. 2, 2000, pp. 1-11.

[174] Beal, B., "Hollow Cathode Information," *Personal Correspondance,* 2006, pp. 1.

[175] Tarter, J., "Hollow Cathode Information," *Personal Correspondance,* 2006, pp. 1.

[176] Patterson, M.J., "High Current Hollow Cathode Information," *Personal Correspondance,* 2006, pp. 1.

[177] Goebel, D.M., "High Current Hollow Cathode Information," *Personal Correspondance,* 2006, pp. 1.

[178] Hansen, B., "High Current Hollow Cathode Information," *Personal Correspondance,* 2006, pp. 1.

[179] Foster, J.E., and Patterson, M.J., "Characterization of Downstream Ion Energy Distributions From a High Current Hollow Cathode in a Ring Cusp Discharge Chamber," *39th Joint Propulsion Conference and Exhibit,* AIAA, 2003, pp. 1-17.

[180] Foster, J.E., and Patterson, M.J., "Plasma Emission Characteristics From a High Current Hollow Cathode in an Ion Thruster Discharge Chamber," *38th Joint Propulsion Conference and Exhibit,* AIAA, 2002, pp. 1-17.

[181] Friedly, V.J., and Wilbur, P.J., "High Current Hollow Cathode Phenomena," *Journal of Propulsion and Power,* Vol. 8, No. 3, 1992, pp. 635-643.

[182] Friedly, V.J., and Wilbur, P.J., "High Current Hollow Cathode Phenomena," *AIAA/DGLR/JSASS 21st International Electric Propulsion Conference,* AIAA, 1990, pp. 1-12.

[183] Kameyama, I., and Wilbur, P.J., "Measurements of Ions from High-Current Hollow Cathodes Using Electrostatic Energy Analyzer," *Journal of Propulsion and Power,* Vol. 16, No. 3, 2000, pp. 1-7.

[184] Patterson, M.J., Domonkos, M.T., Carpenter, C., "Recent Development Activities in Hollow CathodeTechnology," *27th International Electric Propulsion Conference,* 2001, pp. 1-17.

[185] Kovaleski, S.D., "Life Model of Hollow Cathodes Using a Barium Calcium Aluminate Impregnated Tungsten Emitter," *27th International Electric Propulsion Conference,* 2001, pp. 1-14.

[186] Katz, I., Gardner, B.M., Mandell, M.J., "Model of Plasma Contactor Performance," *Journal of Spacecraft and Rockets,* Vol. 34, No. 6, 1997, pp. 824-828.

[187] Milellides, I.G., Katz, I., Goebel, D.M., "Plasma Processes Inside Dispenser Hollow Cathodes," *Physics of Plasmas,* Vol. 13, 2006, pp. 1-10.

[188] Salhi, A., "Theoretical and Experimental Studies of Orificed Hollow Cathode Operation," *Ohio State University Ph.D. Thesis*, 1993, pp. 1-189.

[189] Salhi, A., and Turchi, P.J., "Scaling Relations for Design and Operation of Orificed-Hollow Cathodes," *30th AIAA/ASME/SAE/ASEE JointPropulsion Conference,* AIAA, 1994, pp. 1-7.

[190] Gleizer, J.Z., Krokhmal, A., Krasik, Y.E., "High Current Electron Beam Generation by a Pulsed Hollow Cathode," *Journal of Applied Physics,* Vol. 91, No. 5, 2002, pp. 3431-3443.

[191] Sarver-Verhey, T.R., "28,000 Hour Xenon Hollow Cathode Life Test Results," *25th International Electric Propulsion Conference,* 1997, pp. 1-11.

[192] Sarver-Verhey, T.R., "Destructive Evaluation of a Xenon Hollow Cathode After a 28,000 Hour Life Test," *34th AIAA/ASME/SAE/ASEE Joint Propulsion Conference and Exhibit,* AIAA, 1988, pp. 1-14.

[193] Goebel, D.M., and Watkins, R.M., "LaB6 Hollow Cathodes for Ion and Hall Thrusters," *41st AIAA/ASME/SAE/ASEE Joint Propulsion Conference & Exhibit,* AIAA, 2005, pp. 1-9.

[194] Wilbur, P.J., and Williams, J.D., "An Experimental Investigation of the Plasma Contacting Process," *AlAA 25th Aerospace Sciences Meeting,* AIAA, 1987, pp. 1-10.

[195] Badhwar, G.D., "Drift rate of the South Atlantic Anomaly," *Journal of Geophysical Research*, Vol. 102, No. A2, 1997, pp. 2343-2349.